



Università Politecnica delle Marche
Master-degree in Environmental Engineering

**Numerical modelling of the seabed stresses and
scouring at costal structures by means of SWASH**

Student:

Giovanni Palladino

Supervisor:

Prof. Maurizio Brocchini

Co-supervisors:

Dott. Claudia Pizzigalli

Prof. Eng. Matteo Postacchini

Academic year 2018-2019

AKNOWLEDGEMENTS

In primo luogo, voglio ringraziare coloro che mi hanno direttamente accompagnato nella realizzazione di questo lavoro, i professori Prof. M.Brocchini e Prof. M.Postacchini, per avermi dato l'opportunità di svolgere questa attività di tirocinio e per l'aiuto fornitomi e per essere stati sempre disponibili.

Un ringraziamento va anche a SAIPEM S.p.A. per avermi permesso, assieme all'Università Politecnica delle Marche nelle persone dei professori sopra citati, di svolgere l'attività di tirocinio in una delle realtà principi del settore del Oil&Gas. In particolar modo tengo a sottolineare l'importante contributo offertomi da Claudia Pizzigalli, nella figura di tutor aziendale e correlatrice, per aver avuto la pazienza e l'abilità di insegnarmi tanto nel breve periodo a disposizione. Un ringraziamento va anche al capo ufficio Floriano Gianfelici per la disponibilità e cortesia mostratami in ogni occasione. E poi ringrazio tutti i componenti dell'ufficio "Ocean" per la piacevole compagnia soprattutto nelle pause pranzo.

Circa due anni e mezzo quando mi sono iscritto al corso di "Environmental Engineering" (se un giorno mi avessero detto che avrei fatto un corso in inglese, avrei fatto riaprire i manicomi solo per loro) ho conosciuto un gruppo di ragazzi che sono diventati non solo i miei amici ma hanno avuto un ruolo importante nel raggiungimento di questo obiettivo: "DIS IS THE POINT".

In questo gruppo formato da quasi tutte persone che non si conoscevano prima o che si conoscevano poco, c'è quella che è stata la mia prima conoscenza all'UNIVPM: durante una pausa tra una lezione e l'altra in aula 145/2 trovo un ragazzo con cui inizio a scambiare quattro chiacchiere sul calcio e sul fantacalcio quel ragazzo oggi un mio grandissimo amico a cui voglio un gran bene e domani sarà quello che mi porterà a vedere le partite di Inter-Juve senza cacciare un centesimo, un investimento per il futuro :-P, vero Mattia?

Un grande GRAZIE per essere entrati prima nella mia carriera accademica e poi nella vita va ad Andrea e Piero detto Pierangelo.

Un GRAZIE va al gruppo delle tre commari: Marsietta, Alessandra e Cori; per la cronaca io con oggi qui ho finito e non mi avete fatto la mascotte! Uffa >_<

Un GRAZIE va a tutti: Elena, Laura, Serena, Luca, Gaio e Alessia; vi voglio bene siete stati davvero importanti tutti quanti, se non c'eravate voi sarebbe stato tutto più noioso.

Un altro gruppo che ha avuto un ruolo importante nella mia vita anconetana è stato: Panz satoll e patatino un gruppo composta da 5 molisani e uno quasi. Questo è il gruppo con cui ho passato la maggior parte delle serate organizzate dalla movida anconetana, su questo gruppo se ne potrebbero dire tante, troppe. Un grande GRAZIE davvero di cuore a Marco, Marco, Mattia e Gigi per aver condiviso con me 4 anni e mezzo della loro vita. Al "buon" Fulvio che non fa direttamente parte del gruppo whatsapp ma per lui valgono le stesse cose dette sopra, GRAZIE.

Un GRAZIE va anche agli amici di CB: Eli, Buons, Cinci e Alberto a cui mi lega un fortissimo legame di amicizia.

Passiamo adesso alla famiglia, un GRAZIE sentito a MManuela, lo so che ti sarai arrabbiata ma a me piace con la doppia M e non EM.

Un GRAZIE al mio fratellino sarà anche fastidioso e rompiscatole, ma se non fosse per lui le giornate sarebbero più grigie e vuote. A te va anche un altro GRAZIE se non fosse stato per te che dovevi iniziare l'uni forse avrei lasciato o sarei ancora a Roma, con chissà quanti esami ancora da fare.

Un GRAZIE, ai miei sponsor sia in senso figurato che economico, ai miei genitori che hanno sempre creduto in me, spronandomi ad andare avanti a fare a non fermarmi (qualche volta è finita ad appiccico), ma questo non solo un mio traguardo, o come dirà papà è solo il punto di partenza, è anche il VOSTRO... Come dice qualcuno sarò sembrerò anche apatico, anaffettivo ma vi voglio un mondo di bene.

In fine un GRAZIE anche a me stesso e alla mia testardaggine e determinazione che mi ha permesso di arrivare fin qui oggi a festeggiare con voi il mio PRIMO vero traguardo.

SUMMARY

ABSTRACT.....	13
Chapter 1 – Introduction.....	15
1.1 About this thesis	15
1.2 Relevance of the study.....	17
Chapter 2 – Wave theory	17
2.1 Regular wave theory.....	21
2.1.1 Outline of the Linear wave theory	23
2.1.2 Non-linear effects.....	27
2.2 Wave propagation in shallow waters	29
2.2.1 Shoaling.....	30
2.2.2 Refraction	31
2.2.3 Reflection and Transmission	33
2.2.4 Diffraction.....	33
2.2.5 Wave Breaking	35
2.3 Surf Zone.....	37
Chapter 3 – Scouring	39
3.1 Basic concepts.....	39
3.1.1 Introduction.....	39
3.1.2 Amplification factor.....	41
3.1.3 Equilibrium scour depth, equilibrium stage.....	42
3.1.4 Clear-water scour and live-bed scour	43
3.1.5 Time scale.....	46
3.1.5.1 Time scale in steady currents	47
3.1.5.2 Time scale in waves	48
3.2 Shear stress.....	49
3.2.1 Unidirectional flow	49
3.2.2 Oscillatory flow.....	50
3.3 Scouring laboratory test	51
3.3.1 Scour near sea walls	51
3.3.2 Scour near tip of breakwaters and groynes.....	53

3.3.3 Scour near piles and piers due waves and currents	56
3.3.4 Scour near horizontal pipes	59
Chapter 4 – Numerical models	61
4.1 SWAN	61
4.1.1 Governing equations	62
4.1.2 Source and sinks	64
4.1.2.1 Input by wind	64
4.1.2.2 Dissipation by white capping	67
4.1.2.3 Dissipation by bottom friction	68
4.1.2.4 Dissipation by depth-induced wave breaking	70
4.1.2.5 Non-linear wave-wave interaction (quadruplets)	71
4.1.2.6 Non-linear wave-wave interaction (triplets)	72
4.1.3 First- and second-generation model formulation in SWAN	73
4.1.3.1 Linear and exponential growth	74
4.1.3.2 Decay	74
4.1.3.3 Saturated spectrum	75
4.1.4 Boundary conditions	76
4.1.5 Numerical schemes	76
4.1.5.1 The fraction step method	76
4.1.5.2 Wave propagation in frequency and directional space	77
4.2 SWASH	77
4.2.1 Governing equations	80
4.2.2 Physical parameters	83
4.2.2.1 Wind effects	83
4.2.2.2 Bottom friction	85
4.2.2.3 Depth-induced wave breaking	86
4.2.2.4 Horizontal and vertical turbulent mixing	87
4.2.3 Numerical implementation	88
4.2.3.1 Basic principles	88
4.2.3.2 Duration of simulation	88
4.2.3.3 Time step	89
4.2.3.4 Vertical pressure gradient	90
4.2.3.5 Momentum conservation	91

4.2.3.6 Discretization of advective terms in the momentum equations	92
4.2.3.7 Moving shorelines	93
4.2.4 Parallelization strategy	94
4.2.5 Porous structure.....	95
4.2.5.1 Background on porous structure.....	95
4.2.5.2 Porosity in SWASH	98
Chapter 5 – Case study.....	100
5.1 Real case study description	100
5.1.1. Introduction.....	100
5.1.2 Scouring problems description	102
5.1.3 Methodology	104
5.2 Available data.....	105
5.2.1 Wind and waves	105
5.2.1.1 Wind and Waves – Measured data	105
5.2.1.1.1 Wave measured data	105
5.2.1.1.2 Wind measured data	106
5.2.1.2 Wind and Waves - DPR.....	107
5.2.1.3 Wind and Waves -hindcast data from DHI MWM.....	107
5.2.1.3.1 Wave hindcast data	107
5.2.1.3.2 Wind hindcast data	107
5.2.2 Bathymetry.....	108
5.3 SWAN: calibration, validation and set-up.....	110
5.3.1 SWAN input data	111
5.3.1.1 Computational grid.....	111
5.3.1.2 Wind input data.....	112
5.3.2 Boundary condition	113
5.3.3 SWAN calibration	116
5.3.3.1 Physical calibration	117
5.3.4 SWAN results.....	119
5.3.4.1 SWAN post-processing results	119
5.3.4.1.1 North-West storm.....	120
5.3.4.1.2 North storm	122
5.3.4.1.3 North-East storm	123

5.4 SWASH: set-up	125
5.4.1 Introduction.....	125
5.4.2 SWASH input file	126
5.4.2.1 Start-up commands	127
5.4.2.2 Commands for model description	127
5.4.2.2.1 Computational grid	127
5.4.2.2.2 Input fields	128
5.4.2.2.3 Boundary conditions.....	129
5.4.2.2.4 Physics.....	130
5.4.2.2.5 Numerical implementation.....	131
5.4.2.3 Output commands.....	132
5.4.2.4 Lock-up commands.....	132
Chapter 6 – Results and discussion.....	134
6.1 Results.....	134
6.1.1 Significant wave height	135
6.1.2 Sea currents.....	139
6.1.3 Current induced seabed shear stress (τ_c).....	143
6.1.4 Wave induced shear stress (τ_w)	148
6.1.5 Total shear stress τ	157
6.2 Discussion.....	162
6.2.1 Double sponge layer.....	162
6.2.2 Size of computational domain	162
6.2.3 Wave direction	162
6.3 Observation.....	162
6.3.1 Temporal scale of scouring	166
Chapter 7 – Conclusion and Recommendation.....	167
7.1 Conclusion.....	167
7.2 Recommendations	168
7.2.1 Recommendations for the developers of the model.....	168
7.2.2 Recommendations for the SWASH application	169
Reference.....	171
Appendix A.....	172

A.1 SWAN input file.....	172
A.2 SWASH input file (case d)	175

List of Figures

<i>Figure 1 Waves classification through their frequency</i>	18
<i>Figure 2 Long-crested wave (swell waves) on the left and short-crested (wind waves) wave on the right</i>	20
<i>Figure 3 Regular travelling wave properties</i>	21
<i>Figure 4 Ranges of validity for various wave theories; the horizontal axis is a measure of shallowness while the vertical axis is a measure of steepness</i>	22
<i>Figure 5 Trigonometric simplification based on the ratio between water depth and wavelength (h/L)</i>	25
<i>Figure 6 Surface elevation along with velocity and acceleration vectors</i>	26
<i>Figure 7 Sketch of a skewed wave</i>	28
<i>Figure 8 Sketch of an asymmetric wave as the sum of two harmonics</i>	28
<i>Figure 9 Shoaling scheme.</i>	30
<i>Figure 10 Shoaling coefficient variation with dimensionless depth</i>	31
<i>Figure 11 Refraction scheme.</i>	32
<i>Figure 12 Wave reflection scheme</i>	33
<i>Figure 13 Wave diffracted scheme</i>	34
<i>Figure 14 K_D for semi-infinite breakwater</i>	34
<i>Figure 15 K_D for contiguous breakwaters (gap width $b = \text{wavelength } L$)</i>	35
<i>Figure 16 Spilling</i>	36
<i>Figure 17 Plunging</i>	36
<i>Figure 18 Surging</i>	37
<i>Figure 19 Surf Zone scheme, with velocity profile</i>	37
<i>Figure 20 Rip Current scheme</i>	39
<i>Figure 21 Time development of scour depth</i>	42
<i>Figure 22 Initiation of motion at the bed</i>	44
<i>Figure 23 Schematic variations of scour depth as function of the Shields parameters: (a) currents; (b) waves</i>	45
<i>Figure 24 Time development of scour depth. $KC=0.61$ $D/L=0.15$. At the point where the scour is maximum</i>	46
<i>Figure 25 Time development of scour depth (a) current $\vartheta=0.098$ (Mao 1986); (b) Wave, $\vartheta=0.035$, $KC=27$ (Fredsoe 1992)</i>	47
<i>Figure 26 Time scale current, live bed</i>	48
<i>Figure 27 Near-bed orbital velocity for monochromatic waves and a spectrum of waves (Soulsby, 1987)</i>	51
<i>Figure 28 Basic shape of scour hole near toe of seawall (Steetzel, 1988)</i>	52
<i>Figure 29 Vortex patterns near tip of wall-type breakwater</i>	54
<i>Figure 30 Scour and deposition locations near vertical breakwaters</i>	55
<i>Figure 31 Scour and deposition locations near rubble-mound breakwaters;</i>	55
<i>Figure 32 Flow pattern and scour near pile (Melville, 1988)</i>	57
<i>Figure 33 Vortices near the pipeline in unidirectional flow</i>	59
<i>Figure 34 Scour in unidirectional and oscillatory flow</i>	60

<i>Figure 35 Observed values of the wind drag coefficient C_D from various studies and the weighted best-fit 2nd- and 4th-order polynomial (n is the number of independent data points per study).</i>	66
<i>Figure 36 Applied arrangements of unknowns in a staggered grid: (a) standard layout, (b) box layout</i>	90
<i>Figure 37 Location of the area of interest</i>	101
<i>Figure 38 Overview of the analysed coastal area</i>	101
<i>Figure 39 Z-type steel sheet piles</i>	102
<i>Figure 40 Scheme of cofferdam and causeway construction</i>	102
<i>Figure 41 Shaded Relief – Post cofferdam construction</i>	103
<i>Figure 42 Shows the evolution of bottom profile at the edges of the cofferdam up to the wide – KP 0 at shoreline,</i>	104
<i>Figure 43 Buoy and gauge devices</i>	106
<i>Figure 44 Position of measuring points (H1, H2 and M1) and DHI modelled gauge</i>	108
<i>Figure 45 SWAN bathymetry, with regular grid</i>	109
<i>Figure 46 SWAN bathymetry, with unstructured grid</i>	109
<i>Figure 47 SWASH bathymetry</i>	110
<i>Figure 48 Unstructured grid</i>	112
<i>Figure 49 TPAR example</i>	113
<i>Figure 50 North-West distribution</i>	114
<i>Figure 51 North distribution</i>	115
<i>Figure 52 North-Est distribution</i>	115
<i>Figure 53 Angelini's SWAN physical scheme.</i>	117
<i>Figure 54 Plot of measurement and model time series of wave height at H2</i>	118
<i>Figure 55 Final physical scheme</i>	118
<i>Figure 56 Significant wave height of N-W storm of 05/02/1992 at 7:00</i>	120
<i>Figure 57 Significant wave height of N-W storm of 05/02/1992 at 12:00</i>	121
<i>Figure 58 Significant wave height at peak of N-W storm (03/02/1992 20:00)</i>	121
<i>Figure 59 Significant wave height of N storm of 07/01/2002 at 09:00</i>	122
<i>Figure 60 Significant wave height of N storm of 07/01/2002 at 14:00</i>	122
<i>Figure 61 Significant wave height at peak of N storm (10/01/2002 11:00)</i>	123
<i>Figure 62 Significant wave height of N-E storm of 08/11/1982 at 1:00</i>	123
<i>Figure 63 Significant wave height of N-E storm of 08/11/1982 at 6:00</i>	124
<i>Figure 64 Significant wave height at peak of N-E storm (09/11/1982 04:00)</i>	124
<i>Figure 65 approximated plan view of the simulation grids. SWAN in green and SWASH in yellow</i>	126
<i>Figure 66 Zoom of porosity map, DELF3D image</i>	129
<i>Figure 67 Boundary conditions in the input file</i>	130
<i>Figure 68 Physics in the input file</i>	131
<i>Figure 69 Numeric in the input file</i>	132

Figure 70 Output part in the input file	132
Figure 71 Lock-up in the input file	133
Figure 72 Significant wave height [m], for case a (dir=27.11 °N; sponge layer on East side)	136
Figure 73 Significant wave height [m], for case b (dir=27.11 °N; sponge layer on East and West side)	136
Figure 74 Significant wave height [m], for case d (dir=20 °N; sponge layer on East side)	137
Figure 75 Significant wave height [m], for case e (dir=20 °N; sponge layer on East and West side)	137
Figure 76 Significant wave height [m], for case g (dir=27.11 °N; sponge layer on East and West side; with a smoothed bathymetry)	138
Figure 77 Significant wave height [m], for case g (dir=27.11 °N; sponge layer on East side; with a large domain)	138
Figure 78 Significant wave height [m], for case g (dir=27.11 °N; sponge layer on East and West side; with a large domain)	139
Figure 79 Current [m/s], for case a (dir=27.11 °N; sponge layer on East side)	140
Figure 80 Current [m/s], for case b (dir=27.11 °N; sponge layer on East and West side)	140
Figure 81 Current [m/s], for case c (dir=27.11 °N; sponge layer on East side; 3 hours of simulation)	141
Figure 82 Current [m/s], for case d (dir=20 °N; sponge layer on East side)	141
Figure 83 Current [m/s], for case e (dir=20 °N; sponge layer on East and West side)	142
Figure 84 Current [m/s], for case f (dir=27.11 °N; sponge layer on East and West side; with a smoothed bathymetry)	142
Figure 85 Currents [m/s], case g (dir=27.11 °N; sponge layer on East side; with a large domain)	143
Figure 86 Currents [m/s], case h (dir=27.11 °N; sponge layer on East and West side; with a large domain)	143
Figure 87 Shear stress produced by the current (τ_c) Kgms ² , case a (dir=27.11 °N; sponge layer on East side)	144
Figure 88 τ_c in interested area Kgms ² , case a (dir=27.11 °N; sponge layer on East side)	145
Figure 89 τ_c in interested area Kgms ² , case b (dir=27.11 °N; sponge layer on East and West side)	145
Figure 90 τ_c in interested area Kgms ² , case c (dir=27.11 °N; sponge layer on East side; 3 hours of simulation)	146
Figure 91 τ_c in interested area Kgms ² , case d (dir=20 °N; sponge layer on East side)	146
Figure 92 τ_c in interested area Kgms ² , case e (dir=20 °N; sponge layer on East and West side)	147
Figure 93 τ_c in interested area Kgms ² , case f (dir=27.11 °N; sponge layer on East and West side; with a smoothed bathymetry)	147
Figure 94 τ_c in interested area Kgms ² , case g (dir=27.11 °N; sponge layer on East side; with a large domain)	148
Figure 95 τ_c in interested area Kgms ² , case h (dir=27.11 °N; sponge layer on East and West side; with a large domain)	148
Figure 96 Shear stress produced by oscillatory flow (τ_w),Kgms ² , case a (dir=27.11 °N; sponge layer on East side)	149
Figure 97 τ_w in interested area Kgms ² , case a (dir=27.11 °N; sponge layer on East side)	150
Figure 98 Shear stress produced by oscillatory flow (τ_w),Kgms ² , case b (dir=27.11 °N; sponge layer on East and West side)	150
Figure 99 τ_w in interested area Kgms ² , case b (dir=27.11 °N; sponge layer on East and West side)	151

Figure 100 Shear stress produced by oscillatory flow (τ_w) Kgms ² , case c (dir=27.11 °N; sponge layer on East side; 3 hours of simulation)	151
Figure 101 τ_w in interested area [Kg/(ms ²)], case c (dir=27.11 °N; sponge layer on East side; 3 hours of simulation)	152
Figure 102 Shear stress produced by oscillatory flow (τ_w) Kgms ² , case d (dir=20 °N; sponge layer on East side)	152
Figure 103 τ_w in interested areaKgms ² , case d (dir=20 °N; sponge layer on East side)	153
Figure 104 Shear stress produced by oscillatory flow (τ_w) Kgms ² , case e (dir=20 °N; sponge layer on East and West side)	153
Figure 105 τ_w in interested area Kgms ² , case e (dir=20 °N; sponge layer on East and West side)	154
Figure 106 Shear stress produced by oscillatory flow (τ_w) Kgms ² , case f (dir=27.11 °N; sponge layer on East and West side; with a smoothed bathymetry)	154
Figure 107 τ_w in interested area Kgms ² , case f (dir=27.11 °N; sponge layer on East and West side; with a smoothed bathymetry)	155
Figure 108 Shear stress produced by oscillatory flow (τ_w) Kgms ² , case g (dir=27.11 °N; sponge layer on East side; with a large domain)	155
Figure 109 τ_w in interested area Kgms ² , case g (dir=27.11 °N; sponge layer on East side; with a large domain)	156
Figure 110 Shear stress produced by oscillatory flow (τ_w) Kgms ² , case h (dir=27.11 °N; sponge layer on East and West side; with a large domain)	156
Figure 111 τ_w in interested area Kgms ² , case h (dir=27.11 °N; sponge layer on East and West side; with a large domain)	157
Figure 112 τ in interested area Kgms ² , case a (dir=27.11 °N; sponge layer on East side)	158
Figure 113 τ in interested area Kgms ² , case b (dir=27.11 °N; sponge layer on East and West side)	158
Figure 114 τ in interested areaKgms ² , case c (dir=27.11 °N; sponge layer on East side; 3 hours of simulation)	159
Figure 115 τ in interested areaKgms ² , case d (dir=20 °N; sponge layer on East side)	159
Figure 116 τ in interested area Kgms ² , case e (dir=20 °N; sponge layer on East and West side)	160
Figure 117 τ in interested area Kgms ² , case f (dir=27.11 °N; sponge layer on East and West side; with a smoothed bathymetry)	160
Figure 118 τ in interested area Kgms ² , case g (dir=27.11 °N; sponge layer on East side; with a large domain)	161
Figure 119 τ in interested area Kgms ² , case h (dir=27.11 °N; sponge layer on East and West side; with a large domain)	161

ABSTRACT

This thesis was born from the partnership between UNIVPM (Università Politecnica delle Marche) and SAIPEM S.p.A. and the need for the company to evaluate the scouring phenomenon that occurred downstream of a temporary structure for the laying of the pipelines that approached the coast.

To analyse the phenomenon of scouring, the study of the bottom shear stresses was carried out, since a variation of them is linked to an unbalance of solid transport.

SWASH, a hydrodynamic wave propagation model, was used to analyse the stresses at the bottom. Through this model the necessary parameters for the calculation of the stresses produced by the currents and the oscillatory motion of the waves have been obtained.

SWASH is not the only hydrodynamic model used; the SWAN model has also been used in this thesis. The use of the double model is motivated by the desire to reduce the calculation times, since the available data were located in deep waters (about 133 m deep, several km away from the coast) while the area where the phenomenon occurred it is in shallow water (about 3 m deep, about 700 m from the coast).

The goal of the SWAN simulation is to find the sea state in shallow water in order to provide boundary conditions for SWASH analysis, with reasonable calculation times. The SWAN simulates the propagation of wave motion, starting from the known values on the boundaries of the domain and then propagates them using the information provided as inputs such as wind and bathymetry. The data used as boundary conditions are a series of storms derived from the DHI hindcast model.

Once the state of the sea in shallow waters was defined, the SWASH model was used, which allows to know how the sea state interacts with an object with variable porosity (as in the case analysed, which is composed of two permeable layers and one in the impermeable layer in the middle) to produce an alteration of the currents that act and the oscillatory movement of the waves.

In order to reach the definitive set-ups for the SWASH model, several sensitivities took place:

- two different measures of the computation domain grid (1.285 Km^2 and 3.209 Km^2);

- Comparison between 2 of the 3 turbulent horizontal viscosity models usable by SWASH:
 - Smagorinsky
 - Prandtl
- Use and their effects on the results of a single or double layer of sponge;
- Modification of the mean wave direction (MWD) SWAN output (20 °N compared to 27.11 °N of SWAN simulation), so as not to have MWD too close to the angle of inclination of the grid (30 °N).

The last step is to derive the stress down using the stress calculation formulas in the literature and the results obtained from the SWASH simulations.

The simulation that best simulates the real case observed, is that with a single layer of sponge and an MWD that deviates from the angle of inclination of the grid. In configurations with a single sponge layer, the energy of the sea state in the area of interest is greater and for this reason it produces greater shear stresses, especially those due to the waves motion. From the simulations even a wave entry angle that is not perpendicular to the coastline has the effect of increasing shear stress.

Chapter 1 – Introduction

1.1 About this thesis

The study of coastal dynamics and wave in shallow water has always been a topic that attracts researchers due to the complexity and charm of the argument. The shallow waters in fact are still a limit of our knowledge which can be partially overcome thanks to modern computing models.

Knowing what is happening in the area closest to the coast is an issue of great interest for many applications such as the study of the evolution of the coastline, the sea-beach-structures interaction but also for coastal protection work. This information is of considerable importance for the greatest companies in the oil industry having the need to know the behaviour of the environment in which pipelines from an offshore installation are approaching the coast.

In this context thanks to the agreement signed between the Università Politecnica delle Marche and Saipem S.p.A., it has been developed a collaboration between the two entities, from which the present thesis arises.

This work can be framed as research thesis, it was carried out a careful research on the theoretical bases of the used software and extensive development of their performance.

The purpose of this thesis is therefore to study the scouring phenomenon that occurred downstream of a temporary structure which was intended to facilitate the operation of laying the pipeline that approached the coast.

The use of SWASH (software of hydrodynamical numerical modelling) has allowed to simulate the coastal hydrodynamics in the presence of an obstacle with different permeation capacity, and to see how the presence of this obstacle changes the sea state causing an imbalance in the solid transport.

To achieve these results, several stages of the work were carried out.

First, a collection and comparison of available data was made, the choice was between data measured or obtained from a hindcast model, the choice fell on those from the model that also allowed to know the direction of the wave. Subsequently, the data were processed to

make them usable in the models. The choice was between data measured or obtained from a hindcast model and fell on the data from the model.

Based on the data, it soon became clear the need to use a propagation model of the sea state in order to have some data even relating to other places than those given by the model, given that the distance in which the parameters of the waves were known and the area of interest is several km. For this purpose, the SWAN (Simulating WAve Nearshore, a third-generation wave model, developed by Delft University of Technology) model that guarantees excellent performances with a modest computational cost. The use of this model is thus directed to obtain information that describes the sea state at the edge of the area of interest, where a non-hydrostatic wave-flow model developed by Delft University of Technology, i.e. the SWASH (Simulating WAVes till SHore) model, is used.

Considering what has been said, the first step was to calibrate the SWAN model based on some measured data deriving from a storm selected as a reference. This calibration focused mainly on the physical phenomena to be activated in the model so that the results are as close as possible to those measured.

Subsequently, using the OUTPUT of SWAN simulations, the input of SWASH was performed. This model is much more recent than the SWAN model and has still some limits of applicability. This model is much more recent than the SWAN model, in fact, it is still a program in continuous evolution and updating. For these reasons, a careful study was initially made on the ways in which the program can be used and on the root causes of the instability of the solution. At the end of this phase, we identified a stable setting from now on taken as the starting setting for the various analyses with different configurations.

The final configuration provides a structure with a different level of permeability, as it is composed by two parts of permeable matter (rocks) for the causeway and in the middle a non-permeable area.

Finally, processing the results provided by the SWASH model, the values of bottom shear stress was obtained, using the maximum instantaneous wave velocity value and the average of wave velocity during its period.

1.2 Relevance of the study

The propagation of waves inshore has been studied for a long time and can be treated from two perspectives.

On the one hand, the physical models that are used, try to emulate the real conditions (or at least the most important features) in a scaled basin or flume. Nonetheless, the drawbacks of this methodology are that the physical models are very expensive and require a lot of time and changes in the layout of the area require a new physical model.

On the other hand, with the development of computers and numerical methods, reality can be simulated by solving the differential equations that explain physics. Those equations that were impossible to solve (e.g. Navier-Stokes equations), except for the very simplified cases where several hypotheses were made. Nowadays, with the development of the finite element and finite difference methods, they can be solved with great precision in a relatively short time but still making some hypotheses and simplifications.

Within this thesis, the performance of SWASH will be tested as it may be a valuable tool to simulate wave propagation which can be very useful in day-to-day designing.

Furthermore, an important characteristic of SWASH is that it is a free software available in the TU DELFT webpage. Therefore, it is more accessible and likely to be widespread than other similar models that are not free to the public.

Ultimately, although SWASH is still in an early stage and there are few bugs to be fixed, further versions will improve this tool and add features that are not considered yet.

Chapter 2 – Wave theory

Waves are the most important phenomena to be considered among the environment conditions affecting maritime structures, because they exercise the greatest influence. The presence of wave makes the design procedure for maritime structure quite different from that of structure on land. Since waves are one of the most complex and changeable phenomena in nature, it is not easy to achieve a full understanding of their fundamental character and behaviour.

Surface gravity waves refer to all kind of waves that can be in general encountered in open water. The surface waves can be characterized by the frequency (or angular frequency $\omega = \frac{2\pi}{T}$, where T is the wave period). In Figure 1, the energy of waves is plotted against the frequency, as well as the forcing and restoring terms relevant in every frequency range.

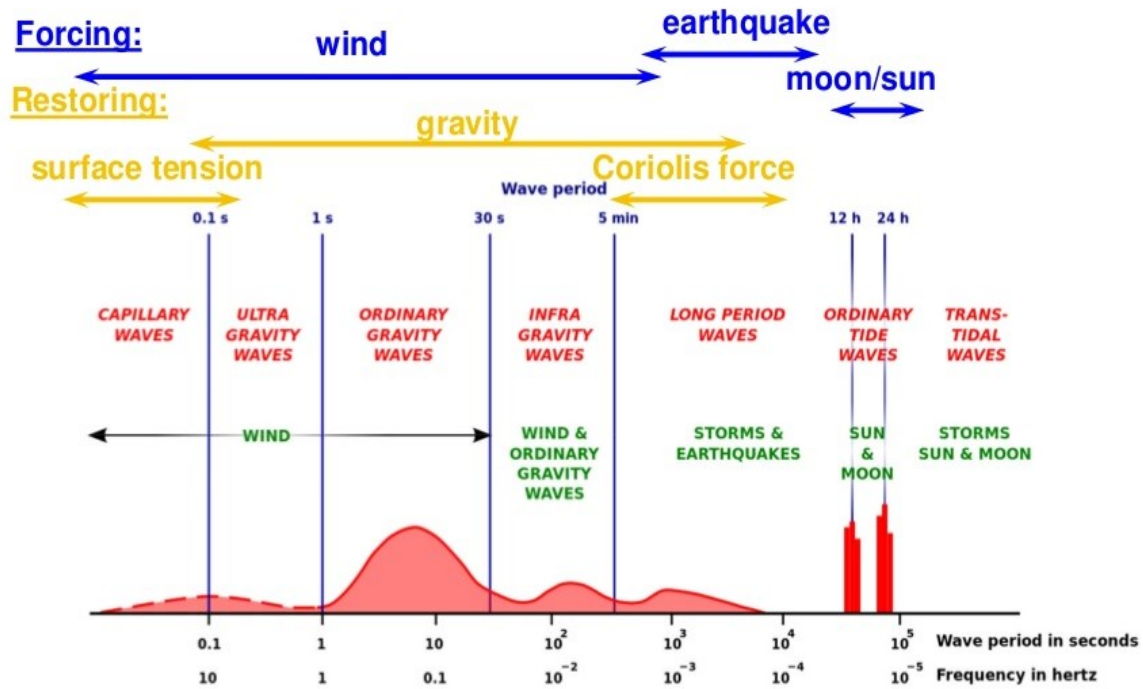


Figure 1 Waves classification through their frequency

The gravity waves correspond to the range of surface waves generated by wind blowing over the fetch region and for which gravity provides the restoring force, hence their name. As seen in the Figure 1, the gravity waves are characterized by a relatively short period ($T \sim 1 - 30s$), with a peak of energy density at $T \sim 10s$. They are main responsible of effects on costal area (shoreline, structures).

To complete the picture outlined in the Figure 1, moving towards higher frequencies, we find the capillary waves, which have a relevant role in wind wave generating phenomena, and are important also for satellite observations of wind speed.

Moving towards lower frequencies we find different phenomena generating waves – such as for example astronomical tides that produce a long period waves, with a length of hundreds of kilometres and periods of several hours. The following classification (Table 1) provides a

synthetic description of surface waves with the aim to give an idea of the kind of waves actually present in the sea, their causes and periods.

Phenomenon	Cause	Period
Wind wave (sea state)	Wind shear	<15 s
Swell wave (swell state)	Wind wave	<30 s
Surf beat	Wave group	1-5 min
Seiche	Wind variation	2-40 min
Harbour resonance	Surf beat, tsunami	2-40 min
Tsunami	Earthquake	5-60 min
Tide	Gravitational attraction	12 or 24 h
Storm surge	Wind stress and atm pressure	1-30 d

Table 1 Gravity waves, causes and periods

In this thesis only the wind and swell waves are considered. The main difference between these two types of gravitational waves (see also Figure 2) are:

- Wind waves: raised by blowing wind
 - Relatively short and steep
 - Short-crested and irregular 3D surface elevation
 - Relatively “broad banded”, depending on development stadiums
- Swell waves: escaping wind influence
 - Relatively long and with low steepness
 - Long crested and with regular almost 2D surface elevation
 - Very narrow banded

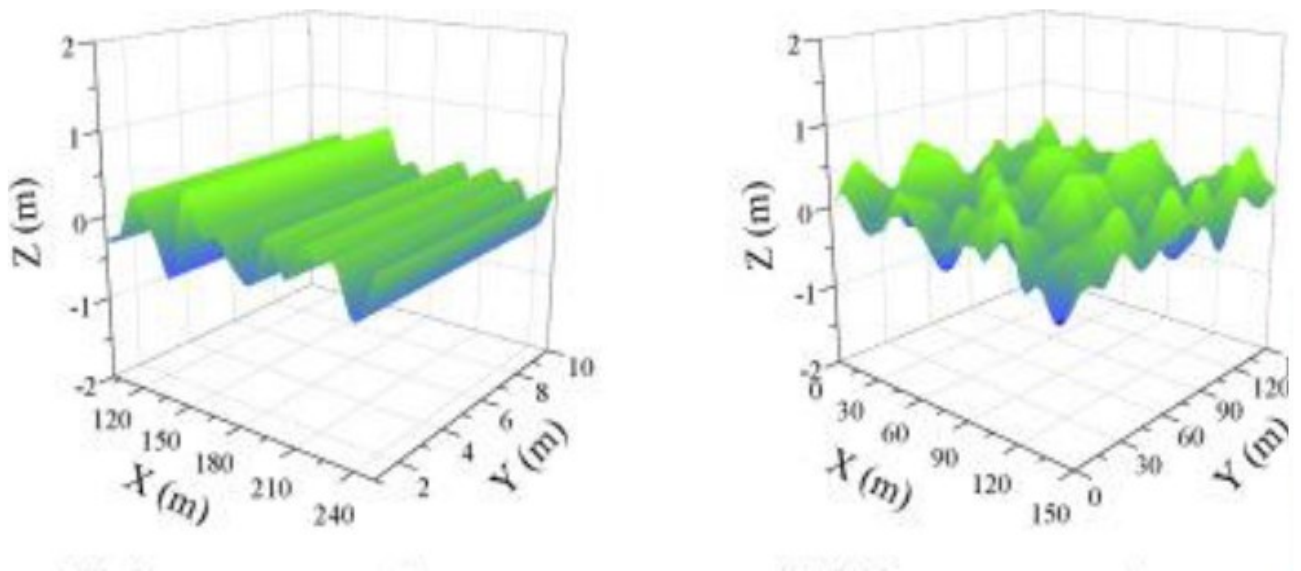


Figure 2 Long-crested wave (swell waves) on the left and short-crested (wind waves) wave on the right

2.1 Regular wave theory

Three wave parameters determine which wave theory to apply to describe the kinematic characteristics in a specific problem. These are the wave height H , the wave period T and the water depth d . These parameters are used to define three nondimensional parameters that determine ranges of validity of different wave theories:

- Wave steepness $S = 2\pi \frac{H}{gT^2} = \frac{H}{\lambda_0}$ (1)

- Nondimensional depth $\mu = 2\pi \frac{h}{gT^2} = \frac{h}{\lambda_0}$ (2)

- Ursell number $U_r = \frac{HL^2}{d^3}$ (3)

Where λ_0 and k_0 are the linear deep-water wavelength and wave number corresponding for wave period T . Note that the three parameters are not independent. When two of the parameters are given, the third is uniquely determined. The relation is:

$$U_r = \frac{S}{\mu^3} \quad (4)$$

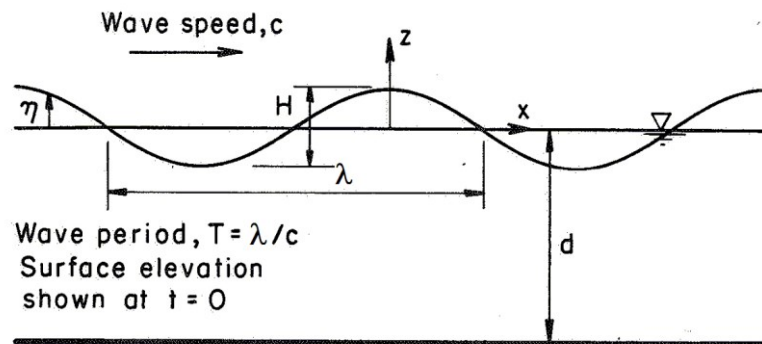


Figure 3 Regular travelling wave properties

The Ursell number is a dimensionless parameter that explain if the wave can be described by a linear or non-linear approach. The range of applicability of the different wave theory are given in.

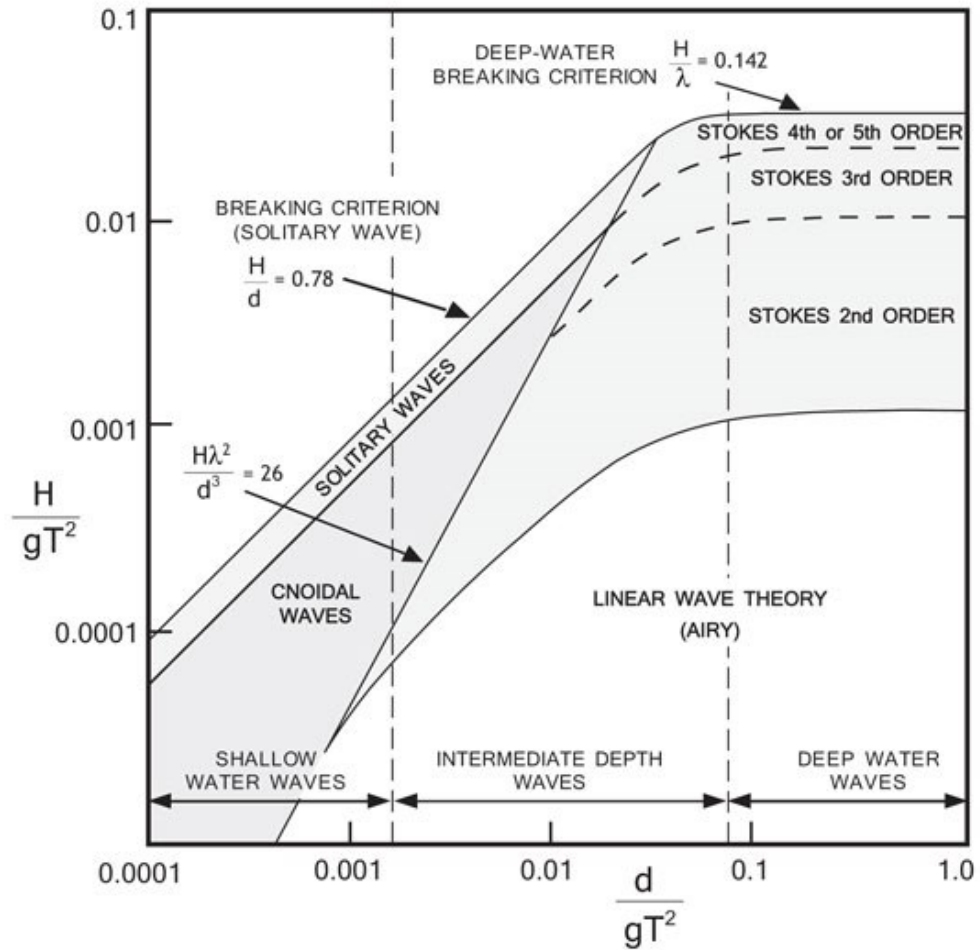


Figure 4 Ranges of validity for various wave theories; the horizontal axis is a measure of shallowness while the vertical axis is a measure of steepness

The wave theories indicated in Figure 4 are based on the following assumptions on the properties of the fluid and the flow:

- Uniform mean depth
- Fluid is inviscid
- Fluid is incompressible
- flow is irrotational

The simplest wave theory is obtained by taking the wave height to be much smaller than both the wavelength and water depth. In this way, the basic hydrodynamic equations can be linearized, and explicit solutions obtained for kinematic parameters. This theory is referred to small amplitude wave theory, linear wave theory, sinusoidal wave theory or Airy wave theory.

2.1.1 Outline of the Linear wave theory

Having a wave that propagate in the horizontal plane (coordinates X,Y), the z axis represents the vertical position with the positive value upwards respect to the mean water level (z=0), and the impermeable layer at z=-h.

Small-amplitude waves is governed by some equations:

- Existence of velocity potential $\phi(x, z, t)$
 - Vorticity $\omega = \nabla \times \mathbf{u} = 0 \rightarrow \mathbf{u} = \nabla \phi$ irrotational flow (5)
- Continuity equation
 - Laplace equation $\nabla \cdot \mathbf{u} = \nabla \cdot \nabla \phi = \nabla^2 \phi = 0$ incompressibility flow (6)

Incompressibility and irrotational flows, Laplace's equation:

$$\nabla^2 \phi = \frac{\partial^2 \phi}{\partial x^2} + \frac{\partial^2 \phi}{\partial z^2} = 0 \quad (7)$$

Laplace's equation is a simplification of Navier-Stokes equation for incompressible, irrotational, inviscid fluid with hydrostatic pressure.

The potential velocity $\phi(x, z, t)$ is defined as:

$$u = \frac{\partial \phi}{\partial x} \quad w = \frac{\partial \phi}{\partial z} \quad (8)$$

Four boundary conditions (BC) are used to solve the Laplace's equation ($\nabla^2 \phi = 0$)

- BBC, bottom BC: $[z = -h(x)]$
 - Horizontal bed $\left(\frac{dh}{dx} = 0\right)$ $[w]_{z=-h} = -\left[\frac{\partial \phi}{\partial z}\right]_{z=-h} = 0$ (9)
- KFSBC, kinematic free-surface BC: $[z = \eta(x, y, t)]$: $w = \frac{\partial \eta}{\partial t} + u \frac{\partial \eta}{\partial x} + v \frac{\partial \eta}{\partial y}$ (10)
 - 2D problem $[w]_{z=\eta} = -\left[\frac{\partial \phi}{\partial z}\right]_{z=\eta} = \frac{\partial \eta}{\partial t} - \frac{\partial \phi}{\partial x} \frac{\partial \eta}{\partial x}$ (11)
- DFSBC, dynamic free-surface BC: $[z = \eta(x, y, t)]$: $-\frac{\partial \phi}{\partial t} + \frac{1}{2}(u^2 + w^2) + \frac{p\eta}{\rho} + gz = C(t)$ (12)
 - $p_\eta = 0$ $-\frac{\partial \phi}{\partial t} + \frac{1}{2}\left(\left(\frac{\partial \phi}{\partial x}\right)^2 + \left(\frac{\partial \phi}{\partial z}\right)^2\right) + gz = C(t)$ (12b)

- Periodicity $\phi(x, z, t) = \phi(x + L, z, t) = \phi(x, z, t + T)$ (13)

The solutions of Laplace's equation are:

- Water-surface level $\eta(x, t) = \frac{H}{2} \cos(kx - \sigma t)$ (14)

- Velocity potential $\phi(x, z, t) = \frac{H g \cosh k(h+z)}{2\sigma \cosh kh} \sin(kx - \sigma t) =$
 $\frac{H \sigma \cosh k(h+z)}{2 k \sinh kh} \sin(kx - \sigma t)$ (16)

In which:

- $\sigma = \frac{2\pi}{L}$ angular frequency
- T wave period
- L wavelength
- $k = \frac{2\pi}{L}$ wave number

The general solutions (intermediate water) are functions of hyperbolic cosine and sine, so there are simplifications in function of water depth, according with Figure 5.

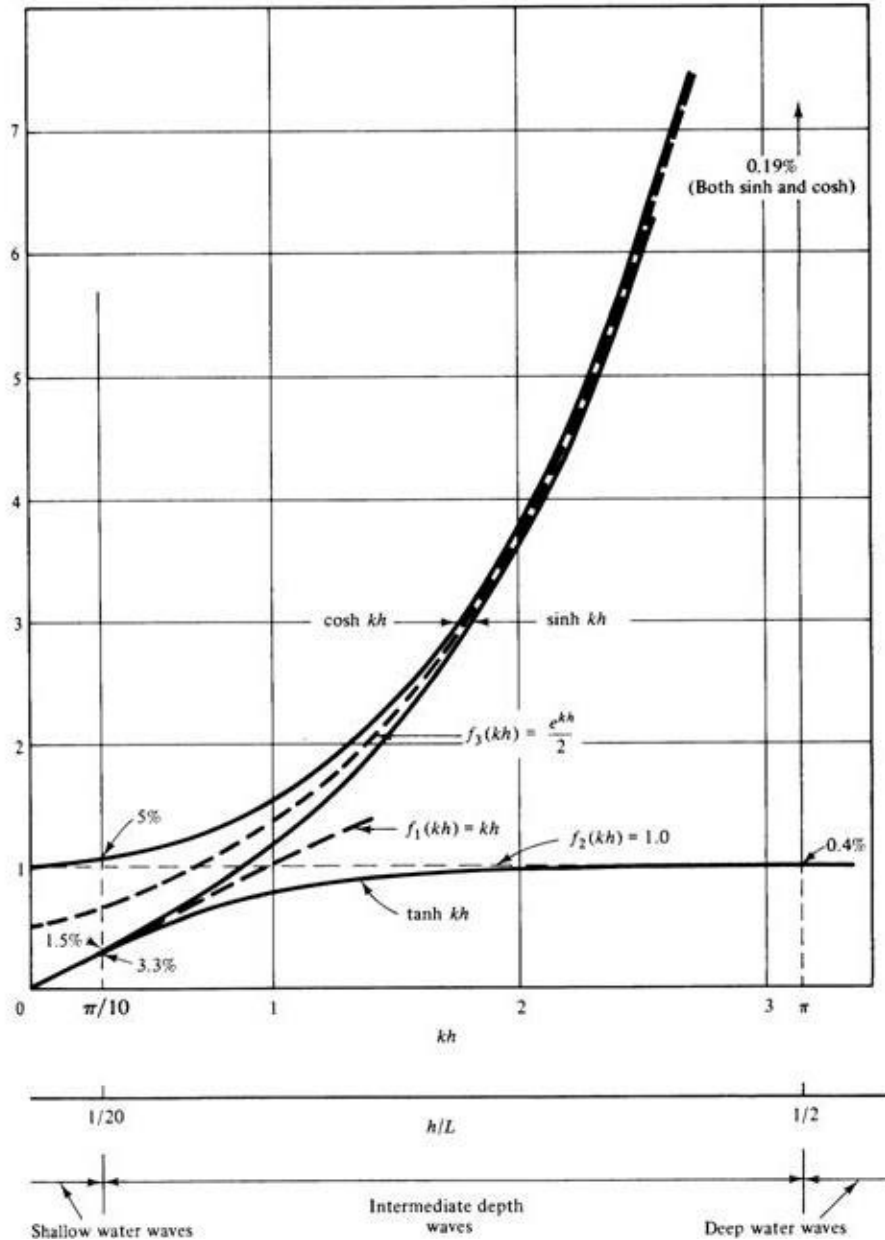


Figure 5 Trigonometric simplification based on the ratio between water depth and wavelength (h/L)

Intermediate waters (no simplifications)

- Dispersion relation $\sigma^2 = gk \tanh kh$ (17)

- Celerity $c = \frac{L}{T} = \frac{\sigma}{k} = \frac{gT}{2\pi} \tanh kh$ (18)

- Length $L = \frac{gT^2}{2\pi} \tanh kh$ (19)

Shallow waters: waves are approaching the coast; the depth became much smaller than wavelength ($\cosh kh = 1, \sinh kh = kh, \tanh kh = kh$)

- Dispersion relation $\sigma^2 = gk^2 h$ (20)

- Celerity $c = \frac{\sigma}{k} = \sqrt{gh}$ (21)

- Length $L = cT = T\sqrt{gh}$ (22)

Deep waters: the depth is much higher than the wave length ($\cosh kh = \frac{e^{kh}}{2}$, $\sinh kh = \frac{e^{kh}}{2}$, $\tanh kh = 1$)

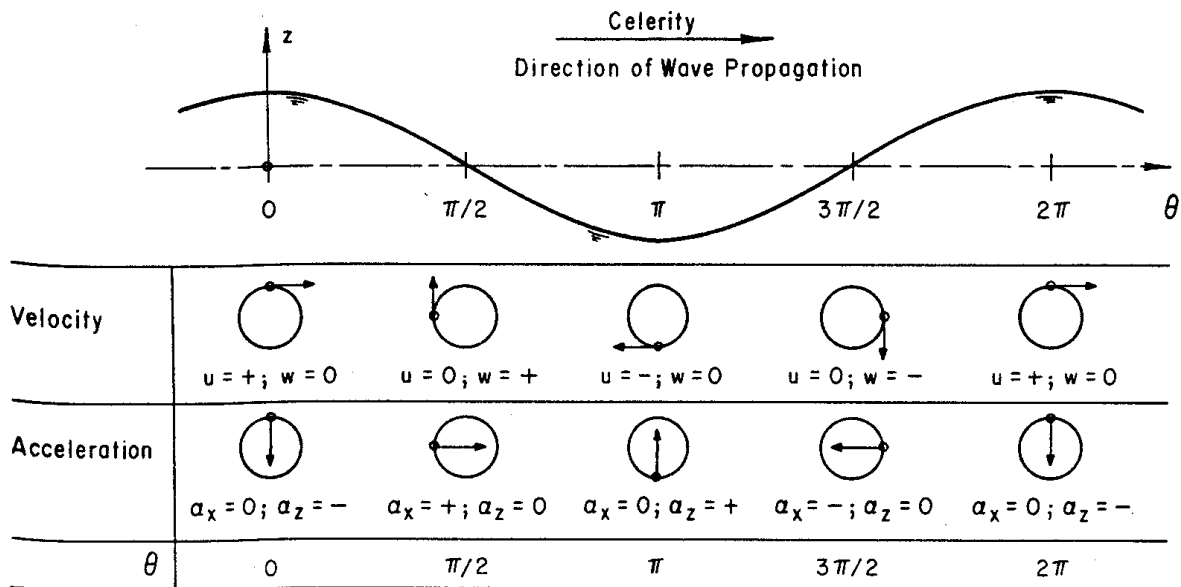
- Dispersion relation $\sigma^2 = gh$ (23)

- Celerity $c = c_0 = \frac{gT}{2\pi} = 1.56 T$ (24)

- Length $L = L_0 = \frac{gT^2}{2\pi} = 1.56 T^2$ (25)

The wave celerity c is the speed at which a single wave propagates.

Another interesting feature from linear wave theory is that underneath the surface the fluid motion is orbital, this can be shown in Figure 6Figure 3.



Local fluid velocities and accelerations.

Figure 6 Surface elevation along with velocity and acceleration vectors

From the linear wave theory, further second order parameters can be obtained, the most important of them being:

- Mean wave-energy per area (E) $E = \rho g \frac{H^2}{8} \left[\frac{J}{m^2} \right]$ (26)

- Radiation stress (S_{ij}) with $n = \frac{1}{2} \left(1 + \frac{2kh}{\sinh 2kh} \right)$ (27)

$$\circ S_{xx} = \left(n - \frac{1}{2} + n \cos^2 \theta\right) E \quad \left[\frac{N}{m}\right] \quad (28a)$$

$$\circ S_{yy} = \left(n - \frac{1}{2} + n \sin^2 \theta\right) E \quad \left[\frac{N}{m}\right] \quad (28b)$$

$$\circ S_{xy} = S_{yx} = n \cos \theta \sin \theta E \quad \left[\frac{N}{m}\right] \quad (28c)$$

$$\bullet \text{ Wave action} \quad A = \frac{E}{\sigma} \quad \left[\frac{Js}{m^2}\right] \quad (29)$$

The radiation stress consists in part of a radiation pressure, exerted at the free surface elevation of the mean flow. If the radiation stress varies spatially, as it does in the surf zone where the wave height reduces by wave breaking, this results in changes of the mean surface elevation called wave set-up (in case of an increased level) and set-down (for a decreased water level).

The mean water level is governed by the cross-shore balance momentum:

$$\frac{d\bar{\eta}}{dx} = -\frac{1}{\rho gh} \frac{dS_{xx}}{dx} \quad (30)$$

In which:

- h still water level
- $\bar{\eta}$ mean water surface elevation

The radiation stress gradient is also the driver of the complex circulation pattern in the surf zone, constituted by the along coast littoral current, the return flow under the wave trough level (undertow) and the offshore directed rip. These phenomena are further described in Section 2.3.

2.1.2 Non-linear effects

As explained in the previous paragraph, linear wave theory is only valid when the wave amplitude is much smaller than the water depth. In such situation the non-linearity in the boundary conditions can be neglected and the sinusoidal wave solution achieved.

With the linear theory the boundary conditions are applied on the mean water level ($z=0$), but when the wave approaches the coast, this assumption is not realistic, non-linear effects start playing a role and the boundary conditions need to “solve” the whole wave, i.e. to provide the instantaneous water surface η .

The non-linear effects can be divided into two phenomena:

- Wave skewness
- Wave asymmetry

Wave skewness is the phenomenon by which wave becomes asymmetrical along the mean sea level. Wave crest become pointed whereas wave trough gets flatter. It is defined as the mean of third power of the surface elevation.

$$skewness \propto \langle \eta^3 \rangle$$

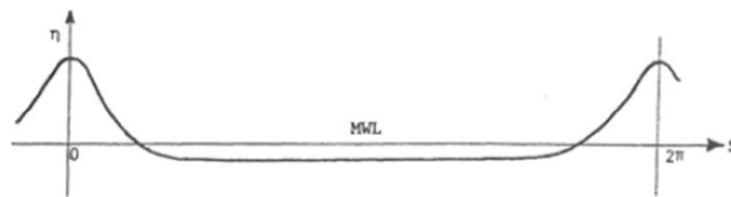


Figure 7 Sketch of a skewed wave

Another effect of non-linearity is the wave asymmetry due to a pitching forward of the wave crest.

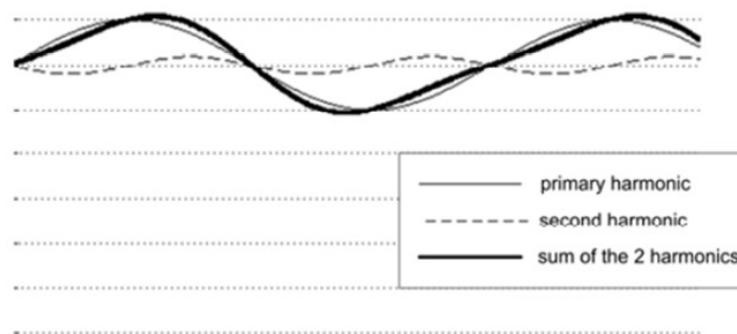


Figure 8 Sketch of an asymmetric wave as the sum of two harmonics

The reason for this asymmetry is that the crest in shallow water moves faster than the trough.

Several different non-linear wave theories have been developed to describe the kinematic of regular waves. All need to cope with the problem that the free surface boundary conditions must be applied at the free surface η , which in itself is one of the unknown problems.

Stokes series expansion method uses the results from the linear wave theory by adding more harmonic terms to the solution. Each new term has a lower period and these terms can be out of phase. Therefore, the solution looks like:

$$\eta = \eta_1 \cos S + \eta_2 \cos 2S + \dots + \eta_n \cos nS$$

However, this theory does not converge in shallow water if the Ursell number is too large, hence the Stokes theory is best suited for deep water. Alternative formulas – like the Stream function theory and the conical theory – have been proposed to describe the waves beyond the limits of the Stokes theory and their relative range of application is shown in Figure 4.

2.2 Wave propagation in shallow waters

When waves travel in shallow waters, they begin to be affected by the ocean bottom. The free orbital motion of the water is disturbed, and water particles in orbital motion no longer return to their original position. As the water becomes shallower, the wave becomes higher and steeper, ultimately assuming the familiar sharp-crested wave shape. After the wave breaks, it becomes a wave of translation and erosion of the ocean bottom intensifies.

With the progressive approach of the waves to the coastal area, the seabed gradually decreases, their propagation begins to be affected by this lowering. In the shallow water, various phenomena due to wave propagation are encountered:

- Shoaling
- Refraction
- Reflection and Transmission
- Diffraction
- Wave Breaking

As regard transmission, when waves hit a porous structure like a breakwater, part of the energy is transmitted through it. The amount of energy transmitted depends on the characteristics of the wave and porosity, gravel size, roughness and height of the structure. Overtopping may also occur. Long-period waves like tidal or swell waves are more easily transmitted than high frequency waves, which are either dissipated or reflected against structure.

Important concepts are the wave celerity, the group celerity and wave direction. The celerity concept is already explained in the previous paragraph, as the velocity of single

monochromatic and unidirectional wave. The group celerity can be understood as the speed at which the wave energy travels and is described by the following equation:

$$C_g = \frac{\partial \sigma}{\partial k} = Cn = \frac{C}{2} \left(1 + \frac{2kh}{\sinh 2kh} \right) \quad (31)$$

2.2.1 Shoaling

Shoaling is the increase in the height of the wave when the waves travel towards shallow waters, due to the decrease in the depth of the water. Then as the energy flux has to remain constant, the energy density must increase. Besides, while the frequency remains constant, like the period, the wavelength must decrease.

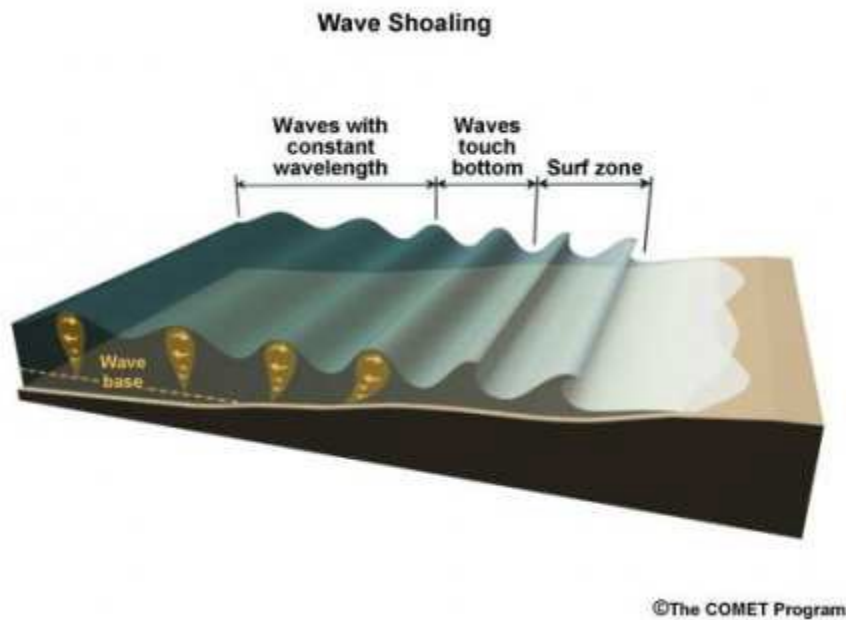


Figure 9 Shoaling scheme.

The energy conservation is used to explain the shoaling phenomena, since it is characterized by constant energy flux, so, the energy that enters is the same as the energy that comes out.

$$U_0 = U_1 \quad (32)$$

$$\frac{1}{8} \rho g H_0^2 n_0 c_0 = \frac{1}{8} \rho g H_1^2 n_1 c_1 \quad (32)$$

U_0 represents the deep-water condition, while U_1 represents the shallow water condition. After some simplification the previous formula becomes:

$$\frac{H_1}{H_0} = \sqrt{\frac{c_{g0}}{c_{g1}}} = \sqrt{\frac{c_0 n_0}{c_1 n_1}} = \sqrt{\frac{c_0}{2c_1 n_1}} = K_s \quad (33)$$

- $n_0 = \frac{1}{2}$ for deep water
- K_s is the shoaling coefficient

The shoaling coefficient represents the variation undergone by the wave height due to the variation in water depth.

The shoaling coefficient can be also recovered using the following graph that relates to K_s with dimensionless depth.

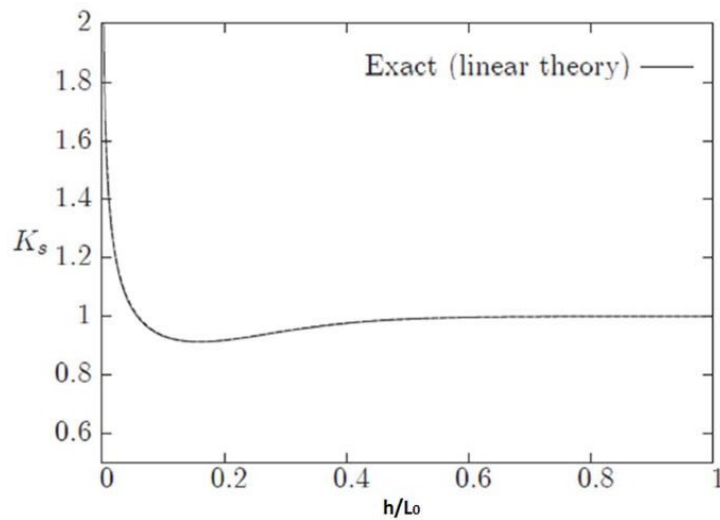
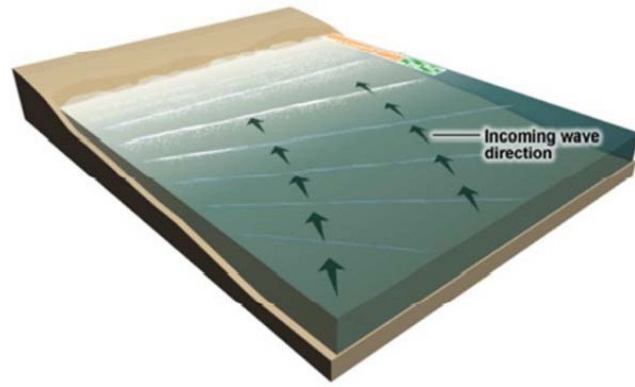


Figure 10 Shoaling coefficient variation with dimensionless depth

2.2.2 Refraction

Refraction is the phenomenon for which wave energy tends to bend when waves approach the shoreline. This phenomenon is a complex effect due to the bottom friction and celerity variation, associated to the seabed variation: $c = \sqrt{gh}$.



©The COMET Program

Figure 11 Refraction scheme.

The refraction has been well described with Snell's law. According to this theory, a relationship is obtained which links the obliquity of the waves to the celerity and the seabed, always starting from the simplifying hypotheses of irrotational motion and energy conservation.

Snell's law: $\frac{\sin \theta}{c} = \frac{\sin \theta_0}{c_0}$; from this formula it is possible to obtain the variation of propagation angle knowing the variation of celerity.

As with shoaling, an energy balance must be made for Refraction, indicate b_0 and b_1 the distance between the *two waves ray* in deep and shallow water respectively.

$$U_0 b_0 = U_1 b_1 \quad (34)$$

$$\frac{1}{8} \rho g H_0^2 n_0 c_0 b_0 = \frac{1}{8} \rho g H_1^2 n_1 c_1 b_1 \quad (34)$$

$$\frac{H_1}{H_0} = \sqrt{\frac{c_{g0}}{c_{g1}}} \sqrt{\frac{b_0}{b_1}} = \sqrt{\frac{c_0 n_0}{c_1 n_1}} \sqrt{\frac{b_0}{b_1}} = \sqrt{\frac{c_0}{2c_1 n_1}} \sqrt{\frac{b_0}{b_1}} = K_s K_r \quad (35)$$

In which

- K_r is the refraction coefficient;
- K_s is the shoaling coefficient;
- b_0 is the width between two flux lines (orthogonal to the wave front) in deep waters;
- b_1 is the width between the same flux lines in the propagated point.

2.2.3 Reflection and Transmission

When waves hit an obstacle, they bounce off and continue in another direction. Those objects may be quay walls, jetties, natural cliffs, ship hulls, breakwaters or any other structure. In an ideal environment, if a wave impacts a wall with an incident angle of ϑ_i , it is reflected with an angle of $\vartheta_r = -\vartheta_i$.

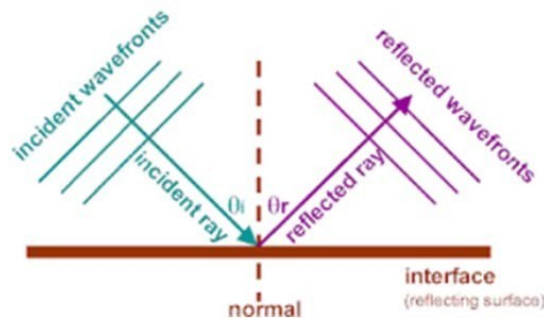


Figure 12 Wave reflection scheme

However, in reality not all incident energy is reflected, part of it is dissipated and part is transmitted. The amount of energy reflected, transmitted and dissipated depends on the characteristic of wave (significant height, period, angle of incident and breaking state) and properties of obstacle (slope, hardness, element size or height). Thus, a reflection coefficient is introduced that relates the incoming and reflected wave height.

When the incoming wave are almost perpendicular to the obstacle, the incident and reflected wave interact together by generating the *stationary wave* that can have twice the amplitude of initial wave.

As regard transmission, when waves hit a porous structure like a breakwater, part of the energy is transmitted through it. The amount of energy transmitted depends on the characteristics of the wave, in addition to porosity, gravel size, roughness and height of the structure. Overtopping may also occur. Long period waves, like tidal or swell waves, are more easily transmitted than high frequency waves, which are either dissipated or reflected against structure.

2.2.4 Diffraction

When waves propagate beyond an obstacle, they tend to bend to the “shadow area”. This mean that they do not follow a straight line, but an along crest transfer of energy results in waves being present also in the shadow area behind the obstacle

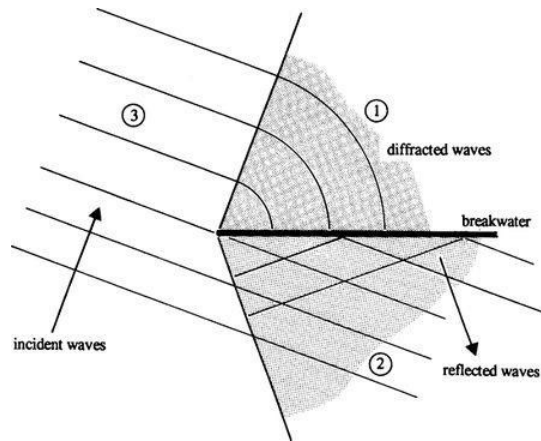


Figure 13 Wave diffracted scheme

Waves bend around obstructions by radiation of the wave energy:

1. Shadow area (diffraction)
2. Short-crested region (incident and reflected waves interact)
3. Undisturbed region (incident wave)

Wave height decrease in the shadow region with consequent energy spread.

The diffraction coefficient describe the amount of diffracted waves.

$$K_D = \frac{H}{H_i} = \frac{\text{wave height}}{\text{incident wave height}} \quad (36)$$

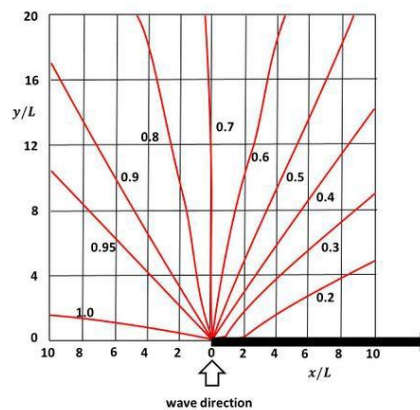


Figure 14 K_D for semi-infinite breakwater

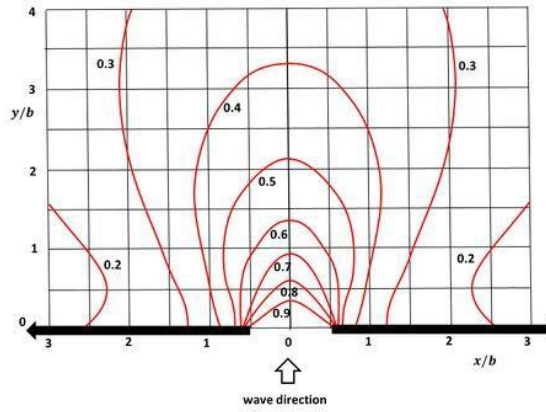


Figure 15 K_D for contiguous breakwaters (gap width $b =$ wavelength L)

2.2.5 Wave Breaking

As it has been argued before, waves when propagating towards the coast will increase their height until infinity due to shoaling in absence of physical limit to the steepness of wave.

With the decrease of the water depth, the celerity decreases, and the orbits covered by the individual particles pass from circular to elliptical increasingly crushed. The wave breaking is produced when the speed of single water particle at wave crest is larger than the wave celerity. It occurs when:

$$H_b = \gamma h_b \quad (37)$$

In which:

- H_b breaking wave height
- $\gamma =$ breaking coefficient (function of seabed and wave characteristics)
- h_b breaking depth

The breaking type and breaking parameters can be expressed with respect to Iribarren number for deep waters:

$$I_{r0} = \frac{\tan \alpha}{\sqrt{\frac{H_0}{L_0}}} \quad (38)$$

In which:

- α slope of seabed
- H_0 wave height in deep water

- L_0 wavelength in deep water
- $\frac{H_0}{L_0}$ steepness of wave

There are three types of breaking:

1. *Spilling* ($I_{r0} < 0.5$); it typically occurs on mildly sloping beaches. The waves begin to break at a considerable distance from the coast and gradually break down once they reach even lower waters. During the breaking, the turbulence develops at the crest, which generates foam.



Figure 16 Spilling

2. *Plunging* ($0.5 < I_{r0} < 3.3$); it typically occurs on moderately sloping beaches. Before breaking the wave "folds" on itself, making the crest fall into the trough (and thus making it ideal for surfers!). At the moment of crushing, a large amount of energy is dissipated of which a large part continues towards the coast, generating high waves, and the rest is reflected offshore.



Figure 17 Plunging

3. *Surging* ($I_{r0} > 3.3$); it typically occurs on highly sloping beaches. This type of breaking occurs in a relatively small portion of the sea and most of the energy dissipated at the crushing is reflected offshore. Before the wave can form the

hedgehog on the crest, the foot of the wave reaches the coast preventing its evolution.



Figure 18 Surging

2.3 Surf Zone

The zone in which there is the wave dissipation, from the breaking point to the coastline is called *Surf Zone*. The breaking point is the point at which the wave starts to break. In the surf zone the principal phenomena that occurs is the wave breaking, that is describe by the breaking coefficient:

$$\gamma = \frac{H_b}{h} = \frac{\text{wave height}}{\text{depth of breaking point}} \quad (37)$$

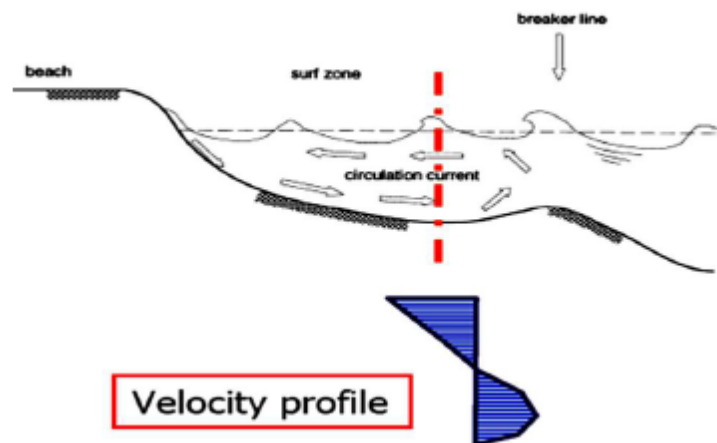


Figure 19 Surf Zone scheme, with velocity profile

The waves propagating towards the coast transport both energy and momentum. The variation of momentum acts on the body of water either generating inclinations of the sea level or giving rise to currents. The intensity of these forces is negligible in deep water conditions while it becomes relevant in surf-zone where they can cause large variations in

water level (set-up) and give rise to important currents (such as longshore current, undertow and rip current).

When the waves impact obliquely on the coast, in addition to the \tilde{S}_{xx} component of the normal stress radiation at the coast, which is balanced by the set-up and the undertow current, there is also a gradient in the \tilde{S}_{xy} component, that produce the longshore current

The set-up phenomenon is due to the fact that a variation of the surface slope is required to balance the hydrodynamic thrust of the wave.

The undertow current is a bottom current that balance the mass transport to the shore due to the wave breaking, occurring above the level of the wave trough. The undertow current is dangerous for swimmers.

The horizontal currents that are established in the surf zone can be classified under two types: longshore currents and rip currents.

The longshore currents occur mainly in the presence of oblique waves and extend over the entire width of the surf zone. They reach maximum intensity close to the breaking depth and then decrease moving towards the open sea and towards the coast. Wider waves generate faster longshore currents, while waves inclined of 45° with respect to the bathymetric lines generate faster currents. Importantly, the longshore current not only moves water in the surf zone, it also moves sediment parallel to the shoreline. The direction of longshore current is a function of the angle of wave approach. For example, if the waves approach the shoreline from the south, longshore current moves from south to north.

The rip currents take on a shape like that of jets of water, directed from the shore towards the open sea, beyond the breaker line (Figure 20) and interrupt the long shore pattern of the longshore current.

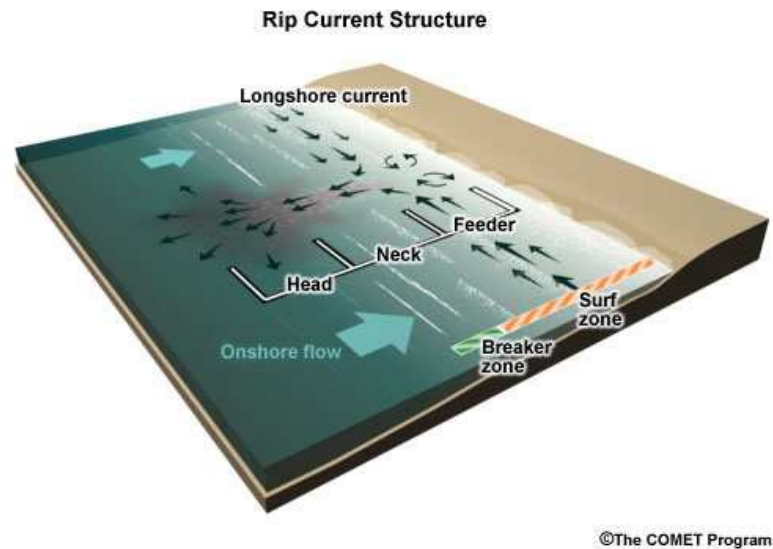


Figure 20 Rip Current scheme

The rip current can be seen from:

- different colour of the water caused by the suspended sediment transported by the rip-currents, which are typically of strong intensity;
- presence of a foam or algae line.

Due to the high velocity $\left(0.5 - 2.5 \frac{m}{s}\right)$, rip currents are considered very dangerous. Since the rip currents are intense, they have a strong erosion power. In fact, they can transport to the open sea the sediments put into suspension by the breaking waves.

Chapter 3 – Scouring

3.1 Basic concepts

3.1.1 Introduction

When structure is placed in a marine environment, the presence of the structure will change the flow pattern in its immediate neighbourhood, resulting in one or more of the following phenomena:

- a. The contraction of flow
- b. The formation of horseshoe vortex in front of the structure

- c. The formation of lee-wake vortices (with or without vortex shedding) behind the structure
- d. The generation of turbulence
- e. The occurrence of reflection and diffraction of waves
- f. The occurrence of wave breaking
- g. The presence of different soils that may produce “quick” condition/liquefaction allowing material to be carried off by currents

The changes usually cause an increase in the local sediment transport capacity and thus lead to scour.

The term “scour” is used instead of the more general term “erosion” to distinguish the process caused by the presence of a structure (Costal Engineering Manual, 2001).

The scour is a threat to the stability of the structure.

The type of structure where such local scour is involved can vary considerably: it may be a simple structure such as a plain pipeline or pile or the trunk section of a vertical-wall breakwater, or it may be a complex structure such as a group of piles, a subsea template, a protection structure with horizontal and vertical members, or an offshore platform.

Such structures are usually exposed to currents, waves and combination of waves and currents. Clearly, scour process in the marine environment (with waves being the dominant flow effect) are more complex than in steady-current flows such as in rivers. In river hydraulics, a long tradition exists for studying scour around hydraulic structures. The scour problems in costal and offshore engineering have not received the same kind of attention. One of the first important contributions is that of Haerbich, who published two early monographs on the subject, 1981 and 1984.

Recent years, however, have witnessed a rapid development of the knowledge of flow and scour processes around marine structures, particularly those which have simple geometries such as pipelines, piles, etc. A substantial volume of knowledge has accumulated as a result of this intensive research activity.

Scour is the removal by hydrodynamic forces of granular bed material in the vicinity of costal structure, it is a specific form of the more general term “erosion”.

Local scour is herein considered to be lowering of the bed in the direct vicinity of a structure due to local accelerations and decelerations of near-bed velocity and the associated turbulence (vortices) leading to an increase of the local sand transport capacity. Once a scour hole is formed, flow separation will take at the edge of the hole and mixing layer will develop increasing the turbulence intensities and stimulating further scour of the bed (self-intensifying process). Excessive scour close to the structure may ultimately lead to instability/failure of the structure.

3.1.2 Amplification factor

Consider a structure placed in a marine environment. The presence of the structure will cause the flow in its neighbourhood to change. This local change in the flow will generally cause an increase in the bed shear stress and in the turbulence level. The sediment transport close to the structure increases mainly because:

- a. The average bed shear stress is increasing close the structure
- b. The degree of turbulence is increasing in the vicinity of the structure

Both features will lead to an increase in the local sediment-transport capacity. Today, however, much more knowledge is available about item (a) than about item (b).

Usually the increase in the bed shear stress is expressed in terms of the so-called amplification factor defined by

$$\alpha = \frac{\tau}{\tau_{\infty}} \quad (39)$$

In which:

- τ bed shear stress
- τ_{∞} the bed shear stress for the undisturbed flow

The amplification factor can be very large near the structure (as large as $O(10)$).

Owing the local increase in α ($\alpha > 1$) the sediment transport capacity will increase (since the rate of sediment transport as bed load $q_b \sim \tau^{3/2}$), starting the local erosion of the sea: the *scour process*.

This process will continue until the scour reaches the level at which the bed shear stress around the structure reduces and the amplification becomes $\alpha = O(1)$. The stage where the scour process comes to an end is called the equilibrium stage.

3.1.3 Equilibrium scour depth, equilibrium stage

From the previous consideration, the scour develops towards the equilibrium stage through a transitional period, as illustrated schematically in Figure 21. The scour depth corresponding to the equilibrium stage, S , is called equilibrium scour depth.

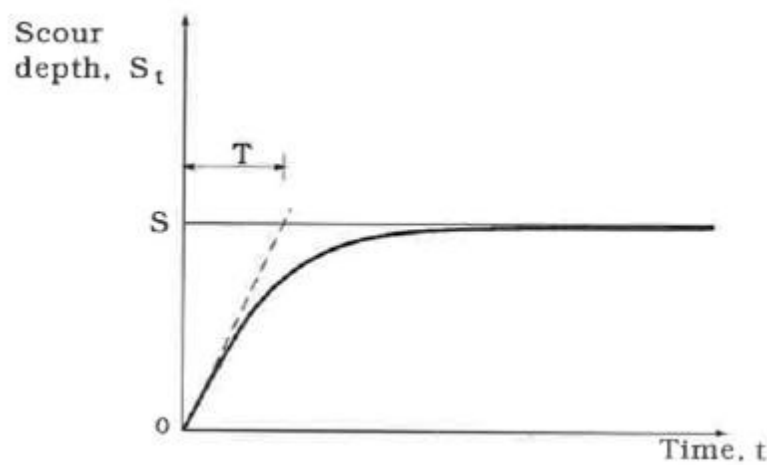


Figure 21 Time development of scour depth

From Figure 21, it can also be seen that, for a substantial amount of scour to develop, a certain amount of time must elapse. This time is called the time scale of scour process. The time scale of the scour process may be defined in several ways. The following definition will be adopted in the present treatment.

$$S_t = S \left(1 - \exp\left(-\frac{t}{T}\right) \right) \quad (40)$$

In which T is the time scale of the scour process, and corresponds to the time period T indicated in Figure 21, where the dashed line is tangent to the scour-depth-versus-time curve at $t = 0$.

The quantities, namely the equilibrium scour depth and the time scale, are two major parameters in scour studies.

The equilibrium scour depth is important because - given the structure and the flow climate - it indicates the degree of scour potential. The assessment of scour depth is essential in the design of both (a) the foundation of the structure and (b) the scour protection work.

The time scale is also equally important. A scour hole produced after a storm may be backfilled. Normally, the question asked in practice is whether any substantial amount of scour would occur over the backfilled area during the next storm. Obviously, for a substantial amount of scour to occur, the storm should prevail over a space of time larger than the time scale of the scour process. Clearly, to answer the question, the time scale of scour must be known.

3.1.4 Clear-water scour and live-bed scour

Scour may be classified into two categories: the clear-water scour and the live-bed scour.

In the case of the *clear-water scour*, no sediment motion takes place far from the structure ($\theta < \theta_{cr}$), while, in the case of *live-bed scour*, the sediment transport prevails over the entire seabed ($\theta > \theta_{cr}$). Here θ is the undisturbed Shields parameter defined by:

$$\theta = \frac{\tau}{(\rho_s - \rho_w)gd_{50}} = \frac{U_f^2}{g(s-1)d} \quad (41)$$

In which:

- τ bed-shear stress
- ρ_s sediment density
- ρ_w fluid density
- g acceleration of gravity
- d_{50} median sediment diameter
- $U_f = \sqrt{\frac{\tau_{\infty}}{\rho}}$ undisturbed bed shear velocity
- s specific gravity of sediment grains
- d grain size

θ_{cr} is the critical value of the Shields parameter corresponding to the initiation of sediment motion at the bed. θ_{cr} is a function of the grain Reynolds number $\left(R_e^* = \frac{u_{cr} d_{50}}{\nu}\right)$.

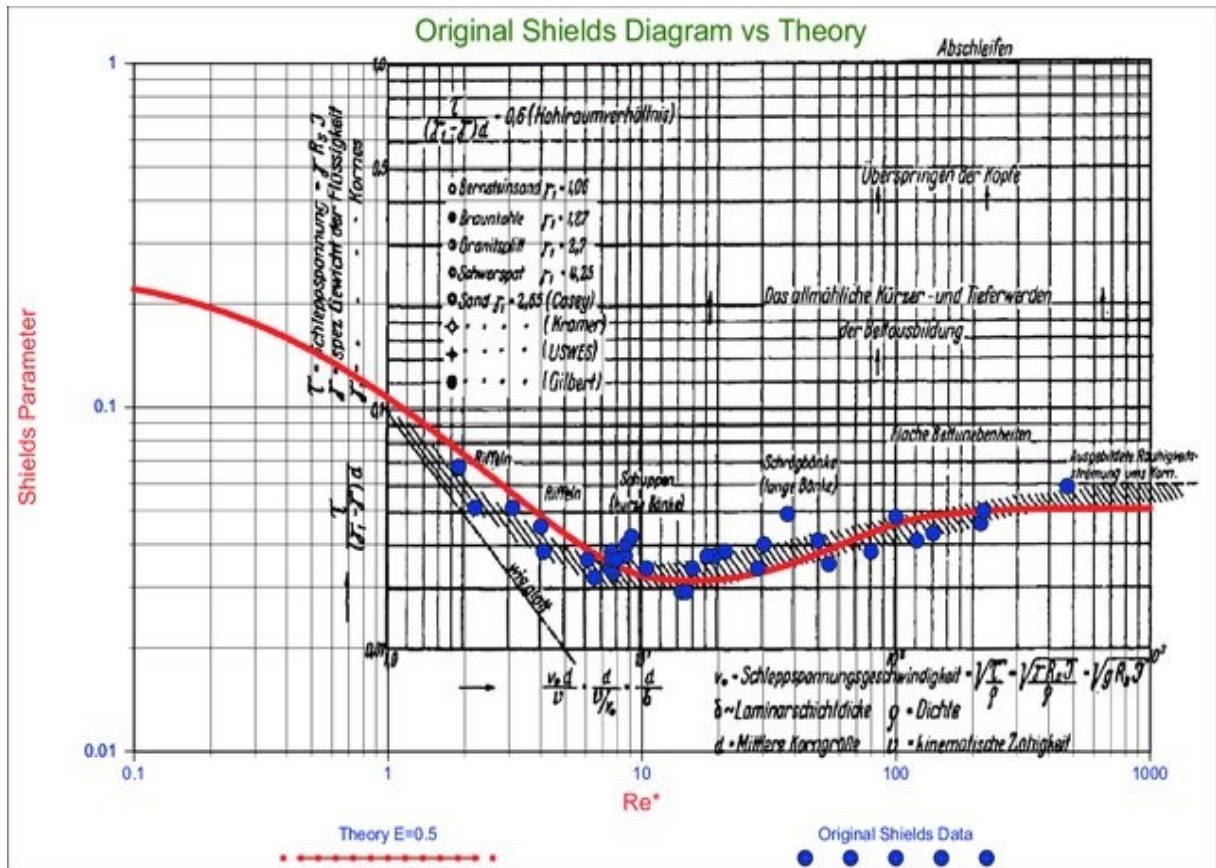


Figure 22 Initiation of motion at the bed

θ_{cr} parameter can be obtained from the graph as function of Reynolds number (Re^*), Figure 22, or it can be calculated from the following equation:

$$\theta_{cr} = \frac{\tau_{cr}}{(\rho_s - \rho_w)gd_{50}} = \frac{u_{*cr}^2}{\Delta gd_{50}} = f(Re^*) \quad (42)$$

For large Reynolds number this equation can be written for sand and gravel as follows:

$$\theta_{cr} = \frac{0.3}{1 + 1.2D^*} + 0.1(1 - \exp(-0.02D^*)) \quad (42)$$

In which:

- τ_{cr} critical value of bed shear stress induced by the fluid at which the stone first begin to move
- Re^* Reynolds number, based on shear velocity ($Re^* = \frac{u_{*cr}^2 d_{50}}{\nu}$)
- Δ relative buoyant density of the stone
- $D^* = d_{50} \left(\frac{(s-1)g}{\nu^2} \right)^{1/3}$ dimensionless sediment size

- $s = \frac{\rho_s}{\rho_w}$ relative density
- ν kinematic viscosity coefficient

In the clear-water case, the variation of the scour depth with θ is more pronounced: the scour depth increases from zero at very small values of θ up to θ_{cr} (Figure 25).

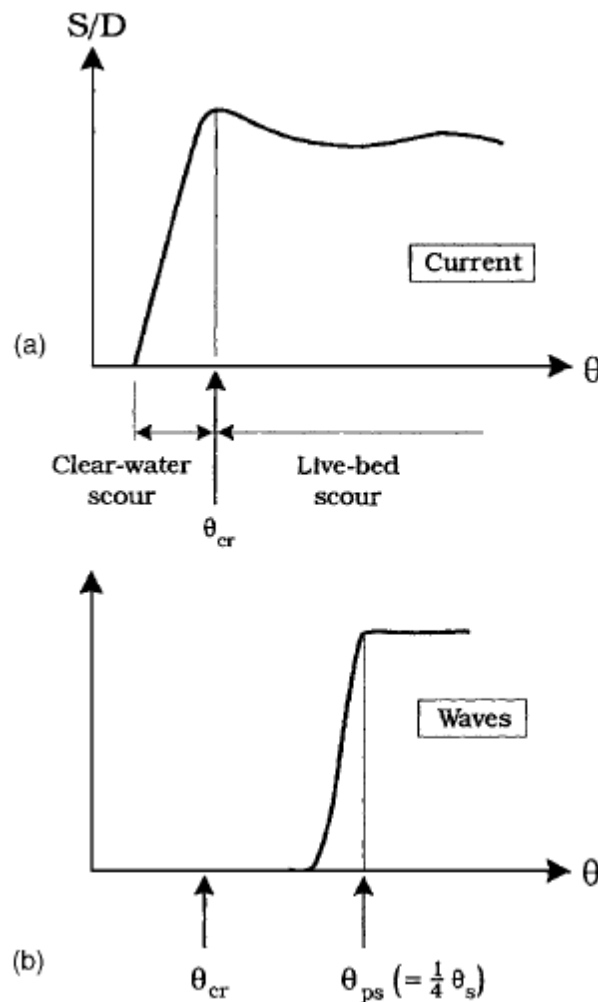


Figure 23 Schematic variations of scour depth as function of the Shields parameters: (a) currents; (b) waves

In which:

- θ_s is the critical value of the Shields parameter for the initiation of suspension
- θ_{ps} can be interpreted as the approach-flow Shields parameter to cause suspension from the bed at the side. Hence the sand is picked-up and put into shed vortex

$$\theta_s = \left(\frac{d_{50} U_0}{\nu} \right)^{-0.05} \left[0.7 \exp \left(-0.04 \frac{d_{50} U_0}{\nu} \right) \right] + 0.26 \left[1 - \exp \left(-0.025 \frac{d_{50} U_0}{\nu} \right) \right] \quad (43)$$

At very low θ values, no scour will occur because, in this case, even the amplified local bed shear stress may still be too small to cause sediment transport. However, when the live-bed case is reached, and beyond ($\theta > \theta_{cr}$), a very small variation of the scour depth with θ is observed. This because any change in θ results in corresponding changes in sediment transport, and these changes occur both inside and outside of the scour hole in almost equivalent amounts, eventually causing only small changes in the equilibrium scour hole.

3.1.5 Time scale

The scour depth develops towards its equilibrium stage through a transitional period, as depicted in Figure 24. It is seen from the figure that the time variation of the scour depth can be approximately represented by relation (40).

Figure 24 presents a typical example of the development of the scour depth with time. The scour depth plotted in this figure corresponds to the maximum scour depth, which develops at the back of the cylinder. As seen from the figure, the scour depth attains its equilibrium value, S , after a transition period.

The time scale, T , is defined by 40, and as mentioned earlier represent the time duration for a substantial amount of scour to develop. T can be found by calculating the slope of the line tangent to the curve $S_t(t)$ at time $t = 0$ (Figure 24).

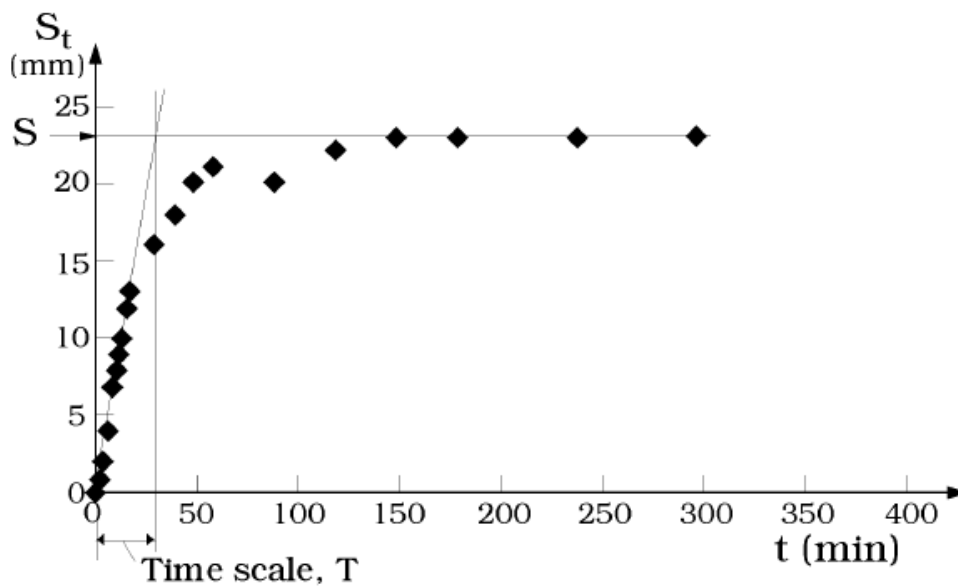


Figure 24 Time development of scour depth. $KC=0.61$ $D/L=0.15$. At the point where the scour is maximum

Fredsøe, Sumer and Arnskov (1992) investigated the time scale both in steady currents and in waves, employing the 40. The following paragraphs will summarize the results of this study.

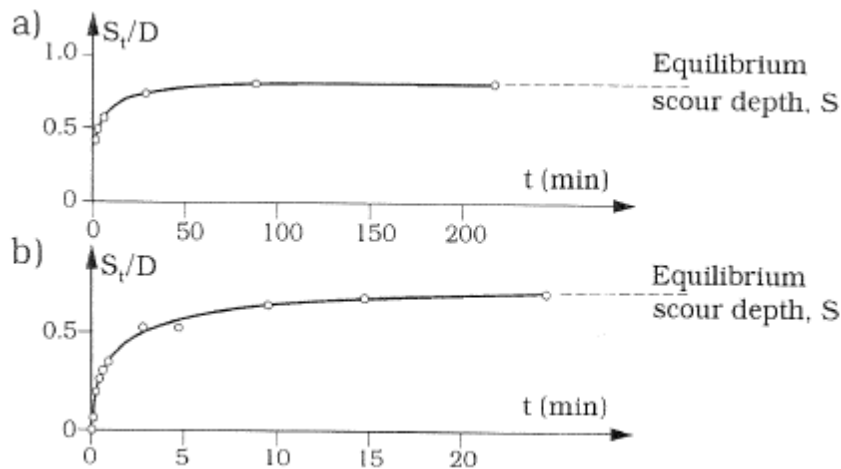


Figure 25 Time development of scour depth (a) current $\vartheta=0.098$ (Mao 1986); (b) Wave, $\vartheta=0.035$, $KC=27$ (Fredsoe 1992)

3.1.5.1 Time scale in steady currents

On dimensional grounds, the time scale can be written as in the following non dimensional function form

$$T^* = f(\theta) \quad (44)$$

In which θ is the Shields parameters, and T^* the normalized time scale defined by

$$T^* = \frac{(g(s-1)d^3)^{\frac{1}{2}}}{D^2} T \quad (44)$$

The preceding non dimensional formulation can also be obtained by normalizing the equation of sediment continuity.

The time scale obtained from the scour-depth-versus-time information given by Kjeldsen (1973) and Mao (1986) is plotted in the preceding nondimensional form in Figure 26. The figure shows that the normalized time scale T^* correlates quite well with the Shields parameter.

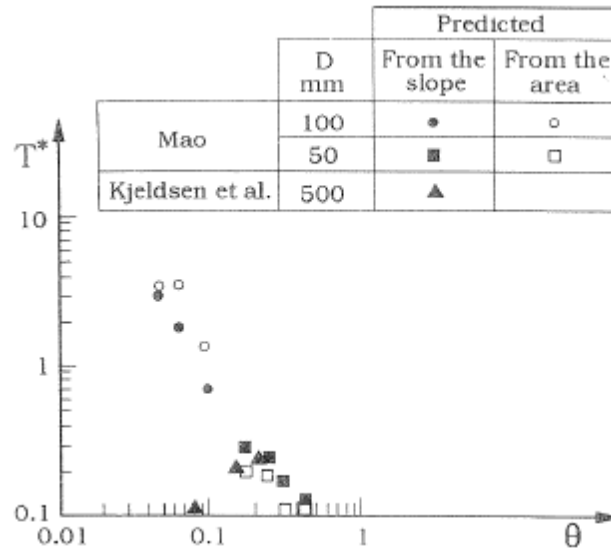


Figure 26 Time scale current, live bed

Furthermore, the figure shows that the larger the Shields parameter, the smaller time scale. This is because the larger the Shield parameter, the larger the sediment transport due to scouring, and therefore the shorter the time period during which a substantial change in the scour depth will occur.

3.1.5.2 Time scale in waves

In the case of waves, one additional parameter, namely the Keulegan-Carpenter number (KC), is involved in the nondimensional formulation of time scale:

$$T^* = f(KC, \theta) \quad (45)$$

$$KC = \frac{UT}{L} \quad (46)$$

In which:

- U peak orbital near-bed velocity,
- T wave period
- L is a characteristic length scale of the object

While the scour depth mainly depends on KC ($\frac{s}{D} = 0.1\sqrt{KC}$), the results of Fredsøe test (1992) indicates that the time scale is governed by the only Shields parameter.

3.2 Shear stress

As previously written, the Shields parameter is a function of shear stress, which is a function of the effort produced by both current and wave.

Literature suggests that for combined wave and steady current the effective shear stress for sediment motion should be taken as the sum of the oscillatory shear stress (waves, $\hat{\tau}_w$) and the current-induced shear stress, τ_c . A formulation for the resulting bed shear stress due to combined waves and currents, which is widely applied in engineering practice, was proposed by Bijker (1967). According to Bijker the resulting shear stress, τ_{cw} , can be found by vector sum of the shear velocities of wave and currents.

$$\bar{\tau}_{cw} = \tau_c + \frac{1}{2} \hat{\tau}_w \quad \tau_c > 0.4 \hat{\tau}_w \quad (47)$$

3.2.1 Unidirectional flow

In steady flow, the current-induced shear stress, $\tau_c \left[\frac{N}{m^2} \right]$, acting on the bed can be calculated using following equation, based on Chezy's roughness equation:

$$\tau_c = \rho_w g \frac{U^2}{C^2} \quad (48)$$

In which:

- U is the depth-average current velocity $\left[\frac{m}{s} \right]$
- C is the Chezy coefficient $\left[\frac{m^{\frac{1}{2}}}{s} \right]$

The Chezy coefficient can be determined by the roughness length scale of Nikuradse ($k_s [m]$).

$$C = 18 \log \left(12 \frac{h}{k_s} \right) \quad (49)$$

Where:

- h water depth $[m]$
- k_s hydraulic roughness $[m]$

- $k_s = (1 \div 10) d_{50}$ for flat and sandy bottom

It should be noted that for small water depths, the previous equation cannot be used. For such cases, Christensen provides a practical alternative approach.

$$C = 18 \log \left(1 + 12 \frac{h}{k_s} \right) \quad (49)$$

3.2.2 Oscillatory flow

The Shields criterion for initial motion has been established from experimental observations for unidirectional steady flow. For slowly varying flows, such as tidal flows in limited water depths, the flow may be reasonably regarded as quasi-steady. For shorter-period oscillations, such as wind or swell waves, having a period of 5s to 20s, the above quasi-steady approach is no longer justified. Various investigators have addressed the phenomena of initial motion under wave action. Mased and Grant (1975) and Komar and Miller (1975) showed, independently, that the results obtained for initial motion in unsteady flow were in reasonable agreement with Shields curve for unidirectional flow if the shear stress was calculated by introducing the concept of the wave friction factor according to Jonsson (1967). The oscillatory shear stress equation gives the relationship between the maximum shear stress under oscillatory flow, $\hat{\tau}_w \left[\frac{N}{m^2} \right]$, and the relevant hydraulic parameters.

$$\hat{\tau}_w = \frac{1}{2} \rho_w f_w u_0^2 \quad (50)$$

In which:

- ρ_w fluid density $\left[\frac{Kg}{m^3} \right]$
- f_w friction factor [-]
- u_0 peak orbital velocity near the bed $\left[\frac{m}{s} \right]$, which may be determined, as first approximation, by linear wave theory

Soulsby (1987) has provided design curve based on linear wave theory (Figure 27) that enable calculation of near-bed orbital velocities for both monochromatic (regular) and random waves, where the maximum horizontal bed velocity u_0 was obtained from acceleration equation applied at the bottom (namely at $z=-h$):

$$u = u_0 = \frac{\pi H_s}{T_p} \frac{1}{\sinh kh_c} \quad (51)$$

Where:

- $k = \frac{2\pi}{L}$ wave number
- h_c is the water depth

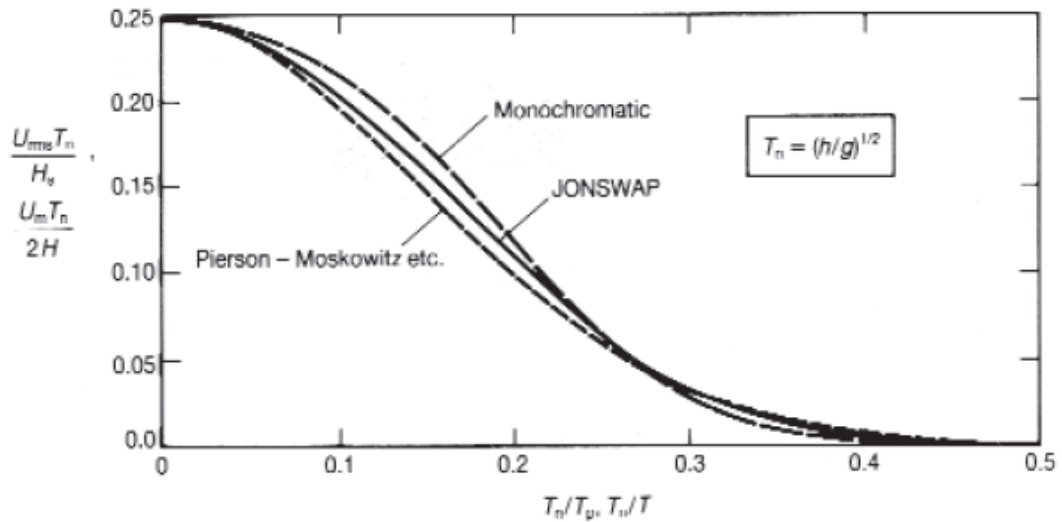


Figure 27 Near-bed orbital velocity for monochromatic waves and a spectrum of waves (Soulsby, 1987)

3.3 Scouring laboratory test

In this paragraph, some specific cases analysed in the laboratory are reported:

- Scour near seawalls
- Scour near tip of breakwaters and groynes
- Scour near piles and piers
- Scour near horizontal pipes

3.3.1 Scour near sea walls

The basic shape of a toe scour hole (Steetzel, 1988) is shown in Figure 28. The proper determination of the water depth at the toe (h_{toe}) of the structure may give problems in field conditions.

According to the Shore Protection Manual (1984), the scour depth is given by the following simple rule:

$$d_{s,max} = \alpha_c H \quad (52)$$

In which:

- H height of maximum unbroken wave at toe of structure
- $\alpha_c = \left(\frac{1+U_c}{U_{cr}}\right)^{0.1}$ current effect
- U_c longshore current velocity
- U_{cr} critical velocity for initiation of motion ($\alpha_c = 1$ for $U = 0 \frac{m}{s}$)

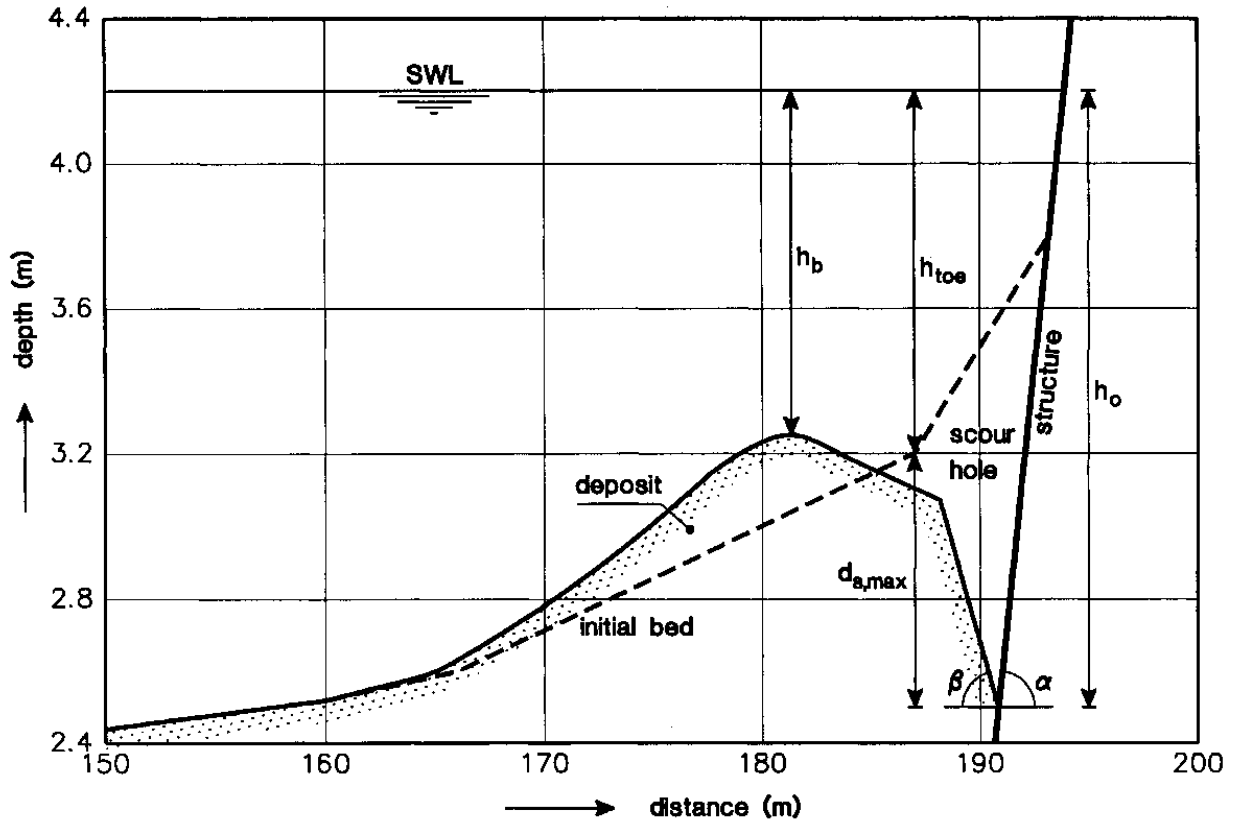


Figure 28 Basic shape of scour hole near toe of seawall (Steetzel, 1988)

Fowler (1992) analyzed laboratory test results and proposed an empirical method to determine the scour depth at the toe of vertical walls. Based on this approach, the maximum scour depth roughly is:

$$\frac{d_{s,max}}{H_{s,0}} = \begin{cases} 0.6 & \text{for } \frac{h_{toe}}{L_0} = 0.005 \\ 0.8 & \text{for } \frac{h_{toe}}{L_0} = 0.02 \\ 1.0 & \text{for } \frac{h_{toe}}{L_0} = 0.04 \end{cases} \quad (52a)$$

In which

- $H_{s,0}$ significant wave height in deep water
- L_0 wave length in deep water
- h_{toe} water depth at toe of structure

The scour depth increases with decreasing wavelength, because shorter waves tend to break against or in front of the wall. Breaking waves produce a larger scour depth.

3.3.2 Scour near tip of breakwaters and groynes

Scour near the tip of breakwaters can be classified as *current-dominated* scour or *wave-dominated* scour. Scour is considerably enhanced, if tide-, wind- and wave-induced longshore currents with velocities exceeding 0.5 m/s are present. Wave-related scour generally is dominant in micro-tidal conditions.

Sumer and Fredsøe (1997) studied wave-dominated scour near the tip of a vertical wall-type (rounded tip) breakwater in laboratory conditions.

Based on flow visualization measurements, the scouring mechanisms were found to be related to the following mechanisms:

- generation of vortices in the lee-side zone of the wall for $KC = 1 \div 12$; vortices are not generated for $KC < 1$; $KC = \frac{U_w T}{B}$ = Keulegan-Carpenter number, U_w = peak orbital near-bed velocity, T = wave period and B = width of wall;
- generation of lee-side vortices and horse-shoe vortices for $KC > 12$; horse-shoe vortices are vortices generated near the bed in front of and along the tip of the wall due to rotation of the approaching flow; in field conditions the KC -number is of the order of 1 and therefore horse-shoe vortices are not of practical relevance.

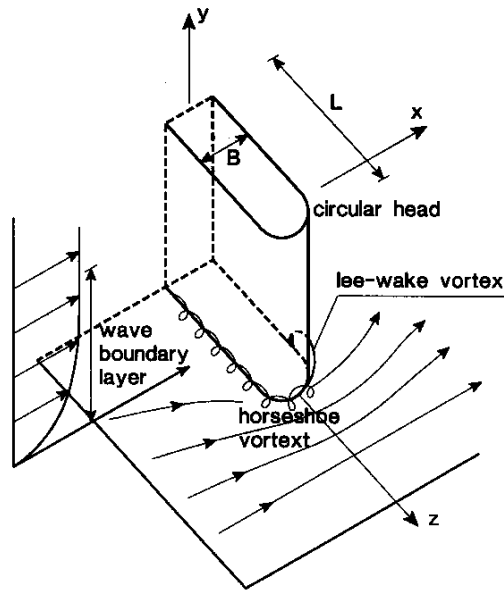


Figure 29 Vortex patterns near tip of wall-type breakwater

Scour tests over a movable bed of 0.17 mm-sand were conducted in a depth of 0.4 m with regular non-breaking waves (periods between 1 and 4 s). The width of the structure was $B = 0.14 \text{ m}$ and 0.40 m . Hence, the width-depth ratios were $B/h = 0.35$ and 1 . The observed maximum scour depths $\left(\frac{d_{s,max}}{B}\right)$ for normal incident waves (90°) were found to be related to the KC-number, see Table 2 and Figure 29. The maximum scour depth was attained after about 1000 waves. The results are only valid for a vertical breakwater with a maximum width equal to the water depth $\left(\frac{B}{h} = 1\right)$.

The scour was maximum at the location of the tip (in the middle of the tip, see Figure 30 and Figure 31 of the breakwater. The observed scour length L_s (normal to wall) is also given in Table 2.

The maximum scour depth roughly increased by a factor 2 for a straight wall tip (sharp edge) instead of a rounded tip.

NON-BREAKING WAVES		
SCOUR DEPTH $\frac{d_{s,max}}{B}$	SCOUR LENGTH $\frac{L_s}{B}$	KC- NUMBER
0.02	0.5	1
0.1	1.5	2
0.2	2.5	4
0.3	3.5*	7
0.4	-	10

Table 2 Scour depth for normal incident non-breaking regular waves over a sand bed of 0.17 mm in a laboratory flume

The scour can be mitigated by means of a protection layer on the bed. The length L normal to the structure should be about $\frac{L}{B} = 2$ for $KC = 2$. In that case the maximum scour depth is reduced by a factor 3. In case of $\frac{L}{B} = 1$, the maximum scour depth is reduced by about 30%.

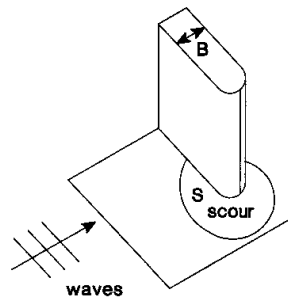


Figure 30 Scour and deposition locations near vertical breakwaters

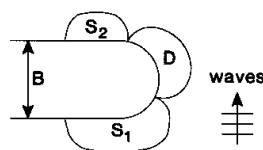


Figure 31 Scour and deposition locations near rubble-mound breakwaters;

In which:

- S and S_1 scour due to non-breaking waves
- S_2 scour due to plunging waves
- D deposition due to non-breaking waves

3.3.3 Scour near piles and piers due waves and currents

The scouring process around vertical piles (bridge piers) is dominated by the following effects:

- local disturbance of the flow field (local scour);
- local reduction of cross-section (constriction of the flow due to the presence of the structure; contraction scour); $h_1 = b_0 h_0 / b_1$ with h_1 = mean depth of cross-section in contraction zone, b_1 = effective flow width of cross-section in contraction zone, b_0 = upstream flow width, h_0 = upstream mean flow depth).

Coleman and Melville (2001) propose to determine the total scour depth near the foundation of a bridge pier based on superposition of general scour and local scour at the foundation. They discuss the failure of bridges in New Zealand due to excessive scour at the piers. The Bulls Road bridge failure in 1973 during an annual flood event with a discharge of $675 \frac{m^3}{s}$ (not an extreme event; maximum recorded value is $3800 \frac{m^3}{s}$) can be attributed to a combination of general scour arising from gravel mining and local pier scour. The local scour was enhanced by:

- i. the obliqueness of the flow to the pier
- ii. the flow constriction caused by the piling up of debris behind old timber piers immediately downstream of the bridge
- iii. the presence of fine sand substrata exposed during the scouring process and accelerating the scouring process. The maximum depth of scour measured below the armoured bed level adjacent to the collapsed pier was about 12 m.

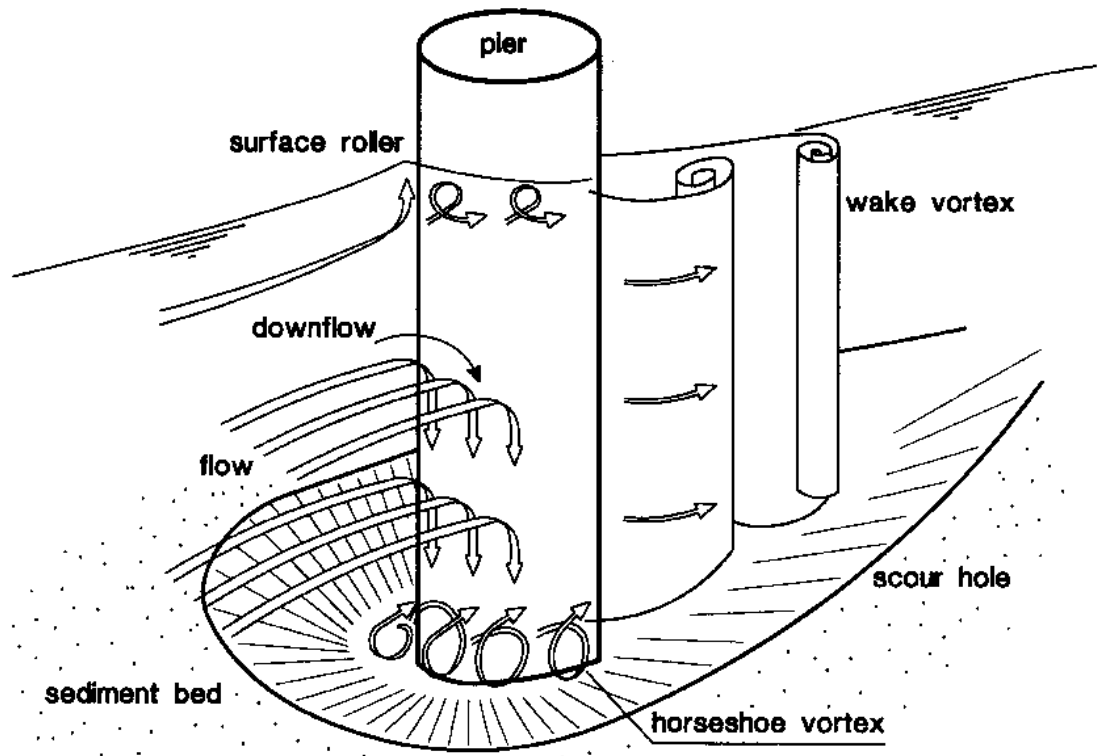


Figure 32 Flow pattern and scour near pile (Melville, 1988)

The flow pattern around a cylindrical pile is characterized by (see Figure 8):

- water surface roller in front of pipe
- downflow in front of pipe
- vortex-shedding in separation zone
- wake flow downstream of pipe
- generation of horseshoe-vortices in scour hole.

Based on analysis of field and flume data, Breusers et al. (1977) have found for a single pipe in uniform bed material:

$$\frac{d_{s,max}}{D} = \alpha_1 \alpha_2 \alpha_3 \alpha_4 \alpha_5 \alpha_6 \alpha_7 \quad (52b)$$

In which:

- $d_{s,max}$ maximum scour depth below original bed
- D Diameter for circular pipe
- α_1 coefficient related to U/U_{cr}
- $\alpha_2 = 2 \tanh\left(\frac{h}{D}\right)$ coefficient related to h/D

- α_3 coefficient related to shape of pipe
- α_4 coefficient related to angle of attacking flow,
- $\alpha_5 = 1 + r$ turbulent effects; r=input value
- $\alpha_6 = \left(\frac{1+U_w}{U_{cr}}\right)^{0.25}$ effect of short surface waves
- α_7 group affect
- U depth-averaged flow velocity upstream of pipe
- U_{cr} critical depth-averaged flow velocity (upstream)
- U_w near-bed orbital velocity
- h flow depth (upstream)

$$\alpha_1 = \begin{cases} 0 & \text{for } U/U_{cr} < 0.5 \\ 2\left(\frac{U}{U_{cr}} - 0.5\right) & \text{for } 0.5 < U/U_{cr} < 1 \\ 1 & \text{for } U/U_{cr} \geq 1 \end{cases} \quad (53)$$

$$\alpha_2 = \begin{cases} 2 & \text{for } \frac{h}{D} \geq 3 \\ 1.5 & \text{for } \frac{h}{D} < 3 \end{cases} \quad (54)$$

$$\alpha_3 = \begin{cases} 1 & \text{for circular pipes} \\ 0.75 & \text{for streamlined pipes} \\ 1.3 & \text{for rectangular pipes} \end{cases} \quad (55)$$

$$\alpha_4 = \begin{cases} 1 & \text{for flow normal to pipe} \\ 1.3 & \text{for flow under angle of } 15^\circ \text{ and } \frac{\text{length}}{\text{width}} = 4 \\ 2 & \text{for flow under angle of } 15^\circ \text{ and } \frac{\text{length}}{\text{width}} = 8 \end{cases} \quad (56)$$

Often the piers of a bridge are connected by a pile cap under water (just above bed level). In that case the width of the pile cap should be taken to estimate the D-parameter. During flood events with relatively large water depths and oblique approaching flow (worst case scenario), the maximum scour will be of the order of $d_{s,max} = 4 \div 5 D$. If a pile cap (say width of 1.5 m) is present, the maximum local scour close to the pile cap can easily go up to values of 5 to 7 m.

3.3.4 Scour near horizontal pipes

Scour near and under a pipeline is caused by changes of the local flow field due to the presence of the pipeline, see Figure 33 and Figure 34. Where there is a local increase in the transport capacity, erosion will take place. Sedimentation will take place where the transport capacity decreases. Usually, the velocity under the pipe will increase when there is a small local gap between the pipe and the seabed. This will initiate and intensify the erosion process.

Experiments have shown that erosion will always take place if a pipeline is placed on an erodible seabed, and when there is transport of sediment upstream of the pipeline. The processes causing onset of scour will be briefly described hereafter.

The mechanisms can be divided into three groups:

- *flow induced pressure differences*, in the case with flow having a component perpendicular to the pipeline axis, there is a pressure difference between the upstream and the downstream part of the pipeline. This difference ΔP is normally written as $\Delta P = \rho C_p (U^2/2g)$ with U = the undisturbed near-bed velocity; the pressure coefficient is approximately $C_p=1$ in steady current and $C_p=3$ for waves; due to these pressure differences, ground water flow can take place and the sediment may be carried away.
- *vortices near the pipeline*, three types of vortices are observed near the pipeline, see Figure 8.1. The vortices can transport the sediment away; suspended as well as bed transport can occur. Vortex A and vortex C move the sand particles away from the pipe area, while vortex B moves the sand particles toward the pipe.
- *imperfections in the seabed near the pipeline*, variations/imperfections of the bed near the pipeline or of the pipeline itself may result in the presence of gaps between the pipeline and the bed and hence to flow under the pipeline.

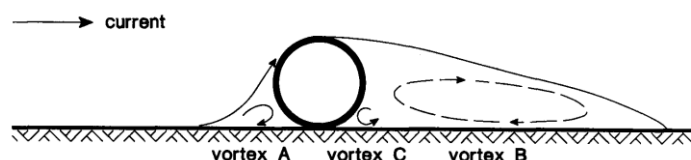


Figure 33 Vortices near the pipeline in unidirectional flow

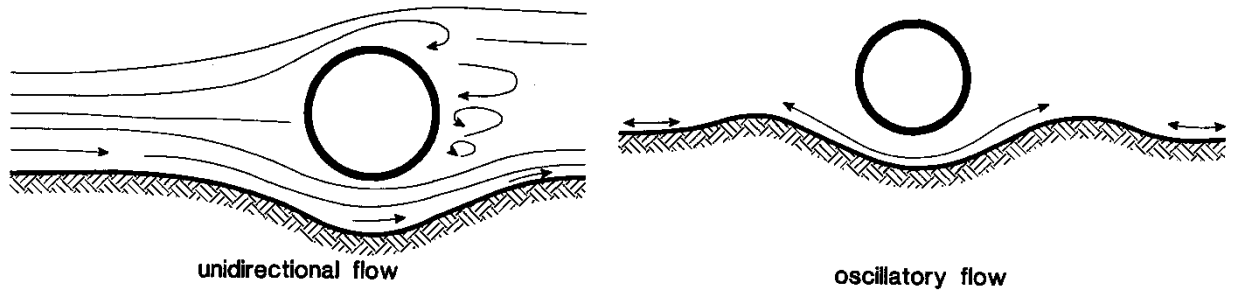


Figure 34 Scour in unidirectional and oscillatory flow

The development of scour in a current is governed by the velocity below the pipeline, the downstream wake and the vortex shedding downstream of the pipeline. From experimental results it appears that the near-bed velocity below the pipeline decreases with the depth of scour and increases with the width of scour.

If a pipeline is placed on a plane seabed in a current, a downstream wake will be developed. The length of this downstream wake is approximately six times the pipeline diameter.

If the pipeline is partly buried, the length of the downstream wake decreases. An analogy can be made with flow past a step.

If the current approaches the pipeline axis at a certain angle, the length of the downstream wake decreases. For flow angles below 30° no vortex shedding occurs.

Kjeldsen (1973) performed flume experiments with pipelines resting on the bed. Based on dimensional analysis, they found that the maximum scour depth can be expressed as:

$$d_{s,max} = 0.97 \alpha_w D^{0.8} \left(\frac{U_c^2}{2g} \right)^{0.2} \quad (52c)$$

In which:

- D pipe diameter
- U_c upstream velocity (undisturbed)
- $\alpha_w = \left(1 + \frac{U_b}{U_{cr}} \right)^{0.25}$ surface wave effects ($\alpha_w = 1$ no waves)
- U_b near-bed peak orbital velocity (undisturbed)
- U_{cr} critical velocity for initiation of motion

Since the scour development underneath, a pipeline is based on not only the pipeline parameters and environment conditions but also on the seabed parameters, a full empirical approach in physical modelling remains attractive. The work of Kjeldsen (1973), as a milestone in empirical physical scour modelling, investigated the local scour around the pipelines under unidirectional currents. It was considered that the scour depth in live-bed conditions depends only on the flow velocity and pipe diameter. The research group at the Delft University of Technology later improved Kjeldsen's model by considering the effect of grain size to scour depth.

$$d_{s,max} = 0.929 \left(\frac{U_0}{2g} \right)^{0.26} D^{0.78} d_{50}^{-0.04} \quad (52d)$$

In which:

- $d_{s,max}$ maximum scour depth below pipelines
- U_0 undisturbed mean velocity
- D diameter pipelines
- d_{50} mean seabed particle size

Chapter 4 – Numerical models

Many coastal and offshore engineering applications require detailed knowledge of wave conditions at specific locations. Usually, such information is not available, due to incomplete (or in absence of) observational records. In such case, predictions of wave conditions by numerical models is useful, as they may provide good estimates of environmental conditions at a location for given wind fields.

4.1 SWAN

SWAN (acronym for Simulating WAVE Nearshore) is a third-generation wave model used to compute spectra of random short-crested waves in coastal waters. It has been developed by Booij (1999) and validated specially in coastal regions with shallow water, islands (barrier), tidal flats, local wind and ambient currents.

SWAN is applicable to describe nearshore wave propagation processes such as shoaling, refraction, wave breaking due to finite-depth effect and triad wave-wave interactions. Moreover, it can also model the quadruplet wave-wave interactions that dominate the wave spectrum evolution in deep-water.

In SWAN, the evolution of the wave spectrum is described by the action balance equation, rather than the energy transport equation, because the wave action density spectrum is conserved in the presence of currents, but the energy density spectrum is not. SWAN solves the action balance equation using a fully implicit upwind scheme in geographic space. A grid of rectangular meshes is implemented through a finite-difference scheme. However, the use of equally spaced meshes for the case of complex geometries of general coastal environments together with the rapid change of the seabed may make SWAN problematic to use and inefficient.

Typically, a uniform grid used in SWAN for an entire domain from deep water to shallow water could result in an over-resolved offshore region and an under-resolved nearshore. To resolve the evolution of a broad spectrum of wind waves, SWAN uses a fine spatial discretization in shallow waters that becomes expensive for large coastal zones.

To overcome the increased computational demands of SWAN for nearshore applications, where the complex bathymetry and irregular shoreline often require a fine resolution, the nested grid system is used. More recently the upgraded SWAN model of version 40.11 (and later) has been developed by Holthuijsen et al. (2000) to provide an option for coupling a fine-nested SWAN simulation for nearshore wave predictions. The entire domain is generally divided into some sub-regions with varying spatial grid sizes according to the desired resolution. Furthermore, using unstructured grids these problems are much reduced.

4.1.1 Governing equations

Using the linear wave theory and the conversion of wave crests, the wave propagation velocities in spatial space within Cartesian framework and spectral space can be obtained from the kinematics of a wave train (Whitham, 1974; Mei, 1983):

$$\frac{dx}{dt} = (c_x, c_y) = \mathbf{c}_g + \mathbf{u} = \frac{1}{2} \left(1 + \frac{2|\mathbf{k}|h}{\sinh 2|\mathbf{k}|h} \right) \frac{\sigma \mathbf{k}}{|\mathbf{k}^2|} + \mathbf{u} \quad (58)$$

$$\frac{d\sigma}{dt} = c_\sigma = \frac{\partial\sigma}{\partial h} \left(\frac{\partial h}{\partial t} + \mathbf{u} \nabla_x h \right) - c_g \mathbf{k} \frac{\partial \mathbf{u}}{\partial s} \quad (59)$$

$$\frac{d}{dt} = c_\theta = -\frac{1}{k} \left(\frac{\partial\sigma}{\partial h} \frac{\partial h}{\partial m} + \mathbf{k} \frac{\partial \mathbf{u}}{\partial m} \right) \quad (60)$$

Where:

- c_x, c_y propagation velocities of wave energy in spatial x, y space
- $c_g = \frac{\partial\sigma}{\partial k}$ group celerity
- c_σ propagation velocities in spectral σ -space
- c_θ propagation velocities in spectral θ -space
- \mathbf{k} wave number vector
- \mathbf{u} speed of possible current
- h water depth
- s space coordinate in the wave propagation direction
- m coordinates perpendicular to s

The vectors are shown in boldface.

Information about the sea surface is all contained in the wave variance spectrum or energy density $E(\sigma, \theta)$, that distributes the wave energy over (angular) frequencies $E(\sigma, \theta)$ and propagation directions θ (the direction normal to the wave crest of each spectral component). Usually, wave models determine the evolution of the action density $N(\mathbf{x}, t; \sigma, \theta)$ in space \mathbf{x} and time t . The action density is defined as $N(\mathbf{x}, t; \sigma, \theta)$ and is preserved during propagation in the presence of ambient current, whereas the energy density E is not (Whitman, 1974).

It is assumed that the ambient current is uniform with respect to the vertical coordinate and is denoted as \mathbf{U} .

The evolution of the action density N is governed by the action balance equation, which reads (e.g., Mei, 1983; Komen et al., 1994):

$$\frac{\partial N}{\partial t} + \nabla_x [(\mathbf{c}_g + \mathbf{U})N] + \frac{\partial c_\sigma N}{\partial \sigma} + \frac{\partial c_\theta N}{\partial \theta} = \frac{S_{tot}}{\sigma} \quad (61)$$

The left-hand side of equation is the kinematic part and is made up to following terms:

- $\frac{\partial N}{\partial t}$ local variation of the action density in time
- $\nabla_x [(\mathbf{c}_g + \mathbf{U})N]$ propagation of wave energy in two-dimensional geographical space
- $\frac{\partial c_\sigma N}{\partial \sigma}$ effect of significant of the angular frequency due to variations in depth and mean current
- $\frac{\partial c_\theta N}{\partial \theta}$ depth induced and current induced refraction

The right-hand side contains S_{tot} which is the source/sink term that represents all physical process which generate, dissipate or redistribute wave energy.

In shallow water, six processes contribute to S_{tot} :

$$S_{tot} = S_{in} + S_{nl3} + S_{nl4} + S_{ds,w} + S_{ds,b} + S_{ds,br} \quad (62)$$

In which:

- S_{in} input by wind
- S_{nl3} non-linear wave-wave interaction (triplets)
- S_{nl4} non-linear wave-wave interaction (quadruplets)
- $S_{ds,w}$ dissipation of wave energy by white capping
- $S_{ds,b}$ dissipation of wave energy caused by the bottom friction
- $S_{ds,br}$ dissipation of wave energy caused by depth-induced wave breaking

Furthermore, the action density equation can be writing in Cartesian or spherical coordinates. For small scale applications the spectral action balance equation may be expressed in Cartesian coordinates as given by:

$$\frac{\partial N}{\partial t} + \frac{\partial c_x N}{\partial x} + \frac{\partial c_y N}{\partial y} + \frac{\partial c_\sigma N}{\partial \sigma} + \frac{\partial c_\theta N}{\partial \theta} = \frac{S_{tot}}{\sigma} \quad (61b)$$

4.1.2 Source and sinks

4.1.2.1 Input by wind

Transfer of wind energy to the waves is described with two possible mechanisms:

- resonance mechanism (Phillips,1957)
- feed-back mechanism (Miles, 1957)

The first mechanism considers the possibility that the pressure distribution induced by wind at the sea surface is random. It propagates more or less a frozen pattern over the surface with wind speed. This can be Fourier transformed to produce harmonic pressure waves that propagate with wind speed. If this harmonic pressure wave remains in phase with a free harmonic surface wave, then the wind energy is transferred from the pressure wave to the surface wave. The energy input by this mechanism, which contributes to the initial stages of wave growth, varies linearly with time. The above description is taken into consideration with the A term.

The second mechanism considers that when a wave has been generated by the resonance mechanism as explained above, it will distort the wind profile just above the water surface. This distortion results in an 'over pressure' on the wind ward side of the crest of the wave and an 'under pressure' at the lee side of the crest. It means that when the sea surface moves up and down, the pressure also follows the same movements, therefore transfer energy to the wave. This energy transfer is proportional to the energy in the wave itself, so the wave grows more as it gets larger. This effect is found to be exponential in time (term B).

Based on the two wave growth mechanisms, wave growth due to wind commonly described as the sum of linear and exponential growth term of a wave component:

$$S_{in} = A + BE(\sigma, \theta) \quad (63)$$

In which:

- $A = \frac{1.5 \cdot 10^{-3}}{2\pi g} \{U_* \max[0, \cos(\theta - \theta_w)]\}^4 H$ (Cavaliere e Malanotte-Rizzoli, 1981)
 - $H = \exp\left[-\left(\frac{\sigma}{\sigma_{PM}^*}\right)^{-4}\right]$ frequency filter to eliminate the wave growth at lower frequencies to the σ_{PM}^*
 - $\sigma_{PM}^* = \frac{0.13g}{28U_*} 2\pi$ frequency of Pearson-Moskowitz (introduced from elaboration of Tolman, 1992)
 - θ_w wind direction
- $B = \max\left[0; 0.25 \frac{\rho_a}{\rho_w} \left(28 \frac{U_*}{c_{ph}} \cos(\theta - \theta_w) - 1\right)\right] \sigma$ (Komen et al., 1984)
 - c_{ph} phase speed
- $B = \beta \frac{\rho_a}{\rho_w} \left(\frac{U_*}{c_{ph}}\right)^2 [\max(0; \cos(\theta - \theta_w))]^2 \sigma$ (Janssen, 1989,1991)

- β Miles constant

The two formulations proposed for the term B are obviously alternative and may both be used in SWAN model.

It should be noted that the SWAN model is driven by the wind speed at 10m elevation (U_{10}) whereas it uses the friction velocity ($U_* = \sqrt{\frac{\tau}{\rho}}$). For the WAM Cycle 3 formulation the transformation from (U_{10}) to (U_*) is obtained with:

$$U_*^2 = C_D U_{10}^2 \quad (64)$$

In which C_D is the drag coefficient which can be expressed by a polynomial expression of the second order such as the following

$$C_D(U_{10}) = (0.55 + 2.97 \tilde{U}^2 - 1.49 \tilde{U}^2) * 10^{-3} \quad (65)$$

In which

- $\tilde{U} = \frac{U_{10}}{U_{ref}}$
 - $U_{ref} = 31.5 \frac{m}{s}$ reference speed for which it has the maximum value of C_D

This expression well represents the trend of the coefficient in function of wind speed and was obtained by Zijlema et al. (2012). They have demonstrated that the coefficient of drag almost linearly increases with the wind speed up to about 20m/s, then has an approximately horizontal trend and finally decreases exceeded 35m/s speeds (Figure 35).

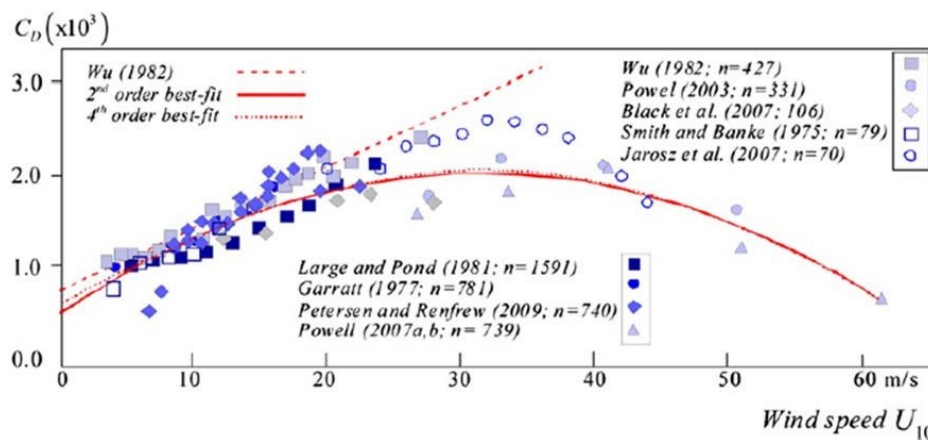


Figure 35 Observed values of the wind drag coefficient C_D from various studies and the weighted best-fit 2nd- and 4th-order polynomial (n is the number of independent data points per study).

4.1.2.2 Dissipation by white capping

The whitecapping is physically described as a superficial dissipation associated with partial wave breaking. The formulations used in SWAN to take into account the effects of this phenomenon are two:

- Komen et al. (1984);
- Van der Wasthuysen et al. (2007).

The Komen formulation is based on the pulse-based model of Hasselmann (1974).

Reformulated in terms of wave number to applicable in finite water depth, this expression is:

$$S_{ds,w}(\sigma, \theta) = -\Gamma \tilde{\sigma} \frac{k}{\tilde{k}} E(\sigma, \theta) \quad (66a)$$

Where:

- \tilde{k} mean wave number
- $\tilde{\sigma}$ mean wave frequency
- $\Gamma = C_{ds} \left((1 - \delta) + \delta \frac{k}{\tilde{k}} \right) \left(\frac{\tilde{s}}{\tilde{s}_{PM}} \right)^p$ factor that depends on the overall wave steepness and the formulation chosen to provide the wind input (Komen or Janssen).
It can be derived by solving the energy of the wave in fully developed sea conditions.
 - C_{ds}, δ, p tunable coefficient
 - $\tilde{s} = \tilde{k} \sqrt{E_{tot}}$ overall wave steepness
 - $\tilde{s}_{PM} = \sqrt{3.02 * 10^{-3}}$ value of \tilde{s} for the Pierson-Moskovitz spectrum (1964)

The values of the tunable coefficients C_{ds}, δ and p in this model have been obtained by closing the energy balance of the waves in idealized wave growth conditions (both for growing and fully developed wind seas) for deep water. This implies that coefficients in the steepness dependent coefficient Γ depend on the wind input formulation that is used. Since two different wind input formulations are used in the SWAN model, two sets of coefficients are used. For the wind input of Komen:

- $C_{ds} = 2.36 * 10^{-5}$
- $\delta = 0$
- $p = 4$

The formulation of Van der Wasthuysen et al. (2007) constitutes the so-called saturation-based model, which is an adapted form of the expression of Alves and Banner (2003). It is based on the apparent relationship between wave groups and white-capping dissipation. The latter considers the wave number and the average steepness of the waves described by the spectrum. This term is problematic in limited depth of the sea near the coast and then the adaptation is to neglect the average quantities abovementioned. The result is the following relationship:

$$S_{ds,w}(\sigma, \theta) = -C_{ds}' \left(\frac{B(k)}{B_r} \right)^{\frac{p}{2}} (\tanh(kd))^{2-\frac{p_0}{4}} \sqrt{gk} E(\sigma, \theta) \quad (66b)$$

In which

- $C_{ds}' = 5.0 * 10^{-5}$ proportionality coefficient
- $B(k)$ azimuthal-integrated spectral saturation
- $B_r = 1.75 * 10^{-3}$ threshold saturation level
- p_0 calibration parameter chosen to obtain the same frequency scale in terms of the white-capping and wind sources

Waves are taken to break when $B(k) > B_r$ (in this case the exponent $p = p_0$) while there is no wave breaking if $B(k) \leq B_r$. This distinction is made since the way of dissipation for white capping of breaking waves and unbroken waves are separated, i.e. are active in different parts of the spectrum. However, as the knowledge of the phenomenon is limited, the dissipation mechanism for the unbroken waves (low frequency) is not modelled in detail while, for the breaking waves it is treated with the formulation of Komen et al. described above. Finally, the input wind formulation used for this expression is the Yan formulation (1987).

4.1.2.3 Dissipation by bottom friction

In shallow water, the orbital motion of the water particles induced by surface waves extends to the seabed and this produces an interaction between the wave surface and the seabed. There are different types of interaction as reported by Shemdin et al. (1978):

- bottom friction;
- percolation;

- scattering on seabed irregularities;
- motion of a soft muddy seabed.

The first process is representative of a local redistribution of wave energy through the dispersion of wave components. The following three processes are dissipative, their magnitude depends on the seabed conditions. For shallow water, close to a mainland coast and in the presence of a sandy seabed, the predominant mechanism is bottom friction (Bertotti and Knights, 1994), which is generally expressed by the equation:

$$S_{ds,b} = -C_b \frac{\sigma^2}{g^2(\sin kd)^2} E(\sigma, \theta) \quad (67)$$

In which

- C_b bottom friction coefficient

This expression is representative of the various simulation models of the bottom friction that can be implemented in SWAN:

- empirical model of JONSWAP (Hasselmann et al., 1973);
- drag law model of Collins (1972);
- eddy-viscosity model of Madsen et al. (1988).

They are mainly distinguished by a different formulation of the C_b coefficient:

- Hasselman et al. (1974), found $C_b = C_{JON} = 0.038 \frac{m^2}{s^3}$ which is in agreement with the JONSWAP result for swell dissipation. Recently, in Zijlema et al. (2012) it was found that a unified value of $0.038 \frac{m^2}{s^3}$ can be used if the second order polynomial fit for wind drag is employed (see equation of C_D in 4.1.2.1 Input by wind). So, in SWAN 41.01 this is default irrespective of swell and wind-sea conditions.
- The expression of Collins is based on a conventional formulation for periodic waves with the appropriate parameters adapted to suit a random wave field. He suggests $C_b = 0.015gU_{rms}$ where U_{rms} is the root mean square (in m/s) of the orbital motions close to the seabed.

- Madsen et al. derived a formulation similar to that of Hasselmann and Collins (1968), but in their model the bottom friction factor is a function of the bottom roughness height and the actual wave conditions. Their bottom friction coefficient is given by:

$$C_b = f_w \frac{g}{\sqrt{2}} U_{rms} \text{ which } f_w \text{ is a non-dimensional friction factor.}$$

Considering the large variations in the nearshore seabed conditions (material, roughness length, ripple height, etc.), there is no field data evidence to give preference to a particular friction model (Luo and Monbaliu, 1994). For this reason, the simplest of each of these types of friction models has been implemented in SWAN: the empirical Joint North Sea Wave Project (JONSWAP) model of *Hasselmann et al (1973)* (with $C_{bottom} = 0.038 \frac{m^2}{s^3}$ for swell conditions and $C_{bottom} = 0.067 \frac{m^2}{s^3}$ for wind sea conditions), the drag law model of *Collins (1972)* (with $C_{bottom} = C_f g U_{rms}$ with bottom friction coefficient C_f , gravitational acceleration g , and rms wave-induced orbital velocity at the bottom U_{rms}), and the eddy-viscosity model of *Madsen et al. (1988)* (with $C_{bottom} = \frac{f_w g U_{rms}}{\sqrt{2}}$ and f_w taken from *Jonsson (1966,1980)* and *Jonsson and Carlsen (1976)*).

4.1.2.4 Dissipation by depth-induced wave breaking

When waves propagate from deep water to water of finite depth, shoaling leads to an increase in wave height. If the wave height to water depth ratio becomes too large the waves start to break and wave energy is rapidly dissipated by depth-induced wave breaking. In extreme shallow water (surf-zone), this process becomes dominant over all other processes.

The process of wave-breaking is still poorly understood, little is known about the spectral modelling (e.g., spectral distribution) of this process. In this study, the work of Battjes and Jansen (1978) is used. They proposed a bore-based model to calculate the total rate of energy dissipation of random breaking waves. Analysis of laboratory observations (e.g., Battjes and Beji, 1992; Vincent et al. 1994; Arcilla et al., 1994 and Eldeberky and Battje, 1996) has shown that the shape of initially uni-modal spectra propagating across simple (barred) beach profiles, is fairly insensitive to the presence of depth-induced breaking. This has led Eldeberky and Battjes (1996) to formulate a simple spectral version of the model of Battjes and Jansen (1978) in which the spectral dissipation rate is proportional to the energy density. Expanding their expression to include directions, the expression that is used in SWAN is:

$$S_{ds,br}(\sigma, \theta) = \frac{D_{tot}}{E_{tot}} E(\sigma, \theta) \quad (68)$$

In which:

- E_{tot} total wave energy density
- $D_{tot} = -\alpha_{BJ} Q_b \tilde{\sigma} \frac{H_{max}^2}{8\pi}$ mean rate of random wave energy dissipation pre unit horizontal area due to wave breaking according to Battjes and Janssen (1978)
 - $\alpha_{BJ} = 1$
 - Q_B fraction of breaking waves
 - $\tilde{\sigma}$ mean frequency
 - $H_{max} = \gamma h$ maximum individual wave height that can exist at the give depth (h)
 - γ breaker parameter usually $\gamma = 0.73$

An alternative to the bore-based model of Battjes and Janssen (1978) is proposed by Thornton and Guza (1983). This model can be regarded as an alteration of Battjes and Janssen (1978) with respect to the description of the wave height probability density function. Based on field observations, the wave heights in the surf zone are assumed to remain Rayleigh distributed, even after breaking. This implies that all waves will break, not only the highest as assumed by Battjes and Janssen (1978), so that:

$$D_{tot} = -\frac{3B^3\tilde{\sigma}}{32\sqrt{\pi}h} Q_b H_{max}^2 \quad (69)$$

where B is a proportionality coefficient, and marks the transition from wave breaking and non-breaking based on the Br value ($B_r = 1.75 * 10^{-3}$ threshold saturation level).

- $B > B_r$ breaking wave
- $B < B_r$ non-breaking wave

4.1.2.5 Non-linear wave-wave interaction (quadruplets)

The physical meaning of the interactions is that resonant sets of wave components exchange energy, redistributing energy over the spectrum. In deep and intermediate water, four-wave interactions (so-called quadruplets) are important, whereas in shallow water three-wave interactions (so-called triads) become important.

In deep water, quadruplet wave-wave interactions dominate the evolution of the spectrum. They transfer wave energy from the spectral peak to lower frequencies (thus moving the peak frequency to lower values) and to higher frequencies (where the energy is dissipated by whitecapping).

A full computation of the quadruplet wave-wave interactions is extremely time consuming and not convenient in an operational wave model. Nevertheless, SWAN has an option to compute the Boltzmann integral in an exact manner. The approach is the exact method developed by Webb, Tracy and Resio (WRT) (Resio et al., 2001). This algorithm was reprogrammed by Van Vledder, bearing the name XNL (Van Vledder and Bottema, 2003). This method is also enabled to capture the frequency shift and the spectral shape changes as water depth decreases.

To reduce the computational time, techniques have been developed based on parametric methods or on other types of approximations. One of these techniques is the Discrete Interaction Approximation (DIA) of Hasselmann et al. (1985).

Using the DIA, the term that appear in the balance equation can be expressed as:

$$S_{nl4}(\sigma, \theta) = S_{nl4}^*(\sigma, \theta) + S_{nl4}^{**}(\sigma, \theta) \quad (70)$$

In which:

- S_{nl4}^* refers to the first quadruplets
- S_{nl4}^{**} refers to the second quadruplets (the expression for S_{nl4}^{**} are identical to those for S_{nl4}^* for the mirror direction)

Finally, it is emphasized that as the nonlinear quadruplet wave-wave interactions at high frequencies are important, it is recommended to choose the maximum frequency of the wave model about six times the peak frequency of the spectra that are expected to occur in a wave model run.

4.1.2.6 Non-linear wave-wave interaction (triplets)

In very shallow water, triad wave-wave interactions transfer energy from lower frequencies to higher frequencies often resulting in higher harmonics (Beji and Battjes, 1993). Low-frequency energy generation by triad wave-wave interactions is not considered here.

To describe triad wave-wave interactions in terms of a spectral energy source term Eldeberky and Battjes (1995) transformed the amplitude part of the Boussinesq model of Madsen and Sørensen (1993) into an energy density formulation and parameterized the bi-phase of the waves on the basis of laboratory observations (Battjes and Beji, 1992; Arcilla et al., 1994). A discrete triad approximation (DTA) for co-linear waves was subsequently obtained by considering only the dominant self-self-interactions. The model appeared to be successful in describing the essential features of the energy transfer from the primary peak of the spectrum to the super harmonics. A slightly different version, the so-called Lumped Triad Approximation (LTA) was later derived by Eldeberky (1996). This LTA technique is employed in SWAN.

Using the LTA, the term that appears in the balance equation can be expressed as:

$$S_{nl3}(\sigma, \theta) = S_{nl3}^-(\sigma, \theta) + S_{nl3}^+(\sigma, \theta) \quad (71)$$

4.1.3 First- and second-generation model formulation in SWAN

The source term S_{tot} for the first- and second- generation formulation (relaxation model) of SWAN is (Holthuijsen and de Boer 1988)

$$S_{tot} = \begin{cases} S_{in} = A + BE & \text{if } E < E_{lim} \text{ and } |\theta - \theta_w| < \frac{\pi}{2} \\ S_{ds,w} = \frac{E_{lim} - E}{\tau} & \text{if } E > E_{lim} \text{ and } |\theta - \theta_w| < \frac{\pi}{2} \\ 0 & \text{if } E > E_{lim} \text{ and } |\theta - \theta_w| > \frac{\pi}{2} \end{cases} \quad (72)$$

Where:

- S_{in} input by wind
- $S_{ds,w}$ decay for over-developed sea states
- A linear growth term
- BE exponential growth term
- E spectral density
- E_{lim} saturated spectrum
- τ time scale
- θ discrete spectral wave direction
- θ_w wind direction

The distinction between first- and second-generation is only in the formulation of the saturated spectrum E_{lim} as outlined below.

4.1.3.1 Linear and exponential growth

The linear growth term A is given by an expression due to Cavaleri and Malanotte-Rizolli (1981) as adapted by Holthuijsen and de Boer (1988) and Holthuijsen et al. (1996):

$$A = \begin{cases} \frac{\beta_1 \pi}{2\pi g^2} C_{drag}^2 \left(\frac{\rho_a}{\rho_w}\right)^2 (U_{10} \max[0; \cos(\theta - \theta_w)])^4 & \sigma \geq 0.7\sigma_{PM,h} \\ 0 & \sigma < 0.7\sigma_{PM,h} \end{cases} \quad (73)$$

Where:

- β_1 a coefficient that has been tuned to be $\beta_1 = 188$
- C_{drag} a drag coefficient equal to $C_{drag} = 0.0012$
- $\sigma_{PM,h} = \frac{\sigma_{PM}}{\tanh(0.833 \bar{h}^{0.375})}$ the fully developed peak frequency including the effect of shallow water and is estimated from the depth dependent relation of the Shore Protection Manual (1973)
 - $\bar{h} = \frac{gh}{U_{10}^2}$ dimensionless depth
 - $\sigma_{PM} = \frac{0.13g}{U_{10}} 2\pi$ Pierson Moskowitz frequency

The exponential growth term BE is due to Snyder (1981) rescaled in terms of U_{10} as adapted by Holthuijsen and de Boer (1988) and Holthuijsen (1996):

$$B = \max \left[0; \beta_2 \frac{5}{2\pi} \frac{\rho_a}{\rho_w} \left(\frac{U_{10}}{\frac{\sigma}{k}} \cos(\theta - \theta_w) - \beta_3 \right) \right] \sigma \quad (74)$$

in which:

- $\beta_2 = 0.59$
- $\beta_3 = 0.12$

4.1.3.2 Decay

If spectral densities are larger than the wind-dependent saturation spectrum E_{lim} (e.g. when wind decreases), energy is dissipated with a relaxation model:

$$S_{ds,w}(\sigma, \theta) = \frac{E_{lim}(\sigma, \theta) - E(\sigma, \theta)}{\tau(\sigma)} \quad (75)$$

in which:

- $\tau(\sigma) = \beta_4 \left(\frac{2\pi}{\sigma}\right)^2 \frac{g}{U_{10} \cos(\theta - \theta_w)}$
 - $\beta_4 = 250$

4.1.3.3 Saturated spectrum

The saturated spectrum has been formulated in term of the wave number with a \cos^2 – directional distribution centered at the local wind direction θ_w . It is essentially an adapted Pierson-Moskowitz (1964) spectrum:

$$S_{tot} = \begin{cases} \frac{\alpha k^{-3}}{2c_g} \exp\left(-\frac{5}{4}\left(\frac{\sigma}{\sigma_{PM,h}}\right)^{-4}\right) \frac{2}{\pi} (\cos(\theta - \theta_w))^2 & \text{for } |\theta - \theta_w| < \frac{\pi}{2} \\ 0 & \text{for } |\theta - \theta_w| \geq \frac{\pi}{2} \end{cases} \quad (76)$$

For the first-generation formulation, the scale α is a constant; $\alpha = 0.0081$.

For the second-generation formulation, the scale factor α depends both on the total dimensionless wave energy $\tilde{E}_{tot,sea}$ of the wind sea part of the spectrum and on the dimensionless depth \tilde{h}

$$\alpha = \max\left[(0.0081 + (0.013 - 0.00819)e^{-\tilde{h}}); 0.0023 \tilde{E}_{tot,sea}^{-0.223}\right] \quad (77)$$

In which:

- $\tilde{E}_{tot,sea} = \frac{g^2 E_{tot,sea}}{U_{10}^4}$ total dimensionless wind sea wave energy
- $E_{tot,sea} = \int_{\theta_w - \pi/2}^{\theta_w + \pi/2} \int_{0.7 \sigma_{PM,h}}^{\infty} E(\sigma, \theta) d\sigma d\theta$

The maximum value of α is $\alpha = 0.155$. This dependency of α on the local dimensionless energy of the wind sea permits an overshoot in the wave spectrum under wave generation conditions. For deep water $\alpha = 0.0081$ as proposed by Pierson and Moskowitz (1964).

4.1.4 Boundary conditions

The boundary conditions in SWAN, both in the geographic space and the spectral space, are fully absorbing boundaries. The wave energy is set to leave the computational domain or cross a coastal line. For coastal regions the incoming wave energy is only provided along the deep-water boundary. The spectral densities are assumed to be zero along the lateral boundaries. To avoid the propagation of numerical errors into the computational domain, the lateral boundaries are placed sufficiently far away from the area of interest.

4.1.5 Numerical schemes

4.1.5.1 *The fraction step method*

In SWAN, the numerical solution of the propagation of waves in both geographic and spectral spaces was described with a large basic matrix that needs to be solved iteratively until some convergence criteria are met. The action balance equation in SWAN is solved by finite-difference scheme in all five dimensions. Time is discretized with a simple time-step for the propagation and source terms. The numerical propagation schemes for both geographic and spectral spaces in SWAN are implicit upwind schemes. Combining refraction, frequency shifting, and nonlinear source terms from this basic matrix leads to a complicated matrix solution, in which the matrix is decomposed into four sections, which are solved in one step. When refined grids are used on small-scale regions, the basic matrix becomes large and requires a large memory storage and computational time. An implicit approach in the multidimensional problem like SWAN requires solving multidimensional implicit equations. This rather formidable task can be circumvented by the application of the split method (Yanenko, 1971). Splitting the wave action balance equation into the geographic and spectral dimensions allows one to construct efficient numerical schemes with one-dimensional algorithms. The strong stability properties of the split method permit us to study the physical features of the equations, because the coefficients for diffusion may be changed over wide ranges without violating stability conditions.

$$\frac{\partial N}{\partial t} + \frac{\partial c_x N}{\partial x} + \frac{\partial c_y N}{\partial y} + \frac{\partial c_\sigma N}{\partial \sigma} + \frac{\partial c_\theta N}{\partial \theta} = \frac{S_{tot}}{\sigma} \quad (78)$$

This is split into three space equations using three fractional steps on one time-step Δt .

4.1.5.2 Wave propagation in frequency and directional space

The integration of the action balance equation has been implemented in SWAN with a finite-difference scheme in five dimensions (the time, the geographic space, and the spectral space). The implicit finite-difference technique is endowed in the model with certain desirable features such as stability and exact conservation. In regions where large gradients of the action density in the frequency space are present, the truncation errors may become as large as the solution and numerical oscillations may arise, resulting in the negative values of the action density. For SWAN, in each sweep step, such negative values are set to be zero to ensure that the frequency- integrated action density per spectral direction is conserved.

To improve the numerical stability the Flux-Corrected Transport (FCT) algorithm (Boris and Book, 1973) can be used.

The numerical scheme for the wave propagation in the directional space is an implicit scheme that is economical with unconditional stability. It allows a larger time-step in the computation than that for the explicit scheme in shallow water.

4.2 SWASH

The SWASH model (acronym of Simulation WAVE till SHore) introduced by Zijlema (2011) is a non-hydrostatic model governed by the non-linear shallow water equation with the addition of a vertical momentum equations and non-hydrostatic pressure in horizontal momentum equation. This recently released model is developed at the TU Delft University and an open source available in the source forge webpage is still in developing process. The current version is 5.01A. It provides a general basis for describing complex changes to rapidly varied flows and wave transformations in coastal waters.

The SWASH model uses an explicit, second order finite difference method for staggered grids whereby mass and momentum are strictly conserved at a discrete level. As a consequence, this simple and efficient scheme is able to track the actual location of incipient waves breaking. The momentum conservation enables the broken waves to propagate with a correct gradual change of a form and to resemble steady bores in a final stage. The energy dissipation due to the turbulence generated by wave breaking is modelled with the Prandtl mixing length hypothesis:

$$v_t = l_m^2 \sqrt{2 \left(\frac{\partial u}{\partial x}\right)^2 + 2 \left(\frac{\partial v}{\partial y}\right)^2 + \left(\frac{\partial u}{\partial y} + \frac{\partial v}{\partial x}\right)^2} \quad (79)$$

in which:

- v_t eddy viscosity
- l_m mixing length taken to be proportional to a typical wave height

With respect to the integration of the continuity and momentum equation, the second order leapfrog scheme (Hansen, 1956) is adopted, as it does not alter the wave amplitude while its numerical dispersion is favorable.

Moreover, for a proper representation of the interface of water and land, a simple approach is adopted that tracks the moving shoreline by ensuring non-negative water depths and using the upwind water depths in the momentum flux approximation.

For the time integration SWASH uses an explicit method (it can be run in implicit mode for 1D though), hence it may encounter stability problems. To avoid them, the Courant-Friedrichs-Lewy condition (CFL, more known as Courant number) must be satisfied. This condition is given by the following inequation in 2D domains (Nwogu & Demirbilek, 2001):

$$C_r = \Delta t \left(\sqrt{gh} + \sqrt{u^2 + v^2} \right) \sqrt{\frac{1}{\Delta x^2} + \frac{1}{\Delta y^2}} \leq 1 \quad (80)$$

Where:

- C_r Courant number
- Δt time discretization
- $\Delta x, \Delta y$ spatial discretization

SWASH accounts for this by introducing a dynamically time step control that doubles or halves Δt for each time step, depending on the number of Courant (80).

Another important feature of this model is that it can be run either in depth-averaged mode or multi-layered mode. In the latter mode the computational grid is divided into a fixed number of vertical layers. Thus, instead of increasing the frequency dispersion by increasing the order of derivatives of the dependent variables like Boussinesq-type models (e.g. BOUSS 2D), SWASH accounts for it by increasing the number of vertical

layers. This compact difference scheme receives good linear dispersion up to $kh = 7$ and $kh = 3$ with 2 equidistant layers at 1% error in phase velocity of standing and progressive waves, respectively (with k = wave number).

In addition, the current version of SWASH (5.01A) accounts for wind effects on wave transformation and the air pressure at sea surface is optionally included.

SWASH accounts for the following physical phenomena:

- wave propagation, frequency dispersion, shoaling, refraction and diffraction;
- depth-limited wave growth by wind;
- nonlinear wave-wave interactions (including surf beat and triads);
- wave breaking;
- wave run-up and run-down;
- moving shoreline;
- bottom friction;
- partial reflection and transmission;
- wave interaction with structures;
- wave-current interaction;
- wave-induced currents;
- vertical turbulent mixing;
- sub-grid turbulence;
- wave damping induced by aquatic vegetation;
- rapidly varied flows;
- tidal waves;
- bores and flood waves;
- wind driven flows;
- space varying wind and atmospheric pressure;
- density driven flows;
- transport of suspended load for (non)cohesive sediment;
- turbidity flows;
- transport of tracer.

4.2.1 Governing equations

The most general coordinate framework that can be used in SWASH is curved orthogonal, and the governing equations may in principle be written in terms of these coordinates. However, such a form is unnecessarily complicated for the present purpose of outlining the principles adopted. Instead, equations are introduced in terms of a Cartesian notation. To simplify the statements without introducing a significant loss of generality, attention is focused on the depth-averaged flow in a two-dimensional horizontal physical domain. The extension to the three-dimensional framework is elaborated in Zijlema and Stelling (2005, 2008). The formulae have the same form but slightly extended.

NSWE are hyperbolic equations that can be obtained from the Navier-Stokes equation for an incompressible and inviscid fluid with constant density and with a free surface. In these equations the pressure is divided into a hydrostatic and a non-hydrostatic part:

$$p = p_h + q \quad (81)$$

in which:

- $p_h = g(\eta - z)$ hydrostatic pressure
- $q = \rho g \eta K_p(z)$ non-hydrostatic pressure
 - $K_p(z) = \frac{\cosh(k(h+z))}{\cosh kh}$ from the linear theory

With these terms, the equations become the following:

- a. Mass conservation equation

$$\frac{\partial \eta}{\partial t} + \frac{\partial hu}{\partial x} + \frac{\partial hv}{\partial y} = 0 \quad (82)$$

- b. Momentum conservation equations (in primitive form):

$$\frac{\partial u}{\partial t} + u \frac{\partial u}{\partial x} + v \frac{\partial u}{\partial y} + g \frac{\partial \eta}{\partial x} + \frac{1}{h} \int_{-d}^{\eta} \frac{\partial q}{\partial x} dz + c_f \frac{u\sqrt{u^2 + v^2}}{h} = \frac{1}{h} \left(\frac{\partial h\tau_{xx}}{\partial x} + \frac{\partial h\tau_{xy}}{\partial y} \right) \quad (83a)$$

$$\frac{\partial v}{\partial t} + u \frac{\partial v}{\partial x} + v \frac{\partial v}{\partial y} + g \frac{\partial \eta}{\partial y} + \frac{1}{h} \int_{-d}^{\eta} \frac{\partial q}{\partial y} dz + c_f \frac{v\sqrt{u^2 + v^2}}{h} = \frac{1}{h} \left(\frac{\partial h\tau_{yx}}{\partial x} + \frac{\partial h\tau_{yy}}{\partial y} \right) \quad (83b)$$

where:

- t time;
- x and y horizontal axes located at the still water level;
- z axis pointing upwards;
- $\eta(x, y, t)$ surface elevation measured from the still water level;
- $d(x, y)$ still water depth or downward measured bottom level;
- $h = \eta + d$ total water depth;
- $u(x, y, t)$ depth-averaged flow velocity in x-direction;
- $v(x, y, t)$ depth-averaged flow velocity in y-direction;
- $q(x, y, z, t)$ non-hydrostatic pressure;
- ρ density;
- g gravitational acceleration;
- c_f dimensionless bottom friction coefficient;
- $\tau_{xx}, \tau_{xy}, \tau_{yx}, \tau_{yy}$ horizontal turbulent stress terms

According to Stelling and Zijlema (2003) the non-hydrostatic pressure q can be expressed as:

$$\int_{-d}^{\eta} \frac{\partial q}{\partial x} dz = \frac{1}{2} h \frac{\partial q_b}{\partial x} + \frac{1}{2} q_b \frac{\partial(\eta - d)}{\partial x} \quad (84)$$

where:

- q_b non-hydrostatic pressure at the bottom

Combinations of the Keller-box method (Lam and Simpson, 1976) and of the momentum equations for vertical velocities in the z-direction produce the following equation:

$$\frac{\partial w_s}{\partial t} = 2 \frac{q_b}{h} - \frac{\partial w_b}{\partial t} \quad (85)$$

in which:

- w_s vertical velocity at the free surface
- w_d vertical velocity at the bed level

Additionally, the vertical velocity w_d , can be obtained from the kinematic condition:

$$w_d = -u \frac{\partial d}{\partial x} - v \frac{\partial d}{\partial y} \quad (85b)$$

At the end, velocities can be expressed from the conservation of local mass as:

$$\frac{\partial u}{\partial x} + \frac{\partial v}{\partial y} + \frac{w_s - w_b}{h} = 0 \quad (86)$$

These equations are solved in time t and along directions x , y and z to determine the value of three unknowns, flow velocities u and v and the surface elevation η , at each layer.

In general, boundary conditions for SWASH are layer averaged velocities and surface elevation series. This boundary conditions are the following (Zijlema & Stelling 2008):

- Free surface with pressure $q(z = \eta) = 0$, as no wind is considered
- Bottom without bottom friction and with normal velocity imposed through the kinematic condition $w(z = d) = -u \frac{\partial d}{\partial x}$
- At the offshore boundary usually the water level is specified and $q = 0$ is assumed, as a consequence the wave enters as a shallow water wave. To avoid mismatches in the deep-water wave amplitude it is imposed the depth-average U .
- The shoreline motion in the swash zone can be simulated in a natural manner. for computational efficiency, the momentum equation is not solved, and the velocity u is set to zero if the water depth is below a threshold value, which is set in the start-up commands of the SWASH input file.

On the offshore side, an incident wave(s) can be imposed as uni- or multi-directional. For regular waves the parameters of height and period must be specified. Alternatively, a surface time series can be implemented. On the other hand, when the waves are irregular the user must choose between a spectrum or a time series as input data. Shapes of the spectrum can be either the usual (Jonswap, Pearson-Moskowitz), TMA (modified from the user) or given entirely from the user (1-D non-directional or 2-D directional wave spectrum). Additionally, a weakly reflective condition (u_b) which allows outgoing waves and avoid the reflection of incoming waves, is introduced (Blayo and Debreu, 2005).

$$u_b = \pm \sqrt{\frac{g}{h}} (2\eta_b - \eta) \quad (87)$$

On the other hand, the shoreline is regarded as moving, in order to take into consideration wave run-up and inundation. In addition, obstacles like structures and breakwaters are schematized by including their slopes and by means porosity layers. Structures are highly

reflective and because of that the Somerfield's radiation condition is implemented $\left(\frac{\partial u}{\partial t} + \sqrt{gh} \frac{\partial u}{\partial x} = 0\right)$, which allows reflective waves to cross the offshore boundary.

A lateral boundary is implemented in order to allow for the calculation of the above system of equations in the Open-Land (along-shore) boundary direction. For simplicity, it is better to take that as fully reflective. These assumptions suggest to locate reference gauges outside of the area of influence of the "lateral boundary".

Finally, in order to calculate the water surface elevation, the continuity equation is integrated over the water depth. Using the kinematic condition at the free surface ($w(z = \eta)$) this gives the free-surface equation:

$$w(z = \eta) = \frac{\partial \eta}{\partial t} + u \frac{\partial \eta}{\partial x} \quad (88)$$

$$\frac{\partial \eta}{\partial t} + \frac{\partial Q}{\partial x} = 0 \quad (89)$$

in which:

- $Q = \int_{-d}^{\eta} u \, dz$

With those equations, all the physics of interest are described and, thus, no approximations should be done nor added as source or sink terms, as it usually happens with phase-average models.

4.2.2 Physical parameters

4.2.2.1 Wind effects

The wind effect is usually meant for large-scale wind driven circulation, tides and storm surges. Inclusion of wind effects may also be beneficial to buoyancy driven flows in coastal seas, estuaries and lakes. However, this option may also be useful for applications concerning wind effects on wave transformation in coastal waters, ports and harbors.

In SWASH seven different wind drag formulation are available:

- Constant;
- Linear on wind speed;
- Charnock;

- Wu
- Garratt;
- Smith and Banke;
- Second order polynomial fit.

The Charnock drag formulation is based on an implicit relationship between the wind and the roughness, while the other formulations, those of Wu, Garratt and Smith and Banke, express a linear relationship between the drag and the wind speed.

As mentioned for SWAN, recent observations indicate that these linear parameterizations overestimate the drag coefficient at high wind speed ($U_{10} > 20 \frac{m}{s}$). Based on many authoritative studies it appears that the drag coefficient increases almost linearly with wind speed up to approximately $20 \frac{m}{s}$, then levels off and decreases again at about $35 \frac{m}{s}$ to rather low values at $60 \frac{m}{s}$ wind speed. The drag coefficient equation is the same that was shown before for SWAN:

$$C_D(U_{10}) = (0.55 + 2.97 \bar{U}^2 - 1.49 \bar{U}^2) * 10^{-3} \quad (90)$$

This drag value is lower than the value of Wu (1982) by 10% ÷ 30% for high wind speeds ($15 \frac{m}{s} \leq U_{10} \leq 30 \frac{m}{s}$) and over 30% for Hurricane wind speed ($U_{10} > 30 \frac{m}{s}$).

Usually, the wind stress depends on the drag and the wind speed at a height of $10m$, U_{10} . However, it might be obvious that the influence of wind stress will reduce if the water is flowing in the same direction and it will increase when the water flow and wind are in opposite directions. This may lead to a smaller wind setup on very shallow areas. Hence, the wind stress may be dependent on the wind velocity relative to the water, i.e. $U_{10} - u$, instead of the wind velocity as such. Here, u is either the depth-averaged flow velocity in the depth-averaged mode or the surface flow velocity in the multi-layered mode. Experiments have shown that the Eigen frequencies damp out much faster when this alternative is employed. The considered wind is at $10 m$ above the surface. However, it might be better to consider the wind at the surface in order to relate this wind to the flow velocity. A factor α ($0 < \alpha \leq 1$) is introduced that accounts for the difference between the wind velocity at $10 m$ height and the wind velocity at the surface, $U_s = \alpha U_{10}$. With the use of α in this formulation the influence of the flow velocity becomes even stronger. However, the exact value of α is yet

unknown; further research on this parameter is needed. Therefore, this parameter is optionally and should be used with care. Wave growth due to wind in shallow areas is included in the model. It is based on a parameterization of the momentum flux transferred from wind to surface waves like the well-known sheltering mechanism of Jeffreys (1925) as described in Chen et al. (J. Waterwy 2004). The wind stress is expressed by:

$$\tau_w = \rho_a C_d |U_{10} - u|(U_{10} - c) \quad (91)$$

Where:

- ρ_a air density
- c celerity

Hence, the wind velocity is taken relative to the wave celerity. The wind stress may vary over a wavelength with a larger wind drag on the wave crest than that in the trough (Chen et al., 2004). This effect is implemented in the model by applying the wind stress on the wave crest only.

4.2.2.2 Bottom friction

Regarding the bottom friction, for depth averaged calculations, four different bottom friction values are available:

- Constant;
- Chezy;
- Manning;
- Colebrook-White;
- Logarithmic wall law.

Note that the Colebrook-White friction value is compatible with the Nikuradse roughness height. Although they are associated with depth-averaged flow velocities, they may be applied in the multi-layered mode as well. However, some inaccuracies may occur in the vertical structure of the velocity, in particular when the depth-averaged velocity is zero. Alternatively, the logarithmic wall law may be applied. In this case, a distinction is made between smooth and rough beds. For rough beds, we must apply a Nikuradse roughness height. The friction formulations are usually derived for quasi-steady flow conditions (e.g. flow in a river). However, numerical experiments, made in the literature, have indicated that the Manning formula

provides a good representation of wave dynamics in the surf zone, and even better to that returned by other friction formulations. Therefore, the Manning coefficient is used:

$$C_f = 0.019 \frac{S}{m^{\frac{1}{3}}}$$

4.2.2.3 Depth-induced wave breaking

Neither Boussinesq-type wave models nor non-hydrostatic wave-flow models can be directly applied to details of breaking waves, since in both models essential processes such as overturning, air-entrainment and wave generated turbulence, are absent. But, if only the macro-scale effects of wave breaking are of interest, such as the effect on the statistics of wave heights, details of the breaking process can be ignored. By observing that both spilling and plunging breakers eventually evolve into a quasi-steady bore, where the entire front-face of the wave is turbulent, a breaking wave becomes analogous to a hydraulic jump. Consequently, its integral properties (rate of energy dissipation, jump height) are approximately captured by regarding the breaking wave as a discontinuity in the flow variables (free surface, velocities). Proper treatment of such a discontinuity in a non-hydrostatic model (conservation of mass and momentum) can therefore be used to determine the energy dissipation of waves in the surf zone.

Though a vertical coarse resolution (1 ÷ 3 layers) is enough to describe the wave physics outside the surf zone (e.g. refraction, shoaling, diffraction, nonlinear wave-wave interactions), dissipation due to wave breaking requires a disproportional high vertical resolution (~10 ÷ 20). A coarse resolution will result in an underestimation of the horizontal velocities near the wave crest, and thus an underestimation of the amplitude dispersion. This underestimation implies that at low vertical resolution the influence of the non-hydrostatic pressure gradient is overestimated. Consequently, the stabilizing dispersive effects (i.e. the non-hydrostatic pressures) postpone the transition into the characteristic saw-tooth shape and therefore also the onset of dissipation. By enforcing a hydrostatic pressure distribution at the front of a wave, we can locally reduce a non-hydrostatic wave-flow model to the nonlinear shallow water equations. The wave then rapidly transitions into the characteristic saw-tooth shape and, consistent with the high-resolution approach, dissipation is captured by ensuring momentum conservation over the resulting discontinuity. The subsequent dissipation is well described by assuming depth

uniform velocities and a hydrostatic pressure distribution. In fact, these assumptions often form the basis to derive dissipation formulations to account for depth-induced breaking in energy balance type models, e.g. Battjes and Janssen (1978) among many others. Hence, prescribing a hydrostatic pressure distribution in the model around the discontinuity should result in the correct bulk dissipation. There is no need to assume a hydrostatic pressure distribution if the vertical resolution is enough (i.e. 10 to 20 layers). However, imposing a hydrostatic distribution at low resolutions (1 ÷ 3 layers) will ensure that, due to the absence of dispersive effects, the front quickly transitions into a bore like shape. Hence, it can be used to initiate the onset of wave breaking, thus allowing for the use of low-vertical resolutions throughout the domain. In practice this means that once a grid point is at the front of a breaking wave, vertical accelerations are no longer resolved, and the non-hydrostatic pressure is set to zero. A grid point is therefore labeled for hydrostatic computation if the local surface steepness $\frac{\partial\eta}{\partial t}$ exceeds a predetermined value $\alpha \left(\frac{\partial\eta}{\partial t} > \alpha\sqrt{gh} \right)$. Once labeled, a point only becomes non-hydrostatic again if the crest of the wave has passed. This is assumed to occur when $\frac{\partial\eta}{\partial t} < 0$.

To represent persistence of wave breaking, the alfa parameter is substituted to beta ($\alpha < \beta$), if a neighbouring grid point (in x- or y-direction) has been labelled for hydrostatic computation. In this case a point is thus also labelled for hydrostatic computation if $\frac{\partial\eta}{\partial t} > \beta\sqrt{gh}$. In all other grid points, the computations are non-hydrostatic. Based on calibration, the default value for the maximum steepness parameter $\alpha = 0.6$, while the persistence parameter $\beta = 0.3$.

4.2.2.4 Horizontal and vertical turbulent mixing

Three different horizontal eddy viscosity models are available:

- Constant viscosity
- Smagorinsky model
- Prandtl mixing length hypothesis

Vertical mixing can be modelled by using the standard $k - \varepsilon$ model, with k the turbulent kinetic energy per unit mass and ε the dissipation rate of turbulent kinetic energy per unit mass (Launder and Spalding, 1974).

In case of lateral mixing of momentum, e.g. around the tips of breakwaters and dams, it is recommended to employ the well-know Smagorinsky sub-grid model in which the mixing length is assumed to be proportional to the typical grid spacing. The default value of Smagorinsky constant is 0.2. The standard $k - \varepsilon$ turbulence model is applied if the goal is finding the vertical flow structure, in order to consider the vertical mixing. For stability reason, a background viscosity of $0.0001 \frac{m^2}{s}$ is recommended.

4.2.3 Numerical implementation

4.2.3.1 Basic principles

The basic principles of the finite difference method used in SWASH, as well as the underlying rationale for staggering locations pertaining to mass conservation and velocity components are pursued here. For the sake of clarity these principles are elucidated by means of one-dimensional, depth-averaged shallow water equations in non-conservative form, as follows:

$$\frac{\partial \eta}{\partial t} + \frac{\partial hu}{\partial x} = 0 \quad (92)$$

$$\frac{\partial u}{\partial t} + u \frac{\partial u}{\partial x} + g \frac{\partial \eta}{\partial x} + \frac{1}{2} \frac{\partial q_b}{\partial x} + \frac{1}{2} \frac{q_b}{h} \frac{\partial (\eta - d)}{\partial x} + c_f \frac{u|u|}{h} = \frac{1}{h} \frac{\partial}{\partial x} \left(h \tau_{xx} \frac{\partial u}{\partial x} \right) \quad (93)$$

$$\frac{\partial w_s}{\partial t} = 2 \frac{q_b}{h} - \frac{\partial w_b}{\partial t} \quad w_b = -u \frac{\partial d}{\partial x} \quad (94)$$

4.2.3.2 Duration of simulation

For simplicity, a 1D regular grid $\{x_{i+1/2} | x_{i+1/2} = i\Delta x; i = 0, \dots, I\}$ is analyzed. With I the number of grid cells and Δx the length of the grid cell. The location of the cell center is given by $x_i = \frac{x_{i-\frac{1}{2}} + x_{i+\frac{1}{2}}}{2}$. A staggered grid convention is used in which the velocity component u and surface elevation η are located at $i + \frac{1}{2}$ and i respectively. The staggered grid avoids decoupling of the unknowns, which otherwise may cause non-physical oscillations in non-staggered grids. The variables $d, q_b, v_t, w_b,$ and w_c are all located at i . Therefore, the water depth h is given in point i .

For the time integration the explicit leapfrog scheme in conjunction with a second order explicit time step for advection, a first order explicit time step for the viscosity term and a first order implicit time step for the non-hydrostatic part is used. This scheme as proposed

by Hansen (1956) employs staggering in time. The velocity u is evaluated at a half time step $(n + \frac{1}{2})\Delta t$, whereas the surface elevation at a whole time step $(n + 1)\Delta t$, with Δt the time step and n indicating the time level $t^n = n \Delta t$. This variant of the leapfrog scheme shares with the classical leapfrog scheme the advantages of second order accuracy in time and no wave damping. In addition, it requires less storage and makes the algorithm easy to implement.

There remains the question of how to determine the non-hydrostatic pressure q_b . Since this pressure is governed, indirectly, by the local continuity equation, attention must focus on this equation and its linkage to the momentum equations. The second-order method given in Van Kan (1986) is employed. This is based on combining the discretized forms of the continuity and momentum equations to give a Poisson equation, linking the non-hydrostatic pressure correction at a grid point to its next. Therefore, local mass conservation is enforced. This technique is extensively outlined in Zijlema and Stelling (2005). It is possible to use either SIP (Stone, 1968), in the case of depth-averaged mode, or BiCGSTAB (Van der Vorst, 1992) preconditioned with an ILU, in the case of multi-layered mode, for the solution of the Poisson equation. Further details on this subject can be found in Zijlema and Stelling (2005).

4.2.3.3 Time step

It is recommended to consider both the spin up time and the duration of the time series at the wave-maker boundary. In this way a steady-state condition will be obtained. We assume that the spin up time takes at most 10 to 15% of the total time of the simulation. For a suitable simulation time at least 500 to 1000 waves are needed.

The time integration is of explicit type and thus requires strict conformity of stability criteria for a stable solution. The well-known CFL condition for 1D problems is given by:

$$C_r = \frac{\Delta t(\sqrt{gd} + |u|)}{\Delta x} \leq 1$$

in which:

- C_r Courant number;
- u flow velocity;
- Δx mesh width;

- Δt time step;

For a 2D problem, the Courant number constrain becomes:

$$C_r = \frac{\Delta t(\sqrt{gd} + \sqrt{u^2 + v^2})}{\Delta x^2 + \Delta y^2} \leq 1$$

The actual maximum of the Courant number over all wet grid points is determined. The time step is halved when this number becomes larger than a pre-set constant $C_{r,max} < 1$, and the time step is doubled when this number is smaller than another constant $C_{r,min}$, which is small enough to be sure the time can be doubled. Usually, $C_{r,min}$ is set to $0.1 \div 0.2$, while the $C_{r,max}$ is specified in the range of $0.5 \div 0.8$.

It is advised not to choose a value higher than 0.8 since nonlinear processes, e.g. wave breaking and wave-wave interactions, can affect the stability condition. For high, nonlinear waves, or wave interaction with structures with steep slopes (e.g. jetties, quays), a Courant number of 0.5 is advised.

4.2.3.4 Vertical pressure gradient

Space discretization of the governing equations is carried out in a finite volume/finite difference fashion. A staggered grid arrangement is used in which the velocity components and water level are located at the center of the cell faces. Concerning the non-hydrostatic pressure, two layouts to assign this unknown to grid points are employed. This variable can be given either at the cell center or at the layer interface. The former is called the standard layout, while the latter one is called the box layout (Figure 35).

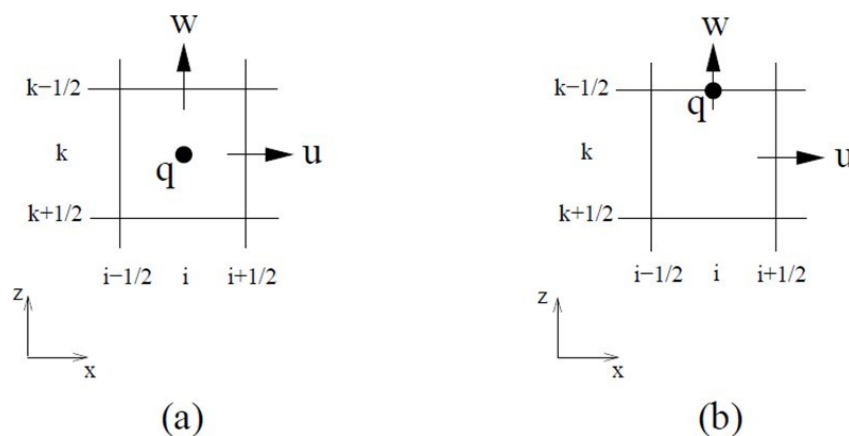


Figure 36 Applied arrangements of unknowns in a staggered grid: (a) standard layout, (b) box layout

The choice depends on the discretization of the vertical pressure gradient, namely, explicit central differences referring as the classical case and the implicit Keller-box or compact scheme, respectively. This compact scheme allows for a straightforward implementation of the zero-pressure boundary condition at the free surface without the need for special attention at interior points near that surface. Moreover, the discretization error is four to six times smaller than the error of classical central differences of the same order and involving the same number of vertical grid points. Hence, use of the compact scheme allows a very few numbers of vertical grid points with relatively low numerical dispersion and dissipation, thereby enhancing the accuracy of the frequency dispersion for relative short waves up to an acceptable level.

At very low vertical resolution (one or two layers), the Keller-box scheme gives good dispersive properties. At high vertical resolutions, however, the standard layout is preferable because it appears to be more robust while its dispersion characteristics are usually sufficiently accurate. To summarize, for wave simulations with 5 layers or less, the Keller-box scheme using the box layout is recommended, while for simulations with typically 10 ÷ 20 layers, the classical central differencing employing the standard layout is preferred (command `NONHYDrostatic STANDard|BOX`). Related to this choice, it might be useful to specify the preconditioner for solving the Poisson pressure equation. Two options are available: ILU and ILUD. For a robust solution, the ILU preconditioner is preferred. This choice might be a good one for applications where high and short waves are involved, or irregular beds with steep slopes (e.g. weir, breakwater, quay, jetty), or when relatively large number of layers (> 30) are involved. On the other hand, the ILUD preconditioner is a better choice to get an efficient solution (e.g. parallel computing) (command `NONHYDrostatic...PREConditioner ILUD|ILU`).

4.2.3.5 Momentum conservation

For simulation of breaking waves, hydraulic jumps and bores, momentum must be conserved. Preference should then be given to a numerical method that conserves momentum, which ensures that the wave properties under breaking waves are modelled correctly. This is set with the command `DISCRET UPW MOM`.

4.2.3.6 Discretization of advective terms in the momentum equations

The program makes a distinction between horizontal and vertical advection terms of the momentum equations. Moreover, it considers the momentum equations separately, the *u-momentum* equation and the *w-momentum* equation. Note that the *v-momentum* equation will be treated as the *u-momentum* equation in the same way. So, there are four different commands:

- DISCRET UPW UMOM H;
- DISCRET UPW WMOM H;
- DISCRET UPW UMOM V;
- DISCRET UPW WMOM V;

For the **horizontal advection** terms of ***u-momentum equation***, the terms considered are:

$$u \frac{\partial u}{\partial x} \text{ and } v \frac{\partial u}{\partial y} \quad (95)$$

There are many schemes to approximate these terms. Some of these schemes are accurate but are prone to generate wiggles – typically central schemes. Other schemes generate a certain amount of numerical diffusion and thus may affect the wave amplitude or wave energy of particularly short waves – typically upwind schemes. Higher order upwind schemes still generate small wiggles. If this is not desired, a flux-limiting scheme may be employed instead. Upwind schemes are known to be more stable than central schemes.

The default scheme for the considered terms is the well-known second order BDF scheme. For many applications this is a good choice. However, in some cases central differences (CDS) is preferred. This is especially the case when the higher harmonics are involved or when wave breaking is present.

Note that when the command BREAK is employed, SWASH will automatically apply central differences to the horizontal advection terms. If, for some reason, SWASH becomes unstable, possibly due to the growth of wiggles, the user is then advised to use the BDF scheme.

For the **horizontal advection** terms of ***w-momentum equation***, the terms considered are:

$$u \frac{\partial w}{\partial x} \text{ and } v \frac{\partial w}{\partial y} \quad (96)$$

These terms are usually ignored. However, they will be automatically taken into account in the simulation of:

- Applications where vertical flow structures are present;
- Applications when wave breaking is important;

If they are included, then the second order BDF scheme will be employed. Sometimes, central differences may be preferred, for instance, when the higher harmonics are involved.

For the **vertical advection** terms of ***u-momentum equation***, the term considered is:

$$w \frac{\partial u}{\partial z}$$

This term is only included in the computation when more than one layer is chosen ($K > 1$).

For the **vertical advection** terms of ***w-momentum equation***, the term considered is:

$$w \frac{\partial w}{\partial z}$$

and is usually ignored (even when $K > 1$). It will be included automatically if:

- The vertical flow structure is present;
- The vertical hyperbolic cosine profile for orbital velocities at the boundary is imposed;

This term is by default approximated with the first order upwind scheme.

4.2.3.7 *Moving shorelines*

For the calculation of wave run-up and run-down on the beach, use of a moving boundary condition is required. The method used in SWASH to track the moving shoreline amounts to ensure non-negative water depths. For a one-dimensionless case, one can show that if:

$$\frac{|u|\Delta t}{\Delta x} \leq 1$$

If a first order upwind scheme is applied to the global continuity equation, we shall have non-negative water depths at every time step; see Stelling and Duijnmeijer (2003) for a proof. Hence, flooding never happens faster than one grid size per time step, which is physically correct. This implies that the calculation of the dry areas does not need any special feature.

For this reason, no complicated drying and flooding procedures are required. Additionally, the shoreline motion in the swash zone can be simulated in a natural manner.

For computational efficiency, the model equations are not solved, and the velocities are set to zero when the water depth is below a threshold value (command SET DEPMIN). Its default value is 0.05 mm. However, a higher threshold value may be chosen for scaling reasons. For instance, at the scale of a field site, a value of 1 mm is an appropriate choice. This will also relax the time step to some extent in case of explicit time stepping. For a large-scale ocean simulation, a threshold value of 1 cm is probably more effective than 0.05 mm. Be careful when choosing a too high value as this may negatively influence mass conservation.

For some two-dimensional cases, however, ensuring non-negative water depths might lead to a time step restriction that appears to be more restrictive than the usual CFL condition. An example is the case where locally all velocities are directed outward of a grid cell. Nevertheless, such a case is rarely encountered and usually the time step is restricted by the Courant number based on the stability criterion.

4.2.4 Parallelization strategy

The scale of the typical two-dimensional applications dictates that the serial code of SWASH must be implemented for parallel computers, since the run time on a present-day single processor is frequently used to overcome such a limit. The conventional methodology for parallelization on distributed computer system is domain decomposition, which not only benefits from carrying out the task simultaneously on many processors but also enables using a large amount of memory. It gives efficient parallel algorithms and is easy to program within message passing environment (e.g. MPI).

A strip-wise grid partitioning is employed. It is based upon a partition of the whole computational domain into several strips, along the x- or y-axis, with each of them being assigned to a different processor. However, in the context of SWASH applications to a coastal area, some difficulties arise. Firstly, wet and dry grid points may unequally distribute over subdomains while no computations must be done in dry grid points. And second, a load imbalance may arise during the simulation due to the flooding and drying e.g. by swash motions. In such cases, one may decide to repartition such that they are balanced again. For the time being, however, is possible to restrict ourselves to balanced, static grid partitions.

Each subdomain can have multiple neighbors on each of its sides. For this, a data structure is implemented to store all the information about the relationship of the subdomain and its neighbors. Next each subdomain, look at in isolation, is surrounded by an auxiliary layer of three grid points width originating from neighboring subdomains. This layer is used to store the so-called halo data from neighboring partition that is needed for the solution within the subdomain in question. Since, each processor needs data that reside in other neighboring subdomains, exchange of data across subdomains is necessary. Moreover, to evaluate the stopping criterion of the iterative solution methods for pressure correction (SIP, preconditioned BiCGSTAB), global communication is required as well. These message passing are implemented by a high-level communication library MPI. Only simple point-to-point and collective communications have been employed.

4.2.5 Porous structure

In nearshore domains one of the most important features that can be found are porous structures such as groins, mound breakwaters, submerged structures or even quay walls. All those structures have an effect on the wave propagation. They can reflect the energy, transmit it or dissipate it even though most of the times the result is a combination of these three effects. Previous models such as SWAN accounted for those structures simply inputting a reflection and transmission coefficients that could be frequency dependent.

The reason for it is that as they worked in the frequency domain by solving the wave action equations it was straightforward to transmit energy or reflect it in that way. This approach has some important lacks as in reality the frequency is not the only factor that determines how much energy is transmitted/reflected. Other parameters such as wave height, porosity, size of the porous elements or even wave direction play important roles when determining these coefficients.

However, SWASH, as it works with the water surface elevation and the flow velocities has a totally different approach to account for the porous structures as will be explained in the following sections.

4.2.5.1 Background on porous structure

This section provides an overview of the actual state of the art when it comes to porous structure treatment.

First of all, the filter velocity is defined. It is the actual pore velocity averaged over the pores:

$$u_f = nu = \frac{V_p}{V_t}u$$

In which:

- V_p volumes of pores;
- V_t total volume;
- u flow velocity;
- $n = \frac{V_p}{V_t}$ porosity.

Using this filter velocity, Forcheimer is a Darcy equation modified by adding a quadratic term (Mellink 2012):

$$I = \alpha u_f + \beta u_f |u_f| \quad (97)$$

in which:

- I hydraulic gradient;
- α laminar coefficient;
- β turbulent coefficient;

The linear term is associated to the laminar flow while the non-linear term (quadratic-term) corresponds to the turbulent part of the flow.

Deriving the Forcheimer formula from the Navier Stokes Equation the following relation can be found

$$I = \alpha \frac{(1-n)^2}{n^3} \frac{v}{gd_{n50}} u_f + \beta \frac{1-n}{n^3} \frac{1}{gd_{n50}} u_f^2 \quad (98a)$$

in which:

- d_{n50} nominal diameter of the through to 50%.

The constants α and β must be experimentally determined and are only applicable for a specific flow regime.

If the flow is non-stationary an additional coefficient should be added to account for the effect of inertia (Polubarinova-Kocina 1962). This yields the next relation:

$$I = \alpha u_f + \beta u_f^2 + \gamma \frac{\partial u_f}{\partial t} \quad (98b)$$

Nevertheless, Van Gent (1992) concluded that the parameters of the stationary formula are not equal for the non-stationary equation. He split the β term in a stationary and non-stationary term β_{NS} which he related to the KC number.

Where:

- $KC = \frac{U_{max} T_p}{n d_{n50}}$;
- U_{max} maximum wave velocity;
- T_p peak period.

The Keulegan-Carpenter (KC) number determines how stationary is the flow and represents the magnitude of the convective acceleration term over the local acceleration term (Mellink 20012). When it comes to the inertia term, very little is known and there are several formulations for it. On the one hand, Bucharth and Andersen (1995) derived the following equation:

$$\gamma = \frac{1 + C_m \frac{1-n}{n}}{g} \quad (99a)$$

with

- $C_m = 1.5 + 12 (1 - n)$

It is important to mention that this relationship was obtained from a limited amount of experiments.

An alternative formulation was derived by Van Gent (1992)

$$\gamma = \frac{1 + c \frac{1-n}{n}}{ng} \quad (99b)$$

However, as Mellink (2012) explains, the inertia term when compared to the laminar and the turbulent terms is almost negligible. Thus, it is usually not taken into account. For further details in the different theoretical formulations for porous flow the reader is referred to Mellink (2012) who gives a detailed overview on all the formulations.

4.2.5.2 Porosity in SWASH

The porosity is accounted in SWASH by including the Forcheimer relation in the porous momentum equation by means of two extra terms f_l and f_t . Each grid cell has a porosity that goes from $n=0$ (impervious layer e.g. a wall) to $n=1$ (pure water).

The governing momentum equation is then:

$$\frac{1}{n} \frac{\partial u}{\partial t} + \frac{1}{n^2} \frac{\partial u^2}{\partial x} + \dots + f_l u + f_t u|u| = 0 \quad (100)$$

in which:

- $f_l = \alpha_E \frac{(1-n)^3}{n^2} \frac{v}{d^2}$;
- $f_t = \beta \frac{(1-n)}{n^2} \frac{v}{d}$;

The porosity should never be 0 as it could create problems as n appears in the denominator of the Forcheimer terms. Therefore, it is suggested to simulate impervious layers with a value of n equal to 0.01.

It is important to point out that the laminar coefficient is not exactly the one explained before. The following correction must be made:

$$\alpha = \alpha_E n (1 - n) \quad (101)$$

The default values in SWASH for those coefficients are $\alpha_0 = 1000$ and $\beta_0 = 2.8$

However, as Mellink (2012) concludes, these coefficients should be calibrated if enough information is known provided that according to his study SWASH tends to underestimate reflection while it overestimates transmission. Nonetheless, in this thesis as the amount of information is limited and not accurate enough, these coefficients will not be modified.

In conclusion the mechanism that SWASH used to account for the porosity is the inclusion of two additional dissipative terms in the momentum equation. These terms are dependent upon the following characteristics:

- Porosity (imputed in SWASH)
- Grain size (imputed in SWASH)

- Flow velocity (this depends on many other wave factors such as the period, wavelength, amplitude or water depth)

Furthermore, nowadays in SWASH the porous layers can only be defined in the x and y directions, this means without variation in depth for same location. Besides, only a single value of the α and β coefficients for all the grid points can be imputed.

Chapter 5 – Case study

5.1 Real case study description

5.1.1. Introduction

This thesis has the aim of study the scouring phenomena that occurred on project carried out by Saipem S.p.A. This project is located on the Egyptian coast between Mina Dumyat (Damietta in the map) and Port Said belonging to the complex of the Nile River delta.

The project consists in the construction of a temporary coastal structure, which served to build the shore approach of a pipeline from an offshore field. This structure had the function of creating a channel, at the end of which there was a gate, which protected the area where the pipeline installation works were carried out.

The cofferdam was composed of steel sheet piles with a vertical interlocking system that created a continuous wall. There are numerous formats of steel sheet pile on market, the ones of this case are made up of Z-shaped sheet piles, this name derived from the fact that the single piles are shaped roughly like a horizontally stretched Z. The interlocks are located as far as possible from the neutral axis to ensure good shear transmission and to increase the strength-to-weight ratio. Z piles are the most common type of sheet pile in North America and can be used in a wide variety of applications; retaining walls, cofferdams, parking garages, environmental barrier walls and bulkhead walls for ports are just a few of their varied uses (Figure 39).

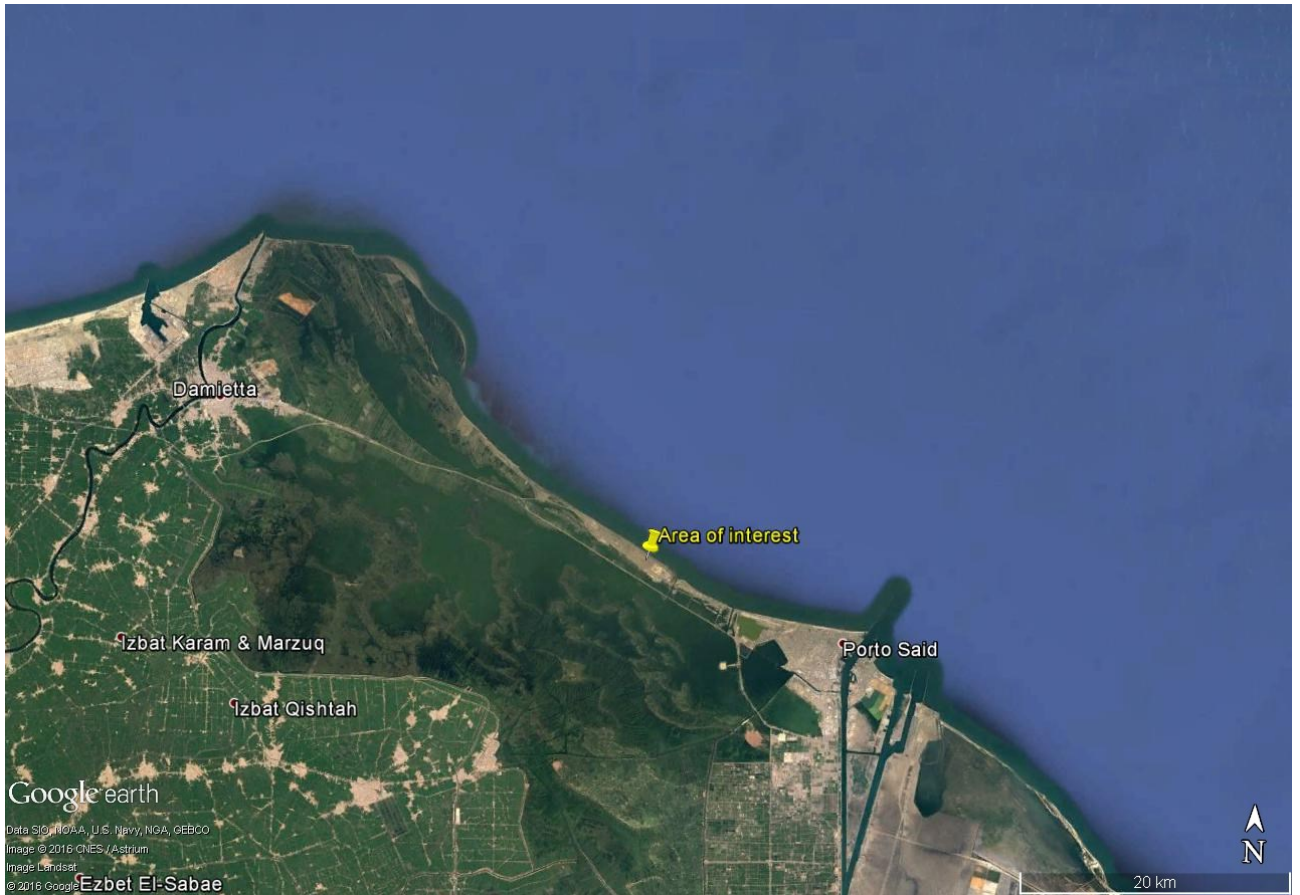


Figure 37 Location of the area of interest

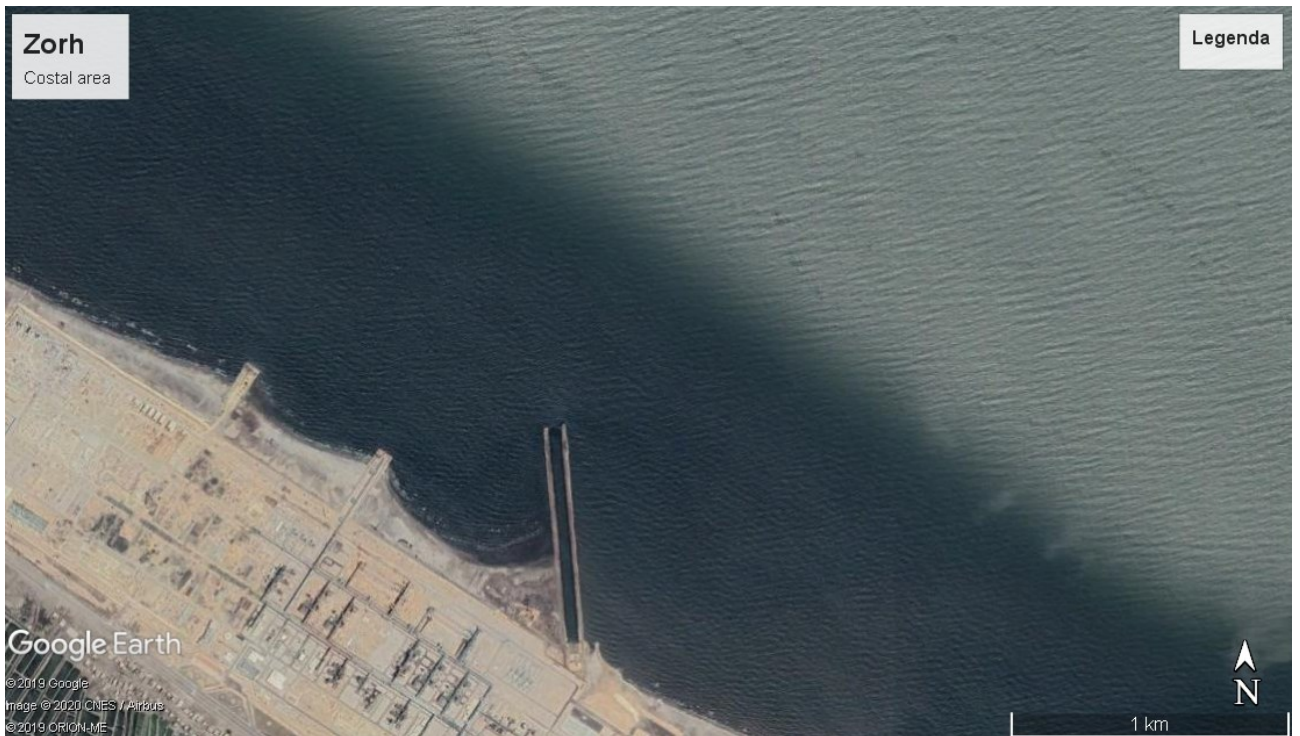


Figure 38 Overview of the analysed coastal area

the highest values of erosion occurred at the edges of the structure, especially in the right corner.

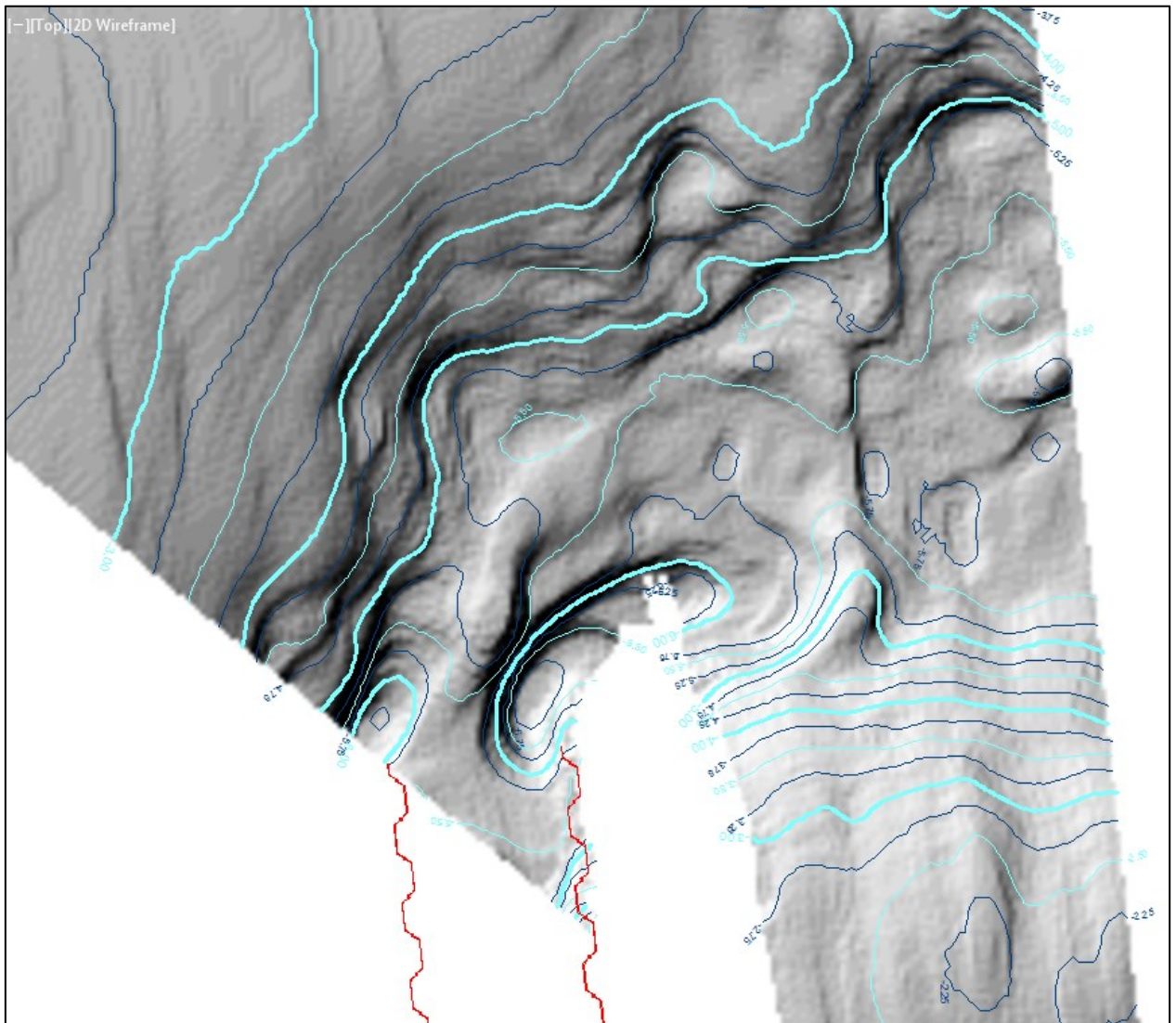


Figure 41 Shaded Relief – Post cofferdam construction

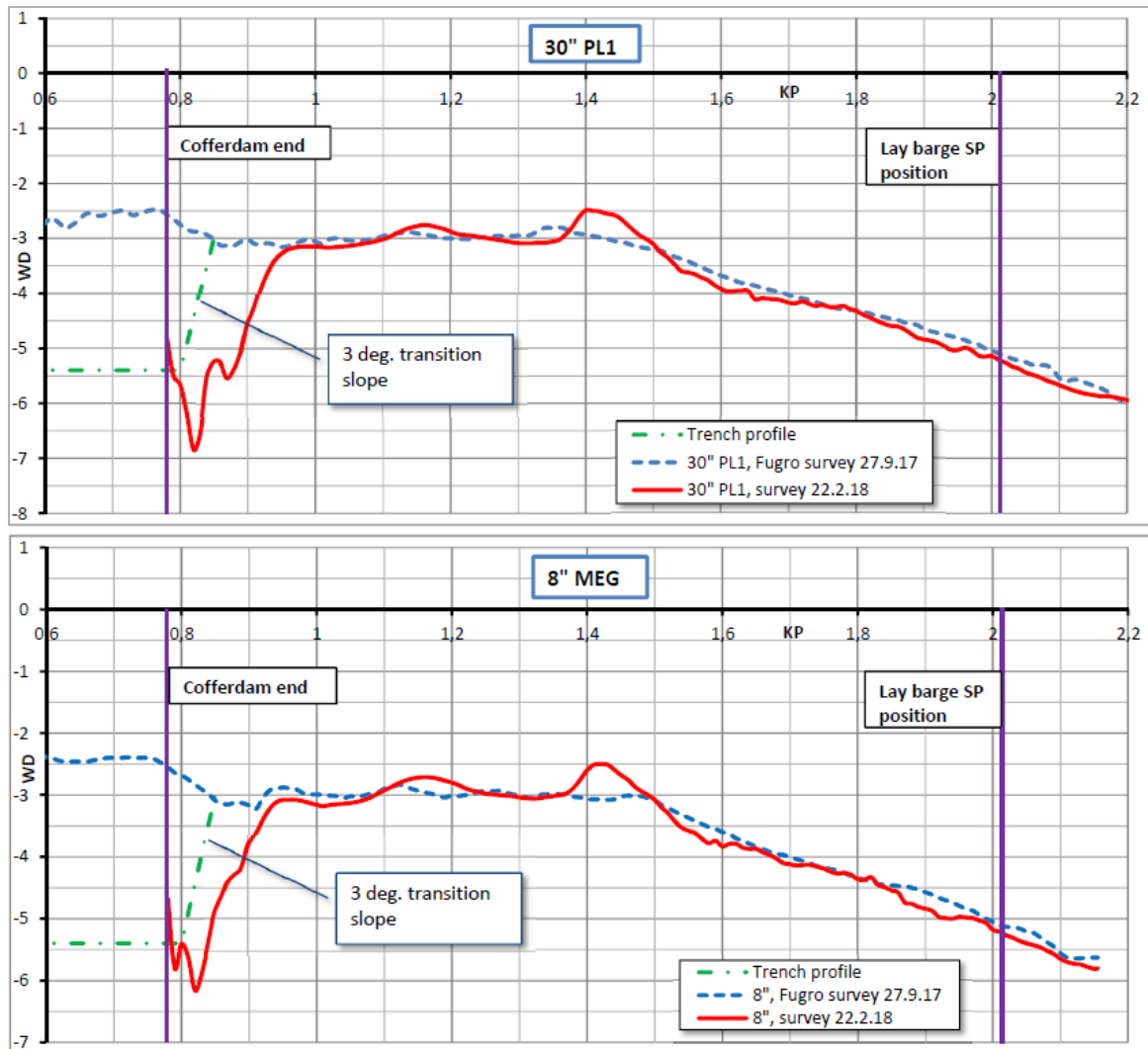


Figure 42 Shows the evolution of bottom profile at the edges of the cofferdam up to the wide – KP 0 at shoreline,

As explained in the chapter on scouring, any structure founded on the seafloor can experience scour at the downstream side. Scour is considerably enhanced, if tide-, wind- and wave-induced longshore currents with velocities exceeding the threshold limits for sediment motion are present. The maximum scour depth with respect to the initial water depth and the extension of the scour depend on the type and size of the structure, the grain size distribution of sediment, the wave and current characteristics.

5.1.3 Methodology

The methodological scheme adopted in the thesis work is:

1. Analysis of available data (waves, wind, bathymetry); the choice fell on three strongest storms that occurred in the area of the Egyptian coast, as available from approx. 34-year offshore hindcasting.
2. SWAN analysis; the goal of the SWAN analysis was to find the sea state in the surf zone (which will be used as boundary conditions for SWASH analysis) starting from the deep-water conditions (several kilometers far from the coastline and the interested area).
3. SWASH analysis, probably the core of this thesis, SWASH analysis. The aim of the SWASH analysis was to find the principal parameters needed to calculate the shear stresses produced (current velocity and oscillatory wave velocity).
4. Post processing of SWASH output, to calculate the shear stress produced.

5.2 Available data

The data used during this work mainly concern two physical properties:

5.2.1 Wind and waves

5.2.2 Bathymetry

5.2.1 Wind and waves

As regards the waves, there are three sources of data:

- Measured data from buoy and wave gauge
- Daily Progress Reports of the shorepull activity (DPR)
- Hindcast model data of wind and wave conditions

5.2.1.1 Wind and Waves – Measured data

5.2.1.1.1 Wave measured data

Between February 1999 and February 2000 Fugro Global Environmental & Ocean Sciences (Fugro GEOS) have undertaken a year-long programme of met-ocean measurements around the Offshore Nile Delta Field. The aim of the survey was to collect current, wave, meteorological, water temperature and salinity data for modelling and design purposes. The wave conditions were measured in two sites at geographical positions respectively, H1 and H2 (in green in Figure 44).

Waves were measured with a Datwell Directional Waverider buoy (DWR) at 133m water depth (H1) and with a Valeport 730 pressure transducer at H2 (8m of depth), respectively. The characteristics of the sensor at H2 precluded the measurement of the wave direction and consequently only H_{m0} , T_p and T_z were recorded. A processor inside the buoy at H1 calculated the directional wave spectrum every half-hour and recorded it internally. The internal data storage was downloaded at service visits to recover a complete data set for processing aims. From the directional spectra, wave height, period, direction and associated parameters were determined. The mooring configuration of the Waverider and the Valeport 730 omnidirectional wave gauge are shown in Figure 43. The Waverider position was monitored from the organization office via satellite link.

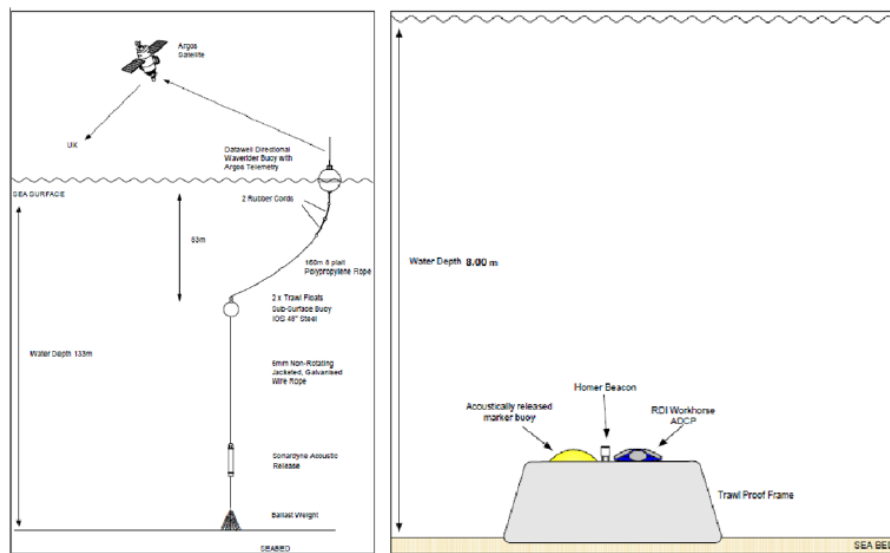


Figure 43 Buoy and gauge devices

The data at H2 are not suitable as boundary for SWAN simulation because the wave direction is missing. Anyway, these data are used for the model calibration.

5.2.1.1.2 Wind measured data

A meteorological station was installed on a platform (in red in Figure 44) on the walkway leading to the flare boom, 28.75m above m.s.l. The measurement system consisted of a self-contained Aanderaa Meteorological Station, including modular sensors mounted on a 2m mast and a multi-channel controller unit fitted with a Data Storage Unit (DSU). The wind measured data cover the period from 01/05/1999 to 03/05/2000.

5.2.1.2 Wind and Waves - DPR

The DPR (Daily Progress Report) contains some information about wind and waves condition during operations. This information is qualitative and gives us an overview of the general wear conditions during the operative life of the cofferdam.

5.2.1.3 Wind and Waves -hindcast data from DHI MWM

5.2.1.3.1 Wave hindcast data

The hindcast approach entails running atmospheric and ocean response models for a historical period (typically several decades long) in order to develop the specification of climate and extremes for an application.

The MWM database, the result of state-of-the-art numerical models of wave and wind, stems from the collaboration between DHI and HyMOLab (Laboratory of Hydrodynamics and Met-Ocean) of the Department of Engineering and Architecture of the University of Trieste. Wind and waves data are at hourly temporal resolution and cover the period 01/01/1979 – 31/12/2013. The grid point is located at water depth of 133m and its position is shown in yellow in Figure 44.

The DHI hindcast time series has been used as input (wind) and boundary conditions (wave) of SWAN simulations.

5.2.1.3.2 Wind hindcast data

From the DHI hindcast data set the following variables are available: wind speed (WS) and wind direction (WD), in hourly data. The wind speed has been decomposed in two components, along the x and y axis, knowing the angle of direction.



Figure 44 Position of measuring points (H1, H2 and M1) and DHI modelled gauge

5.2.2 Bathymetry

The bathymetric data useful in the SWAN analysis was obtained from GEBCO, which has a grid spacing of 30 arc sec and is maintained by the British Oceanographic Data Centre (BODC). In particular, it provides the seabed level through a grid with regular mesh of 1 Km.

To produce more detailed bathymetric grid with mesh size comparable to the mesh of the computational grid used, the GEBCO data were then processed with Delft3D-QUICKIN program. This program allows to create and modify grids and the related parameters like bathymetry, initial conditions and roughness.

For the SWAN analysis, two different bathymetries were used, one with regular square mesh (Figure 45) and another triangular unstructured mesh (Figure 46).

The SWASH bathymetry was created in the same as previously described, the only difference is the use of high-resolution data (2m), coming from previous SAIPEM projects in the same area (Figure 47).

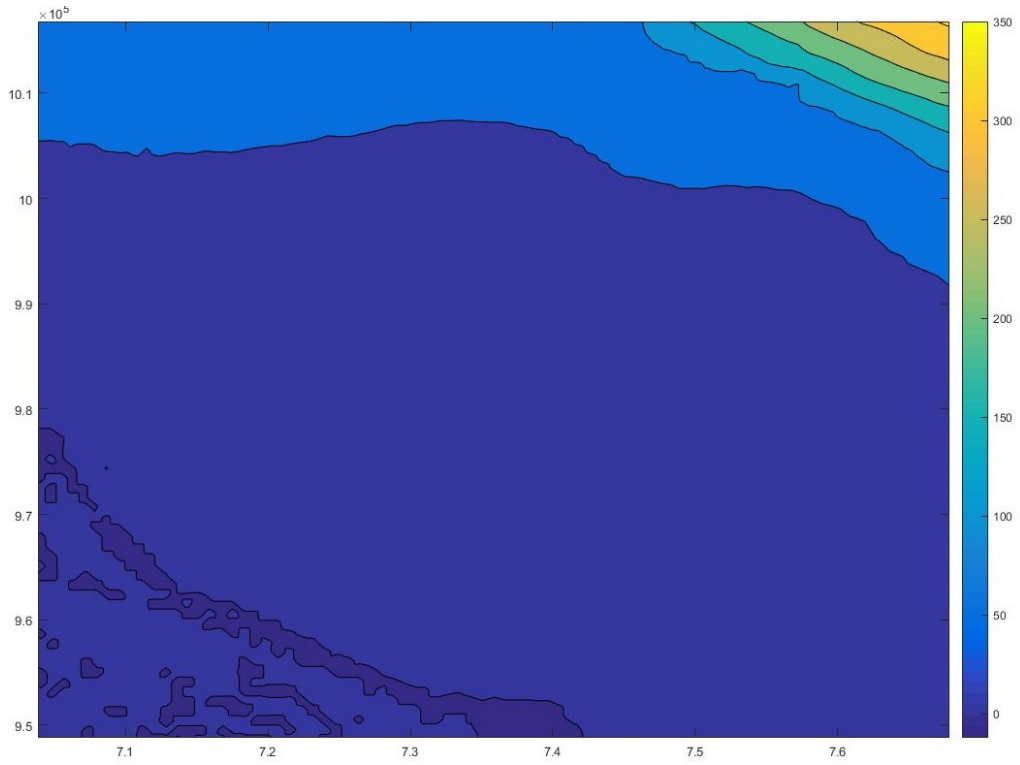


Figure 45 SWAN bathymetry, with regular grid

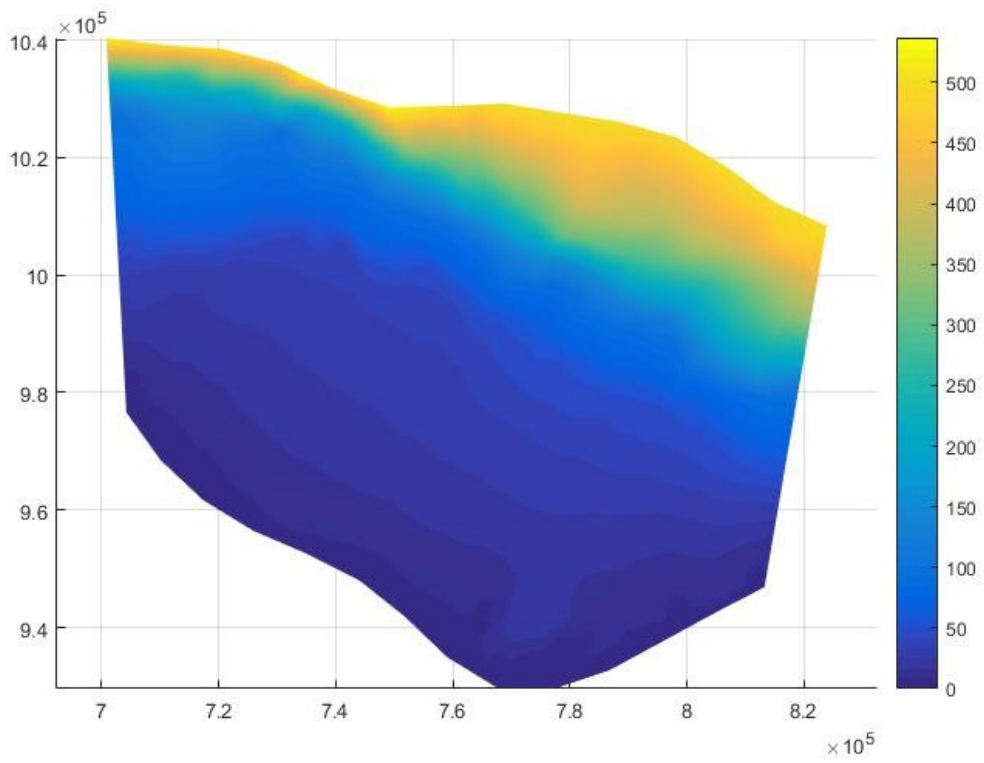


Figure 46 SWAN bathymetry, with unstructured grid

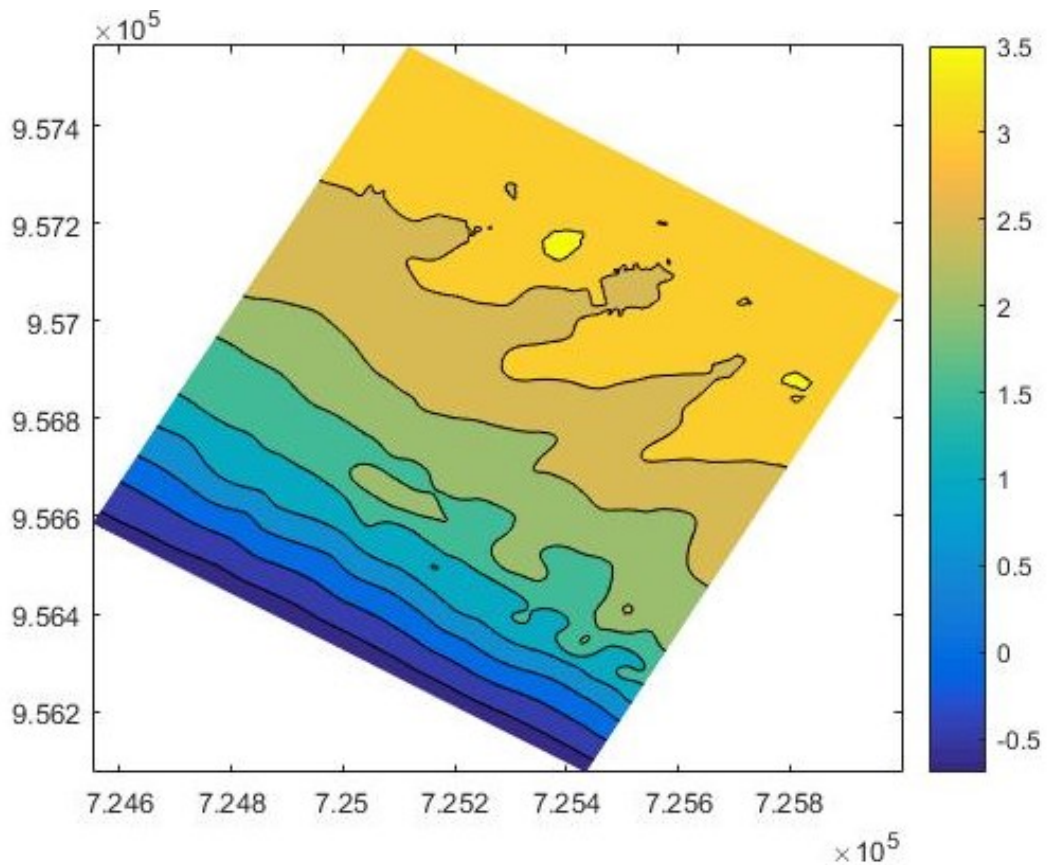


Figure 47 SWASH bathymetry

5.3 SWAN: calibration, validation and set-up

SWAN is a third-generation wave model, developed at Delft University of Technology, that computes random, short-crested wind-generated waves in coastal regions and inland waters.

The target of the SWAN simulation is to find the sea state at shallow water in order to provide boundary conditions for the SWASH analysis.

Previous thesis works: “Wave and coastal circulation modeling. A SWASH application with permeable and impermeable structures” and “Simulation of coastal sea states. SWAN model application on unstructured grid”, by, respectively, M.Cardelli and F.Angelini, were very useful starting point. In fact, the SWAN scheme used, for this project, starts from the one used by F.Angelini with some modifications so that the set-up is better suited to the data available.

5.3.1 SWAN input data

The SWAN analyses, were carried out in non-stationary two-dimensional mode, using the nautical convention for waves and wind while a system of Cartesian coordinates has been used for the computational grid.

The definition of the grid is a fundamental element for the SWAN simulations, as it is necessary to enter the input data: bathymetry, currents, water level, bottom friction and wind (if spatially variable).

The bathymetry has already been discussed in previous paragraph.

5.3.1.1 Computational grid

For the simulations, the unstructured triangular mesh grid produced by F. Angelini (2016) was used; but to get familiar with the program, the preliminary simulation was run with a regular mesh grid.

The structured grid covers an area of 4352 Km² (64X68Km) with square mesh of 0.04Km² (200x200m).

The unstructured grid, which was used as computational grid, covers an area of about 8000 Km² and the triangular meshes have a dimension that decreases closer to the coast in order to have greater accuracy in this region (Figure 48). In particular, the triangular meshes have sizes ranging from 5000 m² near the northern boundary of the domain to about 50 m² in front of the coast.

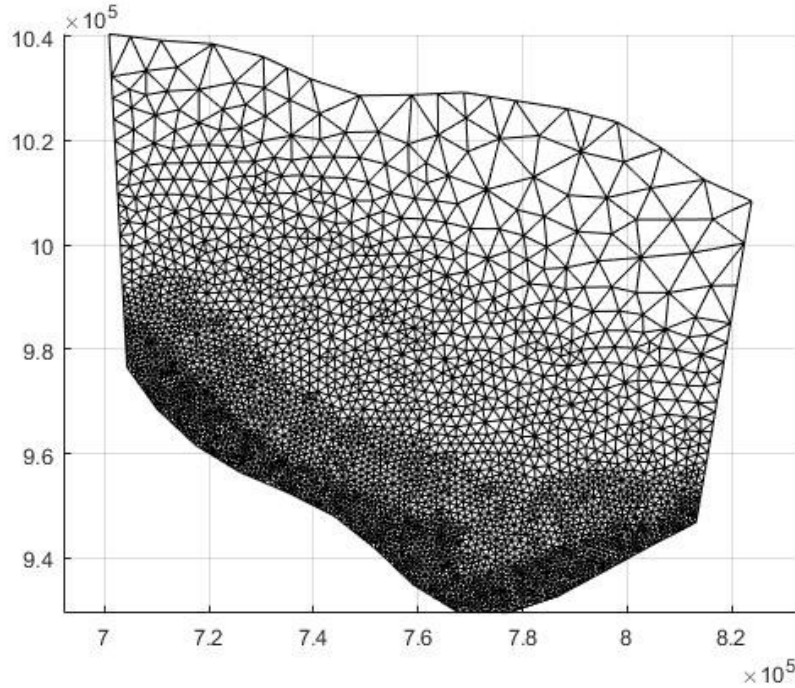


Figure 48 Unstructured grid

5.3.1.2 Wind input data

According to the DNVGL-RP-C205 “Environmental conditions and environmental loads”, for offshore locations, the Frøya profile is recommended unless data indicate otherwise. For extreme mean wind speeds corresponding to specific return periods in excess of approximately 50 years, the Frøya model implies that the following expression can be used for conversion of the one-hour mean wind speed U_0 at height H above the sea level to the mean wind speed U with averaging period T at height z above sea level.

$$U(T, z) = U_0 \left\{ 1 + C \ln \frac{z}{H} \right\} \left\{ 1 - 0.41 I_u \ln \frac{T}{T_0} \right\} \quad (102)$$

where:

- $H = 10m$;
- $T_0 = 1 h$;
- $T < T_0$;
- $C = 5.73 * 10^{-2} \sqrt{1 + 0.148U_0}$;
- $I_u = 0.06 (1 + 0.043 U_0) \left(\frac{z}{H} \right)^{-0.22}$.

The wind value parameters such as waves are derived from the hindcast DHI model in hourly values. For this reason, they are transformed into values of 10 minutes intervals ($T = 10min$) using the formula (102).

5.3.2 Boundary condition

SWAN simulates, the propagation of wave, starting from the values imposed on the boundaries of the domain and then propagates them using the information given as input such as wind and bathymetry.

The boundary conditions are assumed as constant along the domain's edge and it propagates towards the coast. The wave parameters required at the boundary are:

- Significant Wave Height H_s [m];
- Spectral Peak period (T_p) [s];
- Peak Mean Direction (MWD) [°];
- Directional spreading (DSD) [°];

Both in SWAN and SWASH, the file with the wave time series is called TPAR. The following figure (Figure 49) shows an example of the TPAR file.

TPAR				
19920202.020000	1.28	7.59	314.22	30.60
19920202.030000	1.28	7.48	310.33	43.28
19920202.040000	1.36	7.39	292.84	59.75
19920202.050000	1.45	7.32	253.99	64.30
19920202.060000	1.46	7.24	238.16	60.38
19920202.070000	1.44	4.54	229.72	57.18
19920202.080000	1.44	4.57	220.06	54.03
19920202.090000	1.43	4.60	214.52	50.98

Figure 49 TPAR example

For the SWAN analysis three of the most significant storms that occurred in the range of DHI model were chosen. The choice was made by analysing the MWD (mean wave direction), in order to have a storm for each preferential direction of waves that generally occur in the Egyptian coast.

The subdivision of storms was made taking into consideration three ranges of MWD values. The value of MWD is in nautical coordinate, so it is measured clockwise with respect to the North.

- N-W ($285^\circ < MWD < 345^\circ$)

- N ($345^\circ < MWD < 15^\circ$)
- N-E ($15^\circ < MWD < 75^\circ$)

The following tables show the peaks of each storm.

Direction	Time	Hs	Tp	MWD	DSD
N-W	19920203.200000	6.97	11.7	291	23.7
N	20020110.110000	5.13	10.5	353	27.9
N-E	19821109.040000	6.00	10.6	18.1	27

Table 3 Wave characteristics for peak of storms

The time is expressed in ISO-notation: yyyyymmdd.sss.

Below are shown the figures that represent the time series of wave height and direction for each storm:

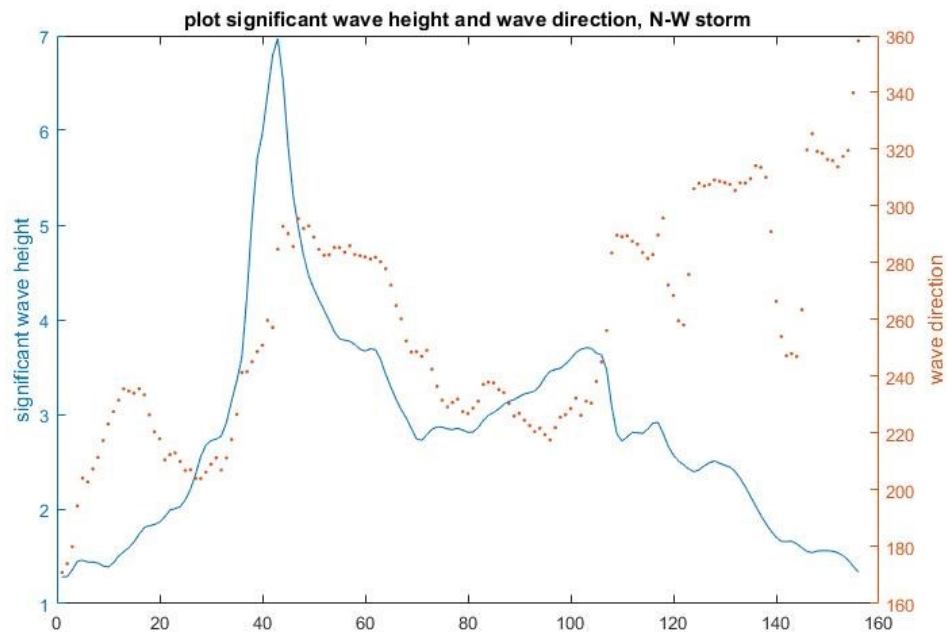


Figure 50 North-West distribution

The storm, from North-West, starts on 02/02/1992 at 02 and ends on 08/02/1992 at 13

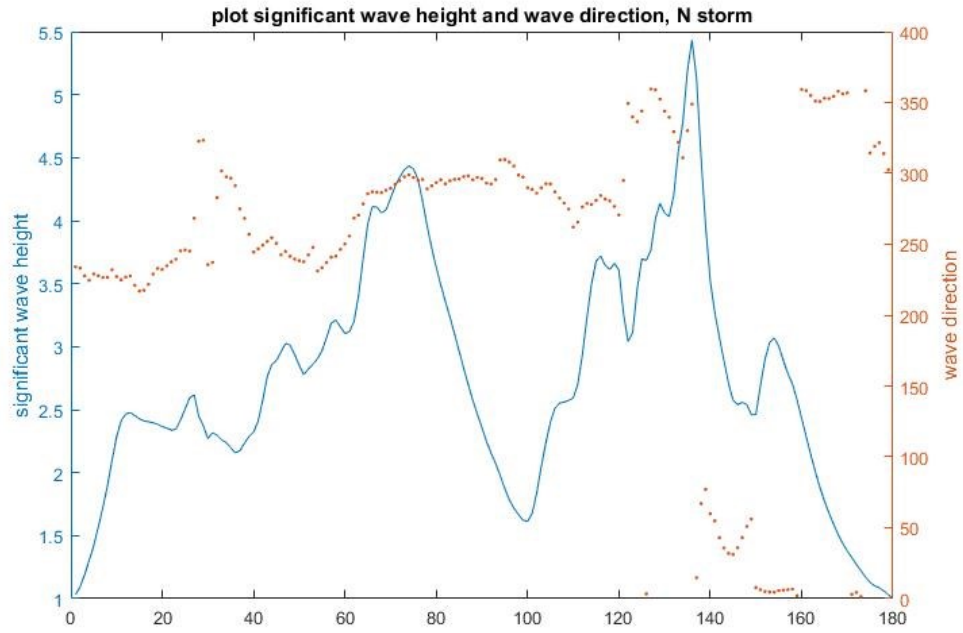


Figure 51 North distribution

The storm, from North, starts on 04/01/2002 at 19 and ends on 12/01/2002 at 06

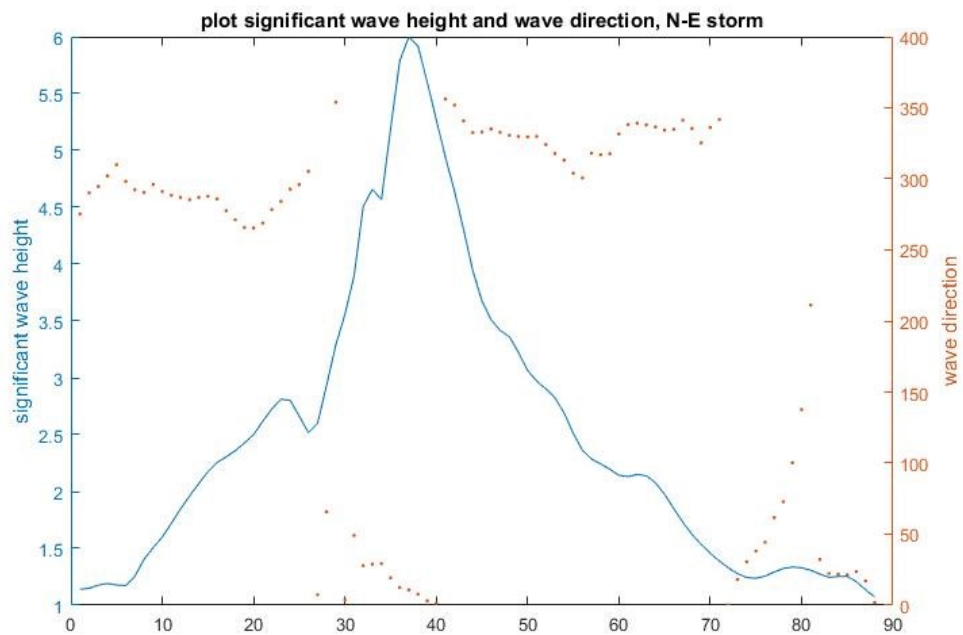


Figure 52 North-Est distribution

The storm, from North-Est, starts on 07/11/1982 at 16 and ends on 11/11/1982 at 07.

As the figure shows, the time interval of storms is variable (from almost 4 days in case of NE storm up to more than 7 days in case of N storm). The time duration of the storm is calculated from when the value of H_s exceeds 1m until it returns to values lower than 1m.

5.3.3 SWAN calibration

The SWAN model used is the same as that used by F. Angelini (2016) in his thesis, with some modifications on the calibration parameters of the physical phenomena described.

SWAN contains a number of physical processes that add or withdraw wave energy to or from the wave field. The processes included are: wind input, whitecapping, bottom friction, depth-induced wave breaking, dissipation due to vegetation, obstacle transmission, nonlinear wave-wave interaction (quadruplets and triads) and wave-induced set-up. SWAN can run in several modes indicating the level of parameterization, it can operate in first- second- and third-generation mode. The improvement made in the second-generation respect to the first- is only the “Phillips constant”, which in the first- is constant and equal to 0.081, while, in the second- it is variable.

An overview of the option which can be activated is give in the following table (Table 4).

process	authors	generation mode		
		1st	2nd	3rd
Linear wind growth	Cavaleri and Malanotte-Rizzoli (1981) (modified)	×	×	
	Cavaleri and Malanotte-Rizzoli (1981)			×
Exponential wind growth	Snyder <i>et al.</i> (1981) (modified)	×	×	
	Snyder <i>et al.</i> (1981)			×
	Janssen (1989, 1991)			×
	Yan (1987) (modified)			×
Whitecapping	Holthuijsen and De Boer (1988)	×	×	
	Komen <i>et al.</i> (1984)			×
	Janssen (1991)			×
	Alves and Banner (2003)			×
Quadruplets	Hasselmann <i>et al.</i> (1985)			×
Triads	Eldeberky (1996)	×	×	×
Depth-induced breaking	Battjes and Janssen (1978)	×	×	×
Bottom friction	JONSWAP (1973)	×	×	×
	Collins (1972)	×	×	×
	Madsen <i>et al.</i> (1988)	×	×	×
Obstacle transmission	Seelig (1979), d’Angremond (1996)	×	×	×
Wave-induced set-up		×	×	×
Vegetation dissipation	Dalrymple (1984)	×	×	×

Table 4 Overview of physical processes and generation mode in SWAN

Considering the results obtained by Angelini (2016) in his master thesis in which SWAN is calibrated for the same area but with different sea storms, the setting that is selected for the next steps is G2.

```

$*****PHYSICS***
GEN2
OFF WCAP
BRE CON 1.0 0.73
FRIC COLL 0.05
TRI 1 0.65
LIM 10.0 1.0
OFF FShift

```

Figure 53 Angelini's SWAN physical scheme.

5.3.3.1 Physical calibration

The SWAN model was calibrated by modifying the values of the physical parameters of breaking (α, β) and friction, starting from Angelini's scheme (shown in Figure 53). The data that was used for SWAN calibration was the measured data, in this method the value of the simulation can be compared with the value that was measured at gauge (H2).

The calibration test was carried out using the data of a storm, taken from the measured data of the buoy (H1), which started on 24/11/1999 at 20:00 and end at 14:00 on 27/11/1999.

The final configuration is the one that produces a distribution of the points closest to the measured one.

Test	Breaking		Friction	Standard deviation
	α	β		
case 1	1.2	0.83	0.05	0.0367
case 2	0.8	0.63	0.05	0.0401
case 3	1.0	0.73	0.1	0.0699
case 4	1.0	0.73	0.015	0.0377
case 5	0.8	0.63	0.015	0.0349
case 6	0.7	0.53	0.015	0.0306

Final calibration	1.2	0.83	0.03	0.0103
Default	1	0.73	0.015	0.0377
Angelini set-up	1	0.73	0.05	0.0384

Table 5 Breaking and Friction parameters for each set-up and standard deviation respect to the measured data

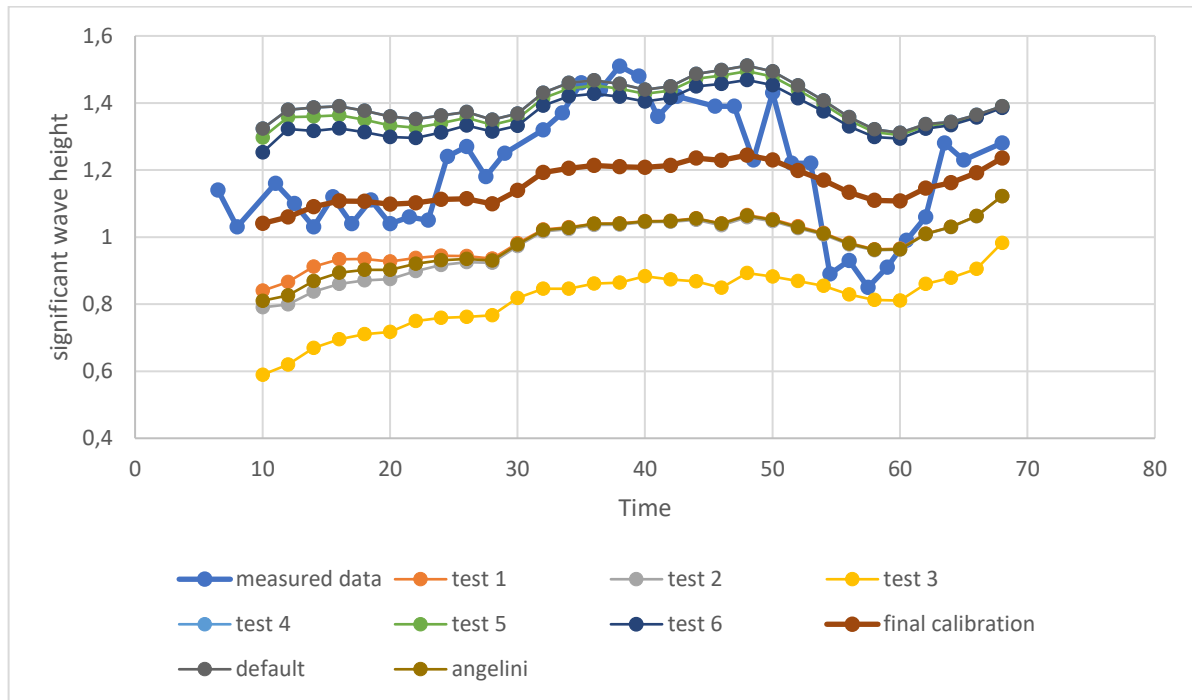


Figure 54 Plot of measurement and model time series of wave height at H2

Hence, the final set-up of SWAN after the validation process is the one shown in Figure 55, in which all the parameters, both for breaking and for friction, are greater than those proposed by the program as default values.

```

$
GEN2
OFF WCAP
BRE CON 1.2 0.83
FRIC COLL 0.03
TRI 1 0.65
LIM 10.0 1.0
OFF FShift
$
$*****

```

Figure 55 Final physical scheme

5.3.4 SWAN results

As previously written, the goal of the SWAN analysis is to derive the sea state that will be used as boundary condition in the SWASH simulations.

The variables required by the outputs are:

- significant wave height (Hs);
- peak period (Tp);
- mean wave direction (MWD);
- directional spreading of wave (DSD);
- water depth;
- bottom level (bathymetry).

The first three parameters are those that are used to characterize the sea state in the SWASH analysis (Hs, Tp and MWD).

Strom	HS [m]	Tp [s]	MWD [°]
N-W	1.62	11,017	34.81
N	1.57	9.71	22.65
N-E	1.61	11.017	27.11

Table 6 Hs, Tp and MWD of peak of each storm at 3.4m of depth (SWASH boundary)

Table 6 shows the characteristics of the wave at 3.4 meters depth, the value of MWD for each storm is in the N-E range ($15^{\circ} \div 75^{\circ}$), due to the effects of shoaling and refraction phenomena.

5.3.4.1 SWAN post-processing results

The significant wave heights (Hs), obtained from the SWAN output, were analyzed through a "plotunswan" MATLAB function. The specific purpose of this function is the post-processing of SWAN results, in which an unstructured triangular grid is used, as in this case (Figure 48).

Three maps are shown for each storm analyzed, the first two show the evolution of Hs in an interval of 5 hours, the third one is the map of peak value of storm (see Table 6).

In the lower part of the side edges of the map there are areas with unrealistic values. The distance between the area with unrealistic values and the area of interest is such as to ensure that it does not interfere with the result.

As previously written, the storm was defined as N-E, N and N-W based on MWD of peak. In fact, in some of the images that show the evolution of Hs, it can be seen how the direction of the incoming waves is different from that of the peak.

5.3.4.1.1 North-West storm

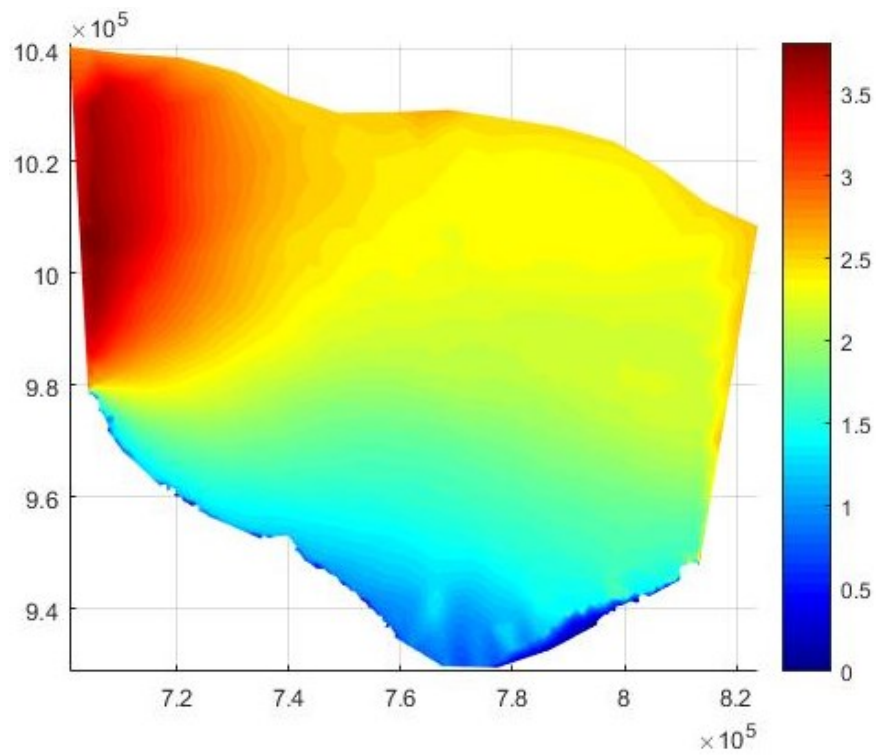


Figure 56 Significant wave height of N-W storm of 05/02/1992 at 7:00

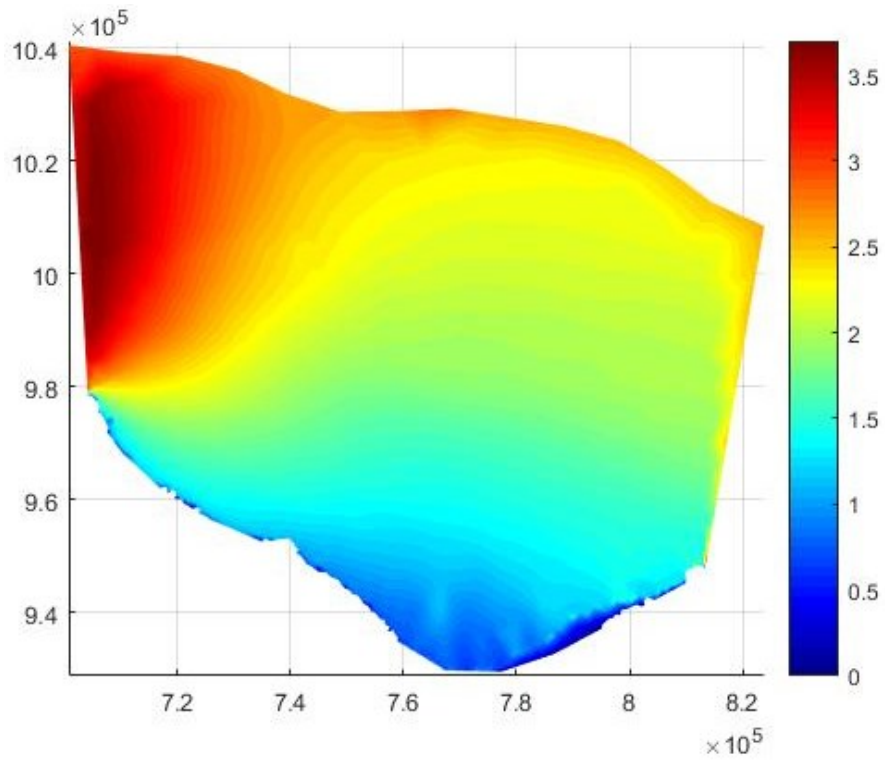


Figure 57 Significant wave height of N-W storm of 05/02/1992 at 12:00

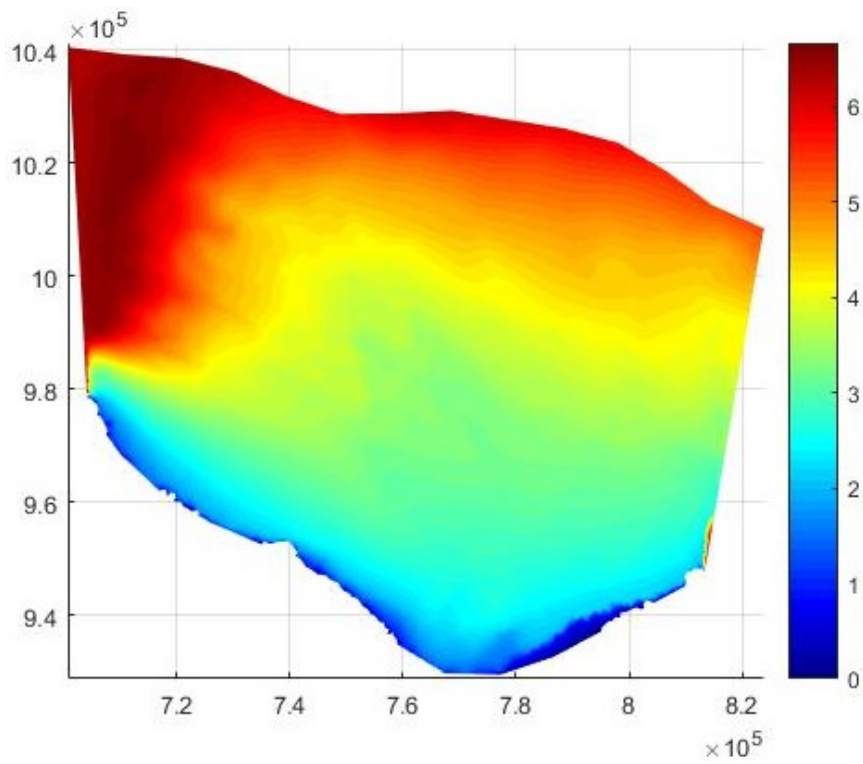


Figure 58 Significant wave height at peak of N-W storm (03/02/1992 20:00)

5.3.4.1.2 North storm

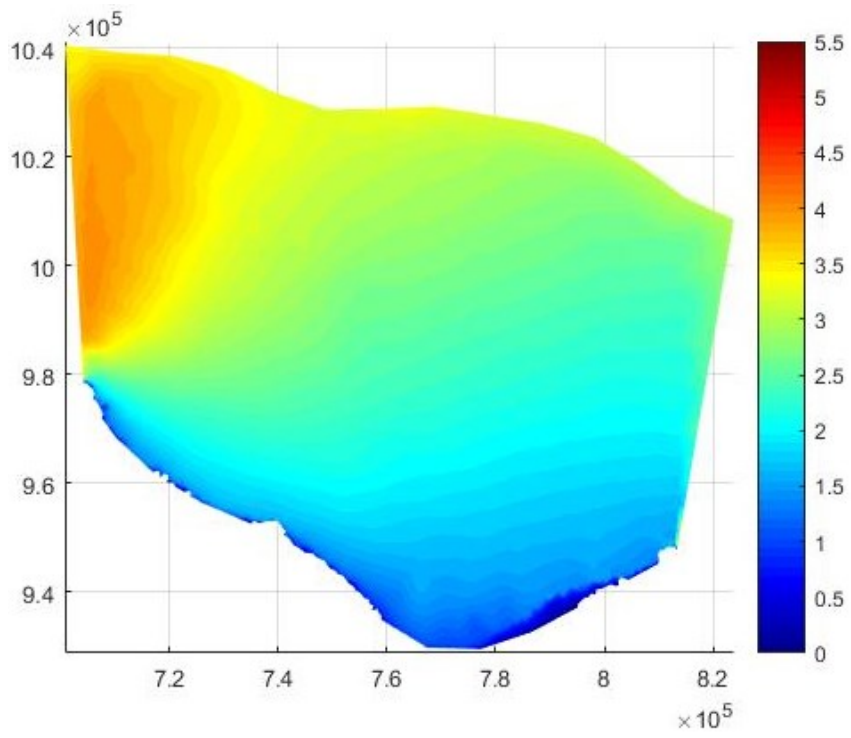


Figure 59 Significant wave height of N storm of 07/01/2002 at 09:00

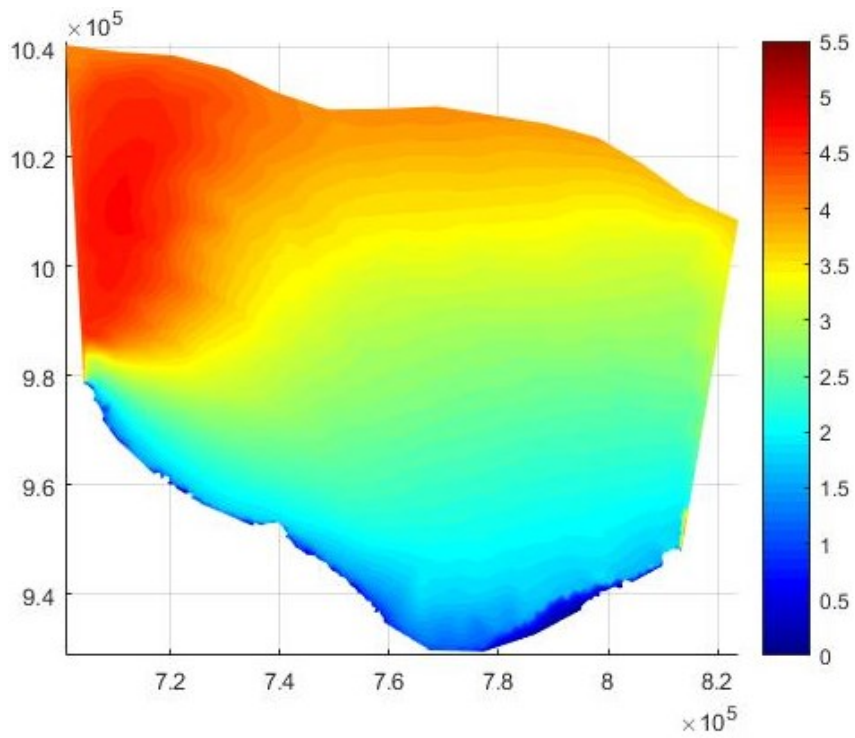


Figure 60 Significant wave height of N storm of 07/01/2002 at 14:00

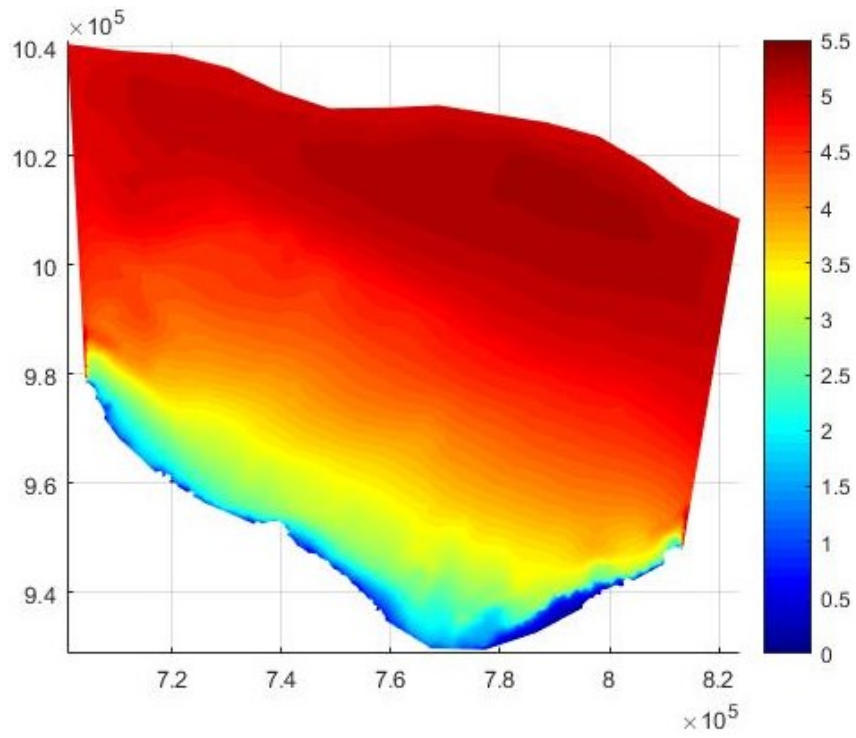


Figure 61 Significant wave height at peak of N storm (10/01/2002 11:00)

5.3.4.1.3 North-East storm

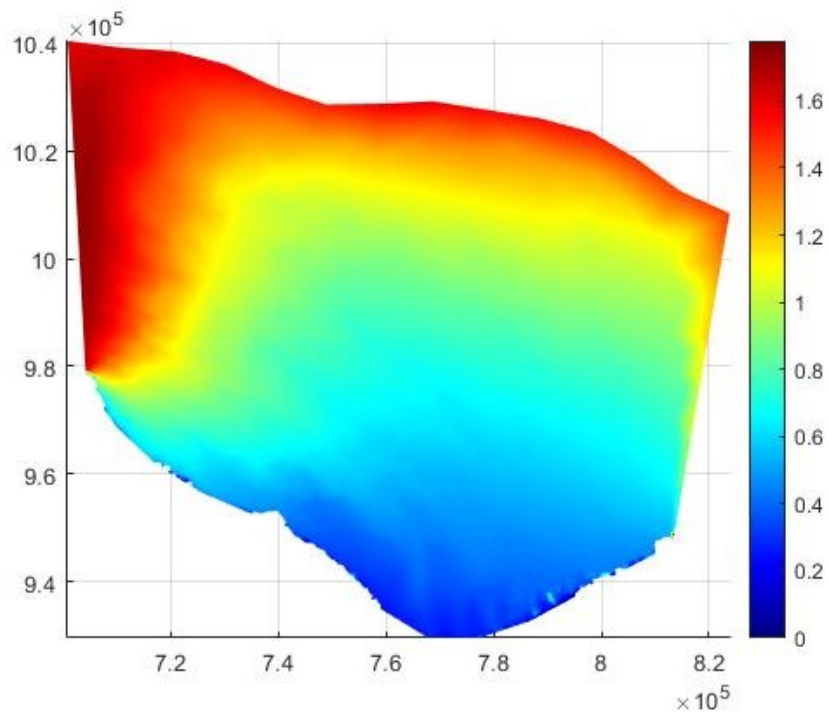


Figure 62 Significant wave height of N-E storm of 08/11/1982 at 1:00

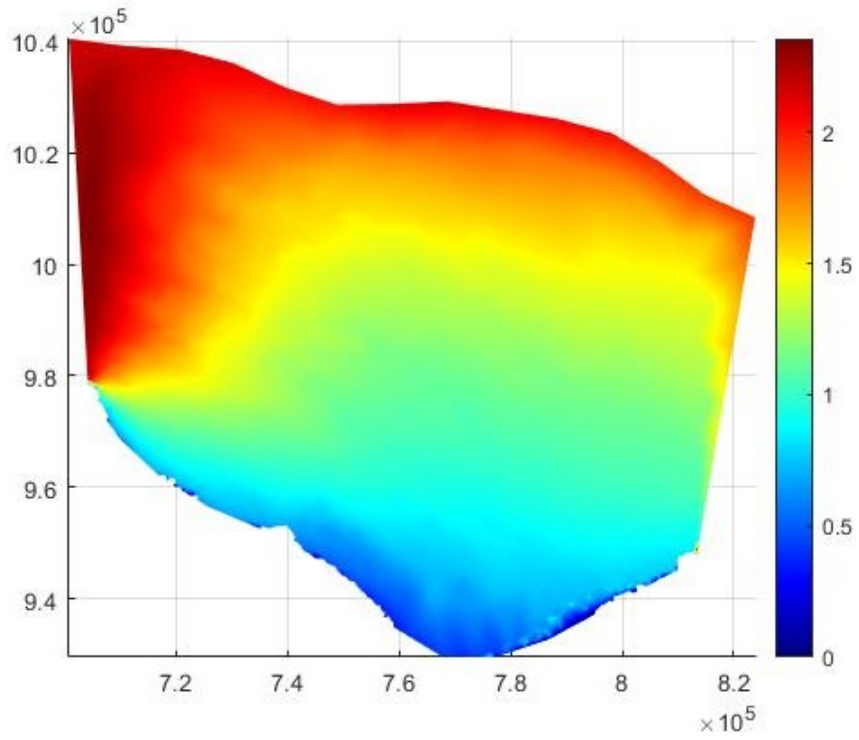


Figure 63 Significant wave height of N-E storm of 08/11/1982 at 6:00

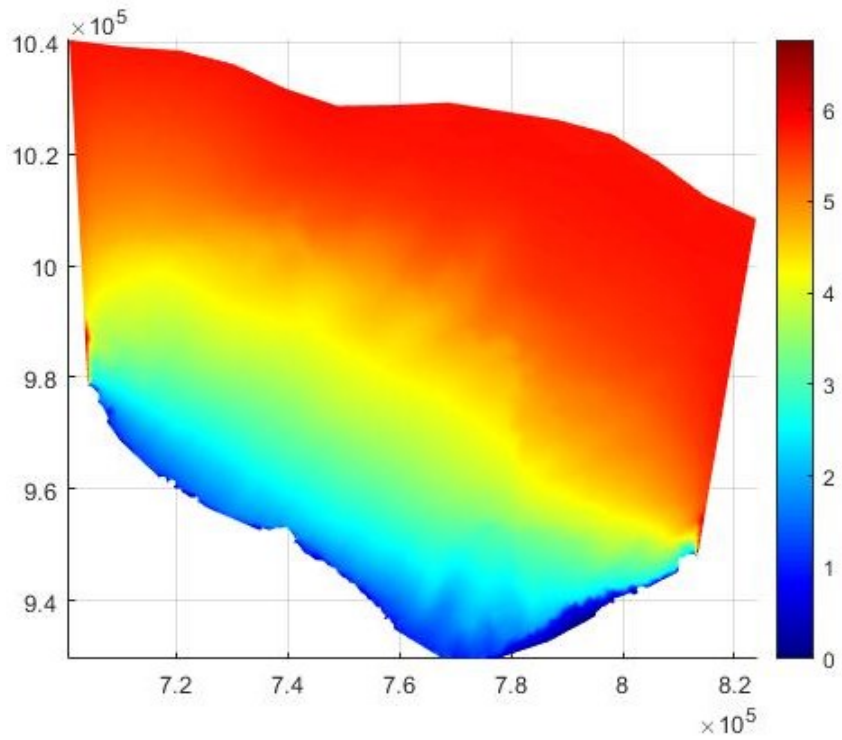


Figure 64 Significant wave height at peak of N-E storm (09/11/1982 04:00)

5.4 SWASH: set-up

5.4.1 Introduction

SWASH (Simulating WAVes till SHore) is a general-purpose numerical tool for simulating non-hydrostatic, free surface, rotational flows and transport phenomena in one, two or three dimensions. The governing equations are the nonlinear shallow water equations including non-hydrostatic pressure and some transport equations (salinity, temperature and suspended solid) and provide a general basis for simulating:

- Wave transformation in both surf and swash zones due to nonlinear wave-wave interactions, interaction of waves with currents, interaction of waves with structures, wave damping due to vegetation, and wave breaking as well as runup at the shoreline.
- Complex changes to rapidly varied flows typically found in coastal flooding resulting from e.g. dike breaks, tsunamis, and flood waves.
- Density driven flows in coastal seas, estuaries, lakes and rivers.
- Large-scale ocean circulation, tides and storm surges.

Figure 65 shows the difference in size between the SWAN and SWASH grids. The SWAN grid covers an area of about 8000 km², while the other has a domain with area of 1.28 Km². The SWASH grid is a structured grid composed by 321300 (510x630) square meshes of 4m² (2x2).

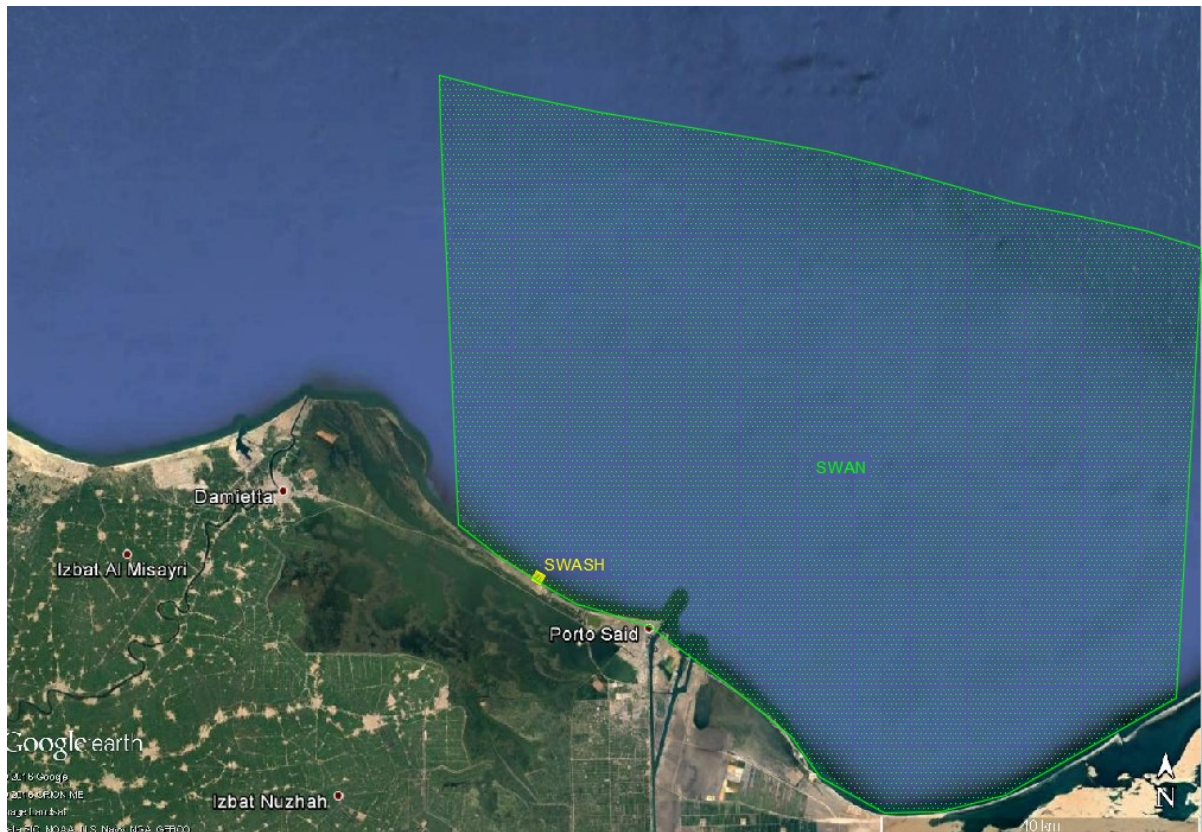


Figure 65 approximated plan view of the simulation grids. SWAN in green and SWASH in yellow

SWASH only admits the propagation of waves or stationary spectra, the wave is propagated from the northern boundary of the domain by means of the SPECTRUM function, which propagates the spectrum of the wave knowing only the spectral parameters: H_s , T_p and dir (MWD) (see Table 6).

5.4.2 SWASH input file

The sequences of commands used to model the geometry and physics of the problem are here described. These commands can be divided into the following classes:

1. Star-up commands;
2. Commands for model description
3. Output commands;
4. Lock-up commands.

For more detail see the APPENDIX, which shows the entire SWASH input file.

5.4.2.1 Start-up commands

With these commands it is possible to choose the simulation title but also a series of initial settings such as the static water level (in m), the North direction with respect to the x axes (measured counter clockwise), the water depth of the threshold (in m) which excludes from the calculation all points that have a water level below this threshold, the number of maximum errors allowed in the pre-processing input control. In this phase it is also possible to set the way in which SWASH will simulate the problem in this case the non-stationary mode has been chosen and a two-dimensional Cartesian reference system is used.

5.4.2.2 Commands for model description

In this section, the user can define the computational grid, input fields, initial and boundary conditions, physics and some parameters for the numerical implementation.

5.4.2.2.1 Computational grid

A distinction is made between the definition of grids in horizontal and vertical directions. In the horizontal direction, rectilinear coordinates are used, while σ –level coordinates in vertical direction.

First, it is necessary to define the size and direction of the computational domain in the horizontal plane. The area of interest must be kept at least two wavelengths from the edges. This criterion is respected since the distance between the cofferdam and the edges is at least 400m and, from linear theory, the estimated of the wavelength is about 70m.

The grid axes are aligned as much as possible to the direction of the dominant wave, which improves the model's performance and stability.

The spatial resolution is chosen to have, enough grid points per wavelength associated with the energy of the peak wave. In our case the H_s/d ratio falls within the $0.25 \div 1$ range and it is enough to take about 50 cells of the grid per peak wavelength. This criterion would give a grid with a mesh of about 1 m; however, to reduce the high calculation time, which is proportional to the third power of the grid size, we opted for a 2 m mesh. This choice is reasonable because it allows us to get around 35 grid points in a wavelength.

It was decided to use one single vertical layer -depth average simulation-, so as to reducing the calculation time as much as possible, without compromising the quality of the result. This

choice is also supported by the fact that the maximum depth in the domain is about 3.5 m, therefore it is assumed that the information lost assuming vertically homogeneous conditions layer is not high.

In summary, the computational grid has dimensions of 1020x1260m² with regular meshes of 2m rotated 330° counter-clockwise with respect to a horizontal axis directed towards the east.

5.4.2.2.2 Input fields

The following input information must be provided:

- *Bathymetric grid*: this grid, implemented in the above described way represents the seabed level at each grid point. The resolution of the bathymetric grid is, in our case, the same as that of the computational grid.
- *Porosity grid*: through this grid, by using layers with different positions, within the domain, reflection and transmission effects through the porous structures are simulated. The porosity (n) is defined as the volumetric porosity of the structures and its value is between 0 and 1. The porosity values lower than 1 indicate the position of the porous structures while the value 1 represents water points. A small value (<0.1) must be interpreted as impermeable regions, such as walls and dams.

A representation of this grid is shown in Figure 66. Where:

- $n = 0.001$ for waterproof part (cofferdam) and for coastline (in green)
- $n = 0.45$ for causeway (in light blue)
- $n = 1$ for water (in blue)

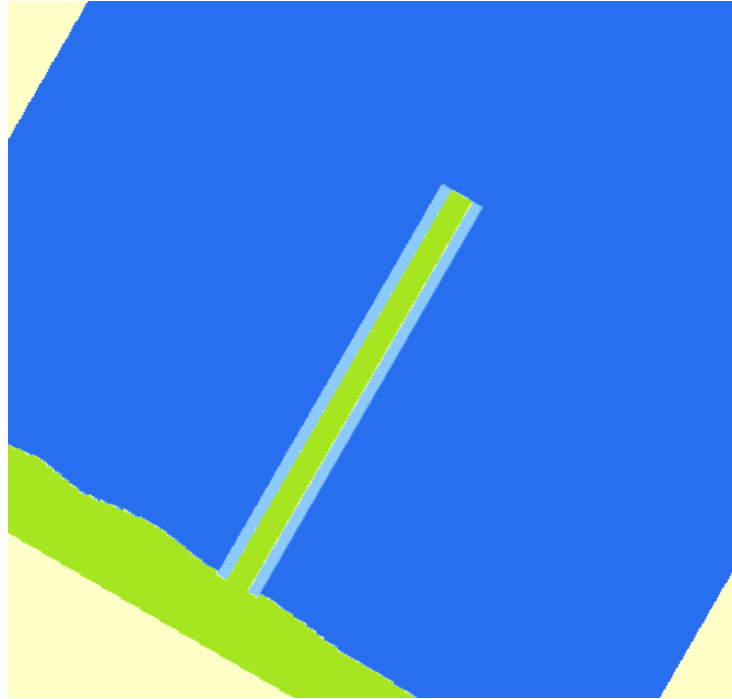


Figure 66 Zoom of porosity map, DELF3D image

5.4.2.2.3 Boundary conditions

SWASH generates the waves starting from the North edge through the SPECTRUM function. This is called wave-maker boundary. As suggested by the SWASH user's manual the depth variation along this wave-maker boundary is slow and it has been positioned away from the interested area.

When imposing a spectrum at the boundary, one must realize that some so-called evanescent modes might be included as well. These modes show an exponential decay proportional to the distance from the boundary at which the spectrum is imposed. As such, they cannot be "seen" by the model. Evanescent waves are a general property of the underlying model equations. The frequency at which the evanescent modes are generated is the cut-off frequency and is determined by the dispersive properties of the model equations. It is given by:

$$f_{cf} = 2 K \sqrt{\frac{g}{d}} \quad (103)$$

in which $K = 1$ (number of layers).

However, these problems have not arisen in the analyses carried out, so we do not further consider this theme.

On the North boundary of the domain the boundary conditions for the propagation of the waves are applied, on the South edge there is the coastline and therefore the impermeable boundary conditions are applied (waterproof, see Figure 66, $dv/dy = 0$).

On the lateral edges of the domain, some sponge layers are located to avoid the production of non-physical reflected waves. Several tests have been carried out to see whether the use of the sponge layer is necessary only from the wave incoming direction (in this case East), or it is better to apply sponge layers on both open edges. The different cases will be discussed in the results chapter.

```
>
$ ****BOUNDARY AND INITIAL CONDITIONS*****
BOU SIDE North CON SPECT 1.61 11.017 27.11 0 3 HR
BOU SIDE East BTYP SOMM
BOU SIDE West BTYP SOMM
SPONGelayer E 40
SPONGelayer W 40
PORO 0.0001 99999 1000 28
$
```

Figure 67 Boundary conditions in the input file

5.4.2.2.4 Physics

In absence of available measurements of the study area, the default settings were used (also used by Cardellini (2016) in his thesis work) which still produced realistic results. The only parameter on which sensitivity has been performed is the horizontal turbulence parameter.

The schemes for horizontal turbulence proposed by the SWASH manual are:

1. Constant horizontal eddy viscosity
2. Smagorinsky model
3. Prandtl mixing length

A sensitivity analysis has been carried out to find the physical scheme that would allow the best time/quality compromise between the Smagorinsky model and that of Prandtl, the constant scheme was not considered because too rough. From the comparison of the results and the calculation time, there were no appreciable changes between the simulations that used the Smagorinsky scheme (with constant of 0.2, recommended by the SWASH manual) and the one with the Prandtl scheme with a mixing length parameter that is the same as the grid resolution (2m). For this reason, the horizontal viscosity scheme used for the final

simulations is the Smagorinsky one, (with constant of 0.2), which was the same used by Cardellini in his thesis.

In conclusion the physic scheme that was used in final simulations is:

- Wind effect disregarded;
- Manning bottom friction (0.019, default value);
- Vertical mixing disregarded;
- Smagorinsky model with a constant value equal to 0.2;
- Wave breaking with $\alpha = 0.6$ and $\beta = 0.3$.

```
$
$ ****PHYSICS*****
FRICtion MANNing 0.019
BREaking 0.6 0.3
VISCOsity Horizontal SMAGorinsky 0.2
$
```

Figure 68 Physics in the input file

5.4.2.2.5 Numerical implementation

The following numerical setting was used:

- Default Keller-box scheme with $\theta = 1$ to include the non-hydrostatic pressure in the shallow water equations;
- The reduced pressure equation method was disregarded;
- Default options of the numerical parameters of iterative solver;
- ILU preconditioner that is more robust;
- CORRDEP space discretization for water depth in velocity points with the second order backward upwind scheme (BDF), which is more robust;
- Explicit time integration with $C_{r,min} = 0.1$ and $C_{r,max} = 0.8$.

Figure 69 illustrates a summary of the input file.

```

$ ****NUMERICSE*****
NONHYDrostatic BOX 1 RED 0 SOLV 0.01 0 500 0.55 PREC ILU
DISCRET CORR BDF
DISCRET UPW UMOM H BDF
DISCRET UPW WMOM H BDF
DISCRET UPW UMOM V BDF
DISCRET UPW WMOM V BDF
TIMEI METH EXPL 0.1 0.8
$

```

Figure 69 Numeric in the input file

5.4.2.3 Output commands

In this part of the input file, the model is provided with the information necessary to achieve the results of interest for this thesis. In particular, the following settings have been provided:

- The output data format;
- The values to be monitored throughout the domain extension (in this case the start time for which the program must "print" the information and the interval for each subsequent print must also be provided, are 82000.000 and 1 SEC respectively in Figure 70) such as:
 - Xp and Yp: to instruct SWASH to write the x- and y- coordinate in the problem coordinate system of the output location;
 - Bottom level or still water depth (WATLEV);
 - Instantaneous velocity (VEL);
 - Significant wave height (Hs);
- Additional information relating to the quantities required for the output (command QUANTity).

```

QUANTity VEL 'VEL' 'Vel' 0 1000 -9999 PROBLEMcoord
QUANTity HSIG 'HS' 'Hsig' 0 1000 -9999 dur 30 MIN
BLOCK 'COMPGRID' NOHEAD 'GRIDOUT.MAT' LAYOUT 3 XP YP VEL HS BOTLEV WATLEV OUTPUT 082000.000 1 SEC
$

```

Figure 70 Output part in the input file

5.4.2.4 Lock-up commands

This command orders SWASH to start the computation from the start computation time to the end. In this section also the initial time step (0.1 sec) is set, which will be automatically modified to test the CFL criterion. The initial time step is chosen by using the Courant number constraint:

$$C_r = \Delta t \left(\sqrt{gd} + \sqrt{u^2 + v^2} \right) \sqrt{\frac{1}{\Delta x^2} + \frac{1}{\Delta y^2}} \leq 1 \quad (104)$$

Finally, the STOP command is used to mark the end of the commands in the command file. Any information in the input file beyond this command is ignored.

```

$
$ *****LOCK-UP*****
COMPUte 080000.000 0.1 SEC 083000.000
STOP

```

Figure 71 Lock-up in the input file

Chapter 6 – Results and discussion

The simulations are defined according to the computation domain (small or larger), the parameters of the wave spectrum (significant wave height, time to peak and wave direction), the number of sponge layers used (on the East side or West and East side) and the simulation time (30min or 3 hours).

1. Smaller domain

Case a $H_s = 1.61\text{m}$, $T_p = 11\text{s}$, $\text{dir} = 27.11^\circ\text{N}$; sponge layer on East side and 30min of simulation

Case b $H_s = 1.61\text{m}$, $T_p = 11\text{s}$, $\text{dir} = 27.11^\circ\text{N}$; sponge layer on West and East sides and 30min of simulation

Case c $H_s = 1.61\text{m}$, $T_p = 11\text{s}$, $\text{dir} = 27.11^\circ\text{N}$; sponge layer on East side and 3 hours of simulation

Case d $H_s = 1.61\text{m}$, $T_p = 11\text{s}$, $\text{dir} = 20^\circ\text{N}$; sponge layer on East side and 30min of simulation

Case e $H_s = 1.61\text{m}$, $T_p = 11\text{s}$, $\text{dir} = 20^\circ\text{N}$; sponge layer on West and East side and 30min of simulation

Case f Same of Case b but more smoothed bathymetry

2. Larger domain

Case g $H_s = 1.61\text{m}$, $T_p = 11\text{s}$, $\text{dir} = 27.11^\circ\text{N}$; sponge layer on East side and 30min of simulation

Case h $H_s = 1.61\text{m}$, $T_p = 11\text{s}$, $\text{dir} = 27.11^\circ\text{N}$; sponge layer on West and East side and 30min of simulation

A larger domain and a wave direction angle, different from that obtained from SWAN (almost the same of the angle of inclination of domain 30°), have been used to enforce a different current distribution from the small domain, especially around the cofferdam.

6.1 Results

For each simulation, the maps of significant wave heights, currents, wave orbital velocity and stresses shown. The significant wave heights, the currents and therefore the shear stress

produced by the current are averaged for the duration of the simulation, while the orbital speed of the wave and therefore the shear stress produced by them is instantaneous.

6.1.1 Significant wave height

The output of significant wave height (H_s) for each simulation, except for case c, whose output does not report values of H_s , are here analysed.

All of the H_s images clearly display, the reflection of the wave on the gate of the cofferdam, with an increase of significant wave heights in the area in front of the causeway. This is possible because the width of the causeway has the same order of magnitude as the wavelength (width=70m, wavelength $L = T\sqrt{gh} = 11 * \sqrt{9.81 * 3} \cong 60m$).

Analysing the images, the parameter that most affects the distribution of the H_s is the presence of the single or double sponge layers (later also written with the acronym SL). In the case with the double sponge layer the significant wave heights are more symmetric than the same simulation with a single SL.

The following images show H_s on the entire domain and the detail of H_s in the area where the scouring occurred, in front of the cofferdam.

The value of significant wave heights is important, because if the instantaneous orbital velocity is not available, H_s allows one to calculate the near-bed orbital velocity for monochromatic waves and a spectrum wave.

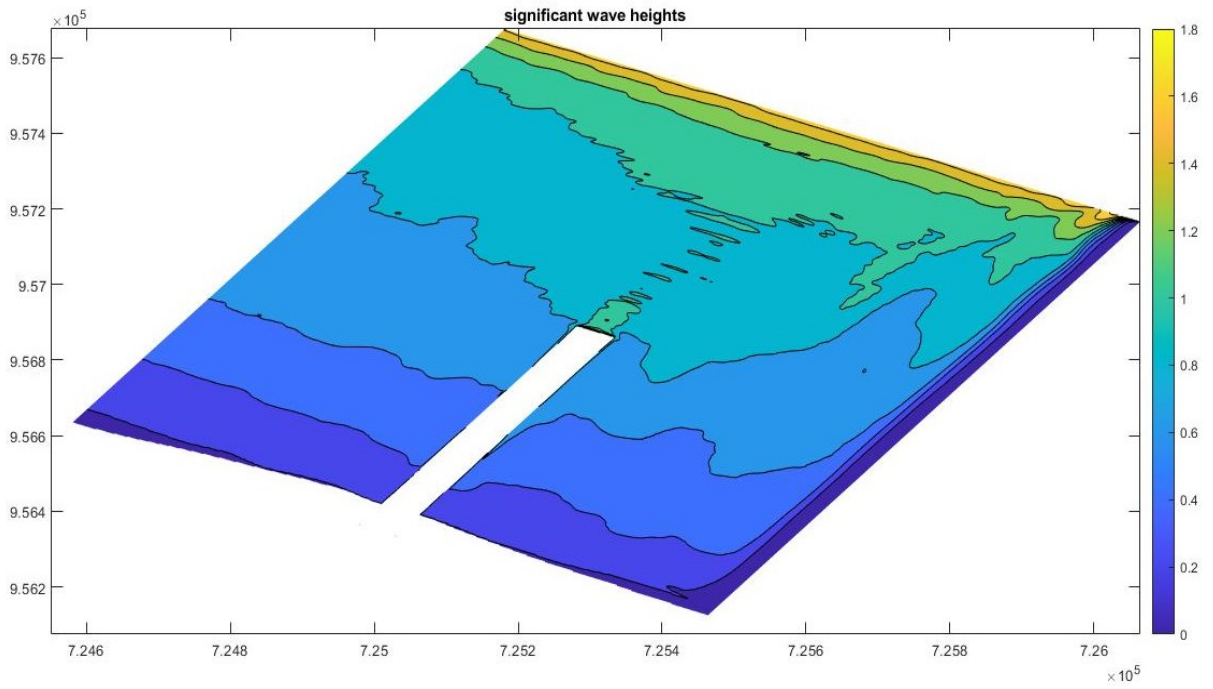


Figure 72 Significant wave height [m], for case a ($dir=27.11^\circ N$; sponge layer on East side)

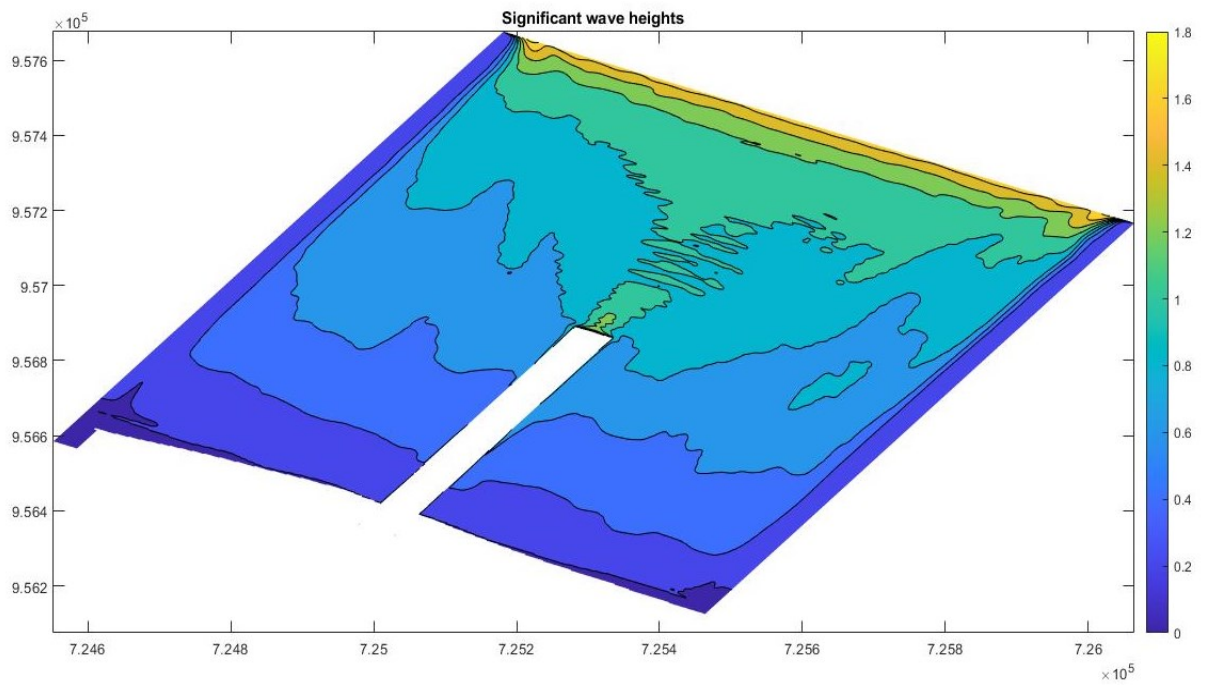


Figure 73 Significant wave height [m], for case b ($dir=27.11^\circ N$; sponge layer on East and West side)

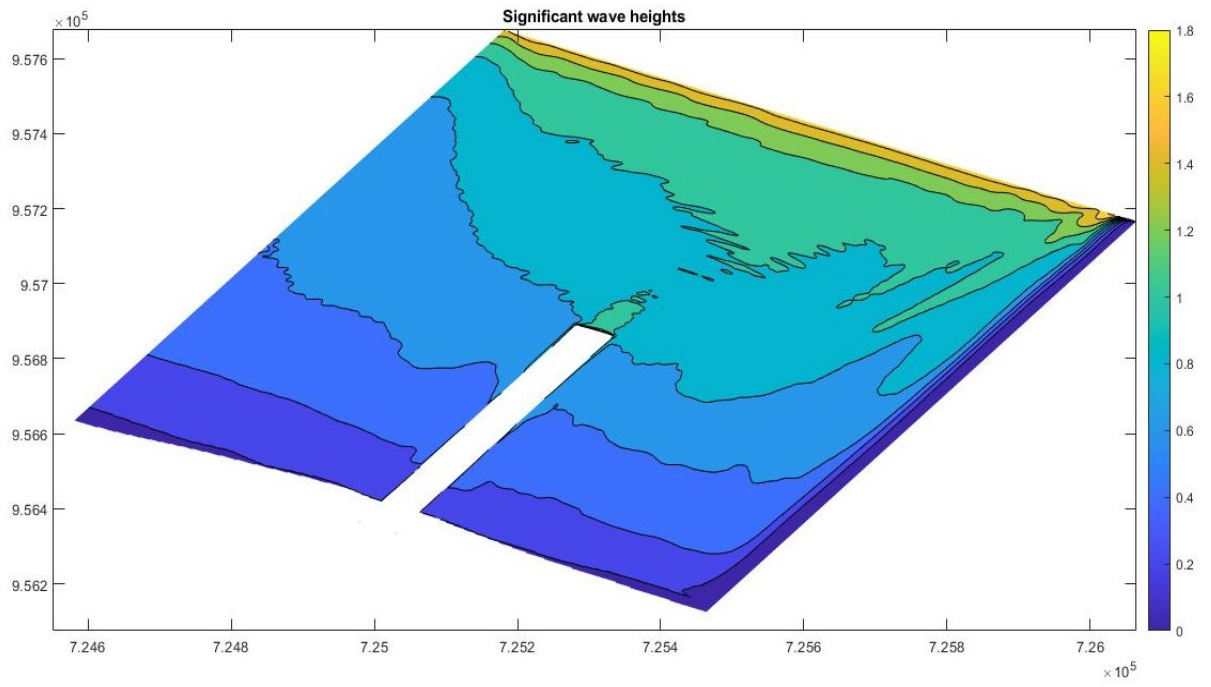


Figure 74 Significant wave height [m], for case d (dir=20 °N; sponge layer on East side)

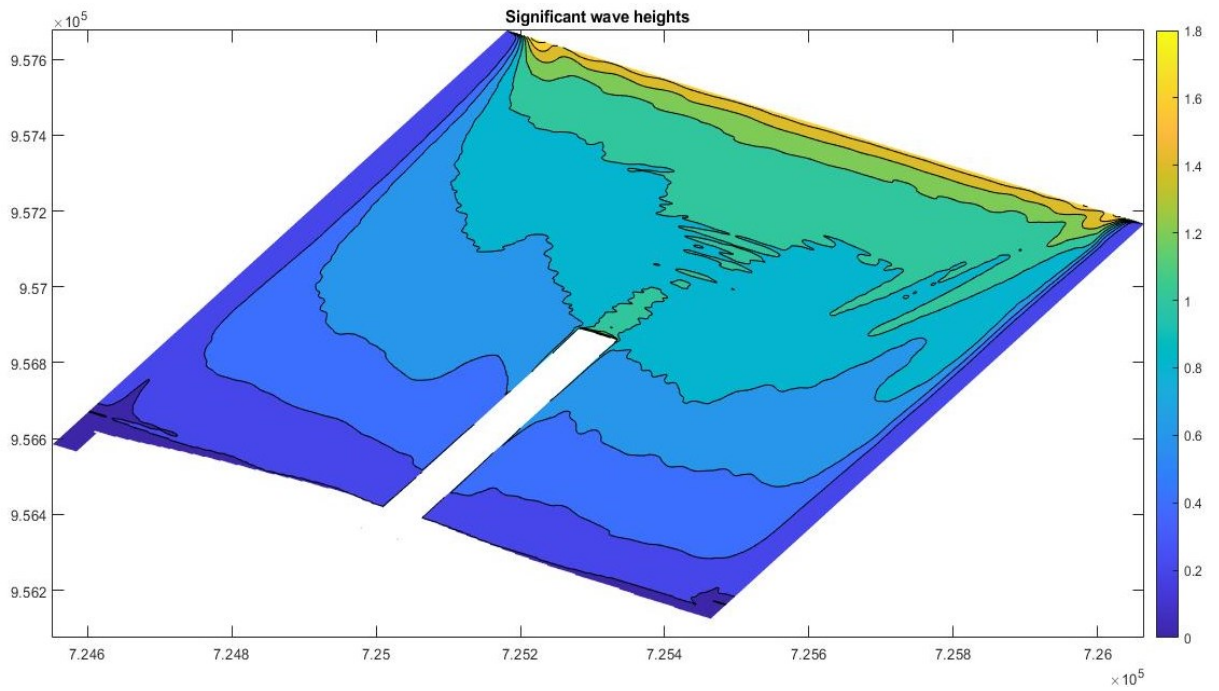


Figure 75 Significant wave height [m], for case e (dir=20 °N; sponge layer on East and West side)

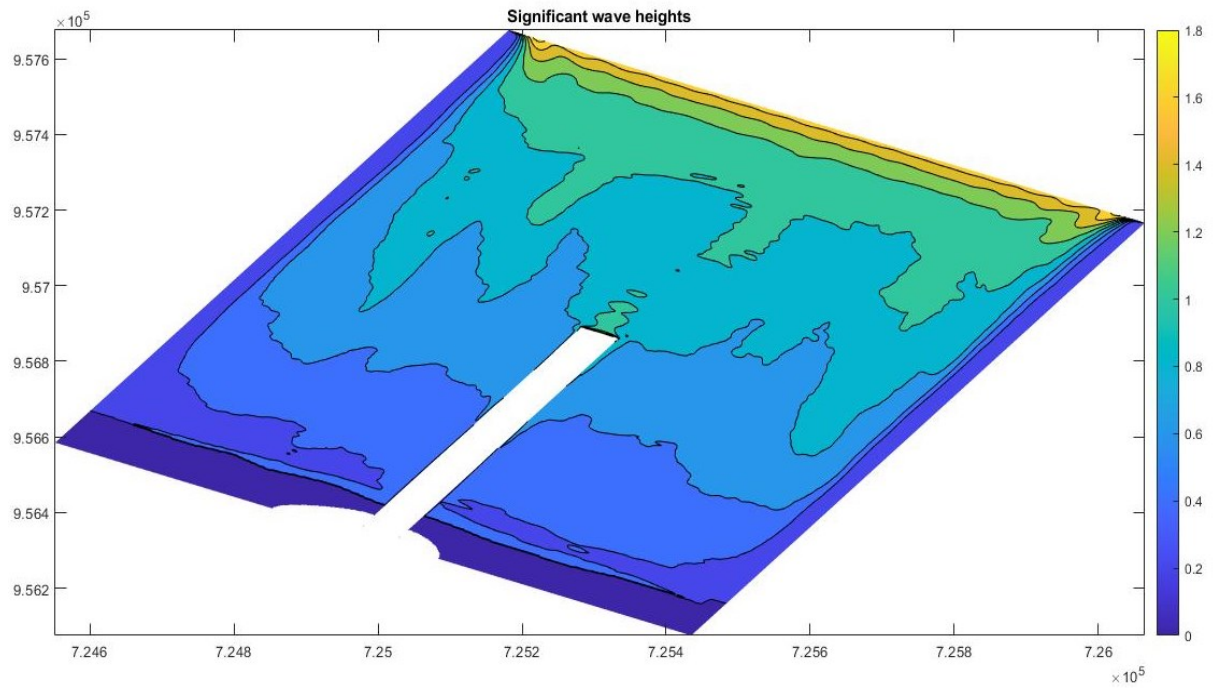


Figure 76 Significant wave height [m], for case g (dir=27.11 °N; sponge layer on East and West side; with a smoothed bathymetry)

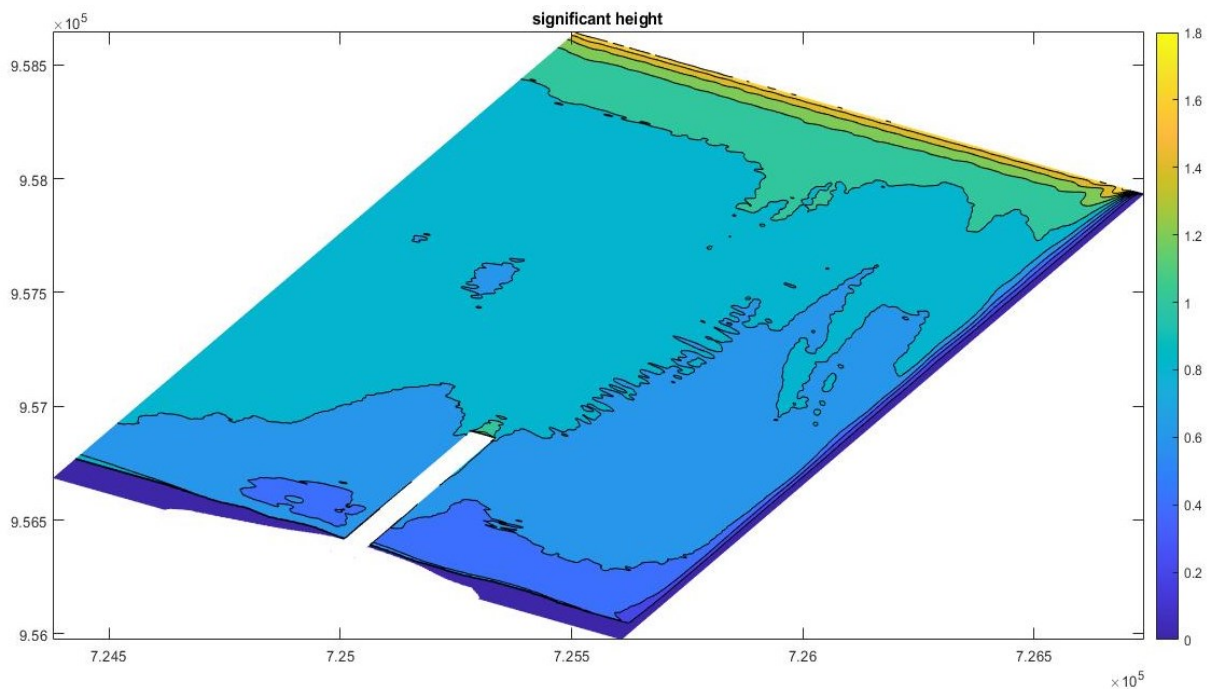


Figure 77 Significant wave height [m], for case g (dir=27.11 °N; sponge layer on East side; with a large domain)

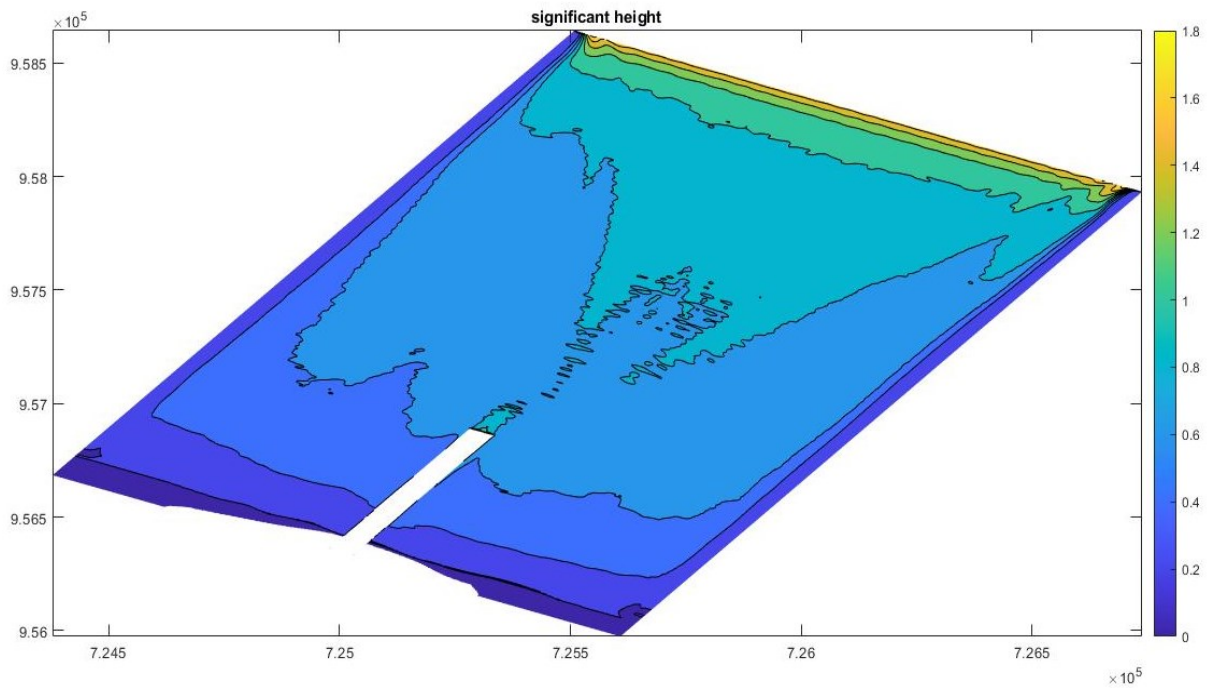


Figure 78 Significant wave height [m], for case g ($dir=27.11^\circ N$; sponge layer on East and West side; with a large domain)

6.1.2 Sea currents

It is useful to remember that the currents evolving in shallow waters, such as the ones analysed, are essentially of three types: rip, longshore and undertow. Knowledge of the current direction (and therefore its sign) suggests which type it belongs to.

The undertow current is directed from the coast to the open sea, for this reason it is defined by a negative value (the Y-axis pointing landward), otherwise the longshore current has a positive value because it is directed parallel to the bathymetry lines (in the same direction of X-axis).

All current maps of the simulations made with small domains are mainly characterized by a negative current velocity. For this reason, it was decided to use a larger domain in which the wave had more space to break and therefore minimize the undertow current. This occurred partially because the maps are still characterized by negative currents. But close to the

cofferdam, as shown in Figure 85, a positive current was obtained, which also corresponds to the maximum current value at the causeway.

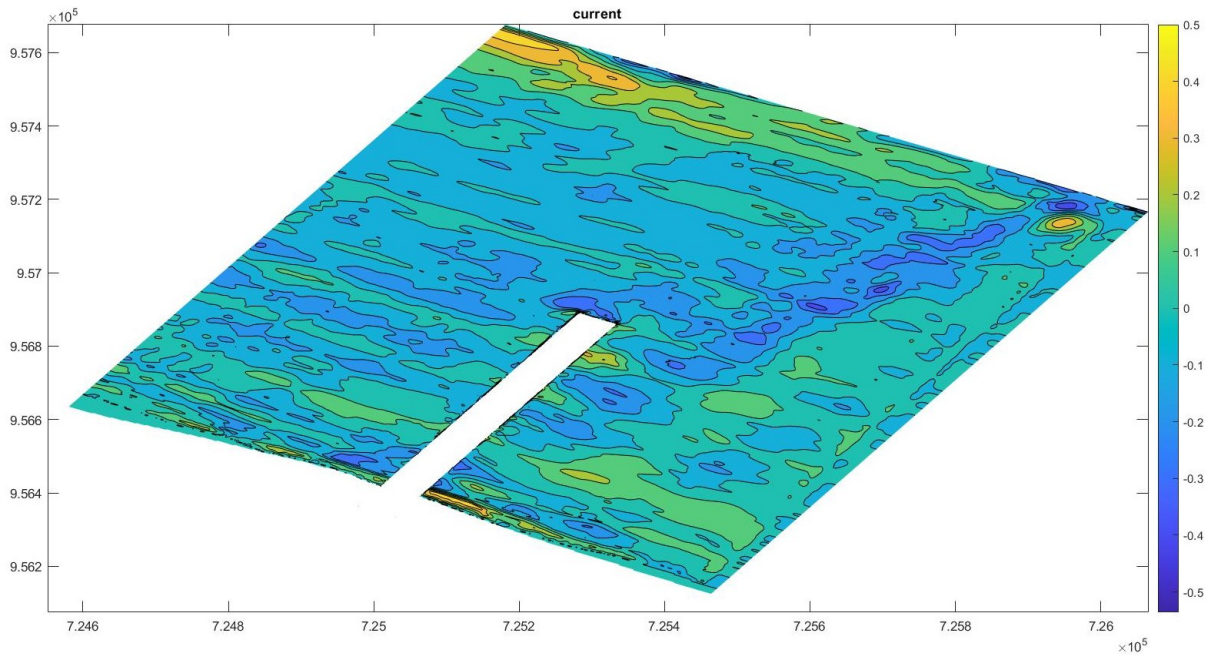


Figure 79 Current [m/s], for case a (dir=27.11 °N; sponge layer on East side)

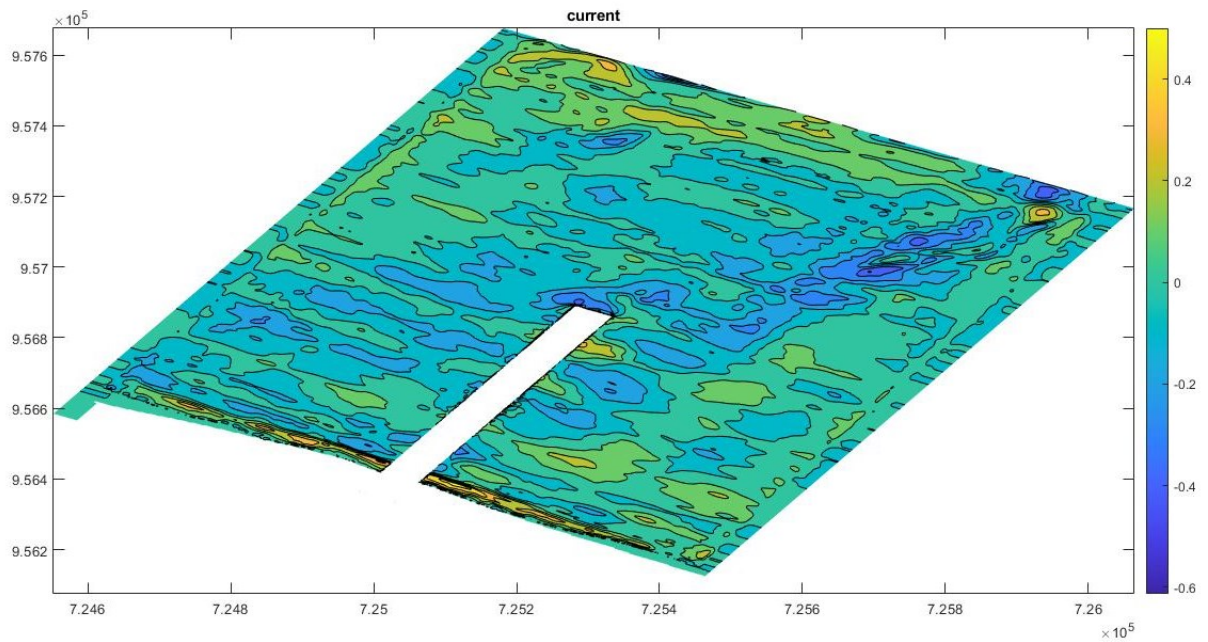


Figure 80 Current [m/s], for case b (dir=27.11 °N; sponge layer on East and West side)

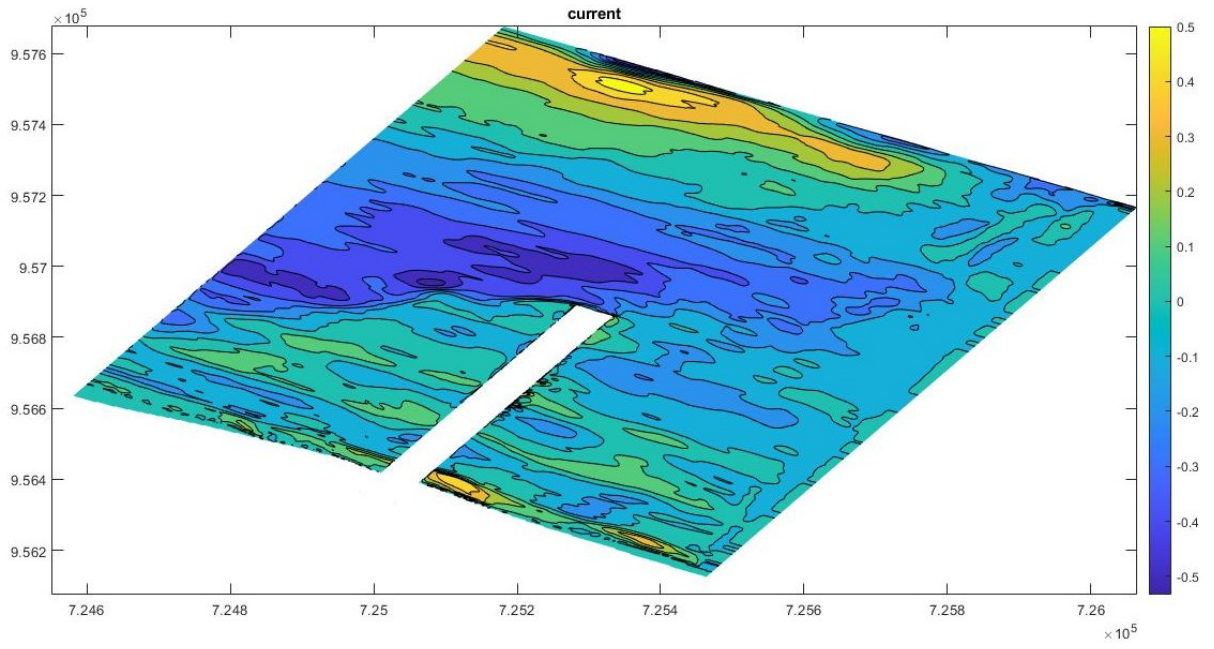


Figure 81 Current [m/s], for case c (dir=27.11 °N; sponge layer on East side; 3 hours of simulation)

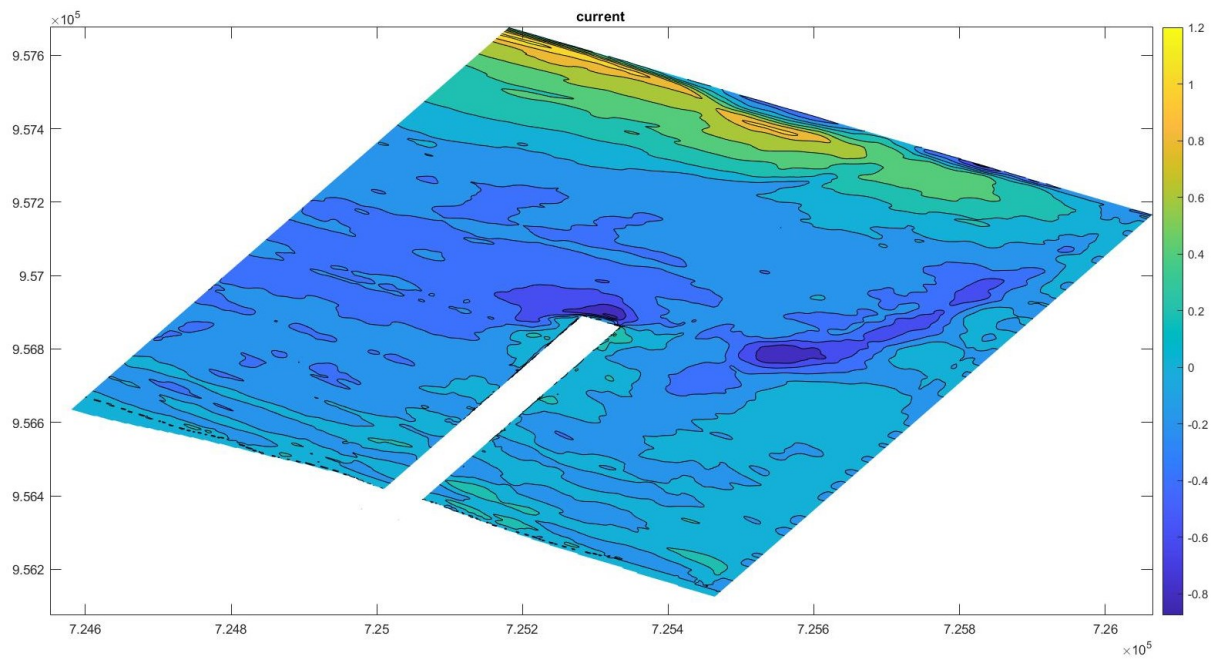


Figure 82 Current [m/s], for case d (dir=20 °N; sponge layer on East side)

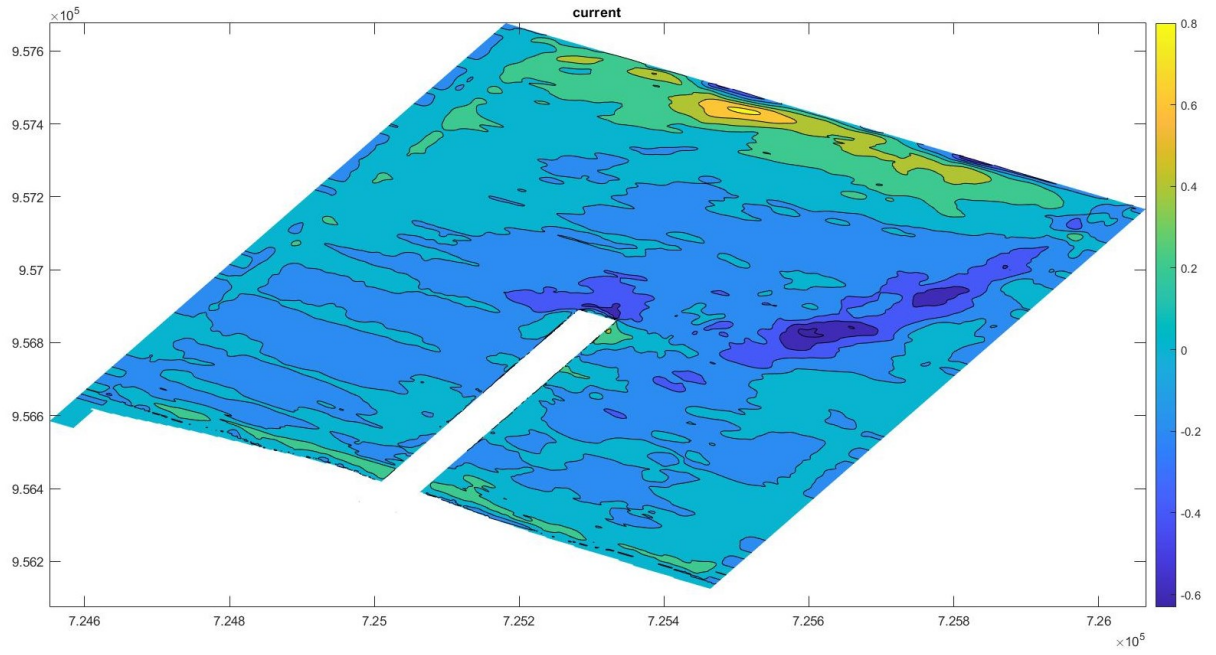


Figure 83 Current [m/s], for case e (dir=20 °N; sponge layer on East and West side)

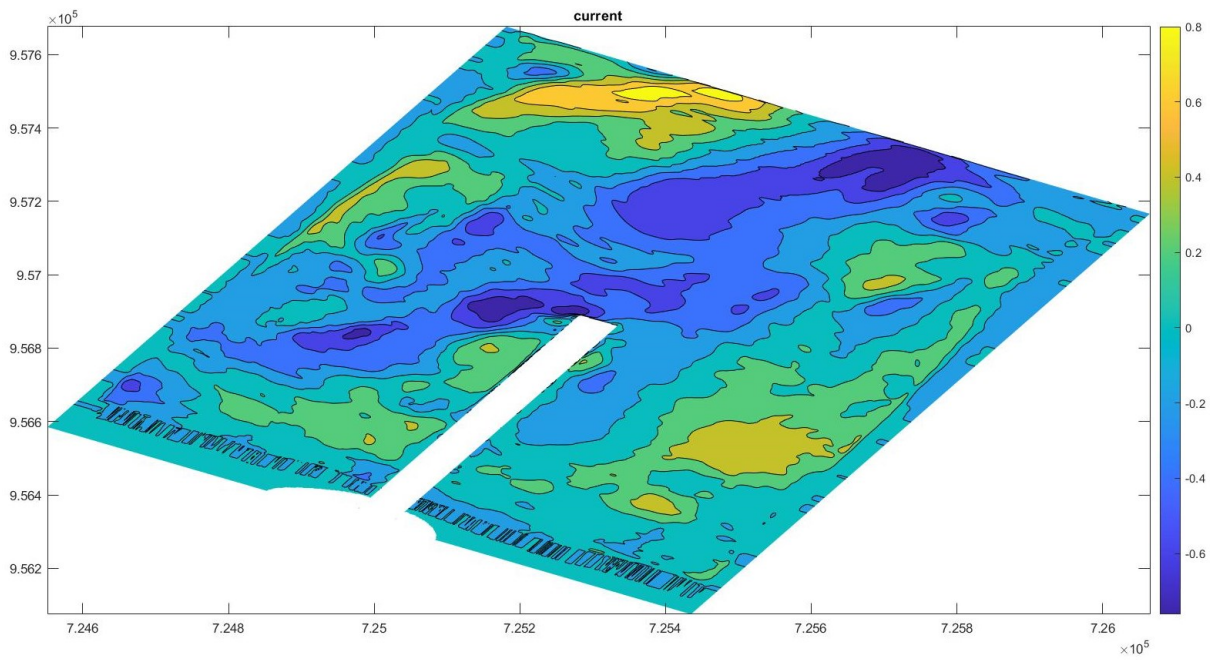


Figure 84 Current [m/s], for case f (dir=27.11 °N; sponge layer on East and West side; with a smoothed bathymetry)

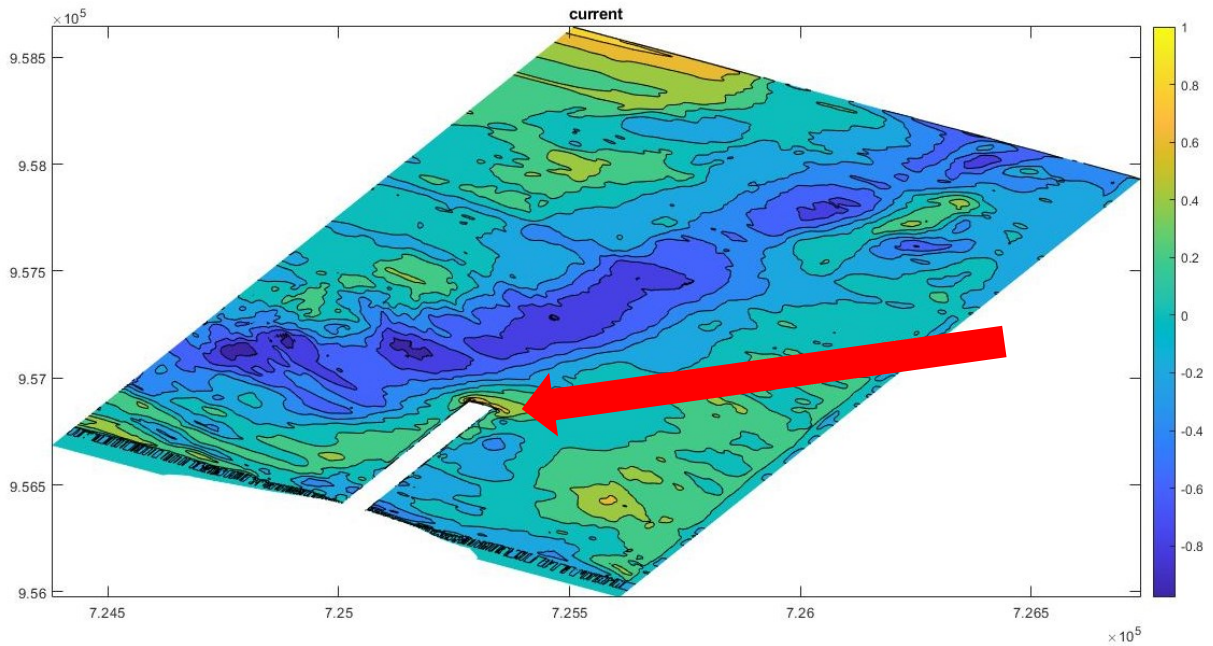


Figure 85 Currents [m/s], case g (dir=27.11 °N; sponge layer on East side; with a large domain)

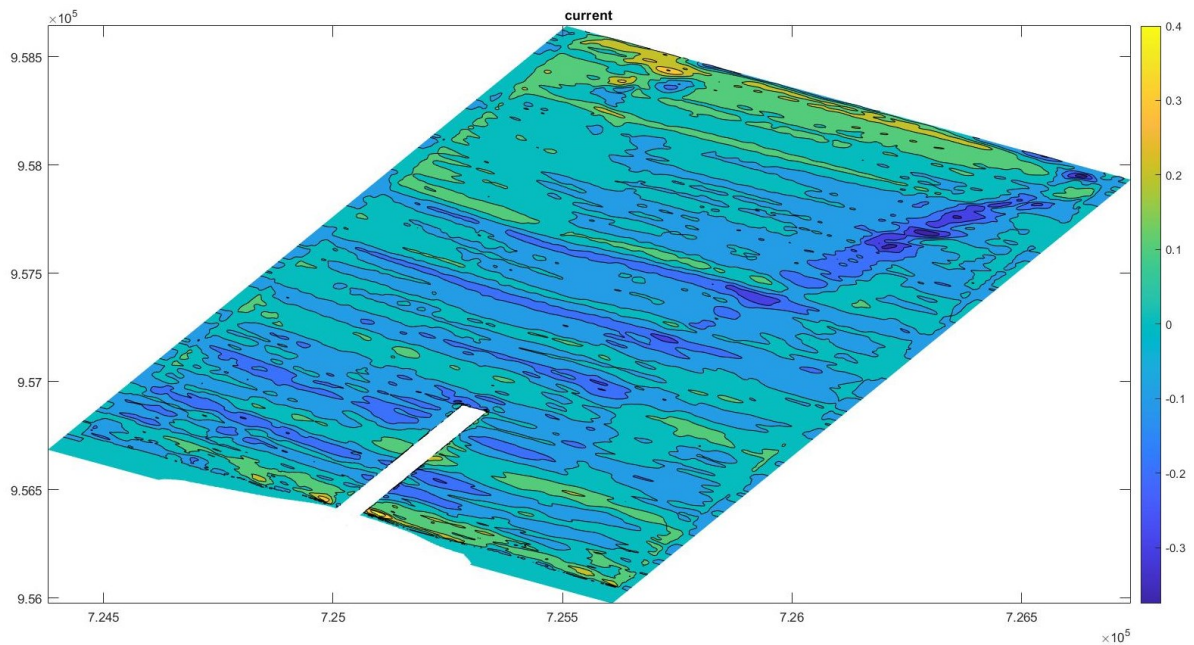


Figure 86 Currents [m/s], case h (dir=27.11 °N; sponge layer on East and West side; with a large domain)

6.1.3 Current induced seabed shear stress (τ_c)

τ_c has the maximum values in areas where the wave motion is altered by the presence of the obstacle, in front of the cofferdam and close to the coast line, as shown by Figure 87. While it is almost constant (zero) throughout the rest of the domain, for this reason only the plots of τ_c in the area in front of the cofferdam are reported.

In Figure 87, the greatest part of domain has a shear stress close to 0, but there are some areas in which $\tau_c > 0$. The lower part of image represents the shear stress that produces the erosion of the coast line, while the upper part, spuriously due to problems at the offshore boundary.

The images show how the choice to increase the size of the domain and to use a wave direction angle of 20° obtained the desired effects. In fact, in both cases peak stresses were seen at the points where the maximum erosion values occurred, at the edges of the cofferdam (Figure 91, Figure 92 and Figure 93).

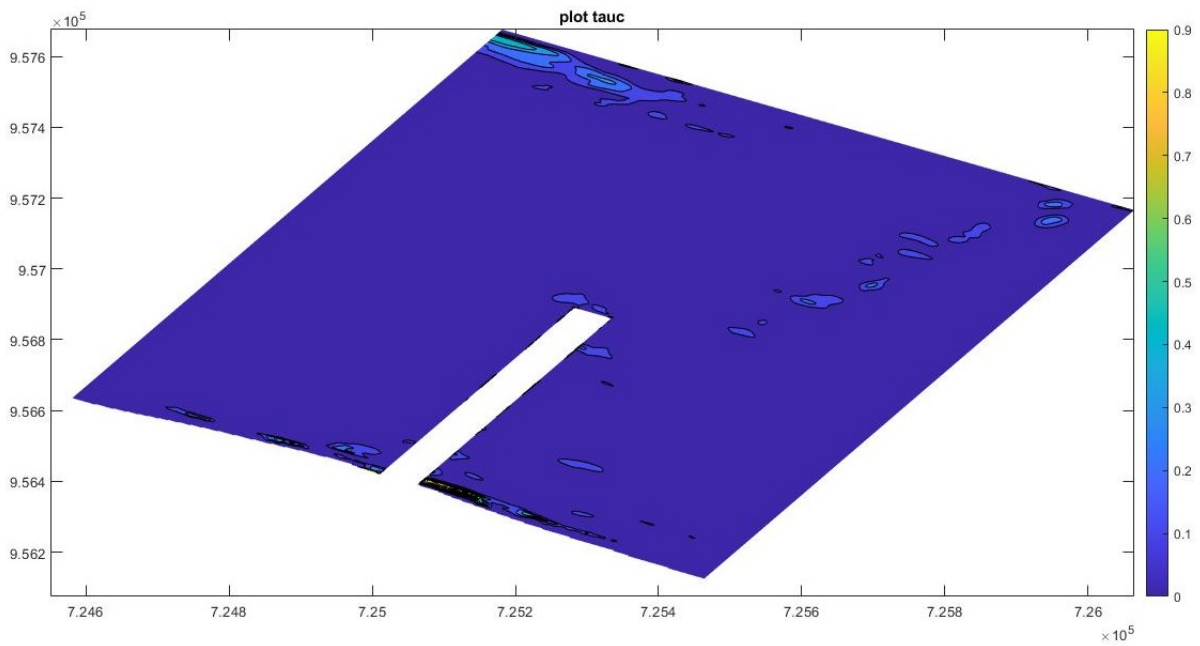


Figure 87 Shear stress produced by the current (τ_c) $\left[\frac{Kg}{ms^2}\right]$, case a (dir=27.11 °N; sponge layer on East side)

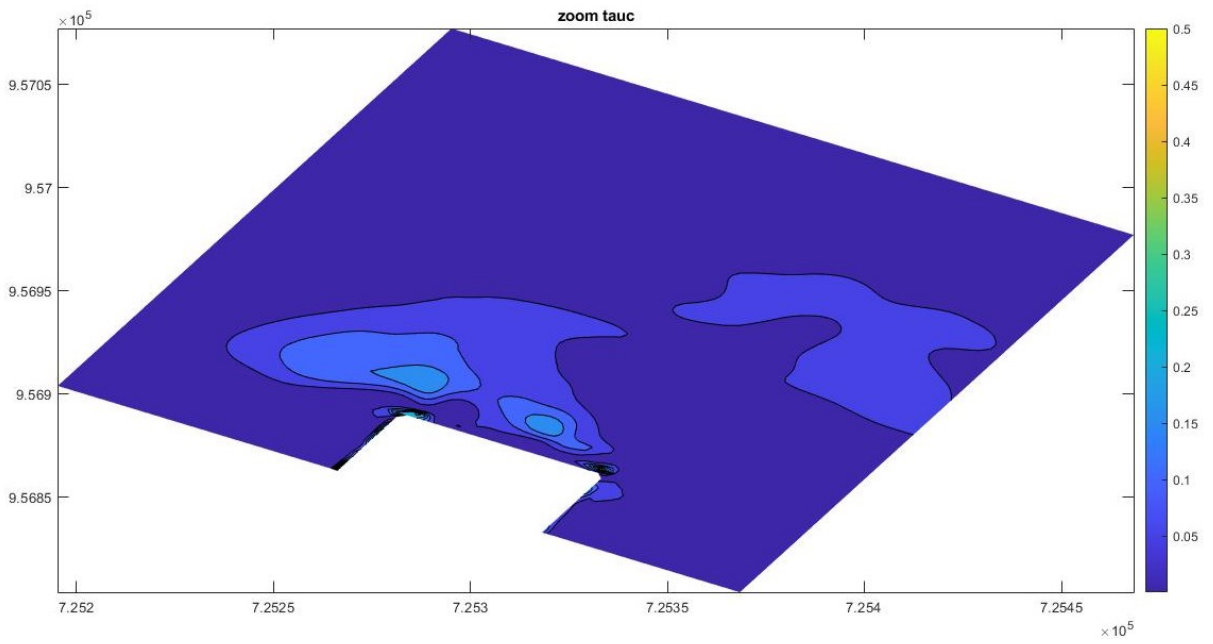


Figure 88 τ_c in interested area $\left[\frac{Kg}{ms^2}\right]$, case a (dir=27.11 °N; sponge layer on East side)

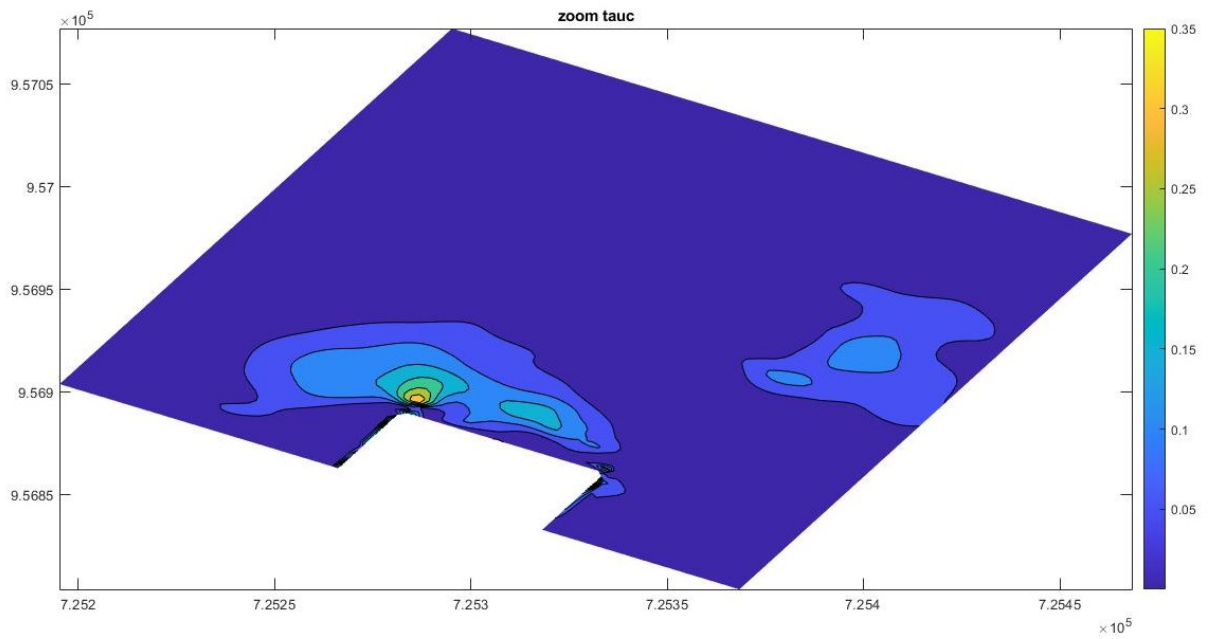


Figure 89 τ_c in interested area $\left[\frac{Kg}{ms^2}\right]$, case b (dir=27.11 °N; sponge layer on East and West side)

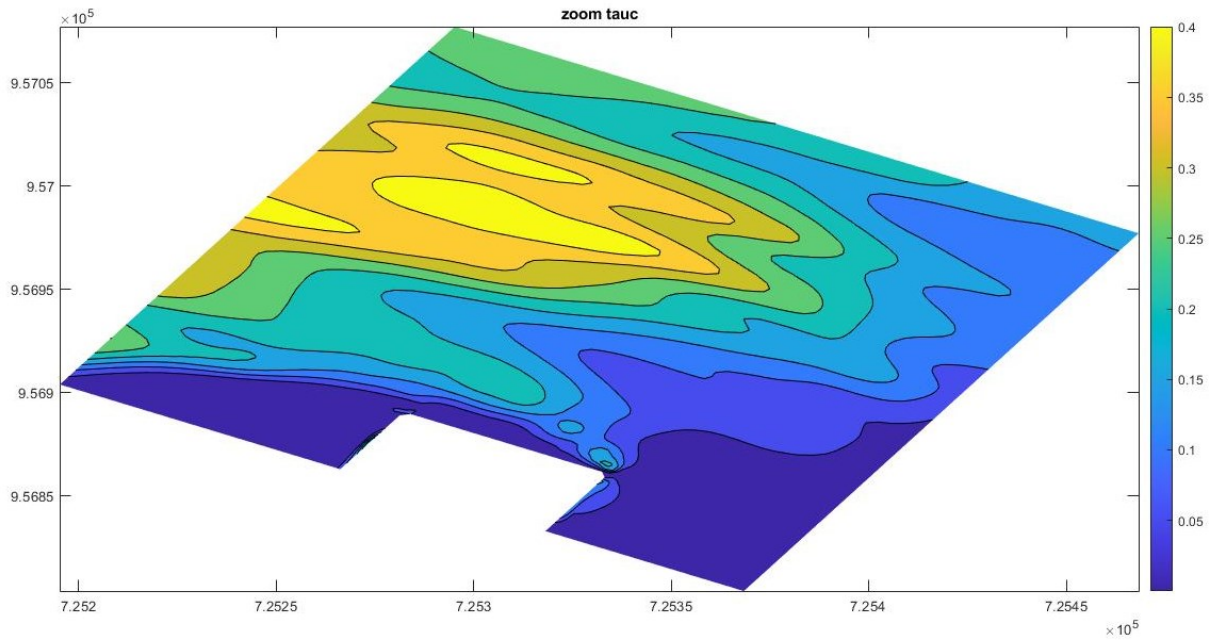


Figure 90 τ_c in interested area $\left[\frac{Kg}{ms^2}\right]$, case c ($dir=27.11^\circ N$; sponge layer on East side; 3 hours of simulation)

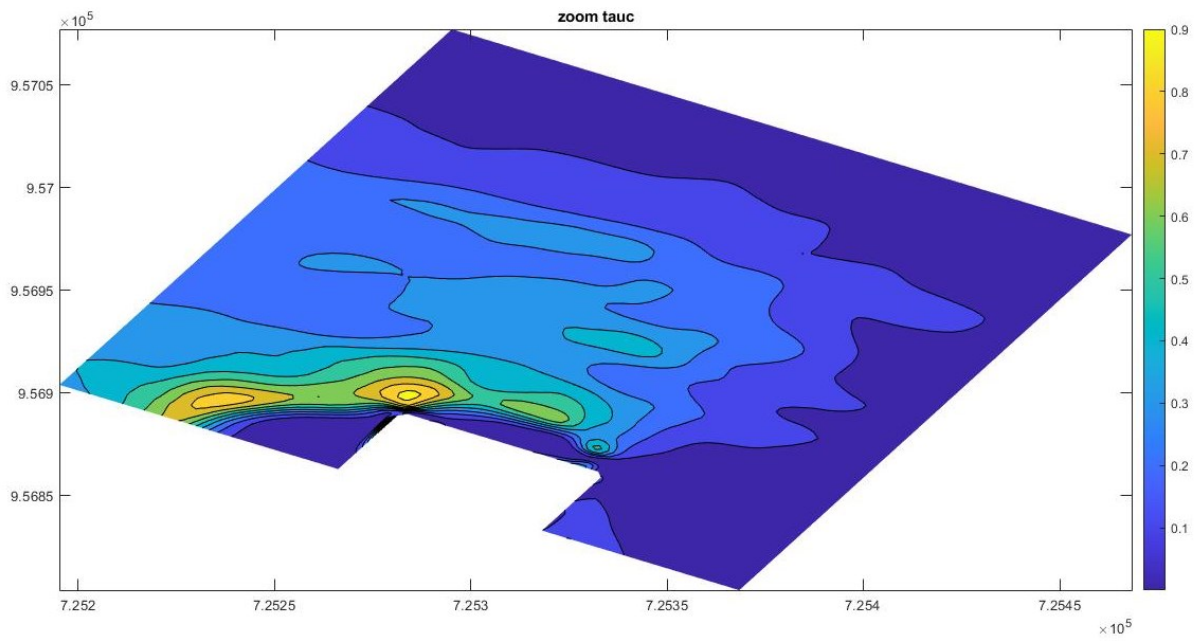


Figure 91 τ_c in interested area $\left[\frac{Kg}{ms^2}\right]$, case d ($dir=20^\circ N$; sponge layer on East side)

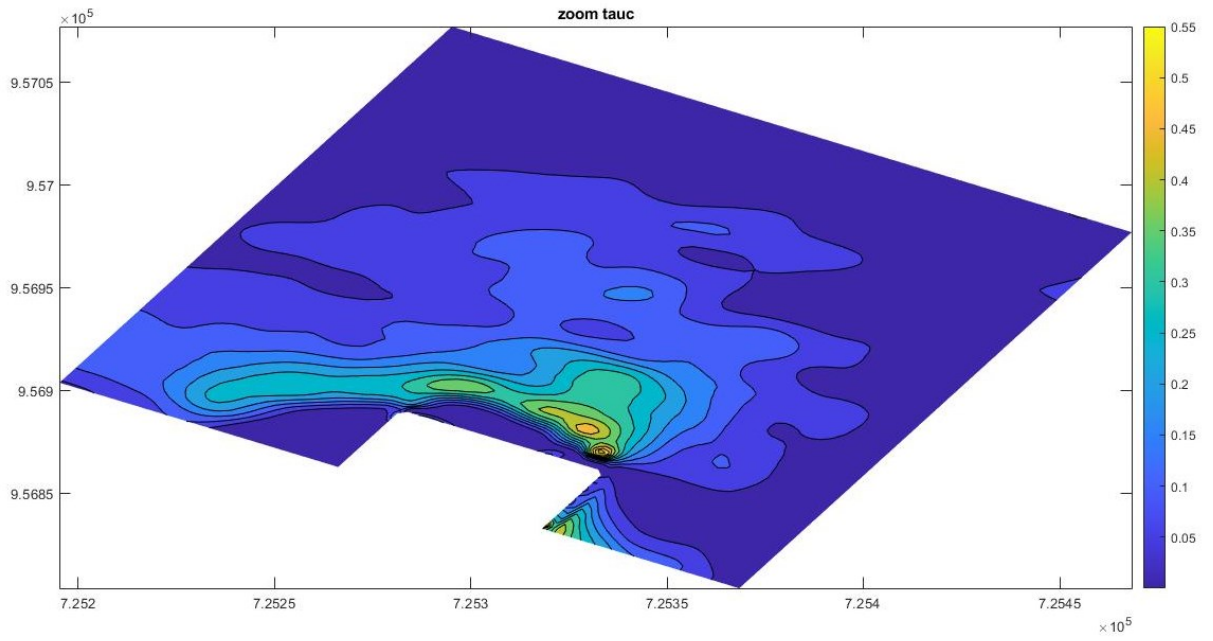


Figure 92 τ_c in interested area $\left[\frac{Kg}{m^2}\right]$, case e ($dir=20^\circ N$; sponge layer on East and West side)

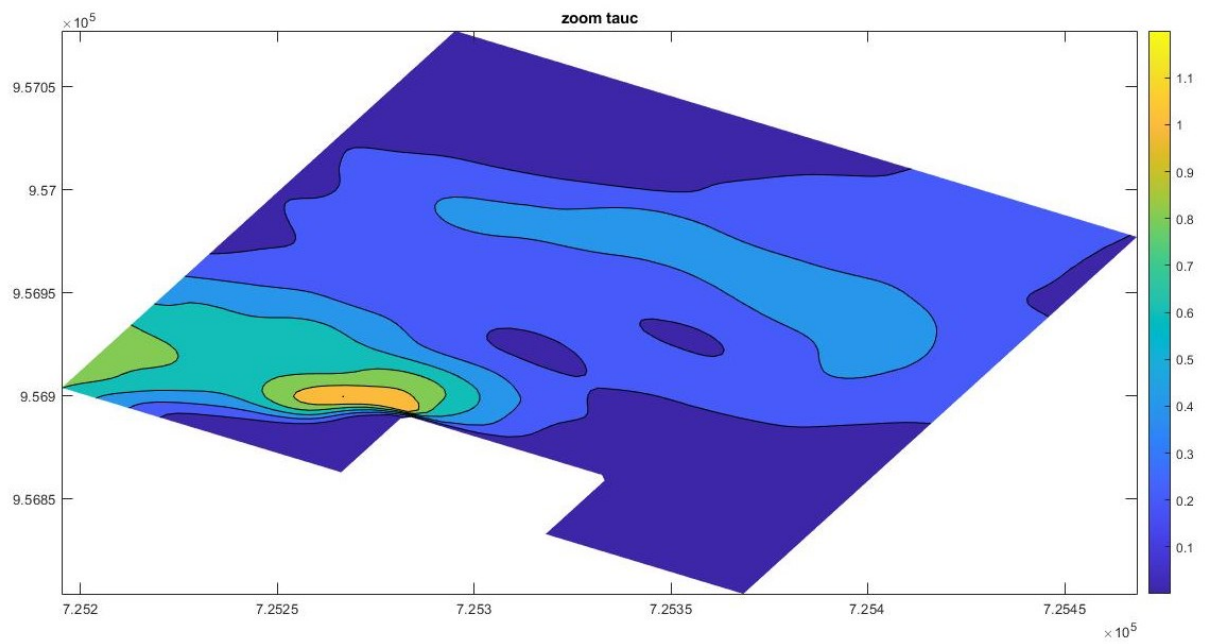


Figure 93 τ_c in interested area $\left[\frac{Kg}{m^2}\right]$, case f ($dir=27.11^\circ N$; sponge layer on East and West side; with a smoothed bathymetry)

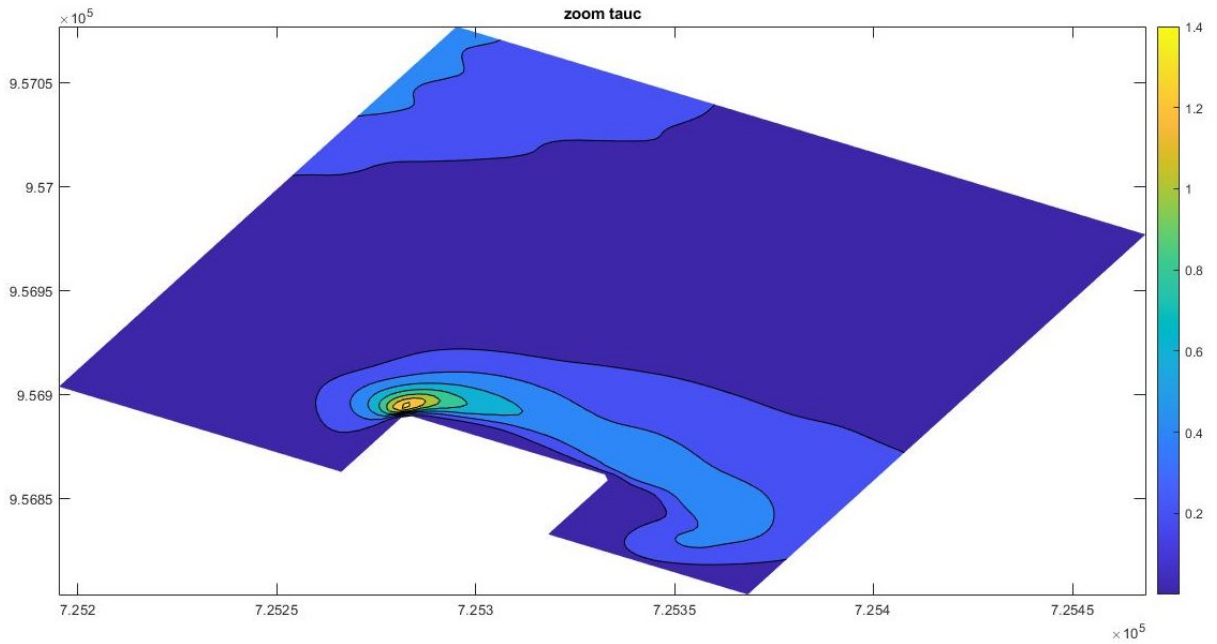


Figure 94 τ_c in interested area $\left[\frac{Kg}{m^2}\right]$, case g (dir=27.11 °N; sponge layer on East side; with a large domain)

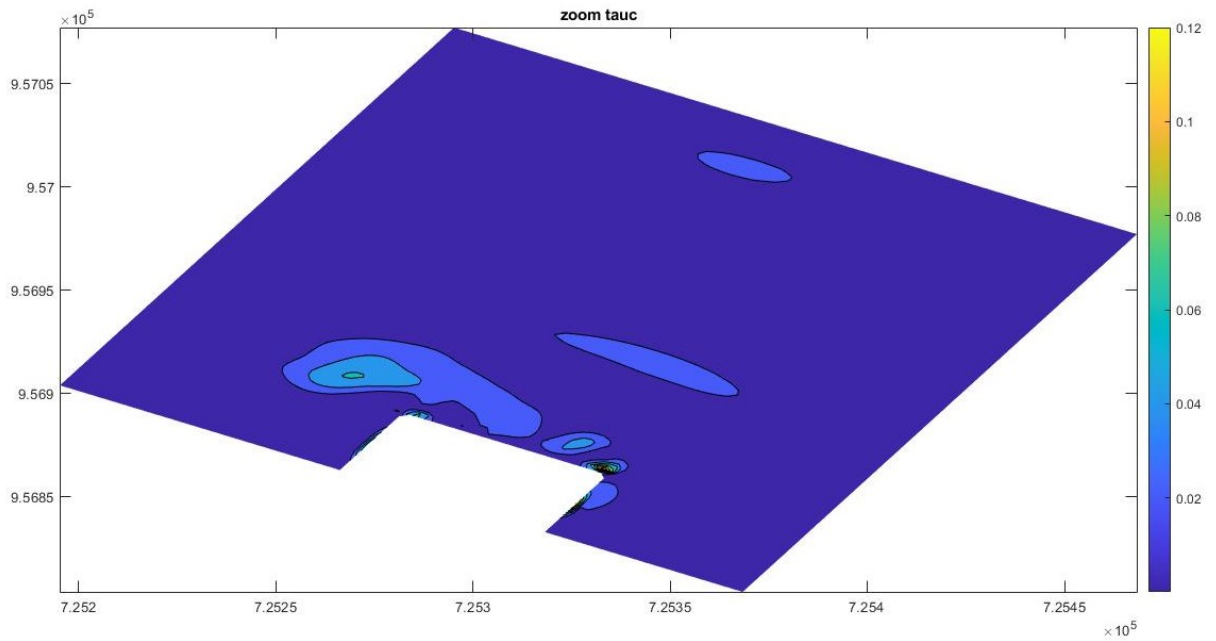


Figure 95 τ_c in interested area $\left[\frac{Kg}{m^2}\right]$, case h (dir=27.11 °N; sponge layer on East and West side; with a large domain)

6.1.4 Wave induced shear stress (τ_w)

Unlike τ_c , the τ_w is appreciable throughout the domain, for this reason both the detailed maps in front of the cofferdam and over the entire domain are shown.

The wave varies in velocity and acceleration over the wave period. In the same way does τ_w , which is directly proportional to the square of the wave velocity. For this reason, for each simulation, the plot that was chosen showed the highest value of τ_w among the 11 analysed (wave time to peak = 11s)

The global shear stress maps show how the maximum values of τ_w are attained at the points where the wave breaks, forming a series of parallel lines to the coastline.

In the detailed images, especially in the simulations with double sponge layer, it is known how the effect of reflection on the cofferdam produces the formation of other lines with high shear stress values.

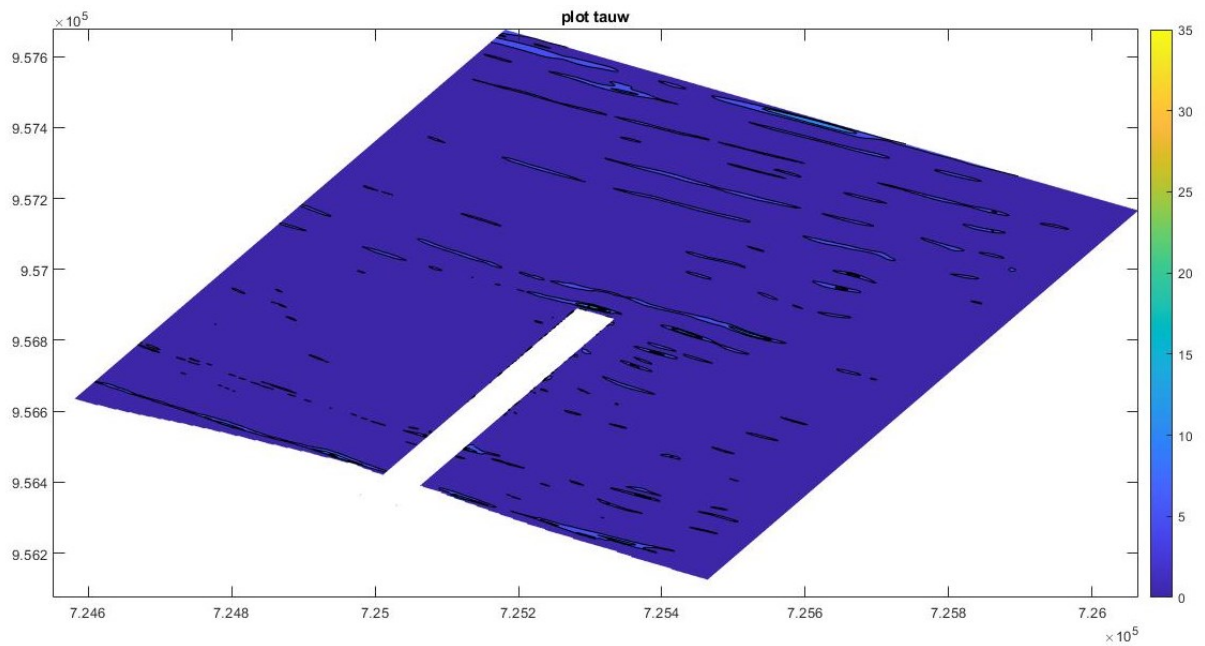


Figure 96 Shear stress produced by oscillatory flow (τ_w), $\left[\frac{Kg}{m^2}\right]$, case a (dir=27.11 °N; sponge layer on East side)

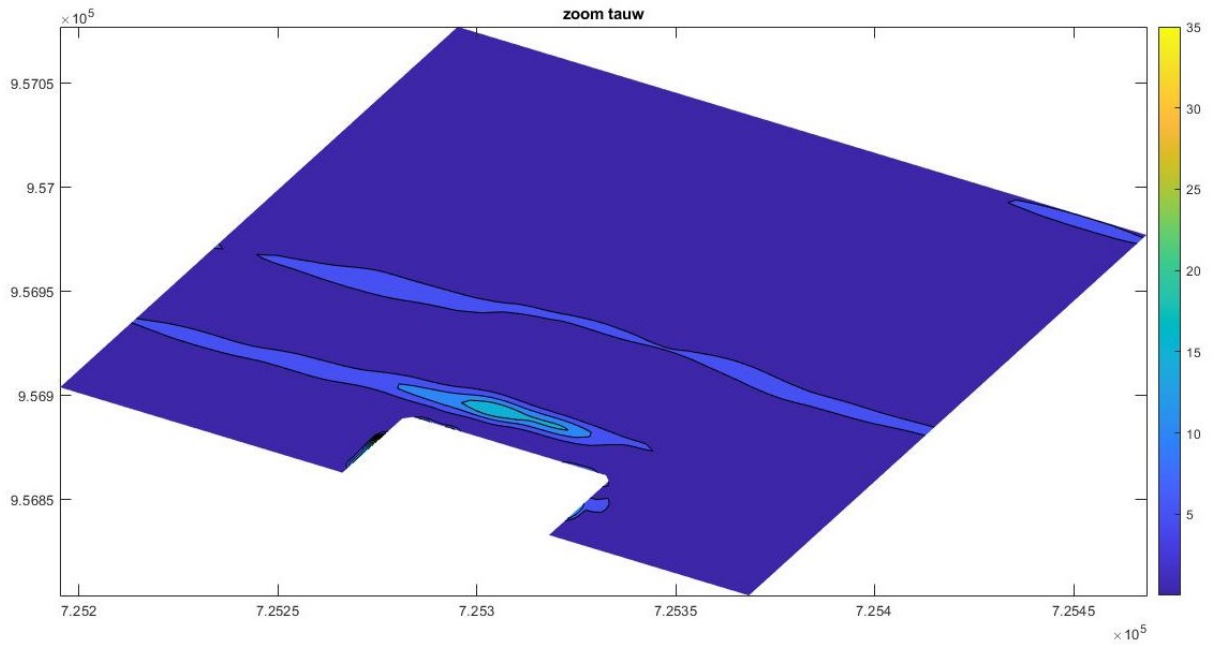


Figure 97 τ_w in interested area $\left[\frac{Kg}{ms^2}\right]$, case a (dir=27.11 °N; sponge layer on East side)

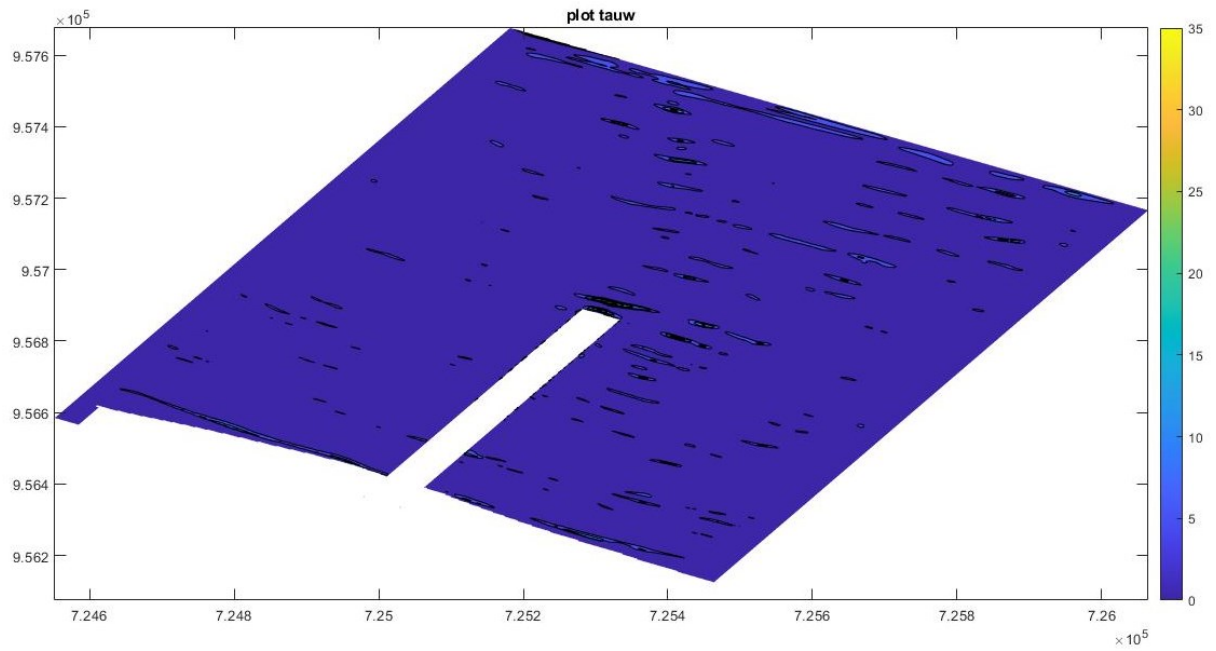


Figure 98 Shear stress produced by oscillatory flow (τ_w), $\left[\frac{Kg}{ms^2}\right]$, case b (dir=27.11 °N; sponge layer on East and West side)

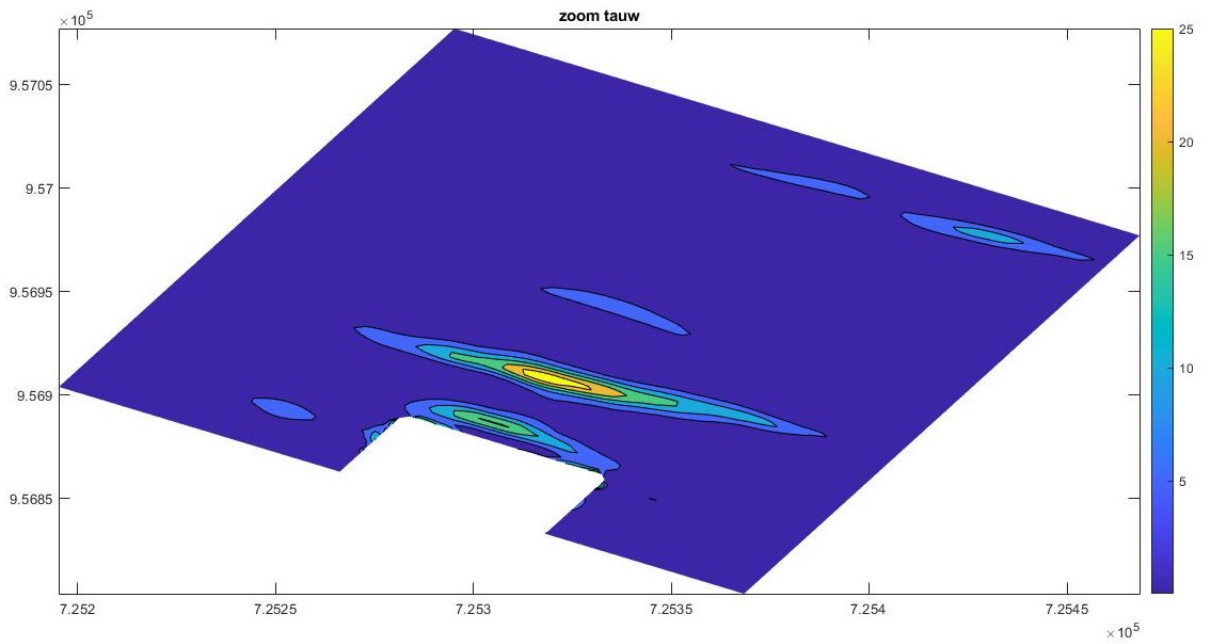


Figure 99 τ_w in interested area $\left[\frac{Kg}{ms^2}\right]$, case b (dir=27.11 °N; sponge layer on East and West side)

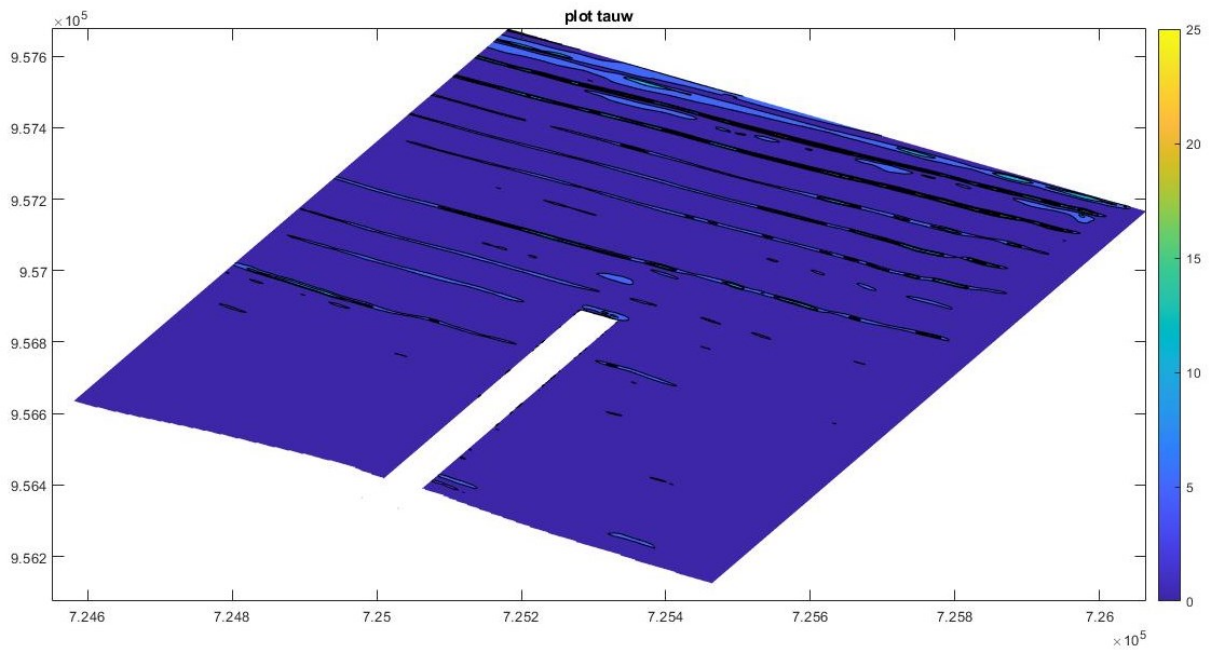


Figure 100 Shear stress produced by oscillatory flow (τ_w) $\left[\frac{Kg}{ms^2}\right]$, case c (dir=27.11 °N; sponge layer on East side; 3 hours of simulation)

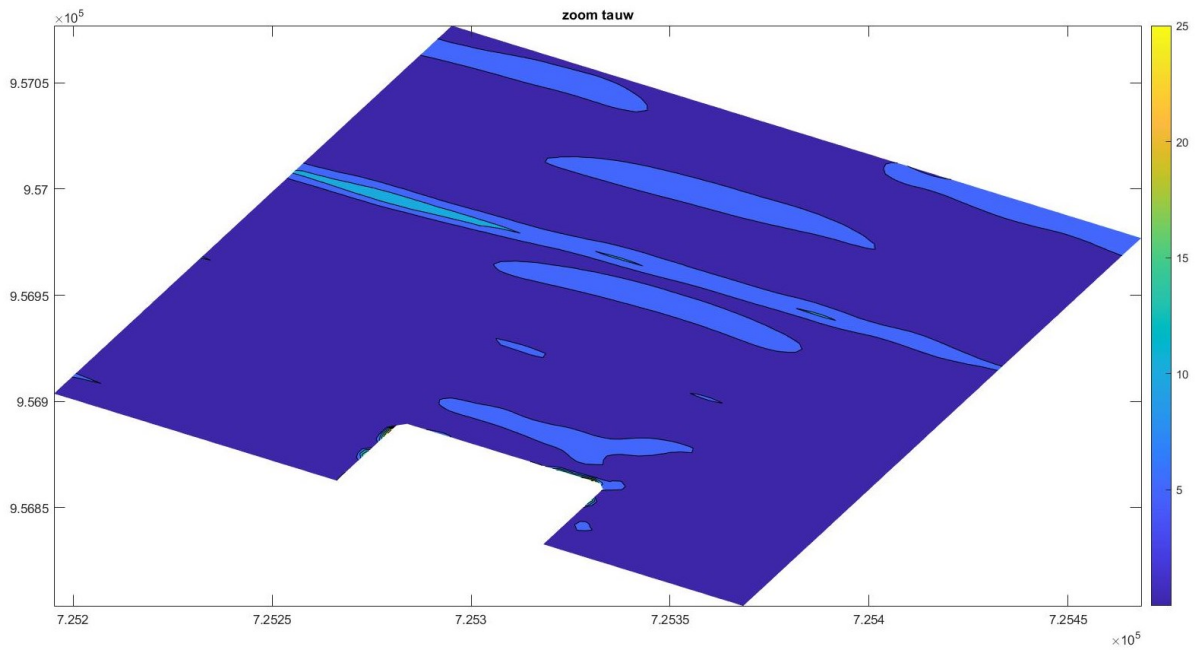


Figure 101 τ_w in interested area [$\text{Kg}/(\text{ms}^2)$], case c (dir=27.11 °N; sponge layer on East side; 3 hours of simulation)

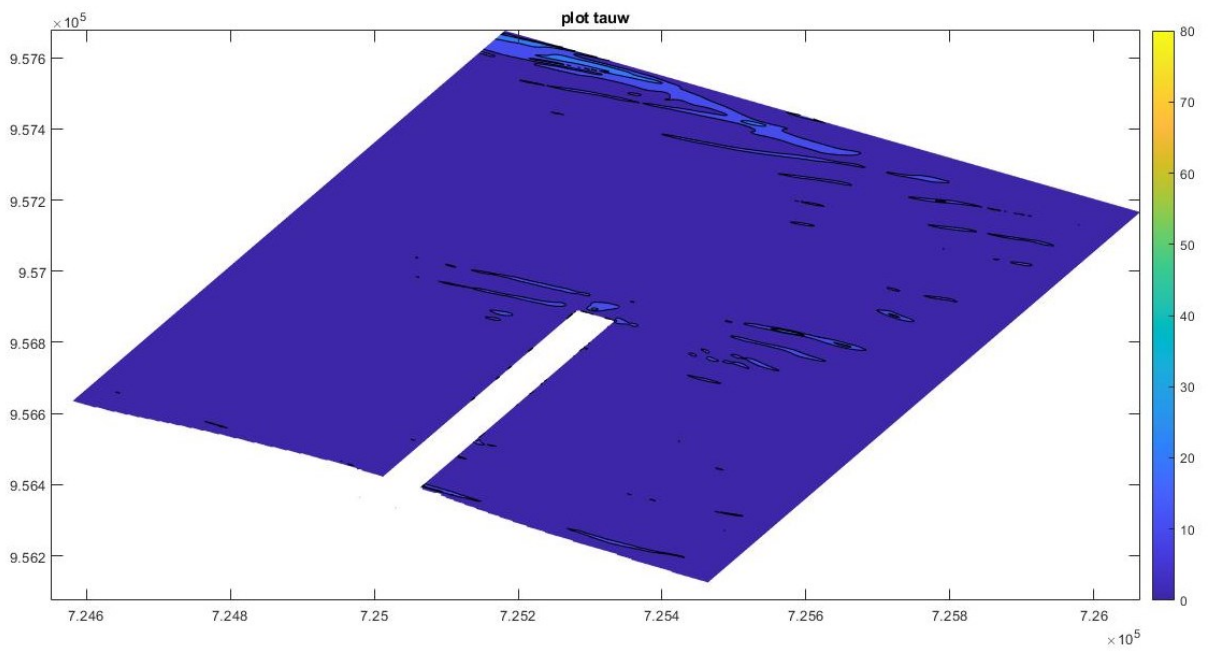


Figure 102 Shear stress produced by oscillatory flow (τ_w) [$\frac{\text{Kg}}{\text{ms}^2}$], case d (dir=20 °N; sponge layer on East side)

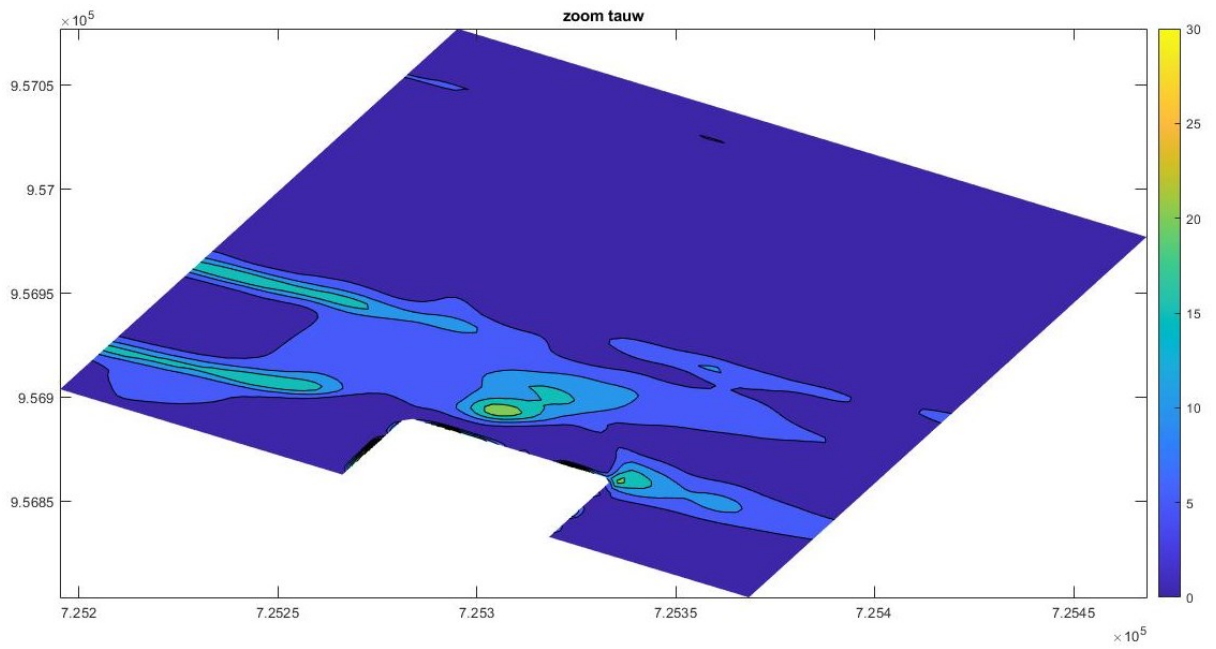


Figure 103 τ_w in interested area $\left[\frac{Kg}{m.s^2}\right]$, case d (dir=20 °N; sponge layer on East side)

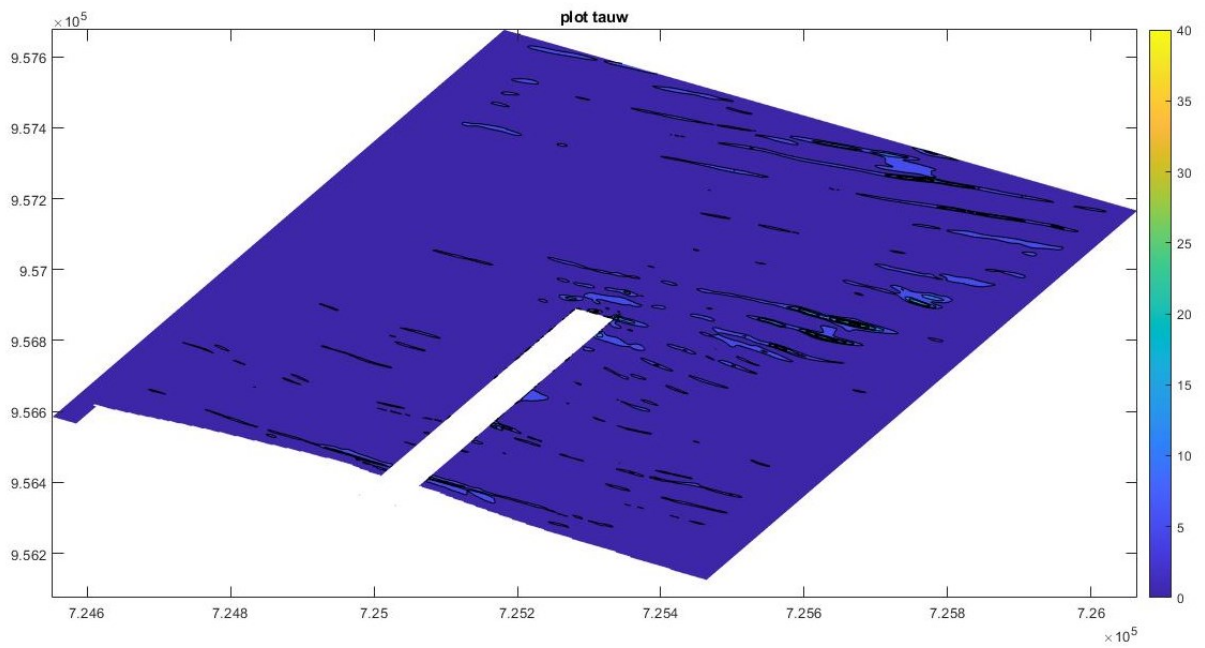


Figure 104 Shear stress produced by oscillatory flow (τ_w) $\left[\frac{Kg}{m.s^2}\right]$, case e (dir=20 °N; sponge layer on East and West side)

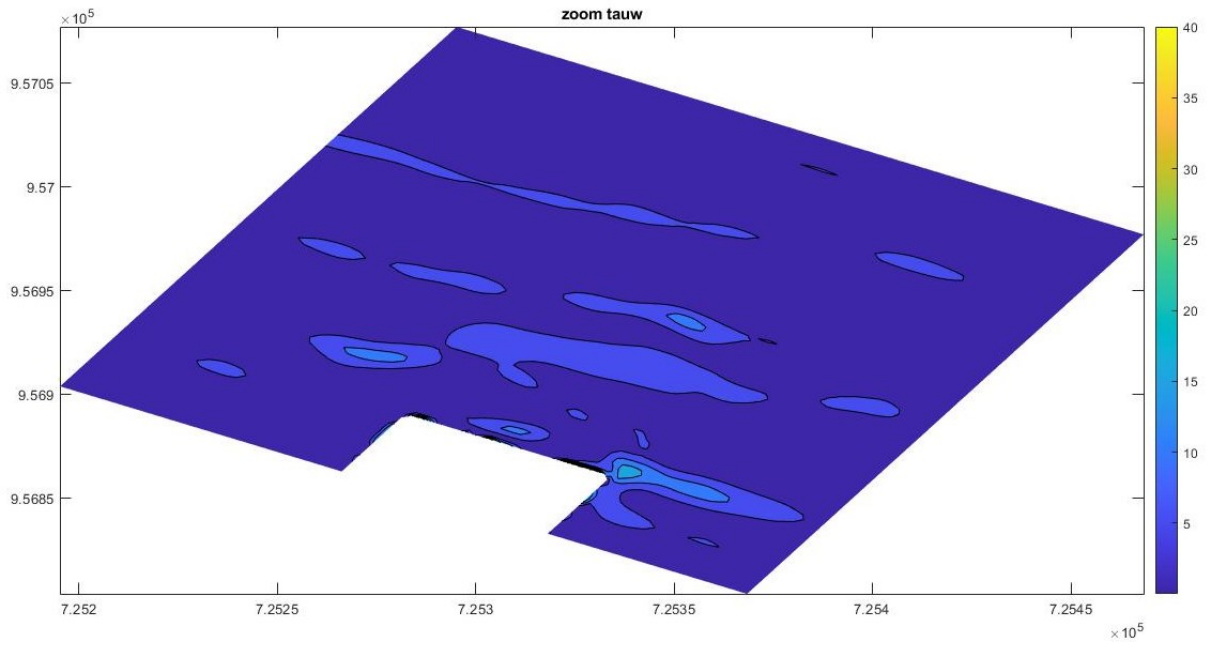


Figure 105 τ_w in interested area $\left[\frac{Kg}{m^2}\right]$, case e (dir=20 °N; sponge layer on East and West side)

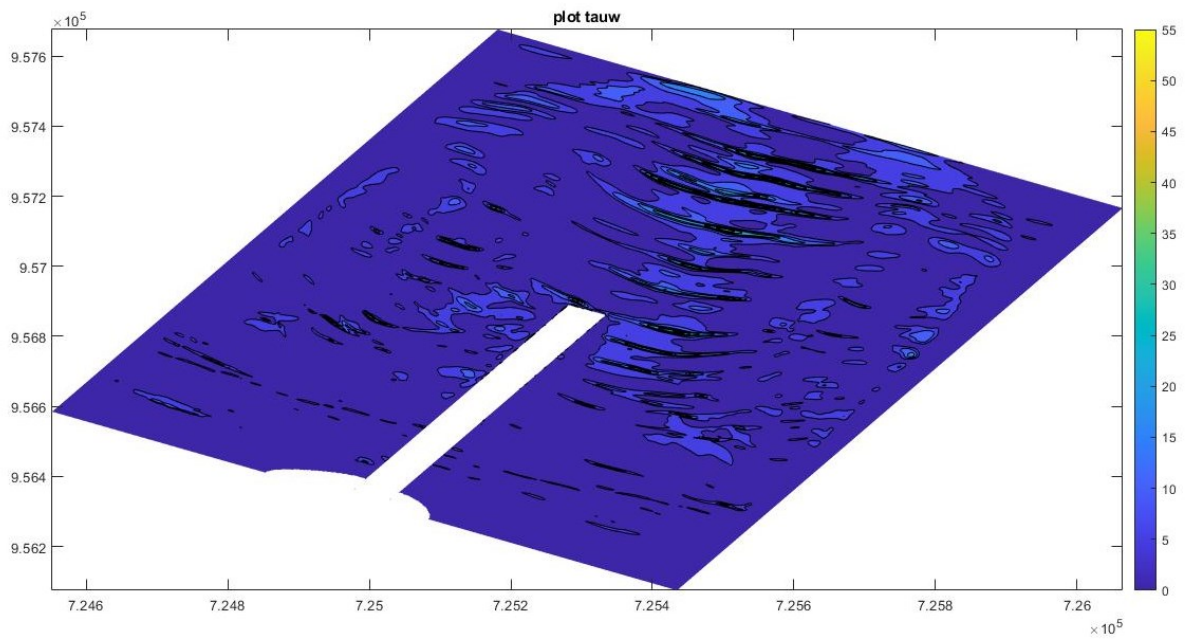


Figure 106 Shear stress produced by oscillatory flow (τ_w) $\left[\frac{Kg}{m^2}\right]$, case f (dir=27.11 °N; sponge layer on East and West side; with a smoothed bathymetry)

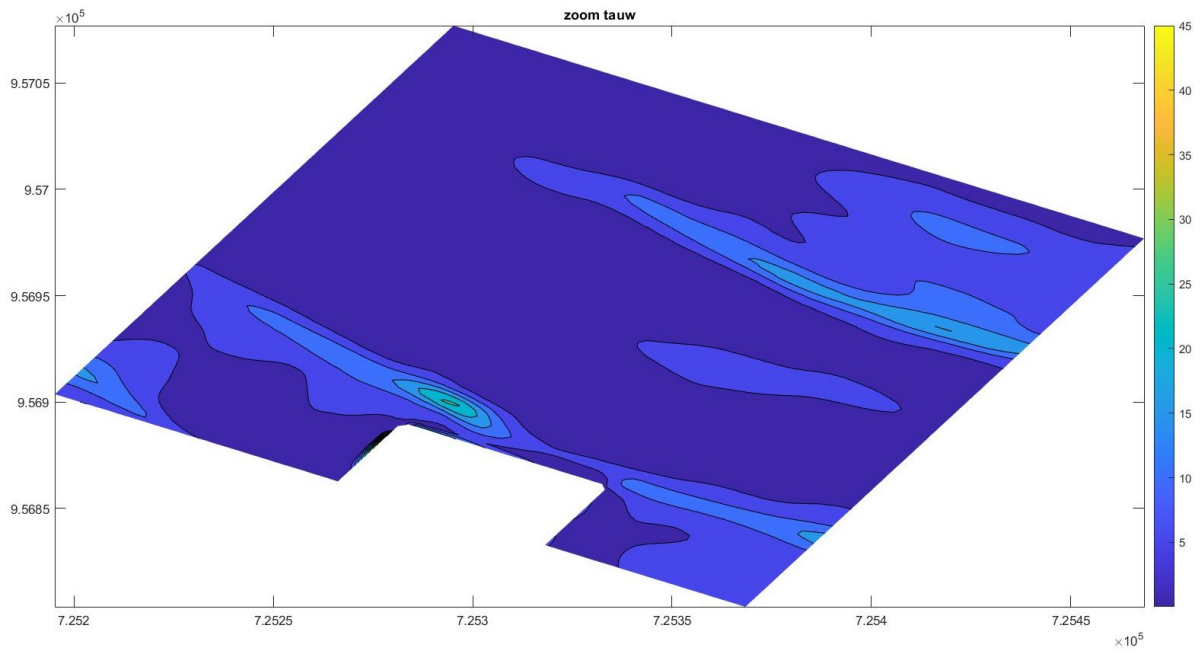


Figure 107 τ_w in interested area $\left[\frac{Kg}{ms^2}\right]$, case f (dir=27.11 °N; sponge layer on East and West side; with a smoothed bathymetry)

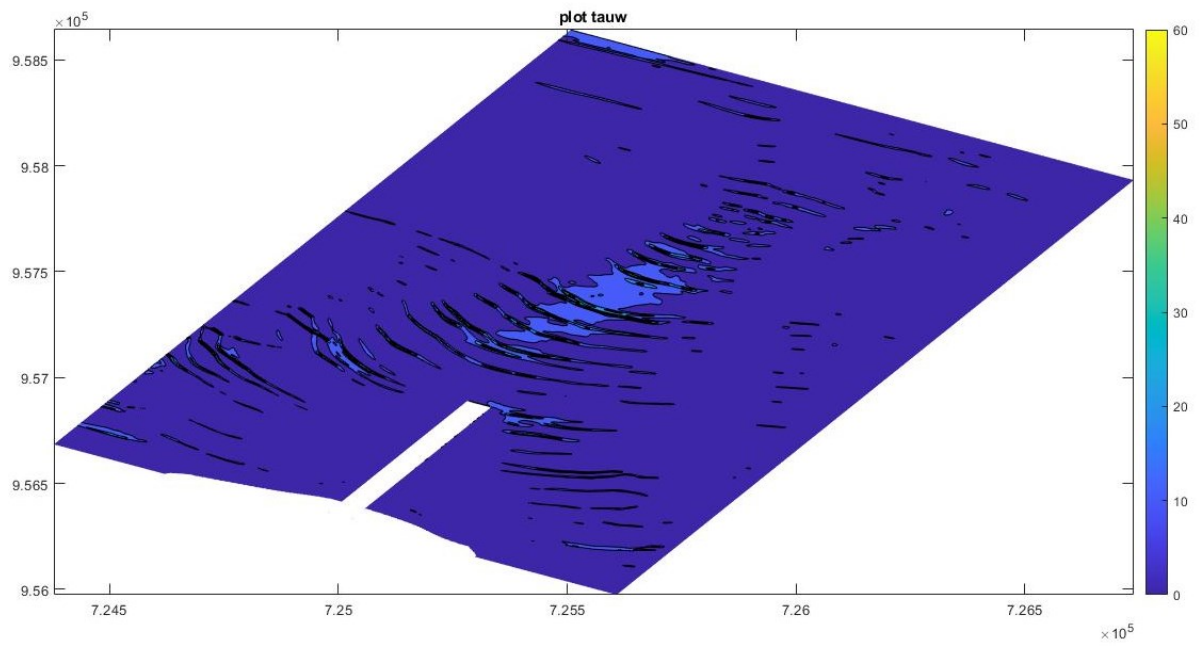


Figure 108 Shear stress produced by oscillatory flow (τ_w) $\left[\frac{Kg}{ms^2}\right]$, case g (dir=27.11 °N; sponge layer on East side; with a large domain)

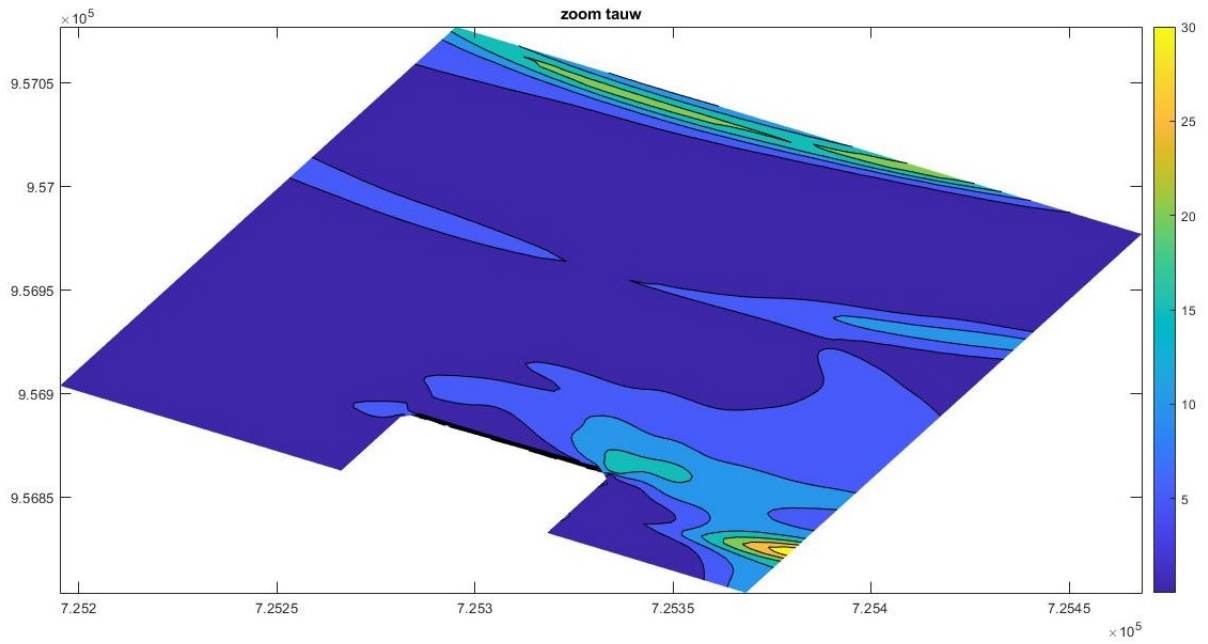


Figure 109 τ_w in interested area $\left[\frac{Kg}{ms^2}\right]$, case g (dir=27.11 °N; sponge layer on East side; with a large domain)

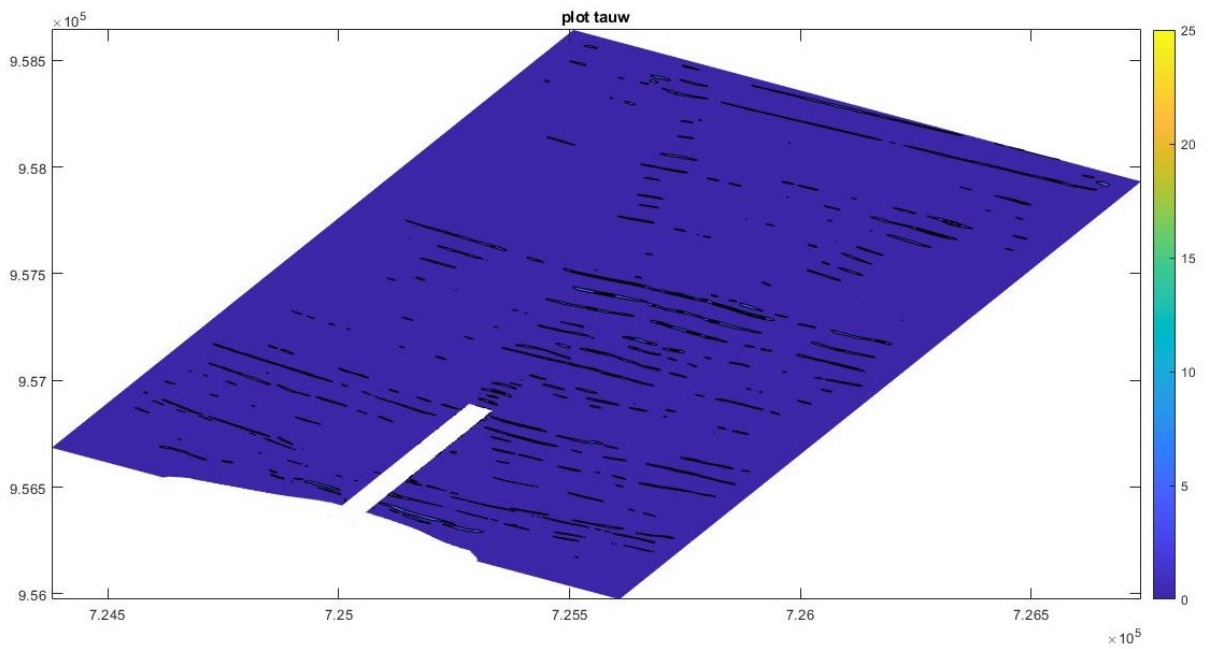


Figure 110 Shear stress produced by oscillatory flow (τ_w) $\left[\frac{Kg}{ms^2}\right]$, case h (dir=27.11 °N; sponge layer on East and West side; with a large domain)

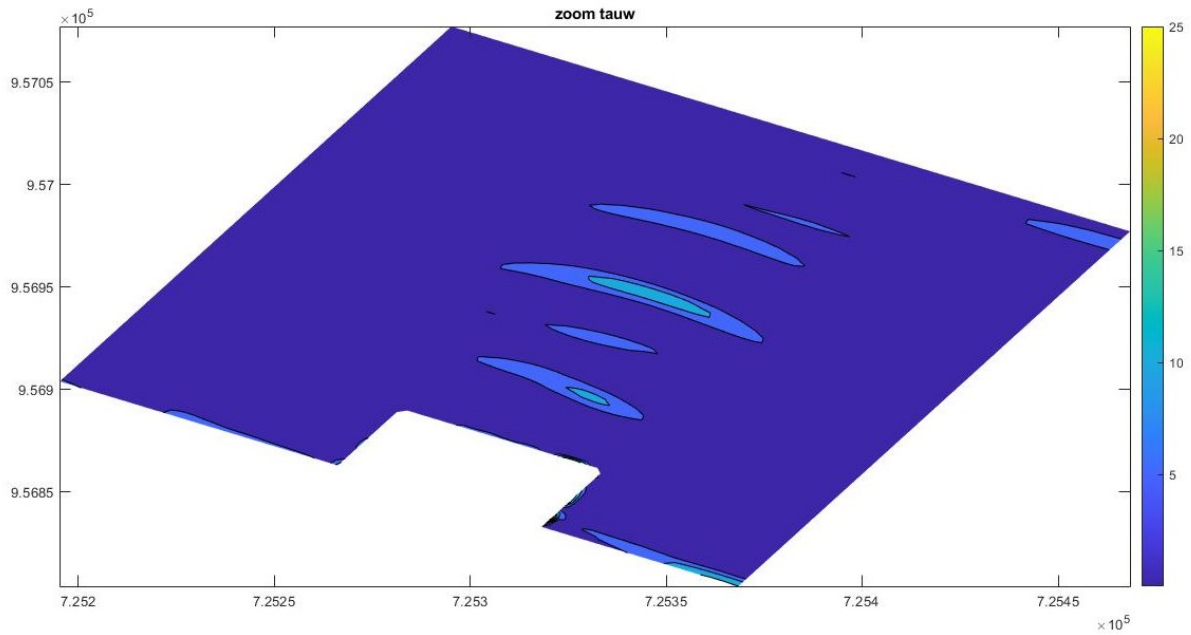


Figure 111 τ_w in interested area $\left[\frac{Kg}{ms^2}\right]$, case h (dir=27.11 °N; sponge layer on East and West side; with a large domain)

6.1.5 Total shear stress τ

As shown in the images of the previous paragraphs, τ_w is two or three orders of magnitude larger than the τ_c . For this reason, the final value of τ almost coincides with that of τ_w , therefore only the detail maps are shown.

It is useful to observe how the maximum τ values that are shown in the colour bar are not visible on the map; however, these exist close to the cofferdam.

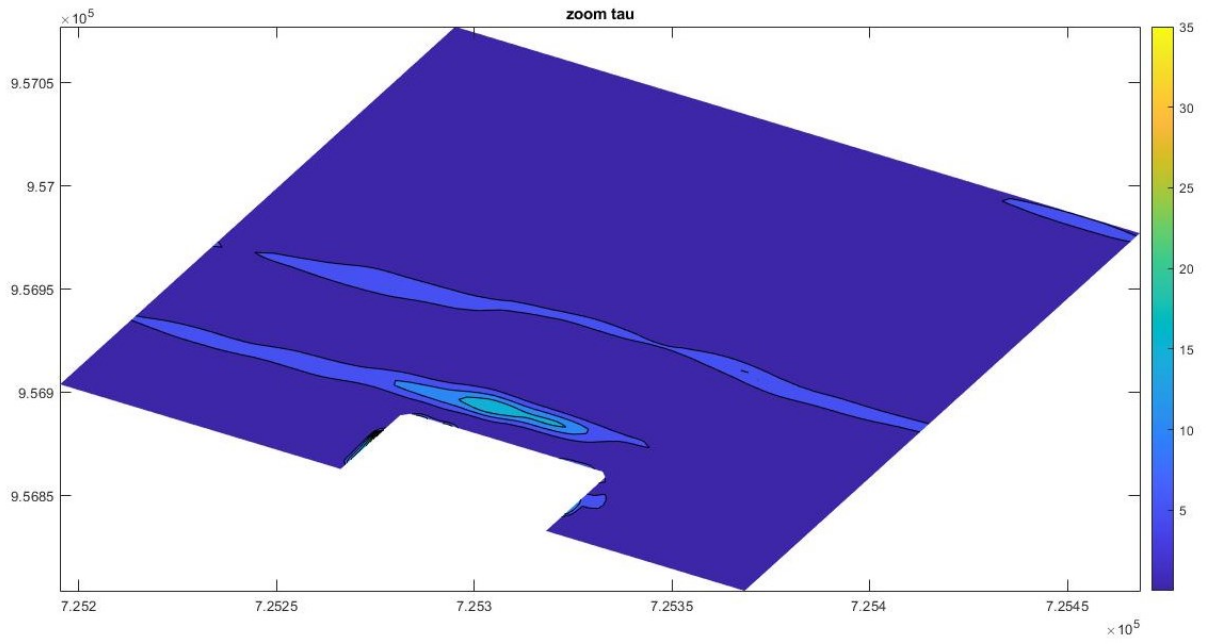


Figure 112 τ in interested area $\left[\frac{Kg}{ms^2}\right]$, case a ($dir=27.11^\circ N$; sponge layer on East side)

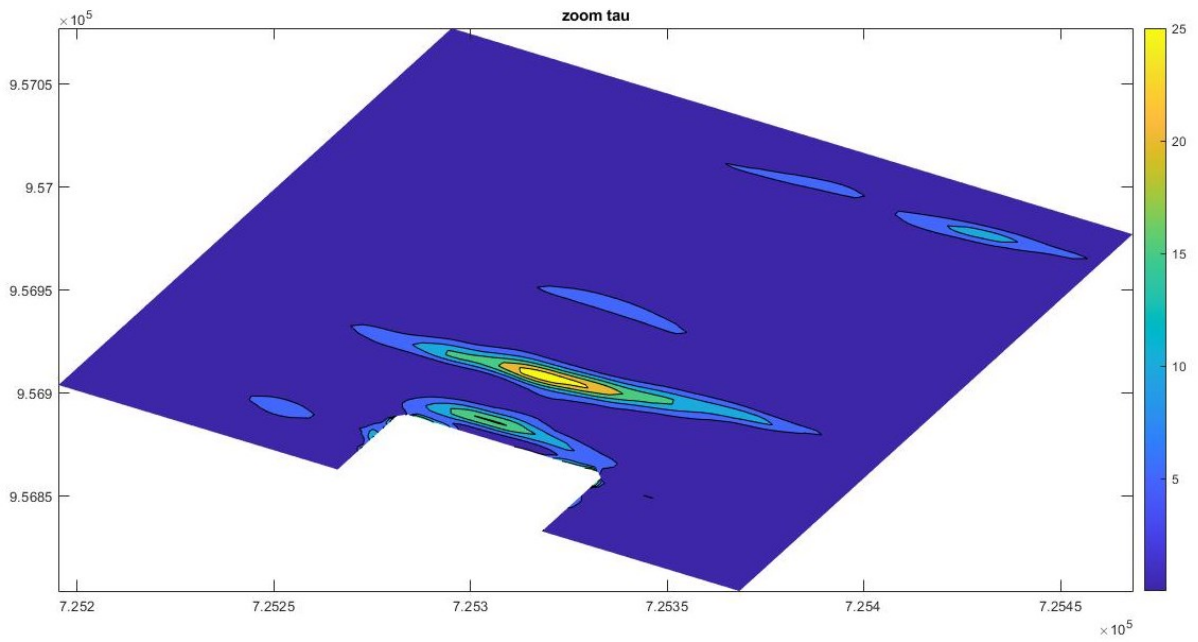


Figure 113 τ in interested area $\left[\frac{Kg}{ms^2}\right]$, case b ($dir=27.11^\circ N$; sponge layer on East and West side)

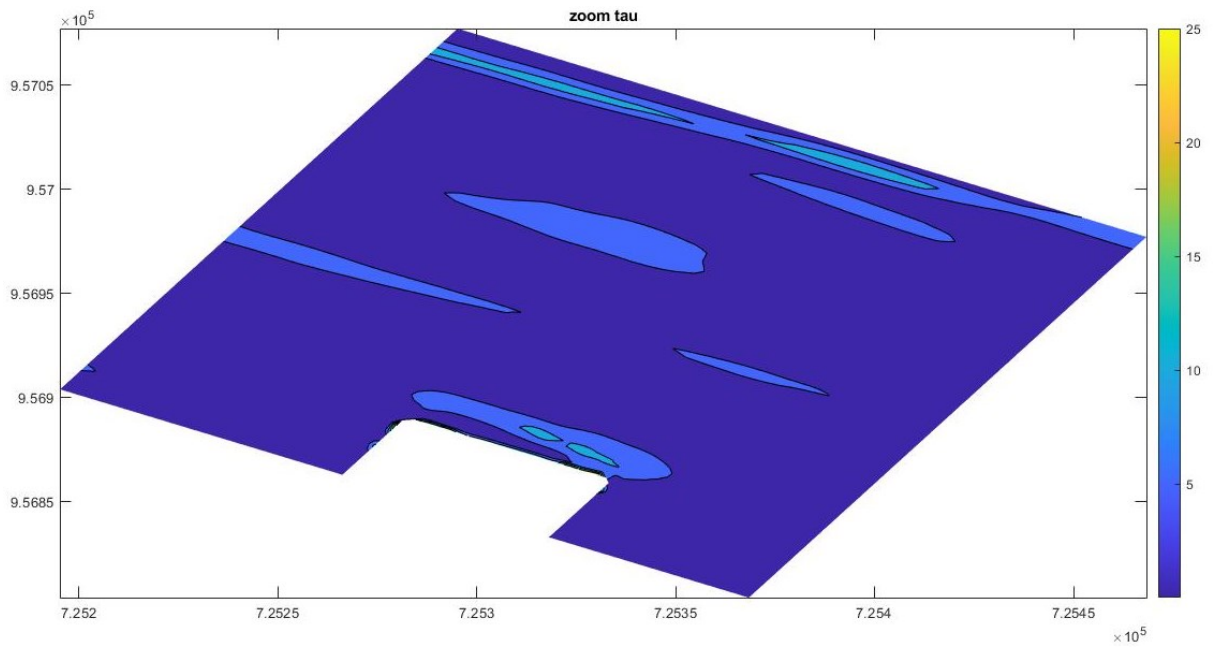


Figure 114 τ in interested area $\left[\frac{Kg}{m.s^2}\right]$, case c ($dir=27.11^\circ N$; sponge layer on East side; 3 hours of simulation)

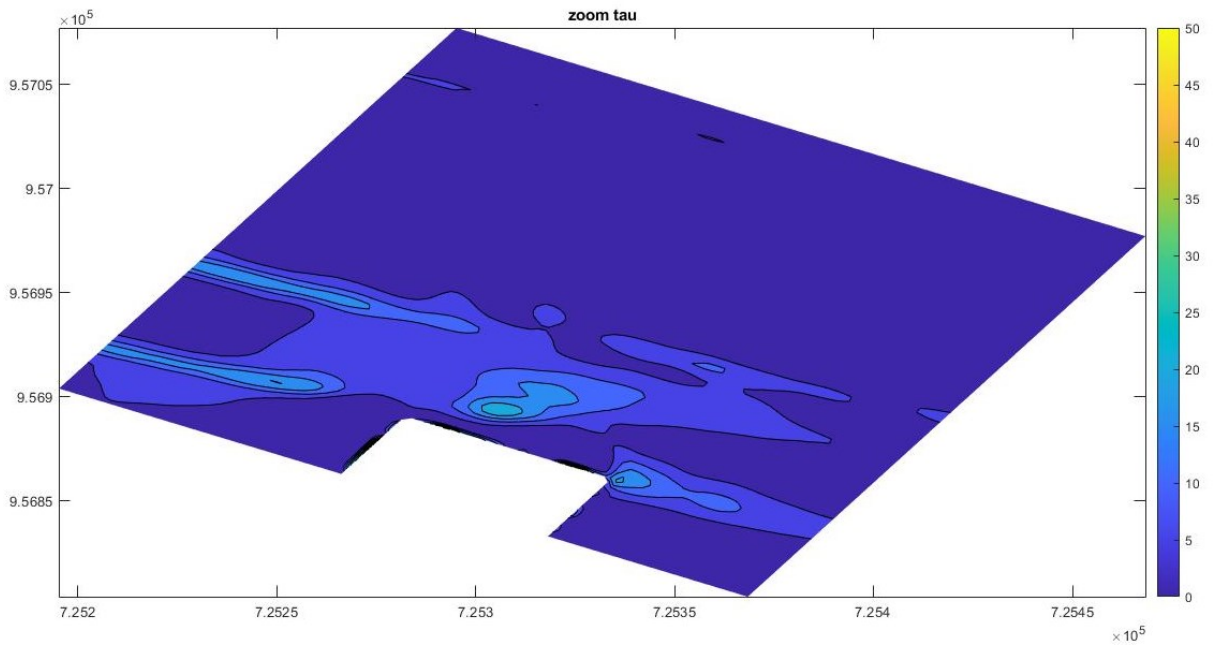


Figure 115 τ in interested area $\left[\frac{Kg}{m.s^2}\right]$, case d ($dir=20^\circ N$; sponge layer on East side)

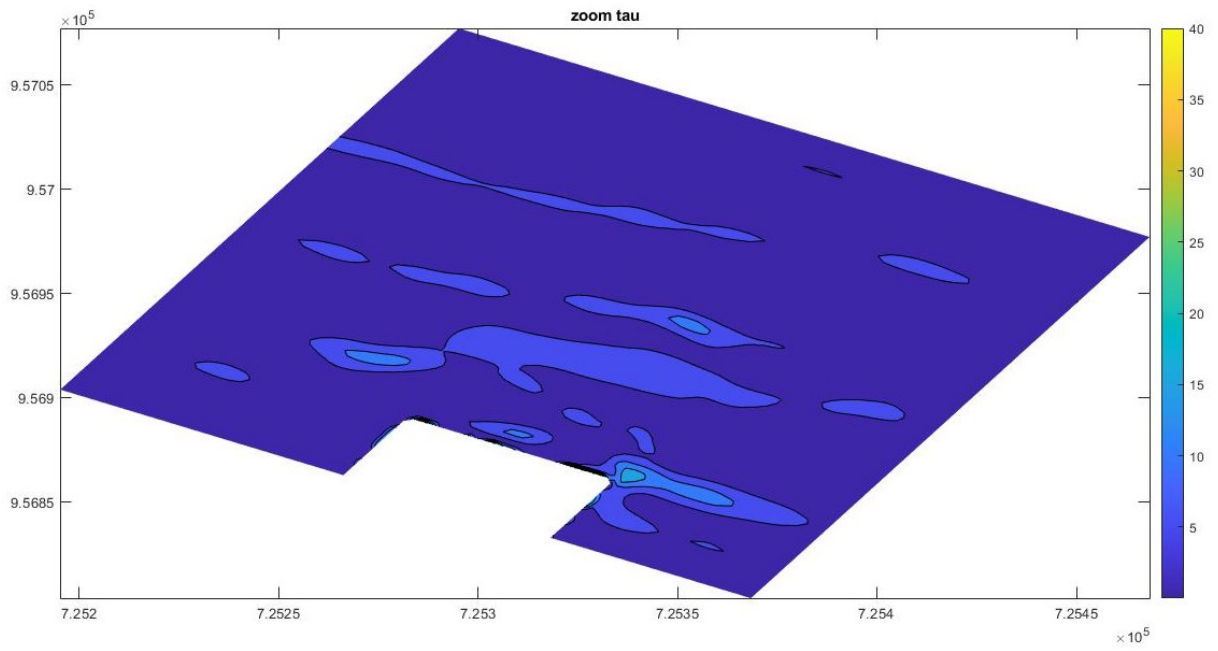


Figure 116 τ in interested area $\left[\frac{Kg}{ms^2}\right]$, case e (dir=20 °N; sponge layer on East and West side)

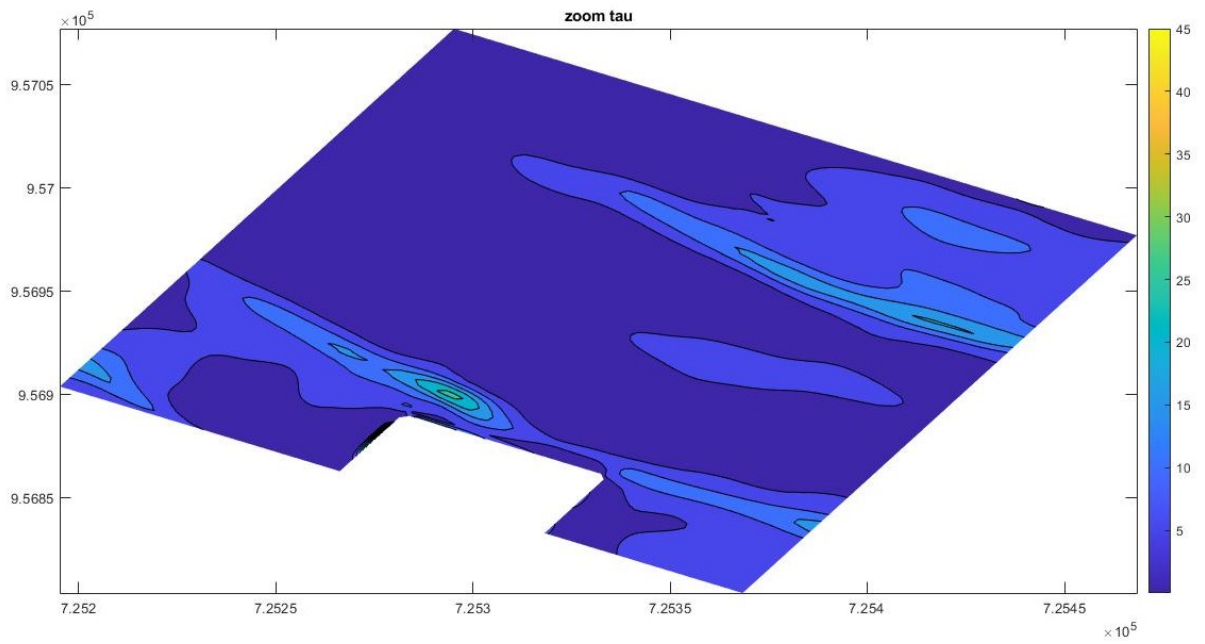


Figure 117 τ in interested area $\left[\frac{Kg}{ms^2}\right]$, case f (dir=27.11 °N; sponge layer on East and West side; with a smoothed bathymetry)

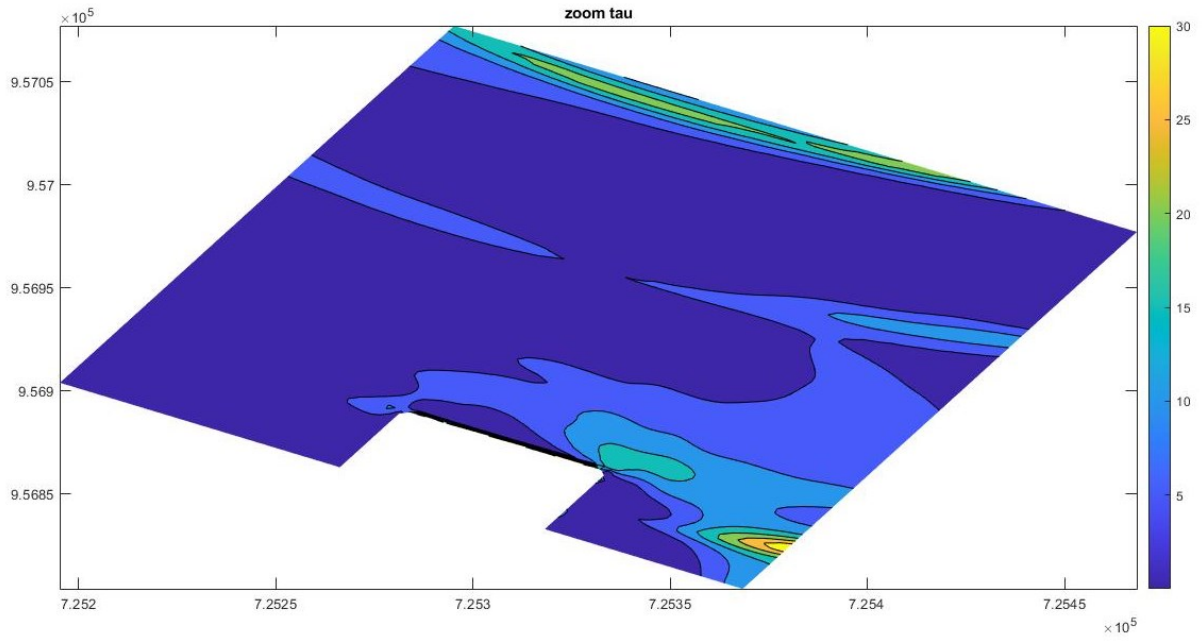


Figure 118 τ in interested area $\left[\frac{Kg}{ms^2}\right]$, case g (dir=27.11 °N; sponge layer on East side; with a large domain)

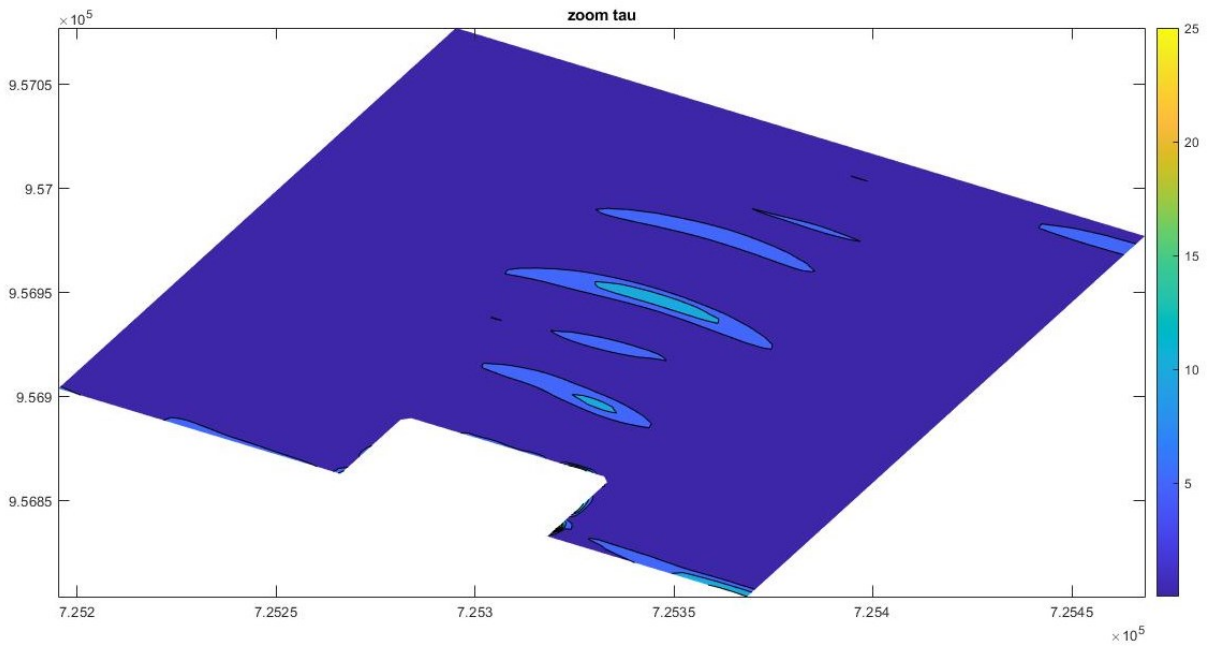


Figure 119 τ in interested area $\left[\frac{Kg}{ms^2}\right]$, case h (dir=27.11 °N; sponge layer on East and West side; with a large domain)

6.2 Discussion

The parameters that most affected the simulation results were: the presence of the double sponge layers, the size of the computational domain and the wave direction.

6.2.1 Double sponge layer

When the simulation is characterized by a double sponge layer, the quality of the results is better, due to the capacity of the sponge layer to absorb the wave energy, avoiding the appearance of parasitic edge effects, such as reflection.

Comparing Figure 72 and Figure 73 it can be seen that the wave field obtained with the double sponge layers is more symmetric.

6.2.2 Size of computational domain

The idea of using a larger computational domain come from the need to reduce the effect of the undertow current close the cofferdam.

The attempt has been successful, especially in the case run with a double sponge layer (Figure 85 and Figure 86), where the undertow current attenuates before reaching the interested area.

6.2.3 Wave direction

It was thought that one of the possible causes of a reduced longshore current was the closeness between the angle of the domain (30°) and that of the wave direction (27°).

The change of wave direction produced an increase in the longshore current intensity especially in the cofferdam area, for both single and double sponge layers and consequently an increase of current shear stress. The value of τ_c , they are almost doubled from 0.5 (Figure 88 τ_c in interested area $\left[\frac{Kg}{ms^2} \right]$, case a (dir=27.11 °N; sponge layer on East side)Figure 88) to 0.9 (Figure 91).

6.3 Observation

In each simulation there is an increase in the bottom shear stress near the causeway. In the following tables (Table 7 and Table 8), the maximum shear stress values are listed in the first table in the whole domain, in the second one in the area close the cofferdam. The maximum

value of total and oscillatory wave shear stress values are highlighted in yellow while the maximum shear stress due to the current is highlighted in green

Case	τ_c	τ_w	τ
a	0.9	35	35
b	1	35	35
c	0.8	25	25
d	2.5	80	80
e	1.4	40	40
f	1.6	55	55
g	1.4	60	60
h	0.4	25	25

Table 7 shear stress for each case analysed, in the total domain

Case	τ_c	τ_w	τ
a	0.5	35	35
b	0.35	25	25
c	0.4	25	25
d	0.9	50	50
e	0.55	40	40
f	1.1	45	45
g	1.4	30	30
h	0.12	25	25

Table 8 shear stress for each case analysed, area in front of the causeway (zoom)

Analysing the tables and figures shown, it can be observed how:

- The oscillatory flow shear stress (τ_w) has two or three orders of magnitude more than the current shear stress (τ_c). It means that the wave propagation has a larger impact on the modification of shear stress and, consequently, on the scouring phenomena.
- The maximum value of the total shear stress has been achieved with a different value of wave direction (MWD = 20°), compared to that obtained from the SWAN analysis. With this simulation it has been analysed how the use of an MWD almost

perpendicular to the coast line (MWD of SWAN outputs 27.11 °N), produced effects on stressful agents. The results show a decrease in shear stress agents for almost perpendicular MWD.

- The maximum shear stress values are close to the cofferdam, as shown also by the vorticity analyses performed. The study of vorticity was not shown for practical reasons. The vorticity of the flow was studied through the Okubo-Weiss (W) parameter:

$$W = s_n^2 + s_s^2 - \omega^2$$

with:

- $s_n = \frac{\partial u}{\partial x} - \frac{\partial v}{\partial y}$;
- $s_s = \frac{\partial v}{\partial x} + \frac{\partial u}{\partial y}$;
- $\omega = \frac{\partial u}{\partial y} - \frac{\partial v}{\partial x}$;

Using the local value of W, the flow domain can be partitioned into three distinct types of regions:

- Vorticity dominated region ($W < 0$)
- Stain-dominated region ($W > 0$)
- Intermediate regions for which ($W \cong 0$) (Kadoch et al. 2011)
- As the previous tables shows, the simulations with double SL (simulations: b, e and h) are characterized by lower shear stress value than the same simulation with one SL. These reductions are probably caused by the absence of boundary reflected effects.
- Comparing the results of simulations b and f, reveals that SWASH is very sensitive to the presence of instability points in the bathymetry, means points with spatial bathymetric gradient, even small variations in the depth of seabed, even in the order of centimeter or less, does not allow the numerical model to reach the convergence. In fact, the set-up of simulations is the same: the only difference is the use, in the case of the simulation f, of a much more smoothed bathymetry than the one used in b. If, on the other hand, there are regions with strong spatial bathymetry gradients, the use of multiple vertical layers, for solvers in shallow water, allows to describe strong vertical flow gradients.

- The use of a greater domain led to the achievement large currents near the causeway and therefore large value of τ_c value. As Figure 85 shows, the current velocity corresponding to the maximum τ_c value is positive. Therefore, it probably corresponds to the longshore current value.
- The simulations characterized by a simulation time of 3 hours do not shown appreciable changes.

6.3.1 Temporal scale of scouring

Case	τ	θ	θ_{cr}	$\theta - \theta_{cr}$
a	35	1.098	0.068	1.03
b	25	0.784	0.068	0.716
c	25	0.784	0.068	0.716
d	50	1.569	0.068	1.50
e	40	1.255	0.068	1.187
f	45	1.412	0.068	1.344
g	30	0.941	0.068	0.873
h	25	0.784	0.068	0.716

Table 9 Shields parameters

As expected, all the cases analysed are characterized by a live bed scouring and therefore they justify the scouring phenomena observed. Obviously, the θ value more distant from the critical Shields number θ_{cr} , is that referring to case d, showing the greatest shear stress value.

Chapter 7 – Conclusion and Recommendation

7.1 Conclusion

SWASH is indeed an extremely valuable tool to simulating the propagation of waves in shallow water. However, this model is still in the early stages of development and still has some bugs and limitations.

A problem encountered during the setting of Swan, is that it is very sensitive to bathymetry variations. In fact, if the bathymetry is not sufficiently smooth in any section of the domain, the simulation moves away from convergence, as can be observed when the residual values are analyzed.

Analysis of the shear stresses shows that the area subject to a strong phenomenon of erosion is roughly where it has been observed in the field. The maximum shear stress is attained close to the cofferdam. Among the set-ups analyzed, the one that shows a result closer to the real case observed, is the set-up e ($H_s = 1.61\text{m}$, $T_p = 11\text{s}$, $\text{dir} = 20^\circ\text{N}$; sponge layer on West and East side and 30min of simulation). In which it is observed that the maximum shear stress value ($50 \frac{\text{Kg}}{\text{m s}^2}$) is close to the right edge, which consequently is the area subject to the maximum scouring, which goes support with what has actually been observed (see Figure 42)

In conclusion, the simulation that best represents the real case is the one with a single sponge layer, as the shear stress produced by simulations with the single sponge layer not only produce the maximum shear stress at the bottom, but they produce it at the right corner, i.e. in the same place where the maximum excavation value was observed (4 meters). From the results of the previous chapter it can be seen that a wave that enters in a non-orthogonal, or almost non-orthogonal way, produces higher shear stress values.

It can also be said that this thesis can be a good starting point for the study of scouring around the temporary structures.

To define the final set-up of the SWASH simulation, several tests were performed, in order to observe the advantages and disadvantages of each single parameter.

- first, different grid size was analyzed, as can also be seen from the analysis shown in the previous chapter. The grids analyzed included areas of different sizes, in the case

of the "small" domain the total area is $1,081 \text{ Km}^2$ ($1020 \times 1260 \text{ m}^2$), in the case of the "large" domain the total area was $3,209 \text{ Km}^2$ ($1420 \times 2260 \text{ m}^2$). The choice to use even a larger grid had the aim of giving more space to the 1.61m wave to stabilize, this choice as mentioned in the previous chapter has been shown to be right because it is known that a positive current value was obtained, which also corresponds to the maximum current value at the causeway.

- the use of one or two layers of sponge. With the single sponge layer, positioned in the direction of origin of the wave, then east (in this case the wave comes from the east, 27.11 or 20°N), values of a greater energy of the flow are obtained compared to the case of the double side of the sponge. However, it should be said that the increase in the value of the various parameters could be influenced by the phenomenon of parasitic reflection of the wave on the opposite edge, which does not occur in the other case.
- the results show that a wave that does not enter almost perpendicular to the coastline produces higher values of the shear stress produced, especially for when it concerns the τ produced by currents.
- the phenomena of horizontal viscosity allowed by SWASH are 3: constant, Smagorinsky and Prandtl. In this work the Smagorinsky and Prandtl models were tested, the constant one was excluded because it was considered too approximate. There were no appreciable variations on the quality of the result or the calculation times, for this reason it was chosen to use that of SMA which has greater precision, the quality of the result of Prandtl is subject to the size of the domain links used (in this case 2m).

7.2 Recommendations

This section will focus on all the ideas that have emerged during the development of the thesis that could help users starting to use SWASH for the first time and facilitate the spread of this model.

7.2.1 Recommendations for the developers of the model

The first suggestion is to make SWASH more user-friendly. The reason for this is that it takes time to learn how to use it unless the user is acquainted with previous models such as SWAN. Thus, the implementation of a GUI (Graphical User Interface) where the user could input easily

the different settings and parameters would help to spread the model. Furthermore, nowadays a post processing of the results using other tools like Matlab is necessary. The implementation of a version where, if requested by the user, plots of the required output parameters were produced, would also help to make it more user-friendly.

Another important factor to be improved in SWASH is the way it models breakwaters. Nowadays the only way to implement the wave breaking is the Forchheimer parameters α and β . These parameters are the same for each layer in the same spot and thus it is not possible to model properly a rubble mound breakwater as SWASH calculates a mean value of the porosity depending on the height of the structure, the porosity and the water depth and applies this value to all the layers. A suggestion to overcome this problem could be to input the values of the parameters for each layer, or in case the height of the structure was less than the water depth, to consider different values for the different layers. This is in essence to use different input parameters for different layers. In addition to this, the Forcheimer dissipative terms should also be included in the vertical momentum equation as Mellink (2012) suggested. By this method, a sloping porous structure would be reproduced in a more realistic way.

It would be good to include wave-breaking-induced turbulence in the model. Presently some extra spreading is provided by the Smagorinsky horizontal mixing model in presence of velocity gradients. If wave-breaking- induced turbulence is included, this would better represent reality and spreading of currents would be improved. In this way, calculations made specifically to identify the value of the currents acting could be avoided, also speeding up the acquisition of a result and reducing the possibility of mistake.

The model also proved very sensitive to the type of bathymetry and becomes unstable in the presence of sawtooth-shaped areas. As recommended by the user manual, extremely steep slopes must be avoided, but at the same time we hope to reduce this sensitivity, in order not to be forced to extremely smooth the real bathymetry, thus losing realism.

7.2.2 Recommendations for the SWASH application

To use SWASH in coastal domains, it is suggested to use the second discretization scheme against the backwash that guarantees the stability of the model. In addition to modeling

structures, the use of porous layers in combination with the inclusion of their slopes in bathymetry seems the best option as it is more flexible and stable.

It is also suggested to start simply by entering a new parameter or input from time to time, in this way it is possible to validate and check that what has been processed works and provides real data, until the simulation is reached as close as possible to reality.

For climates with real waves, it is recommended to start with a grid size of no more than 5 meters, check that the simulation is stable and that the results are realistic, then reduce the grid size to 2 or 1 m according to the required precision and available computing power.

The easiest error code to obtain is "UNSTABLE: the water level is too below the lower level", the error is often due to the presence of instability points in the bathymetry. To overcome this error, it is recommended to use a very smooth bathymetry.

It is also recommended to set a computation time of less than 1 second to improve the performance of the model and avoid too many corrections through the CFL criterion which slow down the analysis.

Reference

- [1] M.Postacchini lecture notes of *“Hydraulic engineering and Renewable energy A.A. 2018/19”*
- [2] Y. Goda *“Random sea and design of maritime structures”* Advanced Series on Ocean Engineering
- [3] *“Environmental conditions and environmental loads”* DNVGL-RP-C205, edition August 2017
- [4] B.Mutlu Sumer & Jørgen Fredsøe *“The Mechanics of Scour in the Marine Environment”* World Scientific
- [5] *“The Rock Manual, the use of rock in hydraulic engineering”* CIRIA
- [6] Leo C. van Rijn *“Local scour near structure”*
- [7] B. Mutlu Sumer and Jørgen Fredsøe *“TIME SCALE OF SCOUR AROUND A LARGE VERTICAL CYLINDER IN WAVES”*
- [8] B. Mutlu Sumer; Figen Hatipoglu and Jørgen Fredsøe *“Wave Scour around a Pile in Sand, Medium Dense, and Dense Silt”*
- [9] S.A. Miedema *“CONSTRUCTING THE SHIELDS CURVE, A NEW THEORETICAL APPROACH AND ITS APPLICATIONS”*
- [10] Can Chen, S.M. ASCE and Jie Zhang, M. ASCE, Ph.D., P.E. *“A Review on Scour Modeling below Pipelines”*
- [11] SWAN user manual, DELFT3D University
- [12] SWAN scientific and technical documentation, DELFT3D University
- [13] SWASH user manual, DELFT3D University
- [14] SWASH AND SWAN INPUT FILES, DELFT3D University
- [15] M.Zijlema, G.Stelling, P.Smit *“SWASH: An operational public domain code for simulating wave fields and rapidly varied flows in coastal waters”* Coastal Engineering
- [16] M.Cardellini thesis (2016) *“Wave and coastal circulation modeling. A SWASH application with permeable and impermeable structures”*
- [17] F.Angelini thesis (2016) *“Simulation of coastal sea states. SWAN model application on unstructured grid”*

Appendix A

A.1 SWAN input file

```
$*****HEADING*****  
  
$  
PROJ 'Name' '1'  
  
$  
$*****MODEL INPUT*****  
  
$  
SET 0 90 0.01 200 1 9.81 1025 0.0025 0 0.1 NAUTICAL 4 0.8 4 4  
  
MODE NONSTATIONARY TWODimensional  
  
COORDinates CARTesian  
  
$  
CGRID UNSTRUC CIR 18 0.08 1. 20  
  
READ UNSTRUC TRIA 'tesi'  
  
$  
INP BOT UNSTRUC  
  
READ BOT 1 'tesi.bot'  
  
$  
INP WI REG 680000 920000 0 1 1 150000 130000 NONSTAT 20020104.190000 1 HR  
20020112.060000  
  
READ WI 1 'wind_N_01012002_10min.txt' 3 0 FREE  
  
$  
BOU SIDE 2 CCW CON FILE 'TPAR_1_N_01012002.txt' 1
```

BOU SHAP JON PEAK DSPR DEGR

\$

GEN2

OFF WCAP

BRE CON 1.2 0.83

FRIC COLL 0.03

TRI 1 0.65

LIM 10.0 1.0

OFF FShift

\$

\$*****MODEL OUTPUT*****

\$

POINTS 'SWASH' 725520.5625 957329.6875

Table 'SWASH' HEADER 'OUTPUT_SWASH.dat' TIME HSIGN RTP DIR DSPR OUTPUT

20020104.190000 1 HR

POINTS 'H1' 749431.102 1015998.279

Table 'H1' HEADER 'OUTPUT_H1.dat' TIME HSIGN RTP DIR DSPR OUTPUT 20020104.190000

1 HR

POINTS 'MIS' 721059.84 963845.91

Table 'MIS' HEADER 'OUTPUT_MIS.dat' TIME HSIGN RTP DIR DSPR OUTPUT

20020104.190000 1 HR

BLOCK 'COMPGRID' NOHEAD 'GRIDOUT.MAT' LAYOUT 3 XP YP BOTLEV HSIGN RTP DIR DSPR

DEPTH OUTPUT 20020104.190000 1 HR

CURve 'HH3' 725116.46 957563.41 24 725998.12 957053.41

SPECout 'HH3' SPEC2D ABS 'spec' OUT 20020104.190000 1 HR

TEST 1 0

COMP NONSTAT 20020104.190000 1 HR 20020112.060000

STOP

A.2 SWASH input file (case d)

```
*****STAR-UP*****  
  
PROJect 'Name' '1'  
  
SET 0 90 0.01 200 1 12345678 9.81 1000 0 0 0.001 1.205 2650 0.0025 -1 0 0.4 NAUT 4 4 3  
  
MODE NONSTATIONARY TWODimensional  
  
COORDinates CARTesian  
  
$  
  
$ *****MODEL DESCRIPTION*****  
  
$*****COMPUTATIONAL GRID*****  
  
CGRID REGular 724551.498 956584.85 330 1020 1260 510 630  
  
VERTical 1 100 PERC  
  
$  
  
$*****INPUT GRID AND DATA*****  
  
INPgrid BOTtom REGular 724551.498 956584.85 330 510 630 2 2 EXC -0.8  
  
READinp BOTtom 1 'cofferdam2tris.txt' 3 0 FREE  
  
INPgrid PORO REGular 724551.498 956584.85 330 510 630 2 2  
  
READinp PORO 1 'poro_Slcoff_0.45_0.001.txt' 3 0 FREE$  
  
$*****BOUNDARY AND INITIAL CONDITION*****  
  
BOU SEGM IJ 1 631 511 631 CON SPECT 1.61 11.017 20 0 3 HR  
  
BOU SEGM IJ 1 1 1 631 BTYP SOMM  
  
BOU SEGM IJ 511 1 511 631 BTYP SOMM  
  
SPONGelayer E 40  
  
PORO 0.0001 99999 1000 28
```

\$

\$*****PHYSICS*****

FRICtion MANNing 0.019

BREaking 0.6 0.3

VISCosity Horizontal SMAGorinsky 0.2

\$

\$*****NUMERICS*****

INIT ZERO

TIMEI METH EXPL 0.1 0.8

DISCRET CORR BDF

DISCRET UPW UMOM H BDF

DISCRET UPW WMOM H BDF

DISCRET UPW UMOM V BDF

DISCRET UPW WMOM V BDF

NONHYDrostatic BOX 1 RED 0 SOLV 0.01 0 500 0.55 PREC ILU

\$

\$*****OUTPUT*****

QUANTity VEL 'VEL' 'Vel' 0 1000 -9999 PROBLEMcoord

QUANTity HSIG 'HS' 'Hsig' 0 1000 -9999 dur 30 MIN

QUANTity HRMS 'HRMS' 'Hrms' 0 1000 -9999 dur 30 MIN

BLOCK 'COMPGRID' NOHEAD 'GRIDOUT.MAT' LAYOUT 3 XP YP VEL BRKP HS BOTLEV WATLEV

OUTPUT 082000.000 1 SEC

\$

TEST 1 0

\$

\$*****LOCK-UP*****

COMPute 080000.000 0.1 SEC 083000.000

STOP